

**DESIGN STRATEGIES FOR ROTORCRAFT BLADES AND HALE  
AIRCRAFT WINGS APPLIED TO DAMAGE TOLERANT WIND  
TURBINE BLADE DESIGN**

A Dissertation  
Presented to  
The Academic Faculty

by

Phillip W. Richards

In Partial Fulfillment  
of the Requirements for the Degree  
Doctor of Philosophy in the  
School of Aerospace Engineering

Georgia Institute of Technology  
May 2015

Copyright © 2014 by Phillip W. Richards

**DESIGN STRATEGIES FOR ROTORCRAFT BLADES AND HALE  
AIRCRAFT WINGS APPLIED TO DAMAGE TOLERANT WIND  
TURBINE BLADE DESIGN**

Presented to:

Professor Dewey H. Hodges,  
Committee Chair  
School of Aerospace Engineering  
*Georgia Institute of Technology*

Professor Dewey H. Hodges, Advisor  
School of Aerospace Engineering  
*Georgia Institute of Technology*

Professor George Kardomateas  
School of Aerospace Engineering  
*Georgia Institute of Technology*

Professor Julian J. Rimoli  
School of Aerospace Engineering  
*Georgia Institute of Technology*

Dr. D. Todd Griffith  
Principal Member of the Wind and Water  
Engineering Principal Staff  
*Sandia National Laboratories*

Professor Graeme Kennedy  
School of Aerospace Engineering  
*Georgia Institute of Technology*

Date Approved: December 2, 2014

*To my family,*

*Lyn and John Richards, my parents*

*Joel Richards and Julia Yarei, my siblings*

*Bri McDaniel, my fiance*

*for love, support, and fellowship*

## ACKNOWLEDGEMENTS

I want to sincerely thank Professor Dewey Hodges for his valued advice and friendship. I would also like to acknowledge Professor Marilyn Smith for her support during my undergraduate years as a research advisor. I'd like to thank Dr. Patrick Hu, for taking me on as a young graduate student and setting me on my path. I had an extraordinary amount of help from Jenn Player, Nathan Graybeal, Ryan Neuhart, and Jack Ralston, and had the honor to participate in an extremely rewarding project. Also, I want to thank Sandia National Laboratories and especially Dr. D. Todd Griffith, for instrumental direction and inspiration in completing this work. Throughout the years at Georgia Tech, I have had the honor of working with several other doctoral candidates that have done much to inspire and encourage me, particularly Eliot Quon, Pezhman Mardanpour, and Anurag Rajagopal. Several undergraduate students at Georgia Tech have assisted me as well, but Robert Herd and Yuan Yao were especially helpful with my research efforts.

# TABLE OF CONTENTS

<b>DEDICATION</b>	<b>iii</b>
<b>ACKNOWLEDGEMENTS</b>	<b>iv</b>
<b>LIST OF TABLES</b>	<b>viii</b>
<b>LIST OF FIGURES</b>	<b>x</b>
<b>LIST OF SYMBOLS OR ABBREVIATIONS</b>	<b>xvi</b>
<b>SUMMARY</b>	<b>xx</b>
<b>I INTRODUCTION</b>	<b>1</b>
1.1 Concepts . . . . .	3
1.1.1 Aeroelastic Design . . . . .	3
1.1.2 WT Blade Damage Modeling and Analysis . . . . .	4
1.1.3 Smart Loads Management for Damaged Blades . . . . .	5
1.1.4 Damage Tolerant Design . . . . .	6
<b>II BACKGROUND</b>	<b>7</b>
2.1 Analysis of Damage Effects . . . . .	8
2.1.1 Global Effects of Damage . . . . .	8
2.1.2 Local Effects of Damage . . . . .	10
2.1.3 Stress-based Fatigue Predictions . . . . .	10
2.1.4 Energy-based Fatigue Predictions . . . . .	12
2.2 Operation and Maintenance Strategies . . . . .	15
2.2.1 Control System Considerations . . . . .	16
2.2.2 Optimal Control of Structural Systems . . . . .	18
2.3 Damage Tolerant Design Strategies . . . . .	19
<b>III BLADE OPTIMIZATION FROM ROTORCRAFT PERSPECTIVE</b>	<b>21</b>
3.1 Introduction . . . . .	21
3.2 Optimization Problem Definition . . . . .	22
3.3 Global Level Optimization of non-Uniform Blades . . . . .	23
3.4 Feasibility Constraints and Scaling Laws for Simple Cross Sections . . . . .	29
3.4.1 Isotropic Circular Cross Section . . . . .	29
3.4.2 Isotropic Elliptic Cross Section . . . . .	30
3.5 Demonstration of Multi-Level Process for a Realistic Rotor Blade . . . . .	32
3.5.1 Definition of the Local Design Space . . . . .	32
3.5.2 Sampling of the Local Design Space . . . . .	34
3.5.3 Global Level Optimization . . . . .	36
3.5.4 Local Level Optimization . . . . .	40
3.5.5 Combined Optimization . . . . .	43
3.5.6 Non-Uniform Blade Optimization . . . . .	44
3.6 Conclusions . . . . .	49
<b>IV AEROELASTIC STRUCTURAL AND CONTROL DESIGN FOR HALE AIRCRAFT</b>	<b>51</b>
4.1 Introduction . . . . .	52
4.2 NATASHA Theory . . . . .	53
4.2.1 Finite Element Discretization . . . . .	54

4.2.2	NATASHA Trim Solution Process . . . . .	54
4.3	Flying Wing Model . . . . .	57
4.3.1	Geometric Description of the Model . . . . .	57
4.3.2	Geometric Description of a Typical Section . . . . .	58
4.3.3	Engine/Fuselage Description . . . . .	59
4.3.4	Aerodynamic Model . . . . .	59
4.3.5	Baseline Flutter Results and Eigenvalue Analysis . . . . .	60
4.3.6	“Typical” Flying Wing Model . . . . .	61
4.4	Trade Studies on Body Freedom Flutter . . . . .	63
4.4.1	Effect of Fuselage Properties on Flutter Speed . . . . .	63
4.4.2	Effect of Changing Structural Geometry . . . . .	65
4.5	Eigenvalue and Eigenvector Analysis for Various Cases . . . . .	68
4.5.1	Maximum Skin Thickness . . . . .	68
4.5.2	Maximum Flange Thickness . . . . .	69
4.5.3	Minimum Fuselage Mass . . . . .	71
4.5.4	Maximum Fuselage Inertia . . . . .	71
4.5.5	Comparison Between Linear and Nonlinear Flutter . . . . .	72
4.6	Realistic Structural Model for HALE Aircraft . . . . .	75
4.6.1	Design Requirements for HALE Aircraft . . . . .	75
4.6.2	Realistic Interior Structure for HALE Aircraft . . . . .	76
4.6.3	3D Effects for HALE Aircraft Wings . . . . .	77
4.7	Aeroelastic Control Design . . . . .	81
4.7.1	Control Derivatives . . . . .	82
4.7.2	Symmetric Model . . . . .	84
4.7.3	Linear Output Signal Modification . . . . .	85
4.7.4	Linear Gust Analysis . . . . .	87
4.7.5	Nonlinear Analysis Capability . . . . .	91
4.7.6	Nonlinear Analysis . . . . .	92
4.7.7	State-Space Model . . . . .	92
4.7.8	Modal Reduction of State Space Model . . . . .	96
4.7.9	Discretized Version of the State-Space Equation . . . . .	97
4.7.10	Types of Controllers Considered . . . . .	98
4.7.11	Nonlinear Simulation with Linear Kalman Filter and Controller . . . . .	101
4.8	Conclusions . . . . .	102
<b>V</b>	<b>WT BLADE DAMAGE MODELING AND ANALYSIS</b>	<b>106</b>
5.1	Validation of VCCT for Isotropic Sections . . . . .	107
5.2	Damaged Blade Modeling . . . . .	108
5.3	Healthy Blade Bond Line Stress Results . . . . .	109
5.4	SERR Calculations Under Normal Operation . . . . .	109
5.5	SERR Calculations Under Derated Operation . . . . .	115
5.6	Buckling Capacity of Damaged Blades . . . . .	116
5.7	Conclusions . . . . .	117
<b>VI</b>	<b>SMART LOADS MANAGEMENT FOR DAMAGED WT BLADES</b>	<b>119</b>
6.1	Economic Incentive to Derating . . . . .	119
6.1.1	Derating as an Alternative to Shutdown . . . . .	120
6.1.2	Derating to Delay Maintenance . . . . .	121
6.2	Control Design of WT Blades Using MBC . . . . .	122
6.3	Variable-speed, Variable-pitch Controller . . . . .	125
6.4	Derating . . . . .	128
6.5	Load-mitigating Control Design . . . . .	129
6.6	ANSYS Analysis of Damage Mitigation . . . . .	139
6.7	Conclusions . . . . .	139

<b>VII DAMAGE TOLERANT DESIGN FOR OFFSHORE WT BLADES</b>	<b>141</b>
7.1 Combined Aero/Structural Optimization . . . . .	142
7.2 Blade Cost Comparisons . . . . .	145
7.3 Comparison of Potential 100 m Designs . . . . .	148
7.4 Conclusions . . . . .	151
<b>VIII CONCLUSIONS AND FUTURE WORK</b>	<b>152</b>
8.1 Conclusions . . . . .	152
8.2 Future Work . . . . .	154
<b>REFERENCES</b>	<b>156</b>
<b>VITA</b>	<b>166</b>

## LIST OF TABLES

1	Problem summary for the realistic rotor blade optimization example. . . . .	33
2	Material properties for a realistic rotor blade. $G_{ij}$ refer to shear moduli. . . . .	33
3	Description of surrogate models created from local sampling of design space. . . . .	36
4	Description of the beam geometry for the global level optimization example. . . . .	36
5	Baseline layup and analysis results, where $\omega_i$ refers to the $i^{\text{th}}$ natural frequency, $x_s$ is the shear center relative location (positive is aft of 1/4 chord), and $x_m$ is mass center relative location. . . . .	38
6	Baseline stiffness matrix for the realistic design example. Units are psi. . . . .	39
7	General description of global level optimization problem. . . . .	40
8	A valid result from the global level optimization. . . . .	40
9	A valid result from the global level optimization that was used as a target for the local level optimization inverse design problem. . . . .	40
10	Description of local level optimization design variable bounds and tolerances. . . . .	42
11	General description of local level optimization problem. . . . .	42
12	Natural frequency results from local level optimization candidates with stiffness results satisfying or nearly satisfying target stiffness constraints. $G\omega_i$ , $R\omega_i$ , and $RD_i$ refer respectively to the natural frequency predicted by GEBT and RCAS and the damping predicted by RCAS for the $i^{\text{th}}$ mode. All frequency and damping values are in units of rad/s. . . . .	43
13	Optimized layup and analysis results. . . . .	44
14	GEBT frequency analysis of a linearly tapered blade using two scaling techniques. . . . .	46
15	Valid result from the global level optimization of a non-uniform beam using perfect scaling laws. . . . .	48
16	RCAS frequency analysis results of a linearly tapered blade, using two scaling techniques. $\omega_i$ refers to the $i^{\text{th}}$ natural frequency, and $D_i$ refers to the damping of the $i^{\text{th}}$ mode. Both frequency and damping are given in units of rad/s. . . . .	49
17	Geometric NATASHA inputs for the typical flying wing model. . . . .	58
18	Structural NATASHA inputs for the typical flying wing model. . . . .	59
19	Inertial NATASHA inputs for the typical flying wing model. $H$ refers to the angular momentum of the engine. Note that the fuselage inertias were set as functions of the fuselage mass $\hat{\mu}_f$ . . . . .	59
20	The aerodynamic coefficients used in the NATASHA model. The airfoil profile and coefficients were held constant along the span. . . . .	60
21	Characterization of baseline eigenvalue results in terms of structural vibration and flight dynamical modes. . . . .	61
22	Material properties for realistic structural design of HALE aircraft wing. . . . .	77
23	Trade study of structural design variables for number of skin layers $N_s$ and number of spar layers $N_c$ . . . . .	77
24	Trade study of spar chordwise location for realistic HALE aircraft, with number of skin layers $N_s = 1$ and number of spar layers $N_c = 10$ . . . . .	78
25	Comparison study of maximum direct ( $\sigma_{11}$ ) and shear ( $\tau_{1s}$ ) stresses at wing root between two configurations at design flight condition of 160 m/s and 60 km altitude. Von-Mises equivalent stress measures ( $\sigma_{eq}$ ) are also given. . . . .	78
26	Strain energy release rate of DCB test with respect to grid size. . . . .	107
27	3D ANSYS blade model grid sizes and approximate run times for one analysis on a simple Windows PC. . . . .	109
28	Reduction in averaged SERRs for 8 m disbond location under 50% derated operation, weighted by a Rayleigh wind distribution with average windspeed of 10 m/s. . . . .	116
29	Possible revenues (using 10 ¢/kWh) for operating at derated level for two weeks instead of shutdown. . . . .	124



30	Variations in possible revenue increases (using 10 ¢/kWh) due to monthly windspeed variation, when derating for two weeks instead of shutdown. . . . .	124
31	100 m blade design candidate details, DU series airfoils. . . . .	145
32	100 m blade design details, FB airfoils. . . . .	148

## LIST OF FIGURES

1	Wind profile for “extreme coherent gust with direction change” analysis. $V_x$ is aligned with the shaft axis and $V_y$ is perpendicular to the shaft direction (but not vertical).	8
2	Bilinear constitutive model for cohesive zone elements (Reference [94]). . . . .	15
3	Derated (50% power level) power production control scheduling, and root bending moment compared with normal/baseline operation. . . . .	18
4	Depiction of variable-speed, variable-pitch WT control system [18]. . . . .	18
5	Sampling results for an elliptic cross section primary stiffnesses using Equation (16)	31
6	Blade cross section for realistic rotor blade optimization example . . . . .	34
7	Variation of the inertial properties $\mu$ , $i_{22}$ , $i_{23}$ , and $i_{33}$ as a function of span for a linearly tapered blade which is perfectly scaled. . . . .	46
8	Variation of the components of the smaller components of the upper right $3 \times 3$ subset of the Generalized Timoshenko stiffness matrix as a function of span for a linearly tapered blade which is perfectly scaled. . . . .	46
9	Variation of the inertial properties $\mu$ , $i_{22}$ , $i_{23}$ , and $i_{33}$ as a function of span for a linearly tapered blade which is realistically scaled (by number of plies). . . . .	47
10	Variation of the components of the smaller components of the upper right $3 \times 3$ subset of the Generalized Timoshenko stiffness matrix as a function of span for a linearly tapered blade which is realistically scaled (by number of plies). . . . .	47
11	Finite element model of the typical geometry for input into NATASHA. The axes are in units of meters, and the “X” marks indicate the location of the fuselage center of gravity CG and two engines at their root location. See Table 17 for numerical details about the baseline geometry. . . . .	58
12	Very simple cross-sectional geometry used for VABS analysis to obtain baseline stiffnesses. The axes have units of centimeters. . . . .	59
13	Eigenvalue analysis results for the baseline model. Instability is found at the flight speed of 32 m/s. . . . .	61
14	SP and symmetric out-of-plane bending (SOP) eigenvector characterization in terms of magnitude and phase of root bending moment $M_2$ , tip vertical velocity $V_3$ , and root angular velocity $O_1$ . Eigenvectors were normalized so that root vertical velocity $(V_3)_r$ magnitude was 1 m/s and then phase-shifted so that $(V_3)_r$ phase is zero. . . . .	62
15	Low frequency eigenvalues for the “typical” flying wing model for the baseline and after modifying $c_{l_0}$ , $c_{l_s}$ , and all coefficients related to $c_d$ and $c_m$ . Curves are not labeled because they coincide exactly. . . . .	63
16	Control settings for the “typical” flying wing model for the baseline and after modifying $c_{l_\alpha}$ . . . . .	63
17	Flutter speed and frequency as a function of a multiplicative fuselage mass factor. . . . .	64
18	Flutter speed and frequency as a function of a multiplicative fuselage pitch inertia factor. . . . .	65
19	Flutter speed and frequency as a function of longitudinal CG location, measured forward of the wing. . . . .	65
20	Flutter speed and frequency as a function of fuselage $z$ -location with respect to the wing. . . . .	65
21	Flutter speed as a function of increasing skin thickness. . . . .	66
22	Flutter speed as a function of increasing flange thickness. . . . .	66
23	Change in constitutive properties as skin thickness and flange thickness were increased from their minimum (Geometry Increase = 0) to their maximum (Geometry Increase = 1). Skin thickness was varied from 0.127 to 0.381 cm, and flange thickness varied from 0.127 to 1.016 cm. . . . .	67
24	Flutter speed as a function of increasing skin and flange thickness as a function of mass per length of the root section (left) or bending stiffness of the root section (right). . . . .	67

25	Flutter speed as a function of increasing skin thickness, with each constitutive property varied independently. . . . .	68
26	Eigenvalue analysis results for the model with maximum skin thickness (0.381 cm). Flutter speed is 38.2 m/s. . . . .	69
27	Short-period (SP) and symmetric out-of-plane bending (SOP) eigenvector characterization in terms of magnitude and phase of root bending moment $M_2$ , tip vertical velocity $V_3$ , and root angular velocity $\Omega_1$ . Eigenvectors were normalized so that root vertical velocity $V_3$ magnitude was 1 m/s and zero phase. Results are shown for the maximum skin thickness (0.381 cm). . . . .	69
28	Eigenvalue analysis results for the model with maximum flange thickness (1 cm). Flutter speed is 39.4 m/s. . . . .	70
29	Short-period (SP) and symmetric out-of-plane bending (SOP) eigenvector characterization in terms of magnitude of root bending moment $M_2$ , tip vertical velocity $V_3$ , and root angular velocity $\Omega_1$ . Eigenvectors were normalized so that root vertical velocity $V_3$ magnitude was 1 m/s and phase was zero. Results are shown for the maximum flange thickness (1 cm). . . . .	70
30	Eigenvalue analysis results for the model with small fuselage mass factor of 0.4. . . .	71
31	Short-period (SP) and out-of-plane bending (SOP) eigenvector characterization in terms of magnitude of root bending moment $M_2$ , tip vertical velocity $V_3$ , and root angular velocity $\Omega_1$ . Eigenvectors were normalized so that root vertical velocity $V_3$ magnitude was 1 m/s. Results are shown for a small fuselage mass factor (0.4). . . .	72
32	Eigenvalue analysis results for the model with a large fuselage inertia factor 1.7. . . .	72
33	Short-period (SP) and out-of-plane bending (SOP) eigenvector characterization in terms of magnitude of root bending moment $M_2$ , tip vertical velocity $V_3$ , and root angular velocity $\Omega_1$ . Eigenvectors were normalized so that root vertical velocity $V_3$ magnitude was 1 m/s. Results are shown for a large fuselage inertia factor (1.7). Phase of $O_1$ not shown for SOP mode because for this case the magnitude of $O_1$ for the SOP mode is zero. . . . .	73
34	Three-plot of transient response (left) with Fourier single-sided amplitude spectrum results (middle) and the filtered signal (right), for below flutter speed (top) and above flutter speed (bottom). . . . .	74
35	Change of damping and frequency of SOP mode with respect to flight speed, comparing linear eigenvalue analysis results with post-process of nonlinear timestep data. . . . .	74
36	Magnitude ratio between tip velocity and root velocity (left). Phase shift between tip velocity and root velocity (right). . . . .	75
37	Eigenvalue analysis results for the baseline realistic model at sea level altitude. . . .	78
38	Eigenvalue analysis results for the baseline realistic model at an altitude of 60 km. . .	78
39	Trim results for rigid typical model at altitude of 60 km with and without 3D correction. . . . .	80
40	Lift and drag polars for rigid typical model at altitude of 60 km, with and without 3D correction. . . . .	80
41	Linearized and symmetric state-space model. Note that inputs as well as outputs are perturbations of the trim values. For example, the first output $V_T$ in the model corresponds to $\Delta V_T$ . . . . .	87
42	Frequency response magnitude of the root wing bending moment response with respect to a uniform oscillating gust. The magnitude is normalized by its steady-state value. . . . .	90
43	Frequency response magnitude of the root wing bending moment response with respect to an anti-symmetric oscillating gust. The magnitude is normalized by its steady-state value. . . . .	90
44	The general architecture of the aeroelastic controller within the context of the provided Bihrl controller. . . . .	93
45	The inner feedback loop showing the aeroelastic controller, NATASHA analysis block, and gust model block. . . . .	93

46	The NATASHA analysis process that executes one timestep of the NATASHA nonlinear analysis. . . . .	94
47	The gust model can either be specified by the user in the form of a defined gust profile or if continuous random gusting is desired a continuous gust model is built in. . . . .	94
48	The modified SIMULINK model showing the inner loop of the adaptive aeroelastic controller. . . . .	102
49	The modified NATASHA nonlinear timestep block for the adaptive aeroelastic controller.	103
50	The adaptive Kalman filter, which works as a state-space model with linearly interpolated system matrices. . . . .	103
51	The response to a continuous 0.05 s gust at 75 kts: pitch attitude. . . . .	104
52	The response to a continuous 0.05 s gust at 90 kts: pitch attitude. . . . .	104
53	VCCT test case: rectangular sample with horizontal mid-plane crack. . . . .	107
54	VCCT results for rectangular sample with horizontal mid-plane crack. . . . .	107
55	VCCT test case: double cantilever beam test. . . . .	108
56	VCCT through-thickness normalized distribution results for double cantilever beam test, compared with data from Crews et al. [28]. . . . .	108
57	Depiction of trailing-edge disbond location on blade, and possible directions of damage propagation. . . . .	109
58	Depiction of possible shear web disbond locations on blade, with “upper” referring to the low-pressure side and “lower” referring to the high-pressure side. . . . .	109
59	Stress results for $\sigma_{yy}$ along the bond line for the baseline model during normal operation and derated to 50% power level. . . . .	110
60	Stress results for $\sigma_{zz}$ along the bond line for the baseline model during normal operation and derated to 50% power level. . . . .	110
61	Stress results for $\sigma_{yz}$ along the bond line for the baseline model during normal operation and derated to 50% power level for NREL 5MW blade (61.5 m blade length). . . . .	110
62	Stress results for $\sigma_{xz}$ along the bond line for the baseline model during normal operation and derated to 50% power level for NREL 5MW blade (61.5 m blade length). . . . .	110
63	Geometry transitions from circular cross sections to airfoil sections with blunt trailing edges (left) and transition from blunt trailing edges to sharp trailing edges (right). . . . .	111
64	SERR for mode I fracture of the inner crack tip of TE disbond starting positions (5 – 40 m), showing convergence of result with respect to grid size. . . . .	112
65	SERR for mode I fracture of the outer crack tip of TE disbond starting positions (5 – 40 m), showing convergence of result with respect to grid size. . . . .	112
66	SERR for mode I fracture of the inner crack tip of TE disbond starting positions (5 – 40 m) and crack lengths (0.5 – 2 m), normal operation, rated windspeed. . . . .	112
67	SERR for mode I fracture of the outer crack tip of TE disbond starting positions (5 – 40 m) and crack lengths (0.5 – 2 m), normal operation, rated windspeed. . . . .	112
68	SERR for mode II fracture of the inner crack tip of TE disbond starting positions (5 – 40 m) and crack lengths (0.5 – 2 m), normal operation, rated windspeed. . . . .	113
69	SERR for mode II fracture of the outer crack tip of TE disbond starting positions (5 – 40 m) and crack lengths (0.5 – 2 m), normal operation, rated windspeed. . . . .	113
70	SERR for mode III fracture of the inner crack tip of TE disbond starting positions (5 – 40 m) and crack lengths (0.5 – 2 m), normal operation, rated windspeed. . . . .	113
71	SERR for mode III fracture of the outer crack tip of TE disbond starting positions (5 – 40 m) and crack lengths (0.5 – 2 m), normal operation, rated windspeed. . . . .	113
72	SERR for mode I fracture of the inner crack tip of TE disbond starting positions (5 – 40 m) and crack length of 0.25 m, normal operation, rated windspeed. . . . .	113
73	SERR for mode I fracture of outer crack tip of TE disbond starting positions (5 – 40 m) and crack length of 0.25 m, normal operation, rated windspeed. . . . .	113
74	SERR for mode II fracture of the inner crack tip of TE disbond starting positions (5 – 40 m) and crack length of 0.25 m, normal operation, rated windspeed. . . . .	114
75	SERR for mode II fracture of the outer crack tip of TE disbond starting positions (5 – 40 m) and crack length of 0.25 m, normal operation, rated windspeed. . . . .	114

76	SERR for mode III fracture of the inner crack tip of TE disbond starting positions (5 – 40 m) and crack length of 0.25 m, normal operation, rated windspeed. . . . .	114
77	SERR for mode III fracture of the outer crack tip of TE disbond starting positions (5 – 40 m) and crack length of 0.25 m, normal operation, rated windspeed. . . . .	114
78	SERR for mode I fracture of the inner crack tip of TE disbond starting positions (5 – 40 m) and crack length of 0.5 m, rated windspeed, derated operation. . . . .	115
79	SERR for mode III fracture of the inner crack tip of TE disbond starting positions (5 – 40 m) and crack length of 0.5 m, rated windspeed, derated operation. . . . .	115
80	$G_I$ with respect to windspeed for NREL 5 MW turbine in normal/derated operation.	116
81	$G_{III}$ with respect to windspeed for NREL 5 MW turbine in normal/derated operation.	116
82	Minimum disbond length of trailing-edge disbond to reduce buckling capacity vs. starting position of disbond. . . . .	117
83	Minimum disbond length of shear web disbond to reduce buckling capacity vs. starting position of disbond. . . . .	117
84	Power production, root bending moment, rotor thrust predictions for two derating strategies “A” and “B” and derating level of 50%. The derating strategies are achieved by modifying the pitch control settings as shown in lower-right. . . . .	122
85	Monthly variation in windspeed for a Baltic offshore site with a windspeed average of 11 m/s [103]. . . . .	123
86	Monthly variation in wave height for a British Isles offshore site. . . . .	123
87	3D surface plot of potential benefits of using a derating strategy to delay maintenance for the NREL 5 MW turbine, compared with immediate repair. . . . .	123
88	2D contour plot version of Figure 87, showing benefit of using derating strategy (or cost of delaying maintenance using derating strategy if negative). . . . .	123
89	Optimal maintenance delay (using derating) in months for derating Strategy A (left) and Strategy B (right), for different derating levels and downtime (DT) durations, for an NREL 5 MW turbine at a Baltic offshore site. . . . .	124
90	“Bladed-style” VSVP controller integrated with FAST in Simulink. . . . .	126
91	“Bladed-style” VSVP controller showing generator torque controller and pitch controller. . . . .	127
92	“Bladed-style” VSVP controller showing generator torque controller. . . . .	127
93	“Bladed-style” VSVP controller showing pitch controller. . . . .	127
94	Low-pass filter applied to high-speed generator shaft speed in “Bladed-style” VSVP controller. . . . .	128
95	Pitch controls for quasi-steady operation at 11 m/s wind speed for each derating strategy. . . . .	129
96	Blade out-of-plane deflections for derating controllers for quasi-steady operation at 11 m/s wind speed. . . . .	130
97	Generator speed and torque performance of derating controllers for quasi-steady operation at 11 m/s wind speed. . . . .	130
98	Twisting moment ( $M_x$ ) signals from each blade transformed into MBC coordinates for derating controllers for quasi-steady operation at 11 m/s wind speed. . . . .	130
99	Flapwise bending moment ( $M_y$ ) signals from each blade transformed into MBC coordinates for derating controllers for quasi-steady operation at 11 m/s wind speed. . . . .	131
100	Edgewise bending moment ( $M_z$ ) signals from each blade transformed into MBC coordinates for derating controllers for quasi-steady operation at 11 m/s wind speed. . . . .	131
101	Pitch control response for derating controllers during extreme coherent gust with direction change (ECD) load case. . . . .	131
102	Blade deflection signals for derating controllers during extreme coherent gust with direction change (ECD) load case. . . . .	132
103	Twisting moment ( $M_x$ ) signals from each blade transformed into MBC coordinates for derating controllers during extreme coherent gust with direction change (ECD) load case. . . . .	132

104	Twisting moment ( $M_x$ ) signals from each blade transformed into MBC coordinates for derating controllers during extreme coherent gust with direction change (ECD) load case. . . . .	132
105	Flapwise bending moment ( $M_y$ ) signals from each blade transformed into MBC coordinates for derating controllers during extreme gust with direction change (ECD) load case. . . . .	133
106	Edgewise bending moment ( $M_z$ ) signals from each blade transformed into MBC coordinates for loads management controllers during extreme coherent gust with direction change (ECD) load case. . . . .	133
107	Modified collective pitch controller with additional PI controller added to limit collective flap bending moment $M_{y0}$ . . . . .	134
108	Modified generator torque controller with PI controller. . . . .	134
109	Pitch controls for wind sweep load case for each loads management strategy. . . . .	135
110	Blade out-of-plane deflections for load mitigation controllers during wind speed sweep load case. . . . .	135
111	Generator speed and torque performance of load management controllers during wind sweep load case. . . . .	135
112	Twisting moment ( $M_x$ ) signals from each blade transformed into MBC coordinates for load mitigation controllers during wind speed sweep load case. . . . .	136
113	Flapwise bending moment ( $M_y$ ) signals from each blade transformed into MBC coordinates for load mitigation controllers during wind speed sweep load case. . . . .	136
114	Edgewise bending moment ( $M_z$ ) signals from each blade transformed into MBC coordinates for load mitigation controllers during wind speed sweep load case. . . . .	136
115	Pitch control response for load mitigation controllers during extreme coherent gust with direction change (ECD) load case. . . . .	137
116	Blade deflection signals for load mitigation controllers during extreme coherent gust with direction change (ECD) load case. . . . .	137
117	Generator speed and torque performance for loads management controllers during extreme coherent gust with direction change (ECD) load case. . . . .	137
118	Twisting moment ( $M_x$ ) signals from each blade transformed into MBC coordinates for loads management controllers during extreme coherent gust with direction change (ECD) load case. . . . .	138
119	Flapwise bending moment ( $M_y$ ) signals from each blade transformed into MBC coordinates for load management controllers during extreme coherent gust with direction change (ECD) load case. . . . .	138
120	Edgewise bending moment ( $M_z$ ) signals from each blade transformed into MBC coordinates for loads management controllers during extreme coherent gust with direction change (ECD) load case. . . . .	138
121	SERR results for inboard $G_I$ , for inboard propagation of trailing-edge disbond from 8 – 8.5 m. Results are from dynamic analysis of 3D finite element model subjected to loads from quasi-steady operation at 11 m/s. . . . .	139
122	Example Pareto front of candidates for 100 m blade designs. . . . .	145
123	Chord and twist distributions for two 100 m designs utilizing either DU series or FB airfoils. . . . .	145
124	Spar layer distributions for two 100 m blade designs. . . . .	146
125	Predicted power output in terms of $C_p$ from the four different designs. . . . .	146
126	Root bending moment predictions in kN for 100 m blade designs. . . . .	146
127	Design control scheduling for 100 m blade designs. Pitch schedule is nearly identical for the three designs. . . . .	146
128	Flapping moment predictions for 100 m blade designs from windsweep FAST/AeroDyn analysis. . . . .	146
129	Twisting moment predictions for 100 m blade designs from windsweep FAST/AeroDyn analysis. . . . .	146
130	Root bending moment (kN) time histories from ECD analysis of competing designs. . . . .	147

131	Tip deflection time histories from “extreme coherent gust with direction change” analysis of competing designs. . . . .	147
132	Inboard $G_I$ comparative measures for 100 m blade designs. . . . .	147
133	Outboard $G_I$ comparative measures for 100 m blade designs. . . . .	147
134	Inboard $G_{II}$ comparative measures for 100 m blade designs. . . . .	147
135	Outboard $G_{II}$ comparative measures for 100 m blade designs. . . . .	147
136	Inboard $G_{III}$ comparative measures for 100 m blade designs. . . . .	148
137	Outboard $G_{III}$ comparative measures for 100 m blade designs. . . . .	148
138	Example Pareto front of candidates for 100 m blade designs, with blade weight replaced by material cost model. . . . .	148
139	Blade material cost as a function of blade weight for 100 m blade design candidates. . . . .	149
140	SERR for mode I fracture of the inner crack tip of TE disbond starting positions (5 – 40 m) and 100m-03 blade designs, normal operation, rated windspeed. . . . .	149
141	SERR for mode I fracture of the outer crack tip of TE disbond starting positions (5 – 40 m) and 100m-03 blade designs, normal operation, rated windspeed. . . . .	149
142	SERR for mode II fracture of the inner crack tip of TE disbond starting positions (5 – 40 m) and 100m-03 blade designs, normal operation, rated windspeed. . . . .	150
143	SERR for mode II fracture of the outer crack tip of TE disbond starting positions (5 – 40 m) and 100m-03 blade designs, normal operation, rated windspeed. . . . .	150
144	SERR for mode III fracture of the inner crack tip of TE disbond starting positions (5 – 40 m) and 100m-03 blade designs, normal operation, rated windspeed. . . . .	150
145	SERR for mode III fracture of the outer crack tip of TE disbond starting positions (5 – 40 m) and 100m-03 blade designs, normal operation, rated windspeed. . . . .	150

## LIST OF SYMBOLS OR ABBREVIATIONS

$a$	Characteristic length of damage, p. 11.
$[A] - [G]$	System matrices for aeroelastic control design, p. 81.
<b>AEP</b>	Annual Energy Production, p. 2.
<b>ANSYS</b>	A popular commercial FEM solver (analysis tool), p. 9.
$b$	Semichord ( $c/2$ ), p. 82.
$\bar{c}$	Chord ratio $c/c_R$ , p. 27.
$\bar{t}$	Thickness ratio $t/t_R$ , p. 32.
$\beta$	Flap deflection (HALE aircraft) or blade pitch angle (WT), p. 82.
<b>BFF</b>	Body-Freedom Flutter, p. 52.
<b>BPE</b>	Beam Property Extraction (analysis tool), p. 9.
$C$	Material property for S-N law or Paris Law, p. 11.
$c$	Chord length (streamwise length of beam), p. 27.
<b>CG</b>	Center of gravity, p. x.
$c_{i_0}, c_{l_\alpha}$ , etc.	Aerodynamic section coefficients, p. 59.
<b>CLT</b>	Classical Lamination Theory, p. 9.
<b>CP</b>	Control Point, p. 142.
$c_R$	Reference chord length, p. 27.
$\Delta K$	Change in stress concentration ( $K$ ) for a given cycle, p. 11.
<b>DU</b>	Delft University (airfoil series), p. 141.
$E$	Young's Modulus (or $E_{ii}$ , Young's Modulus along direction $i$ ), p. 30.
$EA$	Axial stiffness of a beam element, p. 23.
<b>EB</b>	Euler-Bernoulli (Assumptions), p. 9.
<b>ECD</b>	Extreme Coherent gust with Direction change (DLC), p. 7.
$EI_2$	Flapwise (out-of-plane) bending stiffness of a beam element, p. 24.
$EI_3$	Edgewise (in-plane) bending stiffness of a beam element, p. 24.
$f(\dots)$	General function of one or more variables, p. 12.
$F$	Nodal force from ANSYS solution, p. 12.
$F$	Nodal displacements from ANSYS solution, p. 12.
<b>Fast/AeroDyn</b>	Fatigue, Aerodynamics, Structures, and Turbulence for WT Systems (analysis tool), p. 9.
$F_B$	Internal force measures in the deformed frame (NATASHA), p. 53.



<b>FB</b>	Flat-back (airfoil series), p. 141.
<i>FC</i>	Frequency Constraint, p. 36.
<b>FEM</b>	Finite Element Modeling, p. 1.
$f_{\text{gust}}, f_{\text{cont}}$	Effect of gust and control inputs on aeroelastic equations, p. 81.
$F_l$	Internal force measures on the left of a node (NATASHA), p. 54.
$F_r$	Internal force measures on the right of a node (NATASHA), p. 54.
<b>GA</b>	Genetic Algorithm, p. 21.
$\gamma$	Generalized strain measures(NATASHA), p. 53.
$g_B$	Gravity vector measures in the deformed frame (NATASHA), p. 53.
$GJ$	Torsional stiffness of a beam element, p. 24.
$H$	Angular momenta (NATASHA), p. 53.
<b>HALE</b>	High Altitude Long Endurance, p. 4.
<b>HARP-Opt</b>	Horizontal Axis Rotor Performance Optimizer (design tool), p. 141.
<b>HARP-Opt-S</b>	HARP-Opt integrated with SNL NuMAD (original design tool), p. 142.
$i$	Inertia per length of a beam element (a 2 <sup>nd</sup> order tensor), p. 26.
$I_a$	Autorotational Inertia, p. 39.
<b>IEC</b>	International Electrotechnical Commission, p. 7.
<b>IP</b>	In-Plane Bending Mode, p. 99.
$[J]$	Jacobian matrix (NATASHA), p. 55.
$\kappa$	Generalized curvatures (NATASHA), p. 53.
$\lambda$	Inflow state from unsteady aerodynamic theory, p. 54.
$\{x\}$	Column matrix of all NATASHA unknowns, p. 55.
$\{u\}$	Inputs for control design, p. 81.
$m$	Material property for S-N law, p. 11.
<b>MATLAB</b>	Matrix Laboratory (commercial software), p. 142.
$M_B$	Internal moment measures in the deformed frame (NATASHA), p. 53.
$M_l$	Internal moment measures on the left of a node (NATASHA), p. 54.
$M_r$	Internal moment measures on the right of a node (NATASHA), p. 54.
$\mu$	Mass per length of a beam element, p. 23.
$n$	Number of cycles at a given stress level, p. 11.
<b>NREL</b>	National Renewable Energy Laboratory, p. 9.
$\nu$	Poisson's ratio $\nu$ , p. 30.
<b>NuMAD</b>	Numerical Manufacturing and Design Tool (for Wind Turbine Blades), p. 9.

<b>O&amp;M</b>	Operations and Maintenance, p. 1.
$\omega$	Beam natural frequency, p. 36.
$\Omega$	Rotor rotation frequency, p. 36.
$\Omega_B$	Angular velocity measures in the deformed frame (NATASHA), p. 53.
$P$	Linear momenta (NATASHA), p. 53.
<b>p</b>	Eigenvalue (NATASHA), p. 57.
$\Pi$	Total potential energy, p. 12.
$P_i$	Percentage of layers in a laminate at a given layup angle $\theta$ , p. 34.
<b>PreComp</b>	Preprocessor for Computing Composite Blade Properties (analysis tool), p. 9.
$[R]$	Upper left $3 \times 3$ matrix of the Timoshenko stiffness matrix, p. 26.
$r$	Spanwise position variable, p. 109.
$R_\sigma$	Loading ratio for Goodman diagram, $\sigma_{\min}/\sigma_{\max}$ , p. 10.
<b>RSM</b>	Response Surface Modeling, p. 35.
$[S]$	Upper right $3 \times 3$ matrix of the Timoshenko stiffness matrix, p. 26.
<b>SERR</b>	Strain Energy Release Rate, p. 1.
<b>SHPM</b>	Structural Health and Prognostics Management, p. 1.
$S_i$	Variables used to parametrize layup angle percentages $P_i$ , p. 34.
$\sigma$	Stress, p. 10.
$S_{ij}$	Element of Timoshenko stiffness matrix on row $i$ and column $j$ , p. 24.
<b>SIMULINK</b>	MATLAB control design environment, p. 91.
<b>SNL</b>	Sandia National Laboratories, p. 1.
<b>SOP</b>	Symmetric Out-of-Plane (Flapwise) Bending (structural mode), p. 60.
<b>SP</b>	Short Period (structural mode), p. 60.
$[T]$	Lower right $3 \times 3$ matrix of the Timoshenko stiffness matrix, p. 26.
$t$	Thickness of beam element (dimension perpendicular to span and chord), p. 30.
$\theta$	Layup angle for composite layer or pitch attitude, p. 33.
$t_R$	Reference thickness, p. 31.
<b>TSR</b>	Tip Speed Ratio $\Omega R/V_\infty$ , p. 144.
$U$	Strain energy, p. 12.
$V$	Potential energy due to applied loads, p. 12.
<b>VABS</b>	Variational Asymptotic Beam Section Analysis (analysis tool), p. 9.
$V_B$	Velocity measures in the deformed frame (NATASHA), p. 53.
<b>VCCT</b>	Virtual Crack Closure Technique, p. 1.

$v_i$	Eigenvectors NATASHA system, p. 96.
<b>WT</b>	Wind Turbine, p. 1.
$x_1$	Spanwise variable along the beam length, p. 26.
$x_m$	Mass center $x_2$ location, p. 41.
$x_s$	Shear center $x_2$ location, p. 41.

## SUMMARY

Offshore wind power production is an attractive clean energy option, but the difficulty of access can lead to expensive and rare opportunities for maintenance. Smart loads management (controls) are investigated for their potential to increase the fatigue life of damaged offshore wind turbine rotor blades. This study will consider two commonly encountered damage types for wind turbine blades, the trailing edge disbond (bond line failure) and shear web disbond, and show how 3D finite element modeling can be used to quantify the effect of operations and control strategies designed to extend the fatigue life of damaged blades.

Modern wind turbine blades are advanced composite structures, and blade optimization problems can be complex with many structural design variables and a wide variety of aeroelastic design requirements. The multi-level design method is an aeroelastic structural design technique for beam-like structures in which the general design problem is divided into a 1D beam optimization and a 2D section optimization. As a demonstration of aeroelastic design, the multi-level design method is demonstrated for the internal structural design of a modern composite rotor blade. Aeroelastic design involves optimization of system geometry features as well as internal features, and this is demonstrated in the design of a flying wing aircraft. Control methods such as feedback control also have the capability alleviate aeroelastic design requirements and this is also demonstrated in the flying wing aircraft example.

In the case of damaged wind turbine blades, load mitigation control strategies have the potential to mitigate the effects of damage, and allow partial operation to avoid shutdown. The load mitigation strategies will be demonstrated for a representative state-of-the-art wind turbine (126m rotor diameter). An economic incentive will be provided for the proposed operations strategies, in terms of weighing the cost and risk of implementation against the benefits of increased revenue due to operation of damaged turbines. The industry trend in wind turbine design is moving towards very large blades, causing the basic design criterion to change as aeroelastic effects become more important. An ongoing 100 m blade (205 m rotor diameter) design effort intends to investigate these design challenges. As a part of that effort, this thesis will investigate damage tolerant design strategies to ensure next-generation blades are more reliable.

# CHAPTER I

## INTRODUCTION

Offshore wind is an attractive clean energy option, but the difficulty of access can lead to expensive and rare opportunities for maintenance. The Structural Health and Prognostics Management (SHPM) project at Sandia National Laboratories (SNL) (see [46], [48]) has developed a roadmap to address these issues, in particular technology development to reduce operations and maintenance (O&M) costs and increase energy capture for offshore wind turbines (WT). In one element of this roadmap, smart loads management (controls) are investigated as fatigue considerations and the potential has been identified to derate a damaged turbine via smart loads management to significantly increase its fatigue life [46, 48]. Derating refers to altering the rotor angular speed and blade pitch to limit loads on the blade at the cost of reduced power production.

High fidelity analysis techniques such as finite element modeling (FEM) should be used alongside beam models to quantitatively and accurately characterize any load mitigation strategy in terms of its effect to mitigate fatigue damage and extend life of turbine blades. High fidelity analysis is critical in the case of damaged blades due to local effects in the damaged area of the blade. This study will consider a commonly encountered damage type for WT blades, the bond line failure (or “disbond”), and show how FEM can be used to quantify the effect of operations and control strategies designed to extend the fatigue life of damaged blades. The FEM strategy will use a multiscale procedure, with a “global” beam model analysis for behavior of most of the blade, and a “local” 3D FEA model to analyze the behavior in the vicinity of the damage. The Virtual Crack Closure Technique (VCCT) [72] will then be used to post-process the displacement and stress results from the 3D FEA to provide estimates of damage severity and damage growth rates. The VCCT provides the means to efficiently calculate an energy-based damage tolerance measure known as the strain energy release rate (SERR). The results of this process will indicate the criticality of common damage features with respect to damage location and type of loading, as well as provide a means to estimate the fatigue life or growth of damage under a given operations and control strategy. A buckling analysis will be used to determine the upper allowable limits for bond line failure along the shear web or trailing-edge bond lines.

The purpose of a smart loads management system for WTs is to (a) avoid a catastrophic failure

through advance warning, (b) plan cheaper maintenance and (c) increase energy capture by avoiding shutdown. The resulting strategies will consist of decisions to shutdown, operate the turbine normally, or operate potentially damaged turbines in a safe way. The recommendation to operate damaged turbines must justify the risk of further damage to the turbine based on the local sensitivity analysis results and the potential to increase the annual energy production (AEP) where inspection and maintenance can be difficult. An effective prognostic control strategy will therefore reduce the total cost of energy by reducing O&M costs as well as increasing power production for offshore wind farms. The implementation of smart loads management strategies for modern WT blades will be demonstrated with a variable-speed, variable-pitch system. Recommendations for the proper input settings for sample loads management controllers will be based on the performance of the damaged turbine as well as high fidelity analysis of the potential reduction in SERRs for the trailing-edge disbond. The resulting loads management controllers are shown to successfully reduce SERRs as well as dynamic blade deflections. These loads management controllers will then allow WT farm operators to utilize damaged turbines during periods of down-time or delay maintenance in order to maximize the profit of the wind farm as a whole.

Wind turbines are non-uniform beam-like structures utilizing advanced composite materials. In many ways the challenges faced by WT designers are very similar to those faced by designers of modern rotor blades or high aspect ratio aircraft wings. All three applications (WT blades, rotor blades, and high aspect ratio wings) must deal with a large number of structural design variables corresponding to the detailed composite structure as well as satisfy a wide variety of manufacturing and aeroelastic constraints. One particular challenge is that the design variables are often at the “local” level, and aeroelastic constraints must be satisfied on the “global” level; this requires that some effort be made to connect the local design variables to global aeroelastic performance. A procedure which treats these two problems nearly independently is the multi-level procedure [138, 7, 74, 80], however this procedure has only been developed for uniform blades. This procedure will be extended to non-uniform blades and demonstrated in an example of modern rotor blade design. The multi-level procedure is especially useful when there is a wide variation in possible structural configurations, but often the general structural configuration will be predetermined by manufacturing constraints or practices. In this case, exploration or optimization of the beam analysis portion still gives much insight into the general design guidelines for the local structural design. This concept will be demonstrated with a design example for a flying wing aircraft, where the behavior of the aeroelastic beam analysis code is explored first and then the structural design is carried out within the limits allowed by the manufacturing procedure. In general, aeroelastic design margins

can be relaxed if aeroelastic control design is used to improve aeroelastic performance. Aeroelastic control design will be demonstrated for a high altitude long endurance (HALE) aircraft.

Average WT blade length has increased significantly, especially for offshore WT blades due to the increased balance of station costs associated with offshore installation. The next generation of offshore WTs will very likely be even larger. The large blade length has led to increased fatigue, buckling, and other aeroelastic structural issues compared with onshore blades. For example, the increased length and weight has led to increased cyclic edgewise loading and an associated increase in trailing-edge fatigue issues. Therefore, aeroelastic design methods should be implemented for the structural and control design processes. The challenges associated with very large blades are then investigated through the 100 m blade project at Sandia National Laboratories (SNL). As part of that effort as well as other SNL blade design projects, a combined aerodynamic and structural design optimization toolkit has been developed. This aero/structural WT blade optimization package then was used to explore potential 100 m blade designs. The effect of trailing edge thickness on WT blade design and damage tolerance is explored through a comparison study where designs with conventional airfoils are compared to designs with airfoils with comparatively thick trailing edges (flat-back airfoils) for aerodynamic performance, structural performance, blade cost, and damage tolerance.

## ***1.1 Concepts***

The scope of this project is ambitious and targets nearly every aspect of WT blade design, including aerodynamic optimization, structural design, controller design and evaluation, and operations strategies for large offshore WTs. However, the main concepts for this work include aeroelastic design, smart loads management, damage tolerance analysis, and design strategies for more reliable blades.

### **1.1.1 Aeroelastic Design**

High fidelity aeroelastic analyses have traditionally been invoked after many design details are already decided. A recent trend is to include these analyses early in the design stages. An anecdotal example of this tradition is the tendency for airplane wing or rotor blade designers to check aeroelastic design requirements after much of the design has been decided; flutter problems are still commonly addressed in modern rotor blades with non-ideal solutions such as tuning weights added to the leading edge. These non-ideal solutions suggest that aeroelastic analysis should be included early in the design stages of rotor blades, aircraft wings, and large wind turbine blades.

Aeroelastic design analysis methods for non-uniform structures are sometimes difficult and costly to perform. Therefore, it can be helpful to separate the analysis or design optimization problem into sub-problems where possible and use surrogate modeling techniques or approximations to replace costly analyses if possible without a significant loss of accuracy. One helpful way to break down an aeroelastic optimization problem is the multi-level method, where a beam-like structure is optimized first at the 1D beam (“global”) level and then at the 2D section (“local”) level, where each level is treated in an appropriate way. This multi-level method was developed for uniform blades but in this thesis it is extended to non-uniform blades. At the global level, care must be exercised to constrain spanwise variables based on possible distributions of beam section properties. At the local level, the optimization method should consider the manufacturing process when choosing design variables. The multi-level method is demonstrated for modern composite helicopter rotor blades, using realistic structural design variables as inputs and aeroelastic stability and performance requirements as constraints.

A successful aeroelastic design strategy should consider the potential for controls to alter or improve the structure’s aeroelastic performance. As a secondary example to introduce the concept of aeroelastic design, a design study is presented for high altitude long endurance (HALE) aircraft. This study introduces the concept using both structural design and controls to tailor the aeroelastic performance of a structure to mitigate design limitations imposed by aeroelasticity. In this example, body-freedom flutter issues may limit the allowable flexibility of flying wing aircraft. Aeroelastic design is performed first to increase the body-freedom flutter speed as much as possible without incurring a significant weight penalty. Then, aeroelastic control design is evaluated for its potential to improve the body-freedom flutter performance of the flying wing design.

### **1.1.2 WT Blade Damage Modeling and Analysis**

The field of damage tolerance concerns a structure’s ability to “tolerate” or withstand damage, which is assumed to exist in every structure at the size just below the threshold of damage detection capability. For example, if the blade measurement technology is only capable of detecting damage 1 mm length and above, then it should be assumed that damage features of sizes less than 1 mm exist within the structure. Then, damage growth rates are predicted and used to plan inspection intervals for the structure to ensure any potential damage does not grow to an unacceptable size.

In the context of this study, it is also desirable to have a damage tolerance analysis procedure that is efficient enough to be used in a control or structural design process. Therefore, the damage



tolerance analysis procedure that requires the least computational effort would be desirable. For applications in which the structural behavior at multiple length scales is of interest, multiscale analysis techniques can often significantly reduce the computational cost required to accurately capture the behavior at each length scale. In this study, the blade behavior as a whole, or its “global” behavior, may be thought of as consisting of blade deflections, blade vibration modes/frequencies/damping, large scale buckling behavior, and power performance, and can be thought to exist on a length scale of meters. The “local” effects of damage may be thought of consisting of local panel deflections in the vicinity of the damage, stress field perturbations due to the presence of the damage, reduced buckling capacities of panels or structural components in the vicinity of the damage, and can be thought to exist on a length scale of mm. Therefore a multiscale analysis procedure would certainly be appropriate for this study to efficiently capture both “global” and “local” effects of damage.

### **1.1.3 Smart Loads Management for Damaged Blades**

If blade damage is detected in a WT blade, the typical response is to avoid further damage completely with a shutdown of the damaged turbine. However, there may be a long span of time between the occurrence of damage and a later opportunity to perform maintenance on the WT blade. Therefore, it would be ideal if damaged WTs can continue to operate, thus increasing the AEP of the wind farm as a whole. It would not be desirable to induce further damage by continued operation of the turbine under normal levels. Smart loads management is proposed as a way to mitigate the effects of the damage during continued operation. Of course, sufficiently accurate models of blade damage should be used to quantify the effects of any continued operation of damaged turbines in terms of risk of inducing further damage.

The purpose of the smart loads management system is to (a) avoid a catastrophic failure through advance warning, (b) plan cheaper maintenance and (c) increase energy capture by avoiding shutdown. The resulting strategies will consist of decisions to shutdown, operate the turbine normally, or operate potentially damaged turbines in a safe way. The recommendation to operate damaged turbines must justify the risk of further damage to the turbine based on the local sensitivity analysis results and the potential to increase the AEP. An effective prognostic control strategy will therefore reduce the total cost of energy by reducing O&M costs as well as increasing power production for offshore wind farms.

#### 1.1.4 Damage Tolerant Design

The aeroelastic design studies featured in this work will demonstrate how aeroelastic design requirements may be included in the early stages of design for modern composite rotor blades and HALE aircraft. Similarly, this work intends to advocate for moving aeroelasticity and damage tolerance considerations into the preliminary and conceptual aerodynamic and structural design processes for WT blades. To this end, combined aerodynamic and structural optimization procedures that account for damage tolerance will be investigated. The primary design drivers for large WTs are listed below:

1. Maximum dynamic deflections, as these can lead to tower strike if they are outside of design limitations
2. Blade fatigue, as WT blades are required to be certified for 20 years of continuous service
3. Skin panel or spar buckling, which is exacerbated for large blades due to increasing panel size and large blade deflections
4. Aeroelastic instability (flutter), which can occur for large wind turbines at angular speeds comparable with operating speeds

This study will add damage tolerance as an additional design consideration for large WT blades, and make recommendations for design of the next generation of more reliable WT blades.

## CHAPTER II

### BACKGROUND

A general cost-benefit analysis of offshore wind energy is presented by Snyder and Kaiser [128]. This analysis identifies the relative cost and risk of offshore turbines (compared with onshore) as a main barrier for acceptance of offshore wind, and highlights the larger percentage of operational and maintenance (O&M) costs of the total offshore cost of energy (compared with onshore). A review of offshore wind development in the UK is given in [56], and the “future” of US offshore wind development was given (in 2004) in [96]. A major goal of the SHPM project is to present operational and control strategies for offshore wind that will minimize the total cost of energy, by avoiding blade damage or mitigating blade damage growth with smart loads management. The strategies developed will consider both the potential to increase revenue and reduce O&M costs for one turbine as well as the potential to optimize power production and O&M costs for an installation of multiple turbines (wind farm).

There has been significant interest in the area of O&M strategies for WTs, as well as control strategies for blade load mitigation. This work ties those two ideas together to attempt to understand the role of load-mitigating control strategies within a WT or farm O&M strategy. Damage tolerance methods utilized in other aerospace industries can then be applied within this framework to determine the necessary level of derating and ensure that damage growth is mitigated.

WTs are typically certified with standards provided by the International Electrotechnical Commission (IEC) [27]. Specifically, there are a number of load cases that designers are required to analyze. These load cases include wind speed sweeps, turbulent fatigue analyses at each wind speeds, dynamic wind events during operation, and extremely high wind speed events for which the turbine will be in a parked (braked) condition. The design blade life specified by the IEC is 20 years. A notable design load case (DLC) is the Extreme Coherent Gust with Direction Change (ECD) load case, which involves a sudden increase of wind speed at the same time as a sudden change of wind direction. Figure 1 shows the wind profile for this DLC, as it will be used to characterize the performance of control strategies or designs throughout this work. This load case is notable for its typically large out-of-plane dynamic blade deflections, which are a primary design driver for large WT blades.

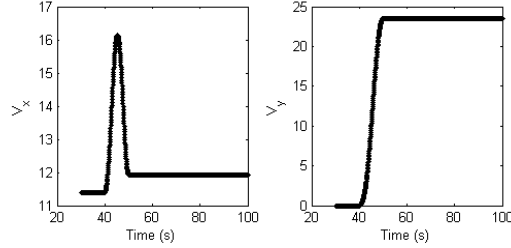


**Figure 1:** Wind profile for “extreme coherent gust with direction change” analysis.  $V_x$  is aligned with the shaft axis and  $V_y$  is perpendicular to the shaft direction (but not vertical).

The following reviews the available literature on the subjects of WTs, blade damage, damage detection strategies, the finite element method, the finite element method for multiscale problems, damage modeling strategies, control strategies, and design strategies.

## ***2.1 Analysis of Damage Effects***

The effects of blade damage are subdivided into “global” and “local” effects. The global effects are large-scale blade behaviors that can generally be fully captured with beam models, while local effects are smaller scale behaviors induced or affected by the damage, and these generally require 3D shell or brick FEA models to capture. This subdivision of damage effects also aligns with the multiscale analysis concept, where global effects are associated with coarse models that capture the whole blade behavior and local effects are associated with refined models that only model the vicinity of the damage.

### **2.1.1 Global Effects of Damage**

It is assumed that effects of damage such as stress field perturbations are fully 3D in nature; that is they may affect the material in the same cross-section as the damage as well as material inboard or outboard of the damage location. Therefore, the presence of damage may violate some of the basic assumptions that are used to reduce the 3D blade structural problem to a 2D section analysis and a 1D beam analysis. Furthermore, many beam models are based on displacement assumptions that will certainly fail to apply in the vicinity of the damage due to these local effects. However, these local stress fields should remain within a characteristic length of the damage and the remainder of the blade should behave as if it were undamaged. However, the presence of the damage will reduce the blade stiffness, and this is the main way blade damage impacts the global performance in terms of beam model results. In this way a beam model can be used to determine the change in displacements and beam section loading due to damage, and the section constitutive data for sections far from the damage location need not change. Although the stress recovery process of the

beam analysis procedure may be invalidated by the presence of damage due to these local effects, other than changes to the model section properties it is assumed that these local effects do not affect the 1D beam displacements and rotations.

To assess the stiffness of healthy blades, there are essentially three options: use displacement assumptions such as the Euler-Bernoulli (EB) assumptions along with Classical Lamination Theory (CLT), use a more accurate section modeling tool that does not make *a priori* assumptions (VABS), or use a 3D shell or brick model to calculate displacements and rotations with respect to a given set of loads (BPE). PreComp is an NREL open source code that uses EB and CLT assumptions to calculate the beam section properties [8]. VABS is a section analysis tool that uses the Variational Asymptotic Method, and is efficient and accurate with respect to fully 3D methods [151, 149]. Although VABS is generally more accurate than PreComp [22], it relies on a finite element mesh of the section whereas PreComp needs only the section structural description. The preprocessor PreVABS is available to generate the mesh for VABS from the section description but has difficulty meshing some geometries [23]. The VABS/ANSYS macro [57] is another preprocessor able to take an ANSYS model of the section description and produce the VABS input file. The NuMAD toolbox includes an approach known as BPE (Beam Property Extraction) that uses the ANSYS shell model to calculate displacements and rotations with respect to a given set of input loads [85].

The efficiency of a section analysis tool would be ideal for design strategies that account for the possible reduction of stiffness due to damage. To assess the reduction of stiffness for sections in the vicinity of the damage, the simplest approach would be to use either PreComp or VABS with either reduced section properties or modified section geometry. Of the two, VABS far more likely to accurately capture the damage effects due to its lack of displacement assumptions. The accuracy of using VABS with a modified section will be compared to fully 3D models of the damage to assess if it appropriate to use VABS for damaged beam models. Although there has been work to include matrix cracking effects into VABS [112], to the author’s knowledge a comprehensive comparison of VABS results of a blade with discrete damage feature with results from a 3D analysis not been made.

A preferred aeroelastic beam analysis tool for WTs is Fast/AeroDyn. This code was developed by the National Renewable Energy Laboratory (NREL) and is widely used within the industry and academic WT communities. The theory manual is not yet available, but a general description of the theory is given within the user’s manual [64]. The analysis of global effects of damage for WTs has been undertaken by Myrent et al. [97, 98] as another part of the SHPM project. Therefore, for this thesis a detailed investigation into “global” damage effects is not intended. However, it is necessary to obtain global models for use in control system design.

### 2.1.2 Local Effects of Damage

Local damage effects have been studied by many, and concepts of damage tolerance are well established for metallic materials such as aluminum or steel. There has also been significant progress in the area of damage tolerance of composite structures, although failure prediction and damage progression analysis of composites is much more difficult due to anisotropy and more complex mechanisms of damage progression.

The mechanism by which damage progresses from one severity level to another is the growth of cracks due to stress concentrations. For WT blades, these stress concentrations will depend on the damage geometry, the atmospheric conditions including the possibility of extreme events, and the behavior of the pitch, yaw, and angular speed (RPM) control systems. One particular type of damage that is typical to WTs is adhesive bond failure, which is described more academically in [2]. The mechanisms of fatigue crack growth in a bonding interface are also studied in [126].

### 2.1.3 Stress-based Fatigue Predictions

The onset of damage is often predicted using an S-N curve and Miner's rule. The S-N curve describes the relationship between stress level  $\sigma$  and the number of cycles  $N$  to failure and can be expressed mathematically as:

$$\sigma^\alpha N = C \tag{1}$$

Here  $\alpha$  and  $C$  are material constants, and this rule assumes tension-compression cycling. In the case of a mean stress  $\sigma_m$  and oscillatory stress  $\sigma_a$ , Goodmans relationship is typically used to find an equivalent stress  $\sigma_0$  for use in the S-N relationship:

$$\frac{\sigma_a}{\sigma_0} + \frac{\sigma_m}{\sigma_u} = 1 \tag{2}$$

Here  $\sigma_u$  is the ultimate failure stress of the material. A more detailed representation of this effect is realized in a Goodman diagram. The Goodman diagram is a plot of cycles to failure as a function of mean stress and stress amplitude, containing information for several loading ratio ( $R_\sigma$ ) values ( $\sigma_{\min}/\sigma_{\max}$ ). Several recent Sandia reports cover the effect of mean stress quite thoroughly, and a Sandia effort has recently produced a very detailed Goodman diagram [133, 134, 86]. A WT blade in service at a constant wind speed will certainly be subjected to both mean stresses due to the equilibrium deflected position and alternating stresses due to aeroelastic deflections of the blade due to wind shear, gravitational loading and other periodic effects. When the stress profile changes from cycle to cycle, the Miner's rule is typically invoked with  $n_i$  referring to the number of cycles at a given stress level  $\sigma_i$ :

$$\sum \frac{n_i}{N_i} = 1 \quad (3)$$

The stresses a WT blade encounters are dependent upon the wind speed and control strategy. The number of cycles at a given wind speed or in the presence of an extreme event are then a function of the time interval and the probability of that wind speed or extreme event. There is a corresponding version of the Miner's rule that accounts for the probabilistic nature of the loading.

The S-N curve / Miner's rule approach can be used to predict damage onset when the stress histories are known. If the damage is assumed to produce a finite stress concentration, then this approach can also be used to estimate damage growth. In this case, the damage is assumed to grow simply when local failure is induced via the Miner's rule and the increased stress due to the presence of the crack. Typically, this approach is usually accompanied by a damage model in which material properties such as stiffness and strength are reduced as a result of exposure to high stress levels [92, 112].

For sharp-edged damage features, the stress levels theoretically approach a singularity in the vicinity of the damage. For ductile materials, the stress levels reach the yield stress of the material, creating a plastic zone near the damage front. In composite materials, the behavior of the stress field in the vicinity of damage is more complex and requires advanced micro-mechanics analysis to determine directly. ANSYS models used for global analysis results or basic stress analyses often have a resolution too coarse to analyze the near vicinity of the crack.

If there is experimental data available, empirical models may be extracted from the data for use in crack growth predictions. The experimental data is typically material dependent but can then be applied to a wide range of geometries. One commonly used model for crack growth in the presence of cyclic loading is the Paris Law:

$$\log (da/dn) = \log (C) + m \log (\Delta K) \quad (4)$$

Here  $a$  is the crack length,  $n$  is a number of loading cycles,  $C$  and  $m$  are material constants determined from experimental testing, and  $\Delta K$  is the change in stress concentration factor due to the cyclic loading. The material constants are typically dependent upon the loading ratio  $R_\sigma$ . A more general way of expressing this relationship is that the growth rate  $da/dn$  is expressed as a function  $f(a, \Delta K, R_\sigma)$ , and the number of cycles to failure  $N$  is then given by the following:

$$N = \int_{a_0}^{a_f} \frac{da}{f(a, \Delta K, R_\sigma)} \quad (5)$$

In the above equation the failure criterion is that the crack length has reached  $a_f$ , which for sudden failure is the crack length at which the crack grows unstably. In this case, one might consider  $a_f$  to be the damage size that defines the transition from an acceptable level of damage to an unacceptable level of damage. In this model, one must obtain the growth model (the form of the growth rate function  $f(\dots)$ ) as well as the values of  $\Delta K$  and  $R_\sigma$  which will depend on the loading. Furthermore, the constantly varying or probabilistic nature of the damage will need to be accounted for in this approach.

Reference [148] gives some insight on how to predict failure in adhesively bonded composites using stress-based failure criteria. Bondline failure is categorized into two failure mechanisms: decohesion and debonding, and the failure is usually a mix of the two mechanisms. Debonding in particular is more sensitive to tensile or peeling stresses than to shear stress. This reference gives some moderately successful damage models for predicting the onset of bondline failures but also recognizes the lack of literature covering bondline failure analysis.

#### 2.1.4 Energy-based Fatigue Predictions

Failure models for disbonding are often expressed in terms of strain energy release rates. The strain energy release rate (SERR)  $G$  is defined as the amount of strain energy released as a new free surface is formed by propagating damage. The SERR information can be used under the assumption that when  $G$  approaches a material-specific critical value  $G_c$ , the crack will propagate. Essentially, the energy required to fracture the material comes from a release of strain energy stored within the structure. Mathematically it is expressed in terms of the total potential energy  $\Pi$  and the damage length  $a$  and width  $b$ :

$$\Pi = U + V \quad G = -\frac{d\Pi}{d(ba)} \quad (6)$$

Here  $U$  is the strain energy and  $V$  is the potential energy of the applied loads. The growth rate results are then calculated from the SERRs, for example in the form of a Paris-type growth law (Eq. 4) with  $\Delta G$  used in place of  $\Delta K$ .

A popular method to predict the onset of bondline failure is the VCCT which has been applied to trailing edge debonding in Ref. [32]. The VCCT is a method based on finite element analysis of an existing crack to find the forces  $F$  and displacements  $F$ , and thus the work required, required to close the crack, and then assuming this corresponds to the SERR of the crack as it opens. The results of Ref. [32] for a realistic WT blade suggest that torsional loading will induce mainly mode III fracture in the bond line. Again, these methods were suggested for use to predict the onset of the disbond, and recognize a lack of progress in the area of the disbond growth. However, the VCCT



method is applicable to geometries with existing cracks as well [29, 147]. An experimental study that compares mode I and mode II fracture in adhesive bonds [19] shows crack growth rates were much higher under mode II loading as they were in mode I. This study also presents a model to estimate an equivalent SERR based on the degree of mixing of modes I and II and the respective SERR. This was the only reference found that specifically covers growth rate predictions of a disbond (as opposed to initiation or onset predictions). When attempting to close a crack from length  $a + da$  to length  $a$ , the energy required will be the opened displacements multiplied by the internal forces that resist the closure. To demonstrate the method, one version of the VCCT allows the forces at the crack tip to be used in this calculation. Therefore, the resulting formulas for the SERR in modes I, II, and III are, respectively,

$$G_I = \frac{1}{2\Delta a} F_y (u_y - \bar{u}_y) \quad G_{II} = \frac{1}{2\Delta a} F_z (u_z - \bar{u}_z) \quad G_{III} = \frac{1}{2\Delta a} F_x (u_x - \bar{u}_x) \quad (7)$$

where  $u_i$  are the displacements of the upper surface and  $\bar{u}_i$  are the displacements of the lower surface. Here,  $y$  refers to the direction perpendicular to the line of the crack in the “opening” direction,  $z$  refers to the direction along the line of the crack, and  $x$  refers to the direction perpendicular to the opening direction and the line of the crack. Of course, the assumption that the forces at the crack tip are equal to those that would resist closure of the crack can be relaxed if a two-step analysis is performed: a closed analysis (crack length  $a$ ) to obtain the forces and an opened analysis (crack length  $a + da$ ) to obtain the displacements.

A high-fidelity ANSYS model could also be used to calculate the SERR by numerical differentiation: simulate the crack growth with length  $a$  and calculate the total potential energy measure  $\Pi$ , and then simulate the crack growth with length  $a + \Delta a$  and calculate the new total potential energy  $\Pi + \Delta \Pi$ . Then the SERR would be found by numerical differentiation:

$$G = - \lim_{\Delta a \rightarrow 0} \left\{ \frac{\Delta \Pi}{\Delta a} \right\} \quad (8)$$

The drawback to this method (a two-step analysis approach) is that several ANSYS runs would have to be made if the disbond is to be tracked over a long distance. However, this method would prove to validate or tune an analytical model that could then efficiently be applied to a variety of different disbond sizes and locations. The VCCT method is valid for linear problems, when the strain energy release is completely absorbed by the material fracture, and may not account for some typical damage phenomena such as fiber bridging in delaminated composite structures. For this study, it is assumed that the damage lies within the adhesive, where the VCCT is applicable. Because the crack is assumed to lie within the adhesive, any issue with the VCCT due to a bimaterial interface was avoided.

One common location for disbond to occur is the bond between the shear web and the upper or lower skin. After the disbond occurs the structure will be susceptible to local buckling near the vicinity of the disbond. Reference [68] studies a similar situation with a fuselage skin constructed from two components bonded together at connecting flanges, where the bond has partially broken down and the flanges are allowed to buckle. In this case, the driving force for disbond growth following buckling initiation is the postbuckled deformations. The postbuckled deformation is obtained for a simple disbond geometry as an analytical expression terms of the disbond length  $a$  and the potential energy  $\Pi$  can be formed and differentiated, giving an analytical expression for the strain energy release rate  $G$ . The approach of using postbuckled deformations as the basis for predicting the SERR for disbond growth predictions may also be applied to the trailing edge or shear web disbond. If an analytical model can be found to define the postbuckled deformations, then the strain energy can be formed and its partial derivatives calculated.

Another study by Wetzel [142] examines disbonding between the shear web and upper skin and finds that for the case where the spar cap is bonded to the skin directly, panel buckling of the skin will lead to growth of a shear web disbond, however stress-based failure criterion are utilized. Therefore, the buckling behavior of the skin in the presence of the disbond is an essential feature of the damage growth in the case of the shear web bondline failure. One of the principal recommendations of [142] is that brick element finite element models be used in preference to the shell models that are currently used in NuMADs ANSYS modeling feature, especially to accurately capture local stress concentrations for using stress-based failure criterion.

Another promising finite element method for predicting the onset and growth of damage is the concept of cohesive zone elements. Refs. [31, 143, 39] give recommendations on how to apply these cohesive zone elements and information about their behavior. These elements simulate the damage by having a bilinear constitutive law that is best exemplified by the depiction in Figure 2. The bilinear constitutive law is related to the strain energy release rate in that the area under the curve in Figure 2 is equal to the maximum SERR material property ( $G_c$ ) of the material. Figure 2 also demonstrates how the cohesive zone elements can be made to model damaged material that has reduced material properties. In this Figure,  $K$  is the undamaged stiffness of the material and  $\tau_c$  is the undamaged strength. The damaged material has a stiffness  $(1-d)K$  and degraded strength (the peak of the inscribed triangle). Reference [31] also describes how to include mixed-mode loading conditions in the constitutive law for cohesive elements, and also how they are formulated for use in brick or shell element models. Refs. [143] and [39] illustrate how these models should be used along stress-based failure criterion, which predict the onset or appearance of the damage, and then

the cohesive zone elements predict the fracture propagation. In the case where the damage location prescribed, like in the disbond of the crack or spar cap, the cohesive elements can be readily applied. Reference [121] gives a model for fatigue crack growth using cohesive zone elements, but instead of using the Paris equation the actual process of material separation is modeled by an irreversible constitutive law. Reference [146] gives more insight about how cohesive zone elements can be used to represent fatigue damage for quasi-brittle materials, and unifies the process of estimating the damage onset and growth. Guimatsia et. al [53] show how automatic placement of cohesive zone elements can improve the method when the crack path is not known. Moroni and Pirondi [94] demonstrate how various mixed-mode propagation criteria can be applied to a cohesive zone model of fatigue crack growth in adhesively bonded joints. Of course, the bilinear constitutive model in Figure 2 can be modified, and the fracture responses of different cohesive zone models are compared in [127]. Chaves et al. [21] demonstrates how experimental procedures can be used to validate cohesive zone elements accounting for mode mixity.

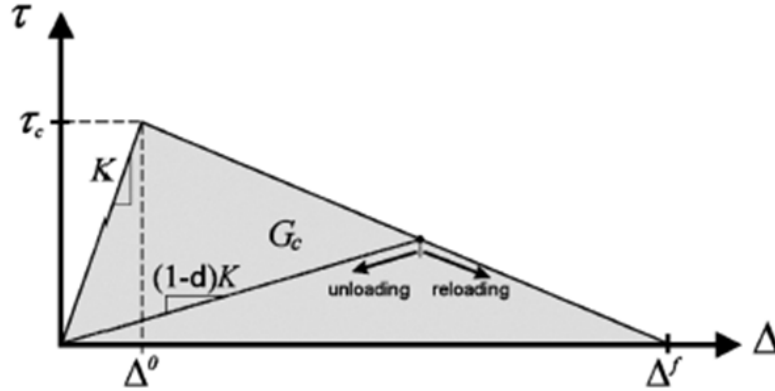


**Figure 2:** Bilinear constitutive model for cohesive zone elements (Reference [94]).

## 2.2 Operation and Maintenance Strategies

Decisions of how to operate a turbine should be made in conjunction with an inspection and maintenance scheduling strategy. An overview of maintenance management is given by [35]. Rangel-Ramirez and Sorensen [114] applied a risk-based inspection strategy from offshore oil industry to offshore wind farms, showing that operational decisions regarding inspections should consider turbulent wake effects of the farm as a whole. Zhang et al. [153] use a wake-loss model and historical data to define an inspection model that accounts for the wake of each turbine. This inspection model would use weather reports when available and historical data when necessary to make up-to-date

decisions. This way WTs heavily affected by the wake(s) of one or more other turbines or whose wake affects other turbines would be shutdown in favor of turbines operating optimally. This model in particular would be an ideal starting point for an operational strategy that includes damage tolerance considerations. A damaged turbine that is forecasted to be partially within the wake of another, for example, would likely remain shutdown, while a damaged turbine that is forecasted to be within a clear inflow would then operate under a prognostic control system. Wenjin et al. [141] proposed a predictive maintenance strategy based on modeling the blade deterioration with Monte Carlo simulations. This is again similar to the proposed operations strategy, except that the damage detection efforts of the SHPM project are intended to augment or replace blade deterioration models [97, 98]. These efforts identified the potential to identify blade damage in constant inflow conditions [97] and also demonstrated the damage detection capability in a wide range of inflow conditions, such as varying turbulence levels or partially waked turbines [98].

The maintenance scheduling can be outlined *a priori*, but must be flexible to accommodate new information from on-board structural health monitoring. Structural health monitoring has been approached in several different ways; overviews can be found in [37, 54, 11, 71, 91, 34, 40]. Structural health monitoring of offshore sites is additionally complicated by the need to adjust for environmental influences or sensor malfunction/failure in the damage detection process as described in Refs. [93, 70, 75, 36]. One strategy for structural health monitoring is to use force identification techniques to determine the loading, such as in [69], and use this data to estimate the remaining blade life. A damage detection strategy based on a validated finite element model is proposed by Reetz [115]. Some novel structural health monitoring strategies include laser displacement sensors placed within the blade [78].

### **2.2.1 Control System Considerations**

Under “normal” operation, a wind farm is operated to maximize power production. Modern WTs of 5 MW or larger are typically controlled in yaw, pitch, and rotor angular speed to optimize their power production capability. The yaw control is used to align the rotor with the wind direction, while pitch and speed controls are primarily used to control aerodynamic loads and generator performance. The angular speed of the turbine rotor is controlled via torque control of the generator. The pitch and speed controls of each turbine can either be used individually to maximize the power output of each individual turbine, or in a collective sense to maximize the power output of the wind farm as a whole [88, 41, 76]. For this research, the NREL 5 MW baseline design [63] will be considered as a representative offshore turbine design with yaw, pitch, and rotor angular speed controls.

Under “damaged” operation, it is possible to use control strategies to produce power while alleviating loads on damaged blades. Bossanyi has studied the blade load reduction problem extensively [13, 14, 15, 16]. One example of individual blade control design using sliding-mode control is given by Xiao et al. [144]. Pitch control is often used to mitigate vibrations of offshore platforms, including the use of individual blade pitch control as in [140, 77, 67, 26, 99], and structural control methods as in [122]. These vibrations create fatigue damage of the foundation [145], so are often the focus of offshore WT control design efforts. Accurate platform fatigue analysis requires nonlinear modeling of the wave conditions [135]. In general, the structural health monitoring systems should be integrated with the operation and controls of the WT as demonstrated by Frost et al. [38] and Griffith et al. [47]. A good prognostic control strategy would address all of these issues in addition to possible blade damage, but these considerations are beyond the scope of the current research. It is enough to say that pitch control techniques have been shown to have a wide variety of applications to blade-load reduction.

The simplest example of a load-reducing, pitch-control method is to utilize the available pitch-control system to control blade RPM and pitch to limit the power production to a lower level [97, 38]. For this research, the derating was accomplished by holding the RPM constant above the windspeed when the power production exceeds its derated level at a  $0^\circ$  pitch setting, and then using the pitch controller to maintain the power production as the windspeed increases. For the NREL 5 MW baseline turbine, a 50% derating strategy, and a Rayleigh wind profile with average windspeed of 10 m/s, the AEP is reduced from  $\approx 2.5e7$  kWh to  $\approx 1.5e7$  kWh. The power production and control scheduling required to achieve this derating is shown in Fig. 3 as well as the root bending moment. The reduction in AEP is less than the reduction in maximum power level because at low windspeed the power production is not changed; the power production is only limited in this case at 9 m/s and above. The loads in terms of maximum bending moments at the root of the blade were reduced by approximately 50%. The advantage to using a simple “derating” method is that it would only involve a change in the software of currently operating offshore turbine control systems, and therefore could be easily retrofitted into pre-existing designs. The justification of using root bending moment as a measure of damage severity is given later in this work, in terms of successfully reducing SERRs (Section 5.5) and in comparison to other section loads (Section 6.7).

To better understand the variable-speed, variable-pitch controlled turbines, see [95, 18, 55]. Figure 4 shows how the controller works: a rotor speed-power relationship is used to govern the torque controller, and the pitch controller is used when the RPM becomes higher than the maximum value. In this way, the power output of the turbine is maximized below the rated wind speed, but

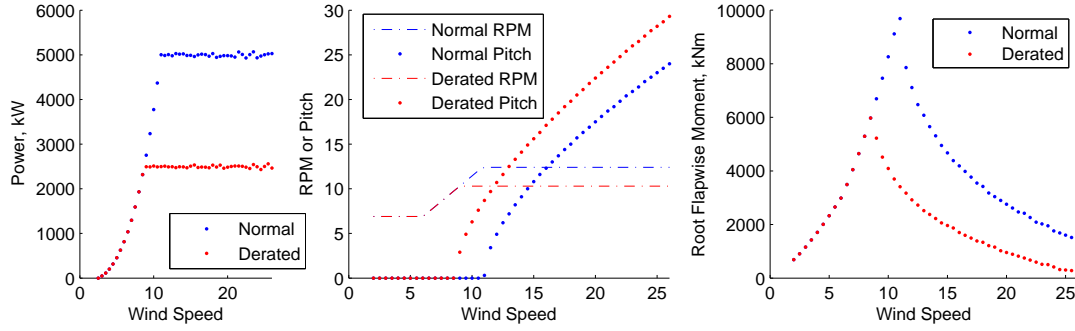


**Figure 3:** Derated (50% power level) power production control scheduling, and root bending moment compared with normal/baseline operation.

above the rated speed the power level and RPM are held constant with the pitch controller.

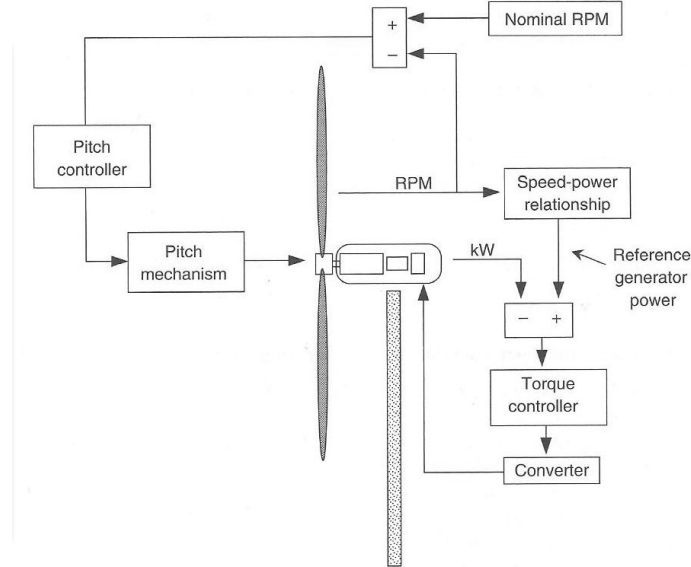


**Figure 4:** Depiction of variable-speed, variable-pitch WT control system [18].

## 2.2.2 Optimal Control of Structural Systems

The optimal control of aeroelastic systems has been extensively studied in a variety of applications, including fixed-wing aircraft, rotorcraft, propulsion systems and WTs. Therefore, a detailed review of this area is not given within this proposal.

Many times, the effects of damage are nonlinear; in the case of disbond, a clear source of nonlinearity would be the opening/closing behavior of the disbond. Control system designs that neglect system nonlinearities for a system with inherent nonlinearities are often unsuccessful, especially when off-design situations are encountered. However, many control design techniques considering these nonlinearities have been developed that are successful in controlling the nonlinear system. These

techniques include gain scheduling [104], sliding mode control [136], and control systems based on neural networks [73]. Robust control design techniques are available for linear systems that can account for system uncertainties [30]. Several authors have studied flutter suppression control design in the presence of structural nonlinearities, which are often introduced in the form of nonlinear stress-strain relationships [152]. One recent study has developed a control system that has the capability to account for damaged or failed control effectors by integrating a controller with an on-line damage detection methodology [12]. This study did not include system nonlinearities that could result from damage to the wing, and also assumed that all of the system states were measurable, which is often true in the case of a rigid body flight controller but is often not true in the case of an aeroelastic controller. On-line damage detection, again, would be assumed to take place in this case within the context of other SHPM work [97, 98].

### ***2.3 Damage Tolerant Design Strategies***

Blade reliability is of primary concern to WT blade designers, as the IEC standards dictate the design life of 20 years. Fatigue life is a primary design driver, and is typically predicted by stress-based means, as in [133, 134, 86]. A good example of damage tolerant design of modern wind turbines is a study by Wetzel [142] on debonding between the shear web and upper skin and finds that for the case where the spar cap is bonded to the skin directly, panel buckling of the skin will lead to growth of the disbond, but if the spar cap is embedded within the skin, the buckling performance of the skin is improved and disbonding is less likely. Schaumann et. al use a time domain approach to consider fatigue loading from wind and waves in the design process of offshore platform support structures [125].

Modern wind turbine blade designs are subject to a wide variety of aeroelastic performance requirements: for example blade maximum deflections, fatigue, panel buckling, and aeroelastic stability. The concepts of damage tolerance and aeroelasticity are closely related as aeroelastic vibration is a primary contribution to fatigue damage initiation and growth. Therefore damage tolerant design strategies for wind turbine blades need to be presented within the overall context of design strategies that target aeroelastic requirements effectively. WT designers should recognize that the aeroelastic challenges faced in WT blade design are very similar to challenges faced in many other aerospace fields. WT blades are non-uniform composite structures with aeroelastic performance requirements, similar to rotorblades on modern rotary wing aircraft or high aspect ratio wings on modern HALE aircraft. A commonly used design strategy for these structures is the multi-level design method

where the design problem, including design variables, objective functions, and constraints, is separated into two or more sub-problems or levels and optimizations are conducted separately. In these optimization methods care must be taken to ensure that the optimization processes are connected through clever construction of design variables, constraints, and objective functions so that the result of each independent optimization “make sense” in terms of feasibility of the design and consistency of similar design variables throughout each independent optimization.

One way that the independent optimization processes can be connected is by the use of surrogate modeling; for example, Liu, Haftka, Watson [82] separate a beam optimization problem into multiple sub-problems. Then the optimum response of these sub-systems were connected to an overall optimization procedure by the use of response surface modeling. This technique is demonstrated again by Liu, Haftka and Akgün [81] for a composite wing, in which each sub-problem represent panel stacking sequence optimization, and again a response surface model is fit to the optimization results of the sub-problems for an overall optimization representing the blade as a whole. The multi-level optimization problem can be thought of as a special case of multi-disciplinary optimization, in which the different levels are the different disciplines to be optimized. Two recent overviews of multi-disciplinary optimization are presented by Martins et al. [89] and Sobieszczanski-Sobieski and Haftka [129]. These reviews highlight a wide variety strategies that may be applied to multi-level optimization of composite structures. Chittick and Martins [24] give insight into how to perform aero-structural optimization with a multi-level process.

In this work, the two-level process consists of a “global” level that optimizes the beam spanwise properties coupled with a “local” level that finds the corresponding structural configuration. This two-level process has been demonstrated by Volovoi, Li, Ku, and Hodges as well as others for uniform composite beam-like structures [138, 7, 74, 80]. In this two-level process, the global process uses local cross-sectional stiffness or mass matrices as the design variables and a beam optimization to find the global structural properties. The resulting optimum stiffness matrices are then passed to the local level optimization process as constraints, and the local problem is to find a structural configuration that meets the stiffness matrices and minimizes local objective functions. The two levels of this process are connected through the use of surrogate models that are created by sampling the local design space.



## CHAPTER III

### BLADE OPTIMIZATION FROM ROTORCRAFT PERSPECTIVE

Wind turbines are non-uniform beam-like structures utilizing advanced composite materials. In many ways the challenges faced by WT designers are very similar to those faced by designers of modern rotor blades, in that designers must deal with a large number of structural design variables corresponding to the detailed composite structure as well as satisfy a wide variety of manufacturing and aeroelastic constraints. One particular challenge is that the design variables are often at the “local” level, and aeroelastic constraints must be satisfied on the “global” level; this requires that some effort be made to connect the local design variables to global aeroelastic performance. A procedure which treats these two problems nearly independently is the multi-level procedure [138, 7, 74, 80], however this procedure has only been developed for uniform blades. This procedure will be extended to non-uniform blades and demonstrated in an example of modern rotor blade design. These concepts were extended to blades with non-uniform spanwise properties. To accomplish this, genetic algorithm (GA) and gradient-based optimization methods were utilized, and surrogate modeling was used to ensure feasibility of the resulting optimized designs. These codes were intended for inclusion within the Integrated Design Environment for advanced composite blades [60]. However, due to forces beyond the author’s control this software was never completed.

#### *3.1 Introduction*

Multi-level optimization refers to aeroelastic optimization divided into multiple levels reflecting the dimensional reduction possible with high aspect-ratio or beam-like structures, and is therefore applicable to helicopter rotor blades, WT blades, or high aspect ratio wings. The fully 3D aeroelastic analysis is reduced to a 2D section analysis to find stiffness and inertial properties of the blade, which are passed to a 1D beam analysis that calculates the aeroelastic performance of the blade, which is then passed back to the section analysis to recover the 3D stress and strain results. The multi-level optimization therefore consists of a beam optimization that optimizes the distribution of stiffness and inertial properties to obtain the desired aeroelastic performance and a cross-sectional optimization that optimizes the structural configuration to obtain desired stiffness and inertial properties. The beam optimization method for non-uniform blades would generally require a very large number of design variables, but assumptions about the possible distribution of properties along the blade can

greatly simplify the design space. Without utilizing these assumptions or at least including them as constraints, global level optimization processes that use the stiffnesses as design variables directly are likely to result in stiffness distributions that are unobtainable by local level optimization methods.

### ***3.2 Optimization Problem Definition***

The general aeroelastic blade optimization problem involves choosing the outer mould line and structural configuration subject to aerodynamic, structural, and aeroelastic performance constraints. Aeroelastic performance considerations include steady effects such as load redistribution and control effectiveness as well as unsteady aeroelastic performance metrics such as damping of aeroelastic vibrations and transient response to gust loading or maneuvering. The aeroelastic analysis tool requires knowledge of the inner structure and the outer mould line, so the structure and blade outer geometry need to be designed together in order to obtain optimal aeroelastic performance. Although it is possible to conduct aeroelastic optimization using both the outer geometry and inner structural configuration as design variables, in practice the aerodynamic and structural optimization are conducted separately in an iterative procedure. This chapter will consider optimizations in which the structural optimization procedure is “loosely” coupled with aerodynamic analysis. In this process the aeroelastic optimization is conducted separately using a baseline structure and the aerodynamic loading is passed to the structural optimizer, which then optimizes the structure and passes the updated structural behavior to an aeroelastic analysis tool, and so on until the process converges. Therefore the structural optimization procedure in this chapter is intended to optimize the following:

1. Local stresses and warping fields (local deformation)
2. Blade deflections (blade bending and torsion global deformations)
3. Blade natural frequency
4. Blade weight and inertia characteristics
5. Configuration of Inner Structure

The aeroelastic analysis is simplified by utilizing a dimensionally reduced analysis that relies on the slenderness of rotor blades, WT blades, or high aspect-ratio wings. The dimensionally reduced analysis takes the form of a 2D section analysis tool coupled with an aeroelastic beam analysis tool. For this study, VABS was used for the section analysis while GEBT and RCAS (with general composite beam elements) were used for the structural dynamics and aeroelastic analyses, respectively. GEBT is a general-purpose beam analysis tool while RCAS is a comprehensive code for rotorcraft. Both GEBT and the general composite beam elements of RCAS are based on the same rigorous reduction of the 3D structural problem into a 1D beam and 2D section analysis problem as VABS. The section

analysis is in this work referred to as the “local” analysis, while the beam analysis is referred to as the “global” analysis.

There are several advantages to “loosely coupled” optimization methodology such as this one. Use of the methodology will not be restricted to a specific application. Global analysis can be conducted for rotating blades (for helicopter and WT rotors) or non-rotating wings (fixed-wing applications), or even non-lifting structures. A more narrowly focused optimization problem is more likely to produce an optimum result, and the structural design problem is very complex, especially for non-uniform blades. The complexity of the structural problem arises from the large number of design variables and constraints along with the existence of local minima and multiple feasible designs. The optimization process will be more efficient if aerodynamics are not reevaluated at each step, while the use of less efficient aerodynamic solvers to speed up optimization will adversely impact solution accuracy. Because changing the blade outer geometry will have the greatest effect on the aerodynamic loading, the optimization process will restrict itself to optimizing the inner structure, leaving the outer geometry constant, so the assumption that aerodynamic loads are not changed from step to step is reasonable. The outer geometry is defined by blade radius, chord distribution, twist distribution, sweep-back angle, root boundary conditions, and control surface definitions.

### ***3.3 Global Level Optimization of non-Uniform Blades***

Previous work (Refs. [138, 7, 74, 80]) has shown that a two-level optimization can be successful in finding a structural configuration with optimum global properties. The two-level process consists of a “global” process that optimizes the general properties of the overall structure coupled with a “local” process that finds the corresponding structural configuration. These optimization “levels” are based on the same dimensional reduction that is utilized in the analysis. In the two-level process, the global process uses local stiffness matrices as the design variables and the beam analysis code to find the global structural properties. The resulting optimum stiffness matrices are then passed to the local level optimization process as constraints, and the local problem is to find a structural configuration that meets the stiffness matrices and minimizes local objective functions. After the blade is divided into cross sections, the user would initialize each cross section and perform a VABS analysis. Then, the global level optimization process begins using the stiffness matrix and mass per unit span of the baseline sections as design variables. The user could choose to use either classical  $4 \times 4$  or the more accurate Timoshenko  $6 \times 6$  stiffness matrices. If the classical stiffness matrix is used with isotropic materials, then the design variables will be the mass per length  $\mu$ , axial stiffness  $EA$ , torsional

stiffness  $GJ$ , flapwise bending stiffness  $EI_2$ , edgewise bending stiffness  $EI_3$ , and possibly the off-diagonal terms of the classical  $4 \times 4$  stiffness matrix. Because this method is intended for composite materials, coupling terms in the stiffness matrices may arise that couple the blade extension, shear, torsion, flap-wise bending, and lead-lag bending, so the  $6 \times 6$  matrix is usually preferred, in which case any of the matrix entries  $S_{ij}$  can be used. This type of coupling is usually avoided in industry, and previous experience with local level optimization has shown that solutions without significant coupling can be obtained. Therefore, there are at least five design variables per cross section that would typically be used in the global level optimization process ( $\mu$ ,  $EA$ ,  $GJ$ ,  $EI_2$ , and  $EI_3$ ).

The stiffness matrices and sectional masses that result from the global level optimization are then passed to local level optimizations at each cross sections as constraints. The design space for the local level optimization is derived from possible structural configurations; the objective functions and constraints could be made from cross-sectional constitutive properties such as shear, mass, and tension center location, percentage error of stiffness results from target stiffnesses, and recovery properties such as local stresses. If all of the local level optimizations succeed in finding a valid solution, that is, the required stiffness matrices were obtained, then the optimization process has finished. Otherwise, the global level process is repeated with constraints placed on the stiffness design variables. For each unsatisfied stiffness constraint, the closest achieved stiffness would be placed as a constraint on further global level optimizations.

The current state of the art in this area mainly treats uniform blades or uses approximations of the stiffness and mass properties during the global level optimization. For conventional metallic materials, it is possible to make approximations of the stiffness and mass properties based on the size of each component (Ref. [7]), however the analysis of sections made from mostly composite materials is much more difficult and such approximations are often not very useful. Fiber-reinforced composite materials are becoming commonplace in the next generation rotor blades due to their better specific stiffness and strength, corrosion and fatigue properties of composites (Ref. [33]). The manufacturing process for such composite materials involves constructing very thin layers of the composite material and stacking them to form the rotor blade skin or main spar. Each layer of the materials can be oriented at a different angle (with respect to the beam axis) allowing designers to tailor the overall properties of the blade; however this introduces a very large number of design variables and precludes the use of rough approximations for the stiffness properties of the blade.

The design variables for a global level optimization process are then the stiffness and inertial properties at each spanwise station. The stiffness and inertial properties are input to a beam analysis code in the form of a mass and stiffness matrix, which are in general symmetric and positive definite.

The mass matrix relates the velocities and angular velocities (arranged in column vector form) to the linear and angular momenta while the stiffness matrix relates the strains and curvatures to section forces and moments. The form of these matrices is given below:

$$[M] = \begin{bmatrix} \mu & 0 & 0 & 0 & \mu x_{m3} & -\mu x_{m2} \\ 0 & \mu & 0 & -\mu x_{m3} & 0 & 0 \\ 0 & 0 & \mu & \mu x_{m2} & 0 & 0 \\ 0 & -\mu x_{m3} & \mu x_{m2} & i_{22} + i_{33} & 0 & 0 \\ \mu x_{m3} & 0 & 0 & 0 & i_{22} & i_{23} \\ -\mu x_{m2} & 0 & 0 & 0 & i_{23} & i_{33} \end{bmatrix} \tag{9}$$

$$[S] = \begin{bmatrix} S_{11} & S_{12} & S_{13} & S_{64} & S_{15} & S_{16} \\ S_{21} & S_{22} & S_{23} & S_{24} & S_{25} & S_{26} \\ S_{31} & S_{32} & S_{33} & S_{34} & S_{35} & S_{36} \\ S_{41} & S_{42} & S_{43} & S_{44} & S_{45} & S_{46} \\ S_{51} & S_{52} & S_{53} & S_{54} & S_{55} & S_{56} \\ S_{61} & S_{62} & S_{63} & S_{64} & S_{65} & S_{66} \end{bmatrix}$$

For a uniform blade with a fixed outer geometry, this results in 21 stiffness design variables and 6 inertial variables to result in 27 design variables. For a non-uniform blade, multiple cross-sectional stiffness inputs would be required, so for just four cross sections over 100 design variables would be required. Some of the stiffness matrix terms are small with respect to others, so it may be possible to hold some of the small terms constant over a global level analysis process and reduce the number of stiffness design variables. If isotropic materials, many terms of the stiffness matrix go to zero or become smaller, therefore allowing the further reduction of stiffness design variables. However, even if the stiffness design variables are reduced as far as possible, say to the six main diagonal terms or even just the axial stiffness ( $S_{11}$ ), torsional stiffness ( $S_{44}$ ), and two bending stiffnesses ( $S_{55}, S_{66}$ ) for each cross section, there will still be at least 10 design variables per cross section. As the accuracy of the beam analysis generally increases with the number of cross sections used, any who wish to perform such an optimization will be forced to choose between optimization efficiency and accuracy.

To further complicate the problem, it may be necessary to enforce constraints on each cross section relating to the feasibility of the geometry actually existing. Generally, it is not possible to increase or decrease one of the stiffness terms individually. Instead, there is a relationship between the stiffness matrix elements that is based on the cross-sectional geometry. For example, an increase in  $EI_2$  that is realized by modifying the section geometry is almost always accompanied by an

increase in  $GJ$ ,  $EI_3$ , inertia per length  $i$ , and mass per length. If the material stiffness properties are changed in order to increase one of the section stiffnesses, it may not affect inertial properties, but it certainly will have an effect on all of the stiffness properties.

Feasibility considerations must also be applied if the stiffnesses of cross sections at different spanwise locations are used as design variables. The dimensions of structural components such as the skin, spar, or other internal components often vary linearly or remain constant over the span of the wing. In these cases it would be impossible or at least very difficult to manufacture a wing that varies dramatically in stiffness over the span of the wing. In fact, the variation of the stiffness design variables in the case of continuously varying wing structures can often be expressed in terms of the root stiffness and a dimensionless function of the span variable  $x_1$ . In general, the upper left  $3 \times 3$  matrix of the generalized Timoshenko stiffness matrix ( $[R]$ ) varies similarly, the upper right  $3 \times 3$  ( $[S]$ ) varies similarly, and the lower right  $3 \times 3$  ( $[T]$ ) varies similarly as well, so that:

$$\begin{aligned}\mu(x_1) &= \bar{\mu}f_\mu(x_1) \\ [R] &= [\bar{R}]f_R(x_1) \\ [S] &= [\bar{S}]f_S(x_1) \\ [T] &= [\bar{T}]f_T(x_1)\end{aligned}\tag{10}$$

If such a relationship exists for the wing considering the outer geometry and manufacturing constraints, then it may be possible to find  $f_R(x_1)$ ,  $f_S(x_1)$ , and  $f_T(x_1)$ , and then use only one set of stiffness and inertial design variables for the entire span. In this case, any number of cross sections could be used without increasing the number of design variables, and it would eliminate the need for spanwise feasibility constraints. Alternatively, if there is the potential for some spanwise variability within the structure, these relationships may be used as constraints by requiring the stiffness variables remain within a certain percentage of the predicted values based on the stiffness relationships.

#### *Source of Blade non-uniformity*

A preliminary step for the global level optimization of non-uniform blades involves investigation of the spanwise variation of constitutive properties for typical rotary wings or high-aspect ratio wings. Helicopter rotor blades, high-aspect ratio wings, and modern WT blades are often linearly tapered, linearly twisted, and may have several different airfoils along the span. To determine how these

non-uniformities affect the variation of stiffness properties along the span, it is first necessary to parameterize the geometry in terms of several types of design variables:

1. Airfoil profile (dimensionless)
2. Chord length
3. Locations of each structural component (spars) (dimensionless)
4. Thicknesses of skin and spars
5. Material properties of skin and spars
6. Layup angles of skin and spar layers in the case of composite materials.

The material properties design variables can either refer to a discrete material selection variable (“1” refers to carbon-fiber, “2” to E-glass fiber, etc.) or use of the material properties directly as continuous variables for fiber-reinforced composites. The material properties of fiber-reinforced properties are functions of the properties of the fiber and matrix and also of the volume fraction of fibers. Models of the material properties as functions of fiber volume fraction would allow use of the volume fraction as a design variable; this would also fall under the category of a material property design variable. Variation of each of the cross-sectional design variables over the span will cause the stiffness variables to vary as a function of the span. There are some special cases where the stiffness varies in predictable ways over the span.

*Perfectly Scaled Cross Section*

The first case where the stiffness variation is predictable is the case of constant airfoil profile, location variables, and constant material/layup properties, but linearly varying chord length and component thicknesses, such that the components vary at the same rate as the chord length. In this case, the constitutive properties can be expressed as a function of the local chord ratio  $\bar{c}$  (ratio of the local chord length  $c$  to a reference chord length  $c_R$ , vary close to

$$\mu = \bar{\mu}\bar{c}^2$$

$$x_{m2} = \bar{x}_{m2}\bar{c}$$

$$[R] = [\bar{R}]\bar{c}^2 \tag{11}$$

$$[S] = [\bar{S}]\bar{c}^3$$

$$[T] = [\bar{T}]\bar{c}^4$$

The variation of each property in this case is then unaffected by the location variables (as long as they remain constant over the span) or the material properties. The thickness of a given cross section is determined by the dimensionless airfoil profile and by the chord length, so if the profile is constant then the thickness will vary with the chord. Mass per unit length and the matrix  $[R]$  are linearly dependent on the area of the cross section, which is then a function of the thickness and the chord length. Therefore, if both the thickness and chord are varying linearly with the same ratio  $\bar{c}$ , then the area will vary with  $\bar{c}^2$ . The bending stiffness in the flap direction is likely a function of the chord length, the thickness of each component and the thickness of the airfoil profile squared, leading to the quartic variation shown in 11. The applicability of this kind of scaling is demonstrated in Section 3.5.6 for composite materials, which often have a thickness determined by the manufacturing process. In this case, the perfectly scaled laws can be applied if the number of layers are varied at the same rate (replacing the linear variation of the layer thickness itself) with reasonable accuracy for most of the components of  $[R]$ ,  $[S]$ , and  $[T]$ . The diagonal terms will be approximated well but due to rounding error the off-diagonal terms may not follow these trends or may even suddenly change sign as plies with “off-axis” layer angles are dropped.

*Linearly Tapered Chord, Isotropic, Constant Component Thickness*

The second case where the stiffness variation is predictable is the case of a linearly tapered chord but constant component thickness. Manufacturing constraints may be placed on the minimum thickness of each component, or in the case of composite materials a given number of layers of a given component could be used for the entire span. In this case, the effect of scaling the chord with a ratio  $\bar{c}$  will have the following effect on the various properties:

$$\begin{aligned}\mu &= \bar{\mu}\bar{c} \\ x_{m2} &= \bar{x}_{m2}\bar{c} \\ [R] &= [\bar{R}]\bar{c} \\ [S] &= [\bar{S}]\bar{c}^2 \\ [T] &= [\bar{T}]\bar{c}^3\end{aligned}\tag{12}$$

This relationship is not proven here but it was found to accurately model the variation of most of the components in  $[R]$ ,  $[S]$ , and  $[T]$ , especially those along the diagonal of  $[R]$  and  $[T]$ .



### 3.4 Feasibility Constraints and Scaling Laws for Simple Cross Sections

The need for feasibility constraints and scaling laws for nonuniform beams can be demonstrated by using very simple cross sections for which there are closed form expressions for the various constitutive properties.

#### 3.4.1 Isotropic Circular Cross Section

One of the simplest cases to consider is that of an isotropic circular cross section. In this case, there is one cross-sectional design variable, the radius  $R$ , and there are closed form expressions for the mass and primary stiffnesses (which are also related to the inertias  $i_{22}$ ,  $i_{23}$ ,  $i_{33}$ ).

$$\mu = \rho\pi R^2$$

$$EA = \pi ER^2 \tag{13}$$

$$GJ = \frac{\pi}{2}GR^4 = \frac{\pi}{4}\frac{E}{1+\nu}R^4$$

$$EI_2 = EI_3 = \frac{\pi}{4}ER^4$$

#### *Feasibility Considerations*

The closed-form expressions for the four stiffnesses considered here would allow global level optimization of a beam with this cross section with only the axial stiffness  $EA$  as a design variable. The remaining stiffnesses can then be calculated as functions of this single design variable.

$$EA = \pi ER^2$$

$$GJ = \frac{1}{4\pi E(1+\nu)}(EA)^2 \tag{14}$$

$$EI_2 = EI_3 = \frac{1}{4\pi E}(EA)^2$$

A global level optimization which uses the different stiffnesses separately and results in a set of stiffnesses that do not satisfy the relationship found in (14) will have resulted in an infeasible set of stiffnesses. That is, it will be impossible for a local level optimization to find the beam radius  $R$  for a circular cross section that satisfies a set of stiffness constraints that do not satisfy (14).

### *Tapered Beams*

If the beam is tapered so that  $\bar{c} \neq 1$  then it is still possible to conduct a global level optimization using one variable. The global level optimization just needs to scale the stiffnesses of each section accordingly:

$$EA(y) = \pi ER^2 = \pi ER_0^2 \bar{c}^2 = (EA)_0 \bar{c}^2$$
$$GJ(y) = \frac{1}{4\pi E(1+\nu)} (EA)_0^2 \bar{c}^4 = (GJ)_0 \bar{c}^4 \quad (15)$$

$$EI_2 = EI_3 = \frac{1}{4\pi E} (EA)_0^2 \bar{c}^4 = (EI_2)_0 \bar{c}^4$$

It will be shown later that for any general cross-sectional shape, the quadratic and quartic relationships given by (15) hold as long as all geometric dimensions are scaled by the same taper ratio  $\bar{c}$ .

#### **3.4.2 Isotropic Elliptic Cross Section**

Consider the case of an elliptic cross section, the outer boundary of which is defined by the curve  $(x_2/c)^2 + (x_3/t)^2 = 1$ . Here,  $c$  and  $t$  are two cross-sectional design variables that fully describe the cross-sectional shape. There are also closed-form relationships that can be used to calculate the four primary stiffnesses.

$$EA = \pi Ect$$
$$GJ = G\pi \frac{c^3 t^3}{c^2 + t^2} \quad (16)$$
$$EI_2 = \frac{\pi}{4} ct^3$$
$$EI_3 = \frac{\pi}{4} c^3 t$$

#### *Feasibility Considerations*

Now there is not a clear relationship between these primary stiffnesses that does not involve the design variables  $a$  and  $b$ , that is, knowledge of the cross-sectional dimension is required to calculate one stiffness based on the others. However, sampling of the design space may allow construction of some basic feasibility constraints for use in a global level optimization problem. To show how such feasibility constraints might be formed,  $c$  and  $t$  were sampled between 0.1 and 1.0 in increments of 0.1, and representative  $E$  and  $\nu$  values were taken from some sample aluminum material properties

to be approximately  $1 \times 10^7$  and 0.3. Since a cross-sectional analysis tool is not required for the calculation of these stiffnesses, all values of  $c$  and  $t$  were used in the sampling process. The results of this sampling are shown in Figure 5. This Figure shows that a feasibility relationship might easily be constructed to relate  $EA$  and  $GJ$ . There is a wider variation in the bending stiffnesses  $EI_2$  and  $EI_3$  from the simple regression shown in Figure 5 and would require less stringent feasibility constraint, but this is acceptable because the increased variation also implies that the local level optimization will be able to successfully find candidates that satisfy many different combinations of  $EI_2$  and  $EI_3$  (one candidate for each combination). This agrees with the intuitive result that one could vary the eccentricity of the ellipse as necessary to achieve different combinations of  $EI_2$  and  $EI_3$ .

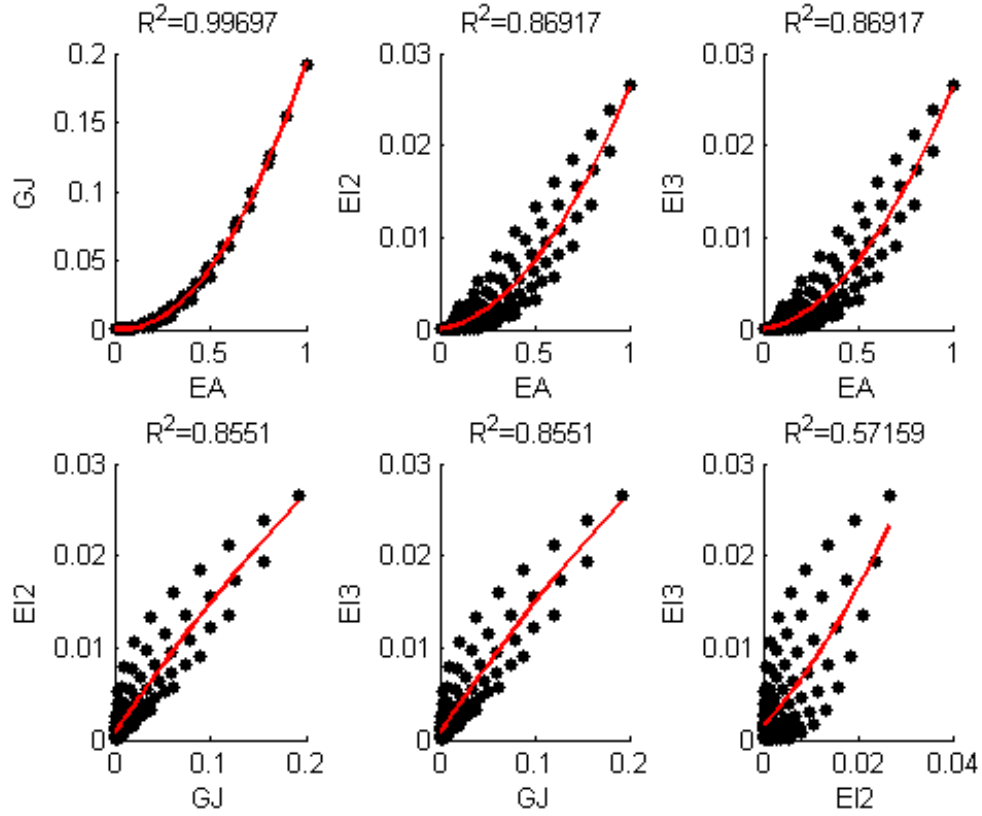


**Figure 5:** Sampling results for an elliptic cross section primary stiffnesses using Equation (16)

### *Tapered Beams*

If the section is perfectly tapered such that  $c = \bar{c}c_R$  and  $t = \bar{c}t_R$ , where  $t_R$  is a reference beam thickness, then it is easy to see that the axial stiffness will vary with  $\bar{c}^2$  and the torsional and bending stiffnesses will vary with  $\bar{c}^4$ . However, it may be that the two dimensions vary at different

rates, with separate taper ratios  $\bar{c}$  and  $\bar{t}$  in which case:

$$EA = \pi E c_R t_R \bar{c} \bar{t} = (EA)_0 \bar{c} \bar{t}$$

$$GJ = G\pi \frac{c_R^3 t_R^3 \bar{c}^3 \bar{t}^3}{c_R^2 \bar{c}^2 + t_R^2 \bar{t}^2} \quad (17)$$

$$EI_2 = \frac{\pi}{4} c_R t_R^3 \bar{c} \bar{t}^3 = (EI_2)_0 \bar{c} \bar{t}^3$$

$$EI_3 = \frac{\pi}{4} c_R^3 t_R \bar{c}^3 \bar{t} = (EI_3)_0 \bar{c}^3 \bar{t}$$

In this case, the axial and bending stiffnesses are readily expressed in terms of their root value and a dimensionless spanwise function. However, the torsional stiffness has a more complicated variation and is not so easily expressed in terms of the root value. In fact, the spanwise distribution function for  $GJ$  will necessarily be a function of the root dimensions  $c_R$  and  $t_R$ . The correlation between  $GJ$  and  $EA$  in this case however would allow a very narrow constraint on  $GJ$  and  $EA$  and feasibility could be expected for candidates with satisfied constraint. The case of an elliptic cross section with different taper ratios for the width and height begins to approach the general problem of a rotor blade that has a tapered chord and a non-uniform airfoil distribution.

### ***3.5 Demonstration of Multi-Level Process for a Realistic Rotor Blade***

This section provides general instructions about how to use the multi-level optimization method for a realistic blade design. The example optimizes the structural geometry of a uniform blade with linear twist for aeroelastic stability. The problem is summarized in Table 1. Throughout this process, the terms “local,” “global,” and “combined” analyses refer to the VABS analysis, the GEBT or RCAS beam analysis, and the combined VABS and GEBT/RCAS analysis.

#### **3.5.1 Definition of the Local Design Space**

To investigate the design space before conducting the fully realistic optimization example with RCAS, a simple beam optimization was completed using the same cross-sectional geometry and constraints. The purpose of this optimization is to (a) investigate the local design space associated with an airfoil-shaped cross section using carbon-epoxy for the skin and D-spar and (b) demonstrate several parts of the optimizer and its use for a simple frequency placement example. In preparation for the realistic helicopter blade optimization, a typical helicopter blade cross section will be used

**Table 1:** Problem summary for the realistic rotor blade optimization example.

Parameter	Value
Number of Blades	4
Airfoil	NACA 0012
Blade Radius	20 ft
Blade Chord	1.5708 ft
Rotational Speed	40 rad/s
Design Variables	Structural Geometry
Constraints	Frequency Avoidance Aeroelastic Stability Autorotational Inertia
Objective	Reduce the Blade Weight

as the beam cross section.

Figure 6 shows the geometry of the cross section, which is comprised of a skin (in the shape of a NACA 0012 airfoil), a D-spar, and a honeycomb filler material. The feasible range for the skin thickness is  $[0.01, 0.05]$  inches, and the D-spar thickness feasible range is  $[0.1, 0.4]$  inches. Layers of carbon-epoxy are often 0.005 inches. Since there are very few layers for the skin, and a conservative balanced layup was desired for the skin, the skin layup was assumed to be  $[\pm \theta]_N$ . Carbon-epoxy is often susceptible to erosion, so a 0.01 inch thick titanium layer was included as the first skin layer. The materials used are then titanium (an outer erosion shield layer), carbon-epoxy (the skin and D-spar) and a honeycomb filler material. The material properties for each material are given in Table 2.

**Table 2:** Material properties for a realistic rotor blade.  $G_{ij}$  refer to shear moduli.

Material	$E_{11}$	$E_{22} = E_{33}$	$G_{12} = G_{13} = G_{23}$	$\nu_{12} = \nu_{13}$	$\nu_{23}$
Titanium	$1.56 \times 10^7$	$1.56 \times 10^7$	$5.90 \times 10^6$	0.32	0.32
Carbon-Epoxy	$2.62 \times 10^7$	$1.49 \times 10^6$	$1.04 \times 10^6$	0.28	0.33
Honeycomb	$2.80 \times 10^4$	$2.80 \times 10^4$	$1.06 \times 10^4$	0.30	0.30

The carbon-epoxy layers in the D-spar are oriented at the following allowable angles ( $\theta$ ): 0,  $\pm 22.5$ ,  $\pm 45$ ,  $\pm 67.5$ , and 90 degrees. The D-spar was allowed to take on all of the allowable layup directions, and the layup directions were parameterized by percentage, so the D-spar layup was not constrained to be balanced. Therefore, since there are five allowable angles, five design variables were used for the D-spar layup angle distribution. To reduce the meshing time for each candidate evaluation by reducing the number of D-spar layers, the D-spar layer thickness was doubled (each D-spar layer then represents two layers).

Because the number of layers for the spar were variable, the layup was defined by a number of layers and a percentage of layers at either  $0^\circ$ ,  $22.5^\circ$ ,  $45^\circ$ ,  $67.5^\circ$ , or  $90^\circ$ . The percentages must all add up to 1, so if these percentages were used as design variables directly additional constraints

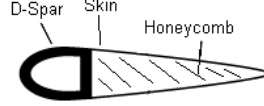


**Figure 6:** Blade cross section for realistic rotor blade optimization example

would be required. In order to avoid this, percentage variables  $S_1 - S_4$  were used to parameterize the percentage of layers at  $0^\circ$ ,  $22.5^\circ$ ,  $45^\circ$ , and  $67.5^\circ$  (respectively). with the percentage variables  $S_i$  allowed to vary between 0 and 1. The percentage of layers at a certain angle ( $P_i$ ) was then calculated by dividing the associated percentage variable by the sum of all the percentage variables:

$$P_i = \frac{S_i}{S_1 + S_2 + S_3 + S_4} \quad (18)$$

The percentage of layers oriented at  $90^\circ$  is then 1 minus the sum of the other percentages  $P_1$  through  $P_4$ .

In total 10 design variables were used to represent the geometry: the number of skin layers (SkinLayers), the angle of the skin (SkinAngle), the number of D-spar layers (SparLayers), the width of the D-spar (SparWidth), the angle of the D-spar (SparAngle), and the five design variables required to parameterize the D-spar layup by percentage ( $S_1 - S_4$ ).

### 3.5.2 Sampling of the Local Design Space

Before conducting the global level optimization, it is advisable to perform sampling of the local design space to find out the upper and lower bounds for the stiffness and mass design variables. Also, the sampled stiffness values can be used to construct surrogate models for the purpose of feasibility. During the sampling, the D-spar layup distribution was simplified to a balanced laminate of only one layup angle, with the following justification: holding all other design variable constant, the stiffness of the cross section should be at either a maximum or minimum when all of the D-spar layers are oriented at either 0 or 90 degrees, and cross sections with more complicated layup distributions, with layers oriented at any arbitrary angle, should have stiffnesses in between. Therefore, the five design variables that describe the D-spar layup distribution are reduced to one (for the sampling process), and then there are six design variables to be sampled. A Box-Behnken sampling design was generated, and a few random samples were taken at the end to evaluate the success of the surrogate models.

The purpose of the sampling process is to achieve feasibility in the following variables: mass per length  $\mu$ ,  $i_{22}$ ,  $i_{23}$ ,  $i_{33}$ , and  $S_{ij}$ , which refer to the mass per unit length, the mass moments of inertia, and the elements of the Timoshenko stiffness matrix, respectively. In preparation for a global

level optimization using GEBT and elements of the stiffness and mass matrix as design variables, surrogate models were created for two purposes: (a) to change the elements of the stiffness and mass matrix that are not used as design variables appropriately and (b) to ensure that the global level optimization does not choose a combination of design variables that is infeasible. An example of an infeasible global level optimization result is if the optimizer chooses the lowest possible sectional mass but the highest possible stiffnesses. Large stiffness results from adding more structural elements (such as an additional spar aft of the D-spar), using the maximum number of layers for each structural element, or having the largest possible D-spar; all of these possibilities indicate a larger sectional mass. Sectional mass (mass per unit length), torsional stiffness, and bending stiffness were chosen as the design variables for the global level optimization. Therefore, there are several other elements of the mass and stiffness matrix that were not chosen as design variables, namely the mass center location, the mass moment of inertia, the axial stiffness and both shear stiffnesses, and all of the coupling (off-diagonal) stiffnesses. Because only balanced laminates were chosen, the stiffness matrix elements that represent coupling between the axial, shear, bending, and twist motions should be very small compared to the axial, torsional, and two bending stiffnesses. Therefore, surrogate models were created of the axial stiffness ( $EA$  or  $S_{11}$ ) and the two shear stiffnesses to use as inputs, as well as the mass moments of inertia. A surrogate model of mass per unit length was created for use in feasibility constraints. The surrogate models were created using the 49 sampling points, and then the success of each model was tested by making predictions for the extra random samples and comparing the predictions with the actual data.

For each model, the two surrogate models, Kriging and Response Surface Modeling (RSM), were compared based on their capability to model each variable based on the extra random samples. RSM is a well known quadratic data fitting technique, but Ref. [10] gives a good overview of the theory behind Kriging. The optimization codes developed for this chapter were written in C++, so the Geostatistical Template Library for C++ [116] was readily integrated with the existing optimization framework. The description of all the surrogate models used for the global level optimization can be found in Table 3.

The surrogate models created thus far can apply to any global level optimization. The beam optimization described below will be conducted in two parts, a “global” beam optimization followed by a “local” PreVABS/VABS optimization. First, a global level optimization that utilizes the surrogate models that have just been established will be conducted, using the constitutive properties as design variables and the mass per length to satisfy natural frequency constraints, and then a local level optimization posed as an inverse design problem to find the structural configuration that

**Table 3:** Description of surrogate models created from local sampling of design space.

Model	Type	Dependents	Purpose	Additional Information
$\mu$	Kriging	$S_{44}, S_{55}, S_{66}$	Feasibility Constraint	Gaussian Semivariogram Model
$S_{11}$	Kriging	$S_{44}, S_{55}, S_{66}$	Input to GEBT	Spherical Semivariogram Model
$S_{22}$	Kriging	$S_{44}, S_{55}, S_{66}$	Input to GEBT	Spherical Semivariogram Model
$S_{44}$	Kriging	$S_{44}, S_{55}, S_{66}$	Feasibility Constraint	Spherical Semivariogram Model
$i_{22}$	RSM	$\mu$	Input to GEBT	2 <sup>nd</sup> order
$i_{33}$	RSM	$\mu$	Input to GEBT	2 <sup>nd</sup> order
$S_{33}$	RSM	$\mu$	Input to GEBT	2 <sup>nd</sup> order

satisfies the global level optimization stiffness and mass results. The local level optimization will utilize the GA, and a significant amount of sampling data may be obtained during this process. This sampling data can be added to the previous sampling results to improve the accuracy of the surrogate models. Then, the improved surrogate models can be used in realistic rotor blade combined optimization, using RCAS for the global analysis part.

### 3.5.3 Global Level Optimization

The purpose of the global or beam optimization is to find the stiffness and mass distribution that satisfies the design problem’s “global” constraints. For this simple example, the purpose of the global level optimization was to minimize a uniform linearly twisted rotating beam’s mass while satisfying frequency avoidance constraints. Table 4 shows the general geometry of the beam in consideration.

**Table 4:** Description of the beam geometry for the global level optimization example.

Dimension	Value
Beam Length	20 ft
Beam Chord	18.85 in
Number of Elements	10
Beam Root B.C.	Cantilever
Beam Tip B.C.	Free
Rotational Frequency	40 rad/s
Linear Twist	20.6 degrees

#### *Constraints*

The frequency avoidance constraints are based on the fact that the first few natural frequencies of the beam should not coincide with integer multiples of the beam rotation frequency. The lowest three natural frequencies  $\omega$  of the blade were constrained to be not within 10% of the 1<sup>st</sup>, 2<sup>nd</sup>, 3<sup>rd</sup>, and 4<sup>th</sup> harmonics of the rotor angular speed  $\Omega$ . Use of the sign( ) function helps to formulate these frequency constraints generally according to the convention that constraints are considered violated when positive, and satisfied when less than zero. An example of such a frequency constraint (*FC*)



is given below:

$$\begin{aligned} d_{ij} &= \text{sign}(\Omega_j - \omega_i) \\ FC_{ij} &= (\omega_i - 0.9\Omega_j)(1 + d_{ij}) + (1.1\Omega_j - \omega_i)(1 - d_{ij}) \end{aligned} \quad (19)$$

Stated in words, the first FC ( $FC_{11}$ ) would be: if the first natural frequency ( $\omega_1$ ) is lower than the rotational frequency ( $\Omega_1$ ), then constrain it to be lower than 0.9  $\Omega_1$  (avoidance by 10%), but if the first natural frequency is larger than  $\Omega_1$ , then constrain it to be larger than 1.1  $\Omega_1$ . The first natural frequency was constrained to avoid the first 4 harmonics, and the 2<sup>nd</sup> and 3<sup>rd</sup> natural frequencies were constrained to avoid the first 6 harmonics. In addition to the frequency avoidance constraints, feasibility constraints were imposed as well:

$$\begin{aligned} d_{ij} &= \text{sign}(\mu - \mu_{\text{model}}) \\ FC_{\text{mass}} &= (10\mu/\mu_{\text{model}} - 12)(1 + d_{ij}) + (8 - 10\mu/\mu_{\text{model}})(1 - d_{ij}) \end{aligned} \quad (20)$$

These constraints enforce the mass design variable ( $\mu$ ) to be within 20% of that for the mass surrogate model  $\mu_{\text{model}}$ . Finally, the mass per unit length design variable was chosen also as the objective function. Similar constraints were created to enforce feasibility between the design variable for torsional stiffness variable and the corresponding feasibility model.

#### *Optimization Methodology*

Initial trials of conducting gradient-based optimization found a complex design space, with multiple valid combinations of stiffness and mass per unit length separated by invalid combinations. Finite differences were used in the gradient-based optimization, and issues such as frequency constraint crossover and numerical/automated identification of structural modes led to difficulty in applying the gradient-based optimizer. Therefore, the GA was used to find a few valid candidates. The GA was conducted for six generations, which was long enough to obtain a few valid candidates. The total analysis time for six generations of the GEBT optimization was 7 minutes, 28 seconds. The GA does not evaluate candidates that have been previously evaluated, so this amounts to around 300-400 function calls. The reasonable optimization time for such a large number of function calls highlights the value of separating the local level and global level optimizations: if geometry creation and meshing were included along with 3D structural analysis based on finite elements, the analysis time would be prohibitively long for effective use of the GA. The best candidates from the GA were then subjected to gradient-based optimization, to continue to reduce the blade mass without violating the constraints.

**Table 5:** Baseline layup and analysis results, where  $\omega_i$  refers to the  $i^{\text{th}}$  natural frequency,  $x_s$  is the shear center relative location (positive is aft of 1/4 chord), and  $x_m$  is mass center relative location.

Design Variable	Value	Layup Description	#	Results	Value
SkinLayers	6	Total Layers	25	$\omega_1$	42.17 rad/s
SkinAngle	45	Layers at $0^\circ$	6	$\omega_2$	61.82 rad/s
SparLayers	25	Layers at $\pm 22.5^\circ$	6	$\omega_3$	126.4 rad/s
SparAngle	90	Layers at $\pm 45^\circ$	6	$\omega_4$	257.4 rad/s
SparWidth	0.3	Layers at $\pm 67.5^\circ$	6	$x_s$	0.8 in (aft)
		Layers at $90^\circ$	1	$x_m$	0.9 in (aft)
				$\mu$	$8.2 \times 10^{-4} \text{ lb-s}^2/\text{ft}^4$

### *Baseline Local and Global Level Analysis Results*

Before conducting the beam optimization, a baseline design can be considered to see which constraints are violated. To conduct this analysis, real VABS constitutive results for the GEBT analysis were used by translating local design variables to a parameterized geometry, performing the PreVABS/VABS analysis, and then passing the constitutive results directly to GEBT. Then, the constitutive results as well as the GEBT analysis results are available for the formation of result-based parameters. The results from this parametrized analysis are shown in Table 5.

From Table 7, it can be seen that the 1<sup>st</sup> and 3<sup>rd</sup> natural frequencies are within 10% of the 1<sup>st</sup> and 3<sup>rd</sup> harmonics of the rotor angular speed, respectively. To characterize the first four natural frequencies and associate them with blade motion, the eigenvector shape in terms of blade deflections was examined. This analysis revealed the 1<sup>st</sup> mode shape to have positive  $x_3$  and negative  $x_2$  deflection. Because the blade is twisted (nose-down), this represents flapping motion of the blade. The 2<sup>nd</sup> mode shape was found to have positive  $x_3$  and  $x_2$  deflections: again, the nose-down twist of the tip must be accounted for, implying that this is a lead-lag motion. The 3<sup>rd</sup> mode shape is the first to have a significant twist deflection, but also has significant  $x_3$  deflection as well, and small  $x_2$  deflection being of the opposite sign: a coupled flap-torsion motion. The 4<sup>th</sup> mode shape also has significant twist deflection, along with a 2<sup>nd</sup> order flap motion, so is also probably a flap-torsion motion. The constitutive properties of the baseline design are given below in terms of a Generalized Timoshenko stiffness matrix in Table 6. The mass matrix can be derived from Table 5 and the VABS manual.

### *Global Level Optimization Results*

The global level optimization procedure used key constitutive and inertial properties as design variables to minimize structural mass subject to frequency avoidance constraints and is summarized in Table 7. The global level optimization using the GA resulted in a valid candidate. This candidate

**Table 6:** Baseline stiffness matrix for the realistic design example. Units are psi.

$S_{i1}$	$S_{i2}$	$S_{i3}$	$S_{i4}$	$S_{i5}$	$S_{i6}$
$5.18 \times 10^7$	$-9.66 \times 10^3$	$-1.67 \times 10^5$	$1.87 \times 10^6$	$3.39 \times 10^4$	$-2.30 \times 10^8$
$-9.66 \times 10^3$	$1.19 \times 10^7$	$9.44 \times 10^2$	$3.36 \times 10^3$	$-5.86 \times 10^5$	$5.33 \times 10^4$
$-1.67 \times 10^5$	$9.44 \times 10^2$	$1.55 \times 10^6$	$6.06 \times 10^6$	$1.13 \times 10^5$	$-2.13 \times 10^5$
$1.87 \times 10^6$	$3.36 \times 10^3$	$6.06 \times 10^6$	$6.42 \times 10^7$	$6.62 \times 10^5$	$-7.66 \times 10^6$
$3.39 \times 10^4$	$-5.86 \times 10^5$	$1.13 \times 10^5$	$6.62 \times 10^5$	$3.06 \times 10^7$	$-2.03 \times 10^5$
$-2.30 \times 10^8$	$5.33 \times 10^4$	$-2.13 \times 10^5$	$-7.66 \times 10^6$	$-2.03 \times 10^5$	$1.80 \times 10^9$

was then subjected to gradient-based optimization. Table 8 shows the valid GA candidate, and then the same candidate after gradient-based optimization. This Table shows that the gradient-based optimization did not succeed in further minimizing the objective function without violating the constraints. The mass predicted by the surrogate model is within 20% of the final value of the design variable. This implies that the result will be achievable by local level optimization methods. In this case, the mass design variable was larger than the prediction, which would mean that non-structural mass could be utilized to make up the gap. The GA was executed a second time (the total analysis time was only 11 minutes, 7 seconds), and another valid candidate was found and is shown in Table 9. This candidate was also subjected to gradient-based optimization, which again failed to minimize the objective function further. The inability of gradient-based optimization to minimize the objective function further is caused by conflicting constraints: the first natural frequency is just above the constraint and the second just below. Reducing one natural frequency often has the effect of reducing the others as well, and vice-versa, so that the two constraints prevent gradient-based optimization from changing the configuration significantly. Note that although the mass listed in Table 9 is almost 50% larger than the mass in Table 8, the flap and lead-lag stiffnesses in Table 9 are larger than those in Table 8 as well. This indicates that the feasibility constraint is correctly imposing the trend that higher sectional mass indicates higher stiffness. The natural frequency results for the heavier valid candidates show significantly lower 2<sup>nd</sup> and 3<sup>rd</sup> frequencies, due to the increased mass, but the 1<sup>st</sup> frequency is still just above 44 rad/s due to the increased flap stiffness ( $S_{55}$ ). The increased mass and significantly lower torsional stiffness in Table 9 compared to the result in Table 8 would make it a less favorable candidate. Although autorotational inertia ( $I_a$ ) was not considered as a constraint during the optimization, it can be applied at this time to make a decision between the two candidates. Leishman in Ref. [79] assesses the autorotational inertia characteristics by an autorotational index, which is defined as

$$I_A = \frac{I_R \Omega^2}{2W} = \frac{\Omega^2}{2W} \int_0^R r^2 \mu dr = \frac{\mu R^3 \Omega^2}{2W} \quad (21)$$

Leishman recommends the value of  $I_A$  be greater than 12. The Bell 222 has a rotor diameter of 20 feet, and a maximum takeoff weight slightly less than 8,000 lb. Using this weight and the other characteristics the autorotational index is around 9.8 for candidate 1 (Table 8) and 16.7 for candidate 2 (Table 9). In the same reference (page 251, Figure 5.29) the Bell 222 is listed as having an autorotational inertia of slightly more than 20. Therefore, it was decided that the 2<sup>nd</sup> candidate (Table 9) be used as the target for the local level optimizer.

**Table 7:** General description of global level optimization problem.  
 Design Variables  $\mu, S_{44}, S_{55}, S_{66}$   
 Constraints Frequency Avoidance, Design Variable Feasibility  
 Objective Function  $\mu$

**Table 8:** A valid result from the global level optimization.

Variable	GA Result	Gradient-based Result
$\mu$ (lb-s <sup>2</sup> /in <sup>2</sup> )	0.001042	0.001041
$\mu_{\text{model}}$ (lb-s <sup>2</sup> /in <sup>2</sup> )	0.00879	0.0008
$S_{44}$ (lb-in <sup>2</sup> )	$6.92 \times 10^7$	$6.93 \times 10^7$
$S_{55}$ (lb-in <sup>2</sup> )	$6.76 \times 10^7$	$6.76 \times 10^7$
$S_{66}$ (lb-in <sup>2</sup> )	$4.25 \times 10^9$	$4.25 \times 10^9$
$\omega_1$ (rad/s)	44.26	44.26
$\omega_2$ (rad/s)	106.35	106.39
$\omega_3$ (rad/s)	142.34	142.38

**Table 9:** A valid result from the global level optimization that was used as a target for the local level optimization inverse design problem.

Variable	GA Result	Gradient-based Result
$\mu$ (lb-s <sup>2</sup> /in <sup>2</sup> )	0.0013598	0.0013598
$\mu_{\text{model}}$ (lb-s <sup>2</sup> /in <sup>2</sup> )	0.00129	0.00129
$S_{44}$ (lb-s <sup>2</sup> )	$3.96 \times 10^7$	$3.96 \times 10^7$
$S_{55}$ (lb-s <sup>2</sup> )	$9.84 \times 10^7$	$9.84 \times 10^7$
$S_{66}$ (lb-s <sup>2</sup> )	$5.36 \times 10^9$	$5.36 \times 10^9$
$\omega_1$ (rad/s)	44.85	44.85
$\omega_2$ (rad/s)	59.36	59.36
$\omega_3$ (rad/s)	106.54	106.54

### 3.5.4 Local Level Optimization

The local level optimization is a more complex problem than the global level optimization, as there are more design variables, more sectional properties to optimize, and the stiffness of the optimized result should be very close to those obtained during the global level optimization process. The GA was utilized to search the complex design space as an inverse design problem, with constraints that the VABS stiffness and mass results be within 5% of the final design variables from the global level optimization. Note that since non-structural mass can be added but not removed, the mass of each

candidate of the lower optimization can be lower than the global level optimization result. However, the stiffness constraints require the absolute value to ensure that they remain within 5% of the global level optimization results. The design variables for this optimization have already been mentioned in Section 3.5.1. Since the mass center was assumed to be at the quarter-chord during the global level optimization, the local level optimization will attempt to minimize the distance from the mass center to the quarter-chord. As the distance between the shear center  $x_s$  and quarter-chord  $x_m$  is also of aeroelastic importance, the optimization will also try to minimize this quantity as well. The objective function will then simply be the sum of the two distances:

$$\text{Objective} = |x_s - 0.25c| + |x_m - 0.25c| \quad (22)$$

#### *Reducing the Design Space Size*

Before starting the GA for the local level optimization, it is highly advantageous to decrease the size of the design space as much as possible. For the two valid candidates resulting from global level optimization, it is a good idea to examine the sampling results to see if any of the candidates already evaluated during the sampling process have stiffnesses that nearly satisfy the geometric constraints. For a given number of D-spar layers, D-spar width, and skin layers, a range of stiffnesses can be achieved by varying the layup directions of each layer. Also, if one of the candidates has skin and D-spar geometry that satisfies the mass constraints, has a mass center very close to  $0.25c$ , and has stiffnesses above and below the targets, then the local level optimization could simply vary the ply orientations and run VABS only, thus avoiding the use of a meshing preprocessor. This would have two advantages: one, the meshing codes are more computationally expensive and lead to a long optimization time, and two, VABS-AD is an automatically differentiated version of VABS that can be used in a ply orientation optimization for increased gradient-based optimization efficiency [150]. This comparison indicated that the structural geometries that will result in sectional masses near global level optimization candidate 1 (Table 8) have between 2-6 skin layers, a skin angle of approximately 45 degrees, 25-40 spar layers, and a spar width of  $0.3-0.5c$ . The candidate that closely matched the global level optimization candidate 2 (Table 9) had 6 skin layers oriented at  $\pm 45$  degrees, a D-spar with a width of  $0.3c$  and 40 layers. The upper and lower bounds and discretization tolerance for the local level optimization variables are given in Table 10 and Table 11 gives a general description of the local level optimization process.

**Table 10:** Description of local level optimization design variable bounds and tolerances.

Variable	Lower Bound	Upper Bound	Tolerance	Bits
SkinLayers	2	6	1	3
SkinAngle	25	65	10	3
SparLayers	25	39	2	3
SparAngle	60	120	15	3
SparWidth	0.3	0.5	0.07	2
S <sub>1</sub>	0	1	0.33	2
S <sub>2</sub>	0	1	0.33	2
S <sub>3</sub>	0	1	0.33	2
S <sub>4</sub>	0	1	0.33	2

**Table 11:** General description of local level optimization problem.

Design Variables	See Table 10
Constraints	$\mu$ , $S_{44}$ , $S_{55}$ , and $S_{66}$ within 5% of targets
Objective Function	sum of mass and shear center offset ( $ x_s - 0.25c  +  x_m - 0.25c $ ).

### *Local Level Optimization Results*

After six generations (with 200 candidates per generation), the GA optimization resulted in several promising candidates, where a promising candidate is one that violates less than two of the target stiffness/mass constraints, and any violated constraint represents less than 10% difference from the target. These candidates were subjected to a GEBT beam analysis and an RCAS analysis using the generalized composite beam (GCB) elements to see if any satisfy the global constraints. Table 12 describes these candidates and the GEBT/RCAS results for each. This table shows that the multi-level optimization process (global, local) succeeded in finding a structural configuration that satisfies the stiffness targets, and these structural configurations also satisfied the original global level optimization constraints. Although some of the potential candidates satisfy all of the frequency constraints according to the GEBT analysis, the RCAS frequency results are slightly different, and for some candidates which satisfy all frequency constraints according to RCAS, the RCAS results for damping for the 2<sup>nd</sup> mode are positive, indicating an aeroelastic instability. The discrepancies between RCAS and GEBT frequency results can likely be attributed the presence of aerodynamics in the RCAS analysis.

Candidate 12 may be a valid candidate already, because even though the 2<sup>nd</sup> natural frequency is within 10% of the 2<sup>nd</sup> harmonic (the difference is 7.5%), the damping of this mode is small. However, RCAS forced-response analysis can give more insight into the behavior of this mode in forward flight. Further gradient-based optimization of Candidate 12 was conducted to determine if the constraints could be satisfied by slightly changing the geometry. Unfortunately, the 2<sup>nd</sup> frequency constraint again contradicts with the 1<sup>st</sup> constraint: lowering the 2<sup>nd</sup> constraint has the effect of lowering the

1<sup>st</sup> constraint also, causing that to be violated instead. Therefore, the GA was again utilized to find a viable candidate according to the RCAS analysis results. The information from these feasible candidates was used to further reduce the design space: the SkinLayers design variable was only allowed to vary between 4 and 5, and the skin layers angle range was reduced to vary between 15 and 35 degrees. This resulted in a shorter binary string length required to represent each candidate, which led to faster convergence and smaller population size requirements for the GA during the final optimization step.

**Table 12:** Natural frequency results from local level optimization candidates with stiffness results satisfying or nearly satisfying target stiffness constraints.  $G\omega_i$ ,  $R\omega_i$ , and  $RD_i$  refer respectively to the natural frequency predicted by GEBT and RCAS and the damping predicted by RCAS for the  $i^{\text{th}}$  mode. All frequency and damping values are in units of rad/s.

#	$G\omega_1$	$G\omega_2$	$G\omega_3$	$R\omega_1$	$R\omega_2$	$R\omega_3$	$RD_1$	$RD_2$	$RD_3$
1	43.33	62.51	137	43.09	62.54	137.2	-0.139	0.0028	-1.386
2	43.22	61.92	136.08	42.97	61.95	136.3	-0.144	0.0027	-1.434
3	44.08	67.36	142.93	43.85	67.34	143.2	-0.142	0.0020	-1.512
4	43.66	61.68	139.92	43.41	61.72	140.09	-0.135	0.0015	-1.453
5	43.82	63.61	142.81	43.57	63.63	143.01	-0.133	0.0014	-1.494
6	43.82	73.21	140.24	43.58	73.06	140.39	-0.128	-0.0012	-0.783
7	43.82	73.21	140.24	46.58	73.06	140.39	-0.128	-0.0012	-0.354
8	43.82	73.21	140.24	43.54	73.06	140.39	-0.128	-0.0013	-1.354
9	44.12	73.51	142.91	43.9	73.37	143.16	-0.137	-0.0014	-1.508
10	44.2	73.6	142.49	43.99	73.46	142.72	-0.140	-0.0016	-0.154
11	44.2	73.6	142.49	43.98	73.46	142.72	-0.140	-0.0016	-1.540
12	44.29	73.98	143.36	44.08	73.83	143.59	-0.136	-0.0017	-1.535
13	44.21	74.02	143.73	44	73.88	143.97	-0.140	-0.0020	-1.501
14	43.86	73.42	139.74	43.62	73.24	139.83	-0.130	-0.0031	-1.351
15	44.21	75.93	143.73	43.99	75.76	143.98	-0.138	-0.0033	-1.473
16	44.48	76.19	146.65	44.26	76.01	146.89	-0.139	-0.0042	-1.539
17	44.22	74.59	143.39	44.01	74.43	143.63	-0.149	-0.0042	-1.555
18	44.27	76.05	143.29	43.82	74.93	141.5	-0.150	-0.0050	-1.502
19	44.04	75.12	141.27	43.82	74.96	141.5	-0.150	-0.0050	-1.502
20	43.95	73.88	142.51	43.71	73.71	142.68	-0.143	-0.0057	-1.465
21	44.72	72.16	147.88	44.5	72.06	148.09	-0.139	-0.0066	-1.593
22	43.97	75.75	142.49	43.73	75.55	142.66	-0.141	-0.0083	-1.421
23	44.15	75.68	142.39	43.93	75.48	142.57	-0.143	-0.0083	-1.454

### 3.5.5 Combined Optimization

Although it is a simpler procedure to consider beam and local level optimizations separately, the eigenvalue analysis feature of RCAS yields non-physical results when provided with “fake” stiffness properties used by the global level optimizer, in contrast to GEBT which gave physical results when the stiffness inputs were modified. Therefore it was determined that a combined optimization process was necessary. In this case, the design variables were the local design variables, and the constraints

**Table 13:** Optimized layup and analysis results.

Design Variable	Value	Layup Description	#	Results	Value
SkinLayers	4	Total Layers	30	$\omega_1$	42.17 rad/s
SkinAngle	30	Layers at $0^\circ$	16	$\omega_2$	71.86 rad/s
SparLayers	30	Layers at $\pm 22.5^\circ$	4	$\omega_3$	143.2 rad/s
SparAngle	120	Layers at $\pm 45^\circ$	6	$\omega_4$	310.2 rad/s
SparWidth	0.5	Layers at $\pm 67.5^\circ$	4	$x_s$	0.74 in (aft)
		Layers at $90^\circ$	0	$x_m$	1.3 in (aft)
				$D_1$	-0.124
				$D_2$	-0.00044
				$D_3$	-1.398
				$\mu$	$1.81 \times 10^{-3}$ lb-s <sup>2</sup> /in <sup>2</sup>

were the global constraints for natural frequency avoidance. However the bounds for the local design variables are very small due to the extensive sampling of the design space at this point. Because the RCAS analysis included the damping effect of aerodynamics, additional constraints were placed on the damping of the first three aeroelastic modes. The damping of the 2<sup>nd</sup> mode was then chosen as the objective function, as this mode is the most lightly damped. The GA succeeded in finding a valid candidate for the design problem as posed so far, which is fully described in Table 13. Further analysis must be conducted to ensure that the light damping of the 2<sup>nd</sup> mode does not induce large limit cycle oscillations, which may induce failure of the rotor blade. However, the 2<sup>nd</sup> mode was identified as a lead-lag motion, which is often lightly damped for rotor blades due to the small aerodynamic forces in the lead-lag direction (drag). The increased sectional mass compared with the global level optimization result of  $\mu = 1.31 \times 10^{-3}$  lb-s<sup>2</sup>/ft<sup>4</sup> is acceptable because it increases the autorotational index from 16.7 to 22.2, satisfying any issue that may have arisen due to the lower sectional mass of the global level optimization result.

### 3.5.6 Non-Uniform Blade Optimization

The same general multi-level optimization methodology can be used to analyze a tapered blade. Utilizing the same cross-sectional shape and inner structural configuration, adding a spanwise non-uniformity will cause the stiffness and inertial properties to vary over the span. However, these spanwise variations are not arbitrary and often follow some surprisingly basic trends. Sampling of the local design space for different combinations of local design variables and at various points along the blade span was used to determine the spanwise stiffness distribution functions for each of the stiffness or inertial properties. For the global level optimization process, the number of stiffness and inertial design variables was considerably reduced by taking advantage of these trends. This process is demonstrated for a common type of spanwise non-uniformity: linear taper. The blade with linear



taper is expected to follow the distribution functions given in Equation (11).

#### *Spanwise Stiffness and Inertia Distribution Due to Linear Taper*

Using the optimized result from Table 13 as the root structural geometry, the spanwise trends caused by linear taper were investigated. There are two possible ways to taper the inner structure: linearly tapering the thickness of each layer or reducing the number of plies in the skin and spar linearly. The first way causes the geometry to scale exactly by taper ratio. The spanwise trends for this case are demonstrated in Figures 7 and 8. These figures show that the hypothesis holds for a perfectly scaled geometry for the majority of the stiffness matrix elements. Small discrepancies appear in several of the off-diagonal terms. However, these terms are all one to two orders of magnitude smaller than the diagonal terms, and have a significantly lower effect on the first few natural frequencies, so the slight variation may have little effect on the global beam analysis.

The second way to vary the cross-sectional geometry is probably more realistic for composite blades, for which the layer thickness is often a material property and cannot be varied. In this case, vary the number of layers of each element, and hold the layer thicknesses constant. Of course, some rounding will occur as the number of layers is varied this way. The results are then shown in Figures 7-8. These figures show that the variation is not as exact as found for the perfectly scaled case, but is still very close for the largest stiffness values. There are two reasons for the variation: the first is the rounding of the numbers, and the second is that although the design percentage of each layup direction was held constant when the number of layers was varied, the discrete nature of the number of layers causes the actual percentage of each layer through the thickness to vary from the design percentage. This variation affected the coupling stiffness terms the most, but again they are a few orders of magnitude lower than the associated diagonal stiffness terms, so this variation should not affect the results as significantly.

#### *GEBT Natural Frequency Analysis of Tapered Blade*

The GEBT frequency analysis results of the optimized uniform blade are compared with the results of the perfectly and realistically scaled models. This comparison is shown in Table 14, and it reveals that although there is a significant difference between the baseline (untapered) case and either tapered case, the difference between the perfect case and the realistic case is small. A beam analysis case in which the stiffness results for all of the cross sections except for the outboard section were replaced by functions of the root stiffness, the span location, and the appropriate spanwise trend function; these results are also shown in Table 14 under the heading “Scaled.” The results from this

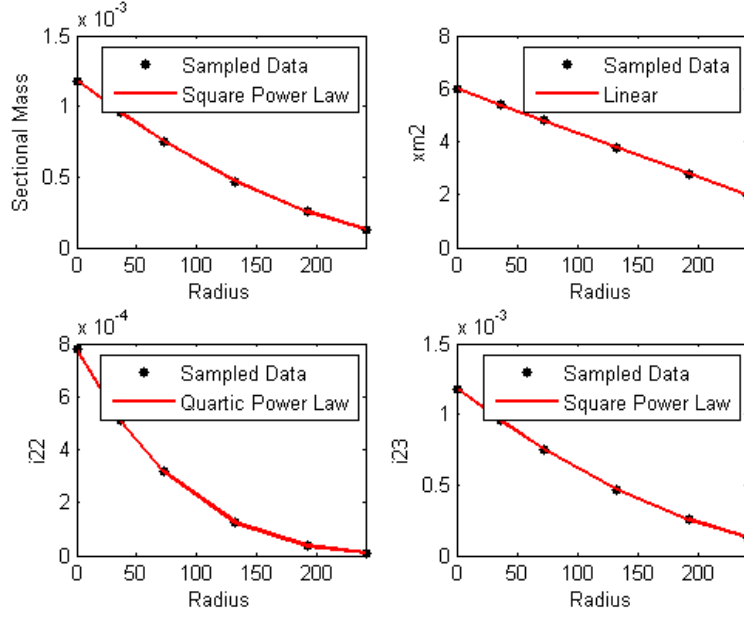


**Figure 7:** Variation of the inertial properties  $\mu$ ,  $i_{22}$ ,  $i_{23}$ , and  $i_{33}$  as a function of span for a linearly tapered blade which is perfectly scaled.

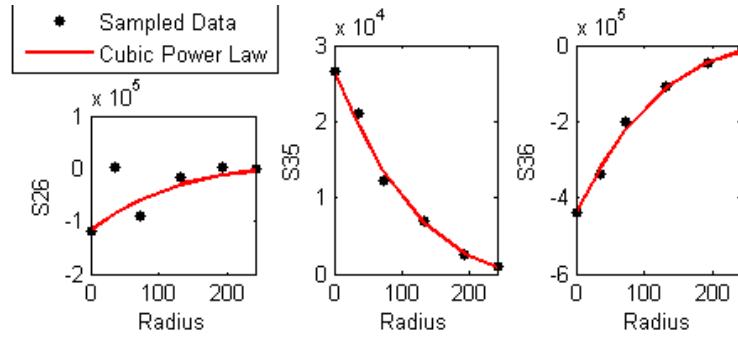


**Figure 8:** Variation of the components of the smaller components of the upper right  $3 \times 3$  subset of the Generalized Timoshenko stiffness matrix as a function of span for a linearly tapered blade which is perfectly scaled.

analysis are nearly identical to the “Perfectly” scaled results, showing that the assumption that the stiffnesses which did not obey the scaling laws (such as  $S_{26}$  in Figure 8) can be scaled anyway with little difference in the frequency analysis results.

**Table 14:** GEBT frequency analysis of a linearly tapered blade using two scaling techniques.

Frequency	Uniform	Perfect	Scaled	Realistic
$\omega_1$	44.23	50	50	51.76
$\omega_2$	71.97	101.48	101.48	109.94
$\omega_3$	142.96	130.33	130.32	134.27

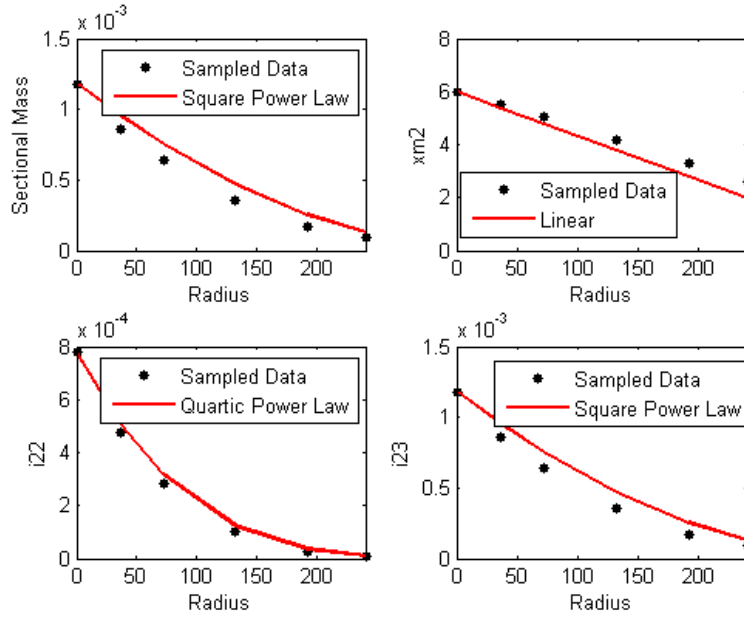


**Figure 9:** Variation of the inertial properties  $\mu$ ,  $i_{22}$ ,  $i_{23}$ , and  $i_{33}$  as a function of span for a linearly tapered blade which is realistically scaled (by number of plies).

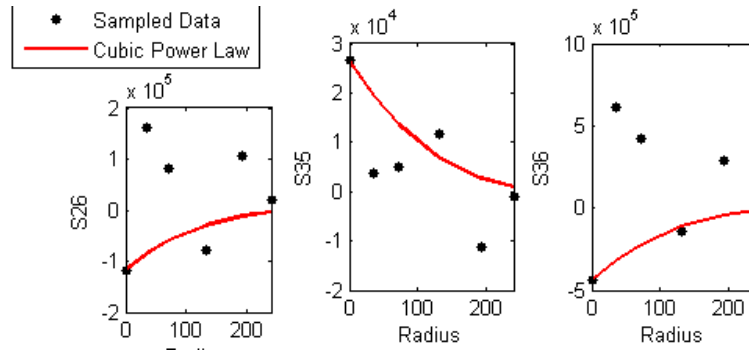


**Figure 10:** Variation of the components of the smaller components of the upper right  $3 \times 3$  subset of the Generalized Timoshenko stiffness matrix as a function of span for a linearly tapered blade which is realistically scaled (by number of plies).

### *Global Level Optimization Using Spanwise Trends*

The good agreement of the first three natural frequency results shown in Table 14 suggest that these spanwise trends can be taken advantage of during global level optimization to use only one set of stiffness and inertial design variables for the root section, and then use parameters to vary the other cross-sectional stiffness and inertial properties according to the observed trends. Tapered blades often raise the consideration that reducing the mass near the tip will drastically reduce the blade autorotational inertia, which is an extremely important blade performance measure in case of engine failure. For a linearly tapered blade, assuming the square power law holds for the sectional mass

distribution, the autorotational inertia index suggested by Ref. [79] can be obtained as a function of the root mass alone (below). Again, taking the Bell 222 representative takeoff weight ( $W$ ) of approximately 8,000 lb, and using the recommendation from Ref. [79] that  $I_A$  be greater than 12, a lower constraint on the root sectional mass can be obtained as  $0.00117 \text{ lb-s}^2/\text{in}^2$ :

$$\tilde{c} = c_t/c_r$$

$$\bar{c} = c/c_R = 1 - (1 - \tilde{c})(r/R)$$

$$\mu = \bar{c}^2 \mu_R \tag{23}$$

$$I = \int_0^R \mu r^2 dr = m_R \int_0^R (1 - (1 - \tilde{c})(r/R))^2 dr = \frac{1}{30}(1 + 3\tilde{c} + 6(\tilde{c})^2)\mu R^3$$

$$I_A = \frac{I\Omega^2}{2W} = \frac{1}{60W}(1 + 3\tilde{c} + 6(\tilde{c})^2)\Omega^2 R^3 \mu \approx 10221\mu$$

The results of the global level optimization using spanwise trends are shown in Table 15. This Table shows that the methodology was able to find a global level optimization result that satisfied all constraints.

**Table 15:** Valid result from the global level optimization of a non-uniform beam using perfect scaling laws.

Variable	GA Result
$\mu$	$0.0013 \text{ lb-s}^2/\text{in}^2$
$S_{44}$	$3.96 \times 10^7 \text{ lb-in}^2$
$S_{55}$	$9.84 \times 10^7 \text{ lb-in}^2$
$S_{66}$	$5.36 \times 10^9 \text{ lb-in}^2$
$\omega_1$	$53.44 \text{ rad/s}$
$\omega_2$	$98.02 \text{ rad/s}$
$\omega_3$	$107.11 \text{ rad/s}$
$\mu_{\text{model}}$	$0.00129 \text{ lb-s}^2/\text{in}^2$
$GJ_{\text{model}}$	$4.31 \times 10^7$

#### *RCAS Analysis of Baseline Tapered Blade*

To examine the effects of aerodynamics, an RCAS eigenvalue analysis was performed for both the perfectly scaled case and the realistically scaled case. Table 16 gives the RCAS results for the baseline design for both scaling cases. Table 16 shows that the baseline configuration satisfies all natural frequency and damping constraints according to the RCAS eigenvalue analysis. The discrepancy between RCAS and GEBT deserves further investigation, as the differences are significant enough to cause violation of constraints for the 3<sup>rd</sup> mode. The aeroelastic damping of all modes

**Table 16:** RCAS frequency analysis results of a linearly tapered blade, using two scaling techniques.  $\omega_i$  refers to the  $i^{\text{th}}$  natural frequency, and  $D_i$  refers to the damping of the  $i^{\text{th}}$  mode. Both frequency and damping are given in units of rad/s.

	Uniform	Perfect	Realistic
$\omega_1$	44.01	51.21	53.30
$\omega_2$	71.86	106.7	112.35
$\omega_3$	143.2	133.2	141.4
$D_1$	-0.124	-0.175	-0.184
$D_2$	-0.00044	-0.314	-0.569
$D_3$	-1.398	-0.712	-0.425

was improved by introducing the taper and completing the multi-level optimization process. This optimization example highlights the value of performing uniform blade optimization, even if the chosen configuration will feature linear taper. The uniform blade optimization provides the user with a logical starting point for the non-uniform blade optimization, and in some cases (such as for this example), satisfying all constraints for the uniform blade analysis will lead to the satisfaction of several constraints on the non-uniform blade analysis. Also, the sampling data obtained from the initial local design space exploration as well as the local level optimization attempts with the GA provide a large database for use during the non-uniform blade optimization.

### 3.6 Conclusions

The two-level optimization methodology is a powerful tool for conceptual design of uniform and non-uniform rotor blades. In the case of non-uniform blades, it can be advantageous to begin with a complete (global and local level simultaneously) uniform blade optimization to find a starting point for the global level optimizer and to build up a database for construction of accurate surrogate models to maintain feasibility. For non-uniform blades with linear taper, there are natural scaling laws for the sectional mass and inertial properties as well as for the stiffnesses. This allows a designer to work with a limited set of structural design variables (representing the root element or other spanwise locations of interest) for the global level optimization and utilize the scaling laws to obtain a realistic distribution of constitutive properties.

There are some issues with the multi-level optimization that warrant further investigation that deal specifically with non-uniform blades, such as a large number of optimization steps necessary to complete the design process. In this work, the multi-level method was extended to nonuniform blades to demonstrate the ability to find a blade satisfying all constraints without a strong desire to prove optimality of the resulting designs. A better effort to maintain and prove optimality between the different levels should be undertaken for future work. These should receive some special attention in further studies dealing with non-uniform blade optimization. More basic investigation may also take

place in how stiffness and inertial properties vary with respect to the other cross-sectional design variables (as they are listed in Section 3.3), especially an investigation into how the stiffness and inertial properties are functions of linearly varying airfoil profile, as this is a very common feature of modern rotor blades.

For wind turbine blades, there are often nonlinear variation of chord lengths or twisting profiles, however using sampling to establish spanwise trends among global level design variables and develop feasibility constraints would allow global level optimization such as was performed in this chapter. It is more typical to use efficient low-fidelity beam models based on EB assumptions and CLT to connect local design variables to global constraints and objective functions such as AEP or blade deflections. In this case, it can still be considered to be global level optimization with the low-fidelity beam representation replacing the role of surrogate modeling. If chord and twist distributions are also to be optimized in the global level process it would be recommended to reevaluate the aerodynamic loads at each step. Any possible error resulting from the representation of the blade using EB and CLT used in global level optimization will be eliminated during the local level optimization, thanks to the use of higher fidelity section analysis tools such as VABS in the local level optimization.

## CHAPTER IV

### AEROELASTIC STRUCTURAL AND CONTROL DESIGN FOR HALE AIRCRAFT

The previous chapter focused on structural design for a rotor blade with fixed outer geometry but a highly variable interior structural configuration. In many cases, however, the outer geometry can also be changed during the design process, leading to both local and global level design variables. There is also the possibility that the interior structural configuration is generally predetermined by manufacturing practices, processes, or constraints. In this case, it is possible to perform the majority of the structural design in the global design space, as local design considerations will be constrained (and simplified) by the predetermined configuration, and changes in local design variables lead to predictable changes in the inertial or constitutive inputs to the global analysis process. It is then valuable to first explore the behavior of the system globally, and then apply the understanding from this exploration to the simple local design problem. These considerations are showcased in the following example of the design of a flying wing aircraft. The flying wing aircraft design example begins by global design space exploration which resulted in conference paper at the AIAA Structural Dynamics and Materials conference of 2013 [119].

Aeroelastic design margins can be relaxed by using active controls. Through collaboration with Bihrl Applied Aerospace, design work was completed for a very high aspect ratio fixed-wing aircraft considering aeroelastic design requirements (flutter speed). As an extension of this work, an active gust suppression system was designed, using the wing bending curvatures and accelerations as inputs. The gust suppression system was effective in damping wing vibration and body motion due to discrete or continuous gusts, as well as increasing the controlled flutter speed by around 30%. This work is currently in preparation for journal submission, under the future title “Aeroelastic Control Design for HALE Aircraft using a Geometrically Exact, Intrinsic Beam Theory.” The details of this design can not be released within this thesis, however the design is very similar to the flying wing design presented in the first part of this chapter. The second part of this chapter will then show the aeroelastic control design efforts that were undertaken for the Bihrl aircraft.

## 4.1 *Introduction*

There is a current interest in high altitude long endurance (HALE) aircraft, especially for applications involving surveillance, communication, or atmospheric measurement. This class of aircraft nearly always utilizes very high aspect-ratio wings, as induced drag issues become critical at very high altitudes. The wing structure for HALE aircraft is minimal to reduce the wing weight as much as possible, and as a result, these aircraft can experience very large wing deformations in trimmed flight. The large wing deformations exhibited by these aircraft lead to geometric nonlinearities that largely affect the aeroelastic analysis process [106, 107, 59]. Conventional aeroelastic analyses often decouple the wing vibrations from the vehicle flight dynamics, but aircraft with these high aspect-ratio wings and minimal structure have been known to experience instabilities characterized by interaction between the vehicle flight dynamics and the structural vibrations. One explanation for this interaction is that the extreme length and low stiffness of the wings result in natural vibration frequencies on the order of the flight dynamics. In any case, aeroelastic analysis of these flight vehicles results in aeroelastic mode shapes that have strong components of wing vibration and vehicle body motion. When these aeroelastic mode shapes become unstable (flutter), the flutter instability is often referred to as body-freedom flutter (BFF).

It has been shown that the study of mode shapes is fundamental to the study of flutter in fixed wing aircraft, and that the coalescence of two or more mode shapes frequently accompanies the flutter instability [102, 83]. Some have suggested that the important flutter modes can be determined by looking for coalescence or near-coalescence of two neighboring modes [101]. Several past studies have examined the effect of various structural and physical parameters on the flutter characteristics of wings, including mass, mass moment of inertia, elastic and torsional moduli [3]. However, the general structural properties are not the only important factor in examining the flutter instability – in addition, the flutter behavior of the wing is also affected by the interior structure and modeling of the wing, including how it is attached to the fuselage [132, 62].

Although the dependence of this body-freedom flutter on some of the wing constitutive properties is recognized by the literature (especially bending and torsional stiffness), it is not clear if other constitutive properties have the potential to affect BFF. Additionally, no BFF study has been found to translate the increases in stiffness or other properties to changes in the actual wing structure. The present chapter examines the effects of actual changes of wing structure in terms of the BFF behavior, and also examines the effect of varying fuselage or payload properties as well.



## 4.2 NATASHA Theory

A intrinsic theory for analyzing high-aspect ratio aircraft is presented in Ref. [105]. This theory retains all geometric nonlinearities and its use of intrinsic variables completely eliminates the potential for singularities. These fully intrinsic equations contain variables expressed in bases attached to the deformed frame  $B(x_1, t)$ , and consist of internal force measures  $F_B$ , internal moment measures  $M_B$ , velocity measures  $V_B$ , angular velocities  $\Omega_B$ , and gravity vector measures  $g_B$ , each arranged into a  $3 \times 1$  column matrix representing components along  $x_1$ ,  $x_2$ , and  $x_3$ . The equations can be written in compact matrix form as in Ref. [58]:

$$\begin{aligned} F'_B + \tilde{K}_B F_B + f_B &= \dot{P}_B + \tilde{\Omega}_B P_B \\ M'_B + \tilde{K}_B M_B + (\tilde{e}_1 + \tilde{\gamma}) F_B + m_B &= \dot{H}_B + \tilde{\Omega}_B H_B + \tilde{V}_B P_B \end{aligned} \quad (24)$$

These formulas utilize the  $(\tilde{\phantom{x}})$  operator which arranges a  $3 \times 1$  column matrix into a  $3 \times 3$  matrix so that for two vectors  $v_1$  and  $v_2$ ,  $\tilde{v}_1 v_2 = v_1 \times v_2$ , where  $\times$  here represents the vector cross product. The generalized strains and curvatures  $(\gamma, \kappa)$  can then be related to stress resultants with constitutive equations and momenta  $(P, H)$  related to velocities and angular velocities with inertial equations:

$$\begin{Bmatrix} \gamma \\ \kappa \end{Bmatrix} = \begin{bmatrix} R & S \\ S^T & T \end{bmatrix} \begin{Bmatrix} F_B \\ M_B \end{Bmatrix} \quad \begin{Bmatrix} P_B \\ H_B \end{Bmatrix} = \begin{bmatrix} \mu \Delta & -\mu \tilde{\xi} \\ \mu \tilde{\xi} & I \end{bmatrix} \begin{Bmatrix} V_B \\ \Omega_B \end{Bmatrix} \quad (25)$$

The kinematics can also be described by compact partial differential equations:

$$\begin{aligned} V'_B + \tilde{K}_B V_B + (\tilde{e}_1 + \tilde{\gamma}) \Omega_B &= \dot{\gamma} \\ \Omega'_B + \tilde{K}_B \Omega_B &= \dot{\kappa} \\ \tilde{K} &= (\tilde{\kappa} + \tilde{k}) \end{aligned} \quad (26)$$

Equations 24 – 26 therefore present a complete set of first-order, partial differential equations suitable for the analysis of aircraft with high-aspect wings. These equations have been implemented by the computer code NATASHA [105, 20], and this code has been validated by several further studies [87, 130]. The force term in Eq. (24) includes gravity loading; the measure of the gravity vector can be found at all nodes using the following:

$$\begin{aligned} g' + \tilde{\kappa} g &= 0 \\ \dot{g} + \tilde{\Omega}_B g &= 0 \end{aligned} \quad (27)$$

Finally, two equations are required for trim to maintain the flight path angle  $\phi$  and the total speed  $U_\infty$  at a reference node:

$$\begin{aligned} \hat{g}_2 \hat{V}_2 + \hat{g}_3 \hat{V}_3 - \tan \phi (\hat{g}_3 \hat{V}_2 - \hat{g}_2 \hat{V}_3) &= 0 \\ \hat{V}_2^2 + \hat{V}_3^2 - U_\infty^2 &= 0 \end{aligned} \quad (28)$$

#### 4.2.1 Finite Element Discretization

The implementation in NATASHA is based on a finite element discretization. The discretized form of Eq. (24) is given as [58]:

$$\begin{aligned} \frac{\hat{F}_l^{n+1} - \hat{F}_r^n}{dl} + (\bar{\kappa}^n + \bar{k}^n)\bar{F}^n + \bar{f}^n - \dot{\bar{P}}^n - \bar{\Omega}^n\bar{P}^n &= 0 \\ \frac{\hat{M}_l^{n+1} - \hat{M}_r^n}{dl} + (\bar{e}_1 + \bar{\gamma}^n)\bar{F}^n + \bar{m}^n - \dot{\bar{H}}^n - \bar{\Omega}^n\bar{H}^n - \bar{V}^n\bar{P}^n &= 0 \end{aligned} \quad (29)$$

The forces and moments on the left and right hand sides of each node are required ( $F_l, F_r, M_l, M_r$ ) to account for discontinuities in internal forces due to concentrated applied loading. The discretized form of the kinematical equations, Eqs. (26), is then:

$$\begin{aligned} \frac{\hat{V}_l^{n+1} - \hat{V}_r^n}{dl} + (\bar{\kappa}^n + \bar{k}^n)\bar{V}^n + (\bar{e}_1 + \bar{\gamma}^n)\bar{\Omega}^n - \dot{\bar{\gamma}}^n &= 0 \\ \frac{\hat{\Omega}_l^{n+1} - \hat{\Omega}_r^n}{dl} + (\bar{\kappa}^n + \bar{k}^n)\bar{\Omega}^n - \dot{\bar{\kappa}}^n &= 0 \end{aligned} \quad (30)$$

Finally, the gravity loading equations given by Eqs. (27) are discretized as well:

$$\begin{aligned} \frac{\hat{g}_l^{n+1} - \hat{g}_r^n}{dl} + (\bar{\kappa}^n + \bar{k}^n)\bar{g}^n &= 0 \\ \dot{\hat{g}} + \bar{\Omega}g &= 0 \end{aligned} \quad (31)$$

This time-differentiated equation only needs to be satisfied at one node, which can be at a boundary. The  $(\bar{\cdot})$  variables represent averaging of nodal variables:  $\bar{d}_n = 0.5(d_n + d_{n+1})$ .

NATASHA uses a strip theory aerodynamic model which assumes that each element's aerodynamics are independent and do not interfere with each other, based on the unsteady theory developed by Peters et al. [111]. A typical 6 inflow states ( $\lambda$ ) were used for each lifting element.

#### 4.2.2 NATASHA Trim Solution Process

The system of discretized equations given above are solved using a Newton-Raphson procedure. The unknown variables are the  $\hat{F}_l, \hat{F}_r, \hat{M}_l, \hat{M}_r, \hat{V}_r, \hat{\Omega}_r$ , and  $\hat{g}_r$ , and six aerodynamic state variables for each lifting element  $\lambda$ . The typical model consists of a beam with  $N_w$  nodes (odd) representing the main wing. If there is a tail,  $N_t$  tail nodes (odd). Then a beam representation of the fuselage can be used to join the center elements of the wing and tail for a total of  $N_w + N_t + N_f$  nodes. There are  $N_w - 1$  lifting elements for the wing, and  $N_t - 1$  lifting elements on the tail, resulting in  $N_w + N_w - 2$  lifting elements for typical configurations. Lifting body configurations may also add  $N_f - 1$  fuselage lifting elements. There are also  $6N_{BC}$  unknowns:  $F_{BC}$  and  $M_{BC}$  that are the

forces and moment measures acting between each beam. The trim calculation assumes steady state, so the time derivatives and the inflow states  $\lambda$  are set to zero, so they can be ignored during the trim solution process. However, the unknown thrust setting and flap deflection add 2 additional unknowns to the problem.

If these unknowns are collectively referred to as  $\{x\}$  (assembled into a column matrix), then the discretized equations given in Section 4.2.1 can be expressed in the following general form:

$$f_1(\{x\}) - f_2(\dot{\{x\}}) = 0 \quad (32)$$

The equations are nonlinear but have the property that  $f_1(0) = 0$  and  $f_2(0) = 0$ . They are similar to the form of a descriptor system as described by Luenberger [84]. Note that  $f_2(\dot{\{x\}})$  represents the nonlinear operations that are performed on the time derivatives of the NATASHA unknowns,  $\{\dot{x}\}$ . The functions  $f_1$  and  $f_2$  input the values of the unknowns and return a column matrix of residuals of the discretized equations. The problem for the equilibrium solution is to find  $\{x\}$  such that  $f_1(\{x\}) = 0$ , where  $f_1(\{x\})$  represents the operations on the LHS of the discretized equations given in Section 4.2.1, neglecting any time-derivatives. The Newton-Raphson iteration is then performed as follows: an initial guess  $\{x\}_0$  is chosen for the unknowns. A first-order Taylor approximation is then used to attempt to drive the variables to zero:

$$f_1(\{x\}_0 + \Delta \{x\}) \approx f_1(\{x\}_0) + [J]\Delta \{x\} = 0 \implies \Delta \{x\} = -[J]^{-1}f_1(\{x\}_0) \quad (33)$$

The function values  $f_1(x)$  for the trim solution process are calculated at each step of the Newton-Raphson iteration using the discretized governing equations neglecting all time derivatives. The simple form of the discretized equations leads to closed-form expressions for the Jacobian  $[J]$ . The Jacobian  $[J]$  and the function values  $f_1(x)$  must be calculated at each step until the maximum value of  $f_1(x)$  or its vector norm is sufficiently small.

For a free-free case, the beams are unloaded at each end, so for each beam the first six components of  $f_1(x)$  are simply  $\hat{F}_l$  and  $\hat{M}_l$  for the left-most node on the beam. For the first beam, the next three components of  $f_1(x)$  are:

$$\begin{bmatrix} \hat{\Omega}_3 \hat{g}_2 - \hat{\Omega}_2 \hat{g}_3 \\ \hat{\Omega}_1 \hat{g}_3 - \hat{\Omega}_3 \hat{g}_1 \\ \hat{g}_1^2 + \hat{g}_2^2 + \hat{g}_3^2 - 1 \end{bmatrix} \quad (34)$$

These satisfy the time-differentiated gravity loading equation, Eq. (31), with one of the components of that equation replaced with a constraint on the length of the  $g$  vector. If it is not the first beam (wing), then three equations are required to maintain the orientation of the beam with respect to the last one, connecting either the fuselage to the wing or the tail to the fuselage.

There are then 21 equations to be satisfied at each node that is associated with an element: the first six are nodal force/moment equilibrium considerations at the right of each node, with  $[C_{lr}]$  being the nodal kink,  $\hat{\mu}$  being the mass of any pods/engines/stores attached to the node,  $\hat{\xi}$  being the offset of the nodal mass, and  $g$  being the gravitational constant:

$$\hat{F}_r - [C_{lr}]^T \hat{F}_l + \hat{f}_{\text{thrust}} + \hat{f}_{\text{aero}} + \hat{\mu}g\hat{g}_r - \tilde{\Omega}\hat{P}_r = 0 \quad (35)$$

$$\hat{M}_r - [C_{lr}]^T \hat{M}_l + \hat{m}_{\text{thrust}} + \hat{m}_{\text{aero}} + \hat{\mu}g\hat{\xi}\hat{g}_r - \tilde{\Omega}_r\hat{H}_r - \tilde{V}_r\hat{P}_r = 0$$

After the nodal equilibrium equations, there are 12 discretized elemental equations, Eqs. (29 – 30), and there are three spatially differentiated gravity equations, Eqs. (31). The right-most node of each beam is not associated with an element, so only the six nodal equilibrium equations, Eqs. (35), are required for this node.

The values of  $\hat{F}_r$  and  $\hat{M}_r$  for the right-most node of the beam are the next six components of  $f_1(\{x\})$ , driving the forces and moments at right-most end of the beam to zero (satisfying the free-free boundary condition). The total number of equations for a beam is then  $21N$ , for a beam with  $N$  nodes and  $21N$  unknowns.

After the components of  $f_1(\{x\})$  for each beam, the beam connections must be treated: for each beam connection, six components of  $f_1(\{x\})$  are used to ensure that  $\hat{V}_r$  and  $\hat{\Omega}_r$  are the same for the connection node on each beam, and then for both connection nodes the nodal force and moment summations, Eqs. (35), are augmented with the nodal force and moment between the two beams. Finally, the trim conditions, Eqs. (28), are the last two components of  $f_1(\{x\})$ .

The Jacobian of  $f_1(\{x\})$  with respect to the unknowns  $\{x\}$  is required for the Newton-Raphson procedure. The element of the Jacobian  $[J]_{ij}$  should be then be the partial derivative  $\frac{\partial f_i}{\partial x_j}$  (here  $f_i$  refers to the  $i$ th component of  $f_1(\{x\})$ ). As the above equations are linear, it is straightforward to find the partial derivatives analytically and populate the Jacobian matrix. For the trim analysis process, the airfoil states  $\lambda$  are not added to the design variables  $x$  nor considered in  $[J]$  or  $f_1(\{x\})$  as they are zero for the steady case.

### *Eigenvalue Analysis*

If the Newton-Raphson iteration is successfully converged the current values of  $\{x\}$  are the values of  $\hat{F}_l$ ,  $\hat{F}_r$ , etc. that satisfy the discretized equations. Up to this point, the time derivatives and aerodynamic states have been neglected, so an additional Jacobian associated with the time derivatives of  $\{x\}$  will be required, and six aerodynamic states  $\lambda$  for each lifting element are added to the unknowns  $\{x\}$ . The Peters' unsteady aerodynamic equations are then added to the system to

account for the additional unknowns [111]. Again, the first-order Taylor approximation is used so that:

$$f_1(\{x\} + \{\Delta x\}) - f_2(\{\dot{\Delta x}\}) \approx f_1(\{x\}) + [J_x] \{\Delta x\} - [J_{\dot{x}}] \{\dot{\Delta x}\} = [J_x] \{\Delta x\} - [J_{\dot{x}}] \{\dot{\Delta x}\} = 0 \quad (36)$$

The eigenvalues can then be found by assuming a solution of the form  $\{\Delta x\} = \{\Delta x\} e^{pt}$ . From this point onwards, the variable  $\{x\}$  is redefined as the perturbation values  $\{\Delta x\}$ . Then, the eigenvalues  $p$  of the system can be found by solving a generalized eigenvalue problem:

$$[J_x] \{x\} = p [J_{\dot{x}}] \{x\} \quad (37)$$

#### *Implementation and Validation of NATASHA System*

These equations have been implemented by the computer code NATASHA [20] and this code has been validated by several further studies [87, 131].

### **4.3 Flying Wing Model**

These analyses used NATASHA, which is a geometrically exact beam analysis code to calculate the behavior as if it were a 1D beam. This type of analysis is suitable for studying wings of high aspect ratio with reasonably continuous structures, and has the capability to calculate the non-linear equilibrium trim state, and then linearize about that state and perform an eigenvalue analysis to determine the stability of the equilibrium state.

#### **4.3.1 Geometric Description of the Model**

The configuration chosen for this study was inspired by the HORTEN flying wing model [87], but was altered significantly to change the character and flight speed of the flutter instability to a body-freedom flutter motion involving body pitching and fuselage reference point (“short-period” motion) and wing out-of-plane bending. The geometry of the model is realized by using 1 beam to represent the main wing. A total of 40 elements was used to represent the wing, 38 flexible elements to represent the left and right wing, and two rigid elements to represent the offset of the wing from the fuselage centerline. To eliminate whatever effect engine placement might have had on the body-freedom flutter characteristics of the model, the engines were placed at the root of the wing and aligned with the forward flight direction. The resulting finite-element model is depicted in Fig. 11 and some relevant dimensions are given in Table 17.

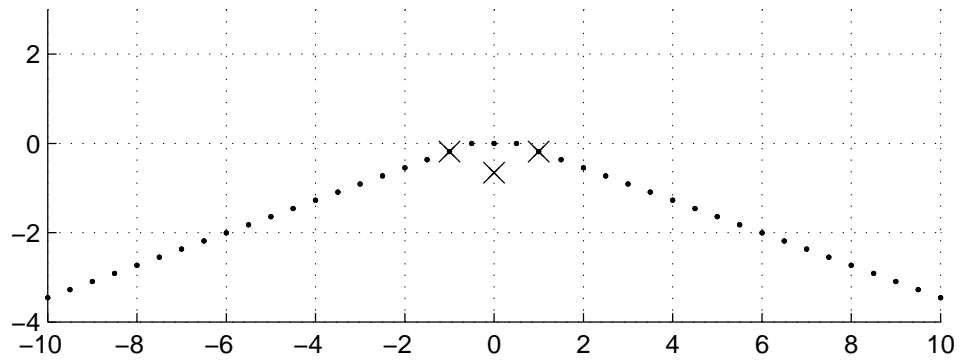


**Figure 11:** Finite element model of the typical geometry for input into NATASHA. The axes are in units of meters, and the “X” marks indicate the location of the fuselage center of gravity CG and two engines at their root location. See Table 17 for numerical details about the baseline geometry.

**Table 17:** Geometric NATASHA inputs for the typical flying wing model.

Parameter	Value
Sweep (deg)	20
Dihedral (deg)	0
Initial Twist (deg/m)	-0.2
Wing Offset (m)	1.65
Span (m)	20
$RootChordc_r$ (m)	1.0
$TipChordc_t$ (m)	0.25

#### 4.3.2 Geometric Description of a Typical Section

The cross-section is defined by a NACA 0012 airfoil profile. A very simple structure with an “I”-beam and skin was used to find the smallest possible stiffness results using VABS. A picture of the VABS model for the root section is shown in Fig. 12. Aluminum material properties were used in the VABS analysis, and a minimum skin and spar thickness of 0.127 cm was used to recover the body-freedom flutter motion at a reasonably low flight speed. The low flutter speed was desired so that changes to the model that increase the flutter speed would not drive it so high to violate the incompressible assumptions made in the aerodynamic model of NATASHA. The resulting mass per length, torsional and bending stiffness from the baseline VABS analysis can be found in Table 18. For each analysis, VABS was run for each element along the wing, so an accurate distribution of stiffness and inertial properties was obtained. The thickness of the skin and “flange,” the horizontal sections of the spar, were varied in this study.

**Table 18:** Structural NATASHA inputs for the typical flying wing model.

Parameter	Value
$\mu$ (kg/m)	9.761
$GJ$ (N-m <sup>2</sup> )	$4.24 \times 10^5$
$EI_2$ (N-m <sup>2</sup> )	$3.84 \times 10^5$
$EI_3$ (N-m <sup>2</sup> )	$2.46 \times 10^7$
$c_{ref}$ m	1

**Table 19:** Inertial NATASHA inputs for the typical flying wing model.  $H$  refers to the angular momentum of the engine. Note that the fuselage inertias were set as functions of the fuselage mass  $\hat{\mu}_f$ .

CG Value	Engine	Fuselage
$mg$ ,(N)	51.445	150
$I_{xx}$ (kg-m <sup>2</sup> )	0.29547	$0.5 \hat{\mu}_f$
$I_{yy}$ (kg-m <sup>2</sup> )	0.29322	$1.0 \hat{\mu}_f$
$I_{zz}$ (kg-m <sup>2</sup> )	0.29547	$1.0 \hat{\mu}_f$
$H$ (N-m-s)	5.24	N/A

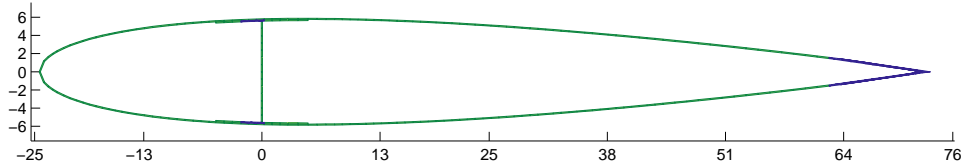


**Figure 12:** Very simple cross-sectional geometry used for VABS analysis to obtain baseline stiffnesses. The axes have units of centimeters.

### 4.3.3 Engine/Fuselage Description

The engines and fuselage are represented by their mass and inertial properties. The fuselage mass and inertia is added at the reference node of the wing and the engines are added at nodes an equal distance left and right from the reference node. Table 19 shows the values for the weights and inertia of the engines and fuselage: this inertial information was transformed appropriately to account for the fuselage offset and orientation of the wing with respect to the engine. All cross-terms in the inertial matrix for both the engine and fuselage (such as  $I_{xy}$ ) are assumed to be zero.

### 4.3.4 Aerodynamic Model

The aerodynamic coefficients ( $c_{l_0}$ ,  $c_{l_\alpha}$ , etc.) were set to be constant over the span, and since the airfoil is symmetric  $c_{l_0} = c_{m_0} = 0$  was assumed. The thin airfoil theory value of  $c_{l_\alpha} = 2\pi$  was used and  $c_{m_\alpha} = -0.08$  was determined by using the online resource JavaFoil for a NACA0012 profile. The root and tip values of each coefficient are then presented in Table 20.

**Table 20:** The aerodynamic coefficients used in the NATASHA model. The airfoil profile and coefficients were held constant along the span.

$c_{l_o}$	$c_{l_\alpha}$	$c_{l_\delta}$	$c_{d_o}$	$c_{d_{\alpha^2}}$	$c_{d_{\delta^2}}$	$c_{m_o}$	$c_{m_\alpha}$	$c_{m_\delta}$
0	$2\pi$	1	0.01	0	0	0.0	-0.08	0

#### 4.3.5 Baseline Flutter Results and Eigenvalue Analysis

The flutter analysis of the baseline model resulted in a flutter speed of approximately 32 m/s. The flutter speed was identified as the flight speed where the real part of the eigenvalue ( $\Re(p)$ ) became positive. The flutter mode shape was found to be a true body-freedom flutter motion, with body pitching and vertical velocity (“short-period” motion) and symmetric out-of-plane bending of the wings. The evolution of the lowest few eigenvalues are shown in Fig. 13, with damping being defined as the real part of the eigenvalue with a change in sign ( $-\Re(p)$ ) and frequency as the imaginary part of the eigenvalue ( $\Im(p)$ ). Upon visualization of each of the mode shapes, the eigenvalues were qualitatively characterized by the type of motion observed, and this characterization can be found in Table 21. Note that the titles associated with each mode in Table 21 describe the “dominant” motion of the mode; for instance, the mode called “short-period” is dominated by rigid body pitching and vertical velocity, but contains significant components of bending as well. It is also worthwhile to note a physical difference between “structural-dynamics” and “flight-dynamics” modes: as the flight speed is reduced to zero, the frequency of all “flight-dynamics” modes should go to zero, while the frequency of all “structural-dynamics” modes go to the *in vacuo* frequencies. Figure 13 seems to show a coalescence between the short-period modes (SP) and the symmetric out-of-plane bending mode (SOP). The stability of the SOP mode begins to decrease at around 27 m/s, before the two modes have coalesced significantly, but the frequencies of the two modes are very close to one another at the flutter speed.

The SP and SOP modes can be examined more closely by characterizing the eigenvectors in terms of the phase and magnitude of the various components. The SP and SOP modes were found to have significant components of rigid body vertical velocity and pitching, and wing symmetric bending. Therefore, the eigenvector components in root vertical velocity  $(V_3)_r$ , root pitch rate  $\Omega_1$ , root bending moment  $M_2$ , and the tip vertical velocity  $(V_3)_t$  were examined in terms of their magnitude and phase. The eigenvectors were scaled so that  $(V_3)_r$  had a magnitude of 1 m/s, and the phases were taken with respect to this component as well (so this component always has magnitude 1 and phase 0). The magnitude and phase characterizations are shown in Fig. 14. Figure 14 shows one reason the “short-period” and “bending” titles were assigned to each mode: the magnitude of



**Table 21:** Characterization of baseline eigenvalue results in terms of structural vibration and flight dynamical modes.

Frequency Range (Hz)	Characterization
0.0 – 0.1	Phugoid and Yaw Stability (two modes)
0.5 – 0.6	Lateral Stability “Dutch Roll”
1.3 – 1.7	Symmetric Out-of-Plane (SOP) Bending / Short-period
1.9 – 2.1	SOP Bending / Short-period
3.0 – 3.5	Anti-symmetric OP Bending
5.6 – 6.0	2 <sup>nd</sup> SOP Bending

$M_2$  is more significant in the “bending” mode. However, both modes have significant components of  $M_2$ . This figure also shows that for both the SP and first SOP mode, the magnitudes of  $M_2$  and  $\Omega_1$  are relatively constant over the flight speed, while the  $(V_3)_t$  magnitude increases for the SP mode but decreases for the SOP mode. This decrease of tip velocity magnitude is related to the phases of  $(V_3)_t$ ,  $(V_3)_r$  and  $M_2$ . Figure 14 shows that the SP mode has  $(V_3)_t$  lagging  $(V_3)_r$  but the SOP mode has  $(V_3)_t$  leading  $(V_3)_r$ . Also, there is a significant change in the phase of  $(M_2)_r$  with increasing flight speed for both modes, with the phase increasing with the SP and decreasing for the SOP mode. The root bending moment is nearly in phase with the root vertical velocity at the onset of instability.

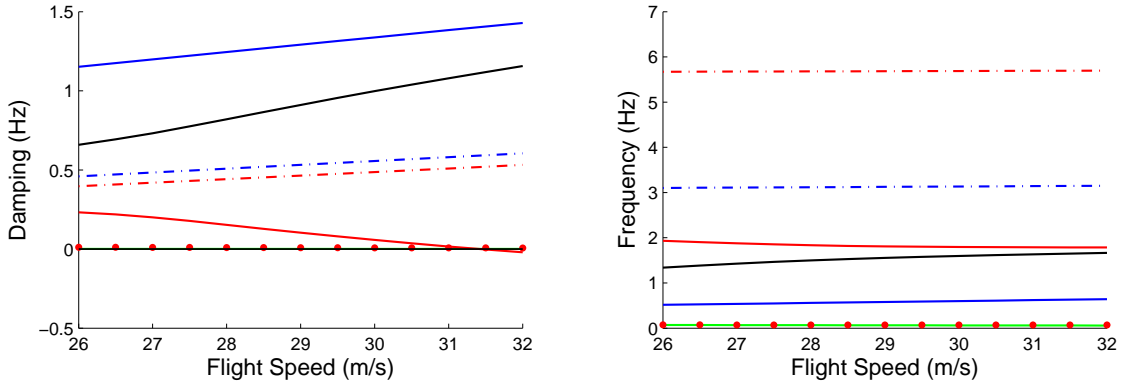


**Figure 13:** Eigenvalue analysis results for the baseline model. Instability is found at the flight speed of 32 m/s.

#### 4.3.6 “Typical” Flying Wing Model

One method that was selected to explore the inputs that affect the body freedom flutter was to create a “typical” flying wing model using as few inputs as possible and attempt to obtain the same behavior. Therefore the information from Tables 17 – 20 were used, and the structural model was

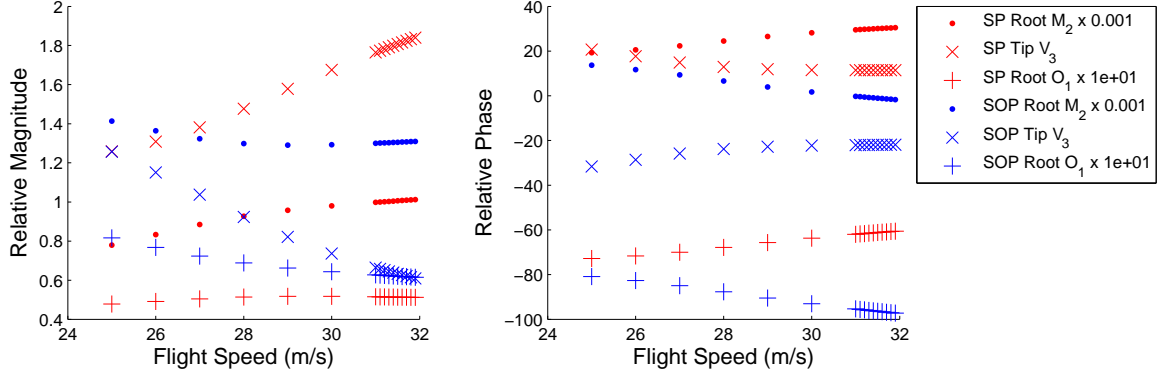


**Figure 14:** SP and symmetric out-of-plane bending (SOP) eigenvector characterization in terms of magnitude and phase of root bending moment  $M_2$ , tip vertical velocity  $V_3$ , and root angular velocity  $O_1$ . Eigenvectors were normalized so that root vertical velocity  $(V_3)_r$  magnitude was 1 m/s and then phase-shifted so that  $(V_3)_r$  phase is zero.

simplified further by assuming the following variation of structural inputs over the span.

$$\bar{c} = c/c_{ref} \quad \mu = \mu_0 \bar{c}^2$$

$$[T]_0 = \begin{bmatrix} 0 & 0 & 0 \\ 0 & 1/EI_2 & 0 \\ 0 & 0 & 0 \end{bmatrix} \quad [T] = [T]_0/\bar{c}^3 \quad (38)$$

The resulting model approximates the low frequency behavior of the realistic flying wing model very well. The effect of the various aerodynamic coefficients was explored by changing each coefficient to an alternate realistic value one by one. This process affected the trim values significantly but only  $c_{l_\alpha}$  and  $c_{m_\alpha}$  had a significant effect on the flutter behavior. In general, trim conditions are difficult to obtain with a non-zero  $c_{l_0}$ , but Fig. 15 shows the eigenvalues for the baseline model and for different values of  $c_{l_0}$ ,  $c_{d_2^2}$ ,  $c_{m_0}$ ,  $c_{m_\delta}$ ; this Fig. shows there is no distinction between these different cases in terms of these lowest eigenvalues, or the flutter speed. Therefore, even though unrealistic trim values may be obtained without an appropriate  $c_{l_0}$ , the BFF behavior is unaffected. Figure 16 shows that  $c_{l_\alpha}$  does affect these dynamics, especially in the frequency of the SP and SOP modes and the damping of most modes. It may be significant that lowering  $c_{l_\alpha}$  pushes the frequency of the relevant BFF modes apart and increases the flutter speed, again suggesting that the similarity of the SP and bending frequencies leads to the instability. In any case, the “typical” model demonstrates very clearly that wing bending flexibility, mass per length, fuselage inertial properties, and  $c_{l_\alpha}$  are the dominant factors at play with this type of BFF. The “typical” model also shows that aerodynamic design can be conducted largely without consideration to the body-freedom flutter (BFF) issue,

because even when  $c_{l_\alpha}$  was adjusted significantly the BFF speed changed only slightly.

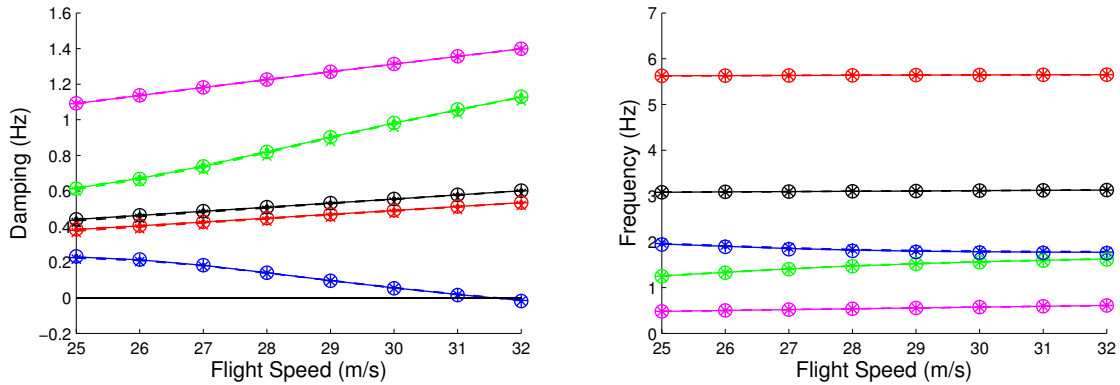


**Figure 15:** Low frequency eigenvalues for the “typical” flying wing model for the baseline and after modifying  $c_{l_0}, c_{l_\delta}$ , and all coefficients related to  $c_d$  and  $c_m$ . Curves are not labeled because they coincide exactly.

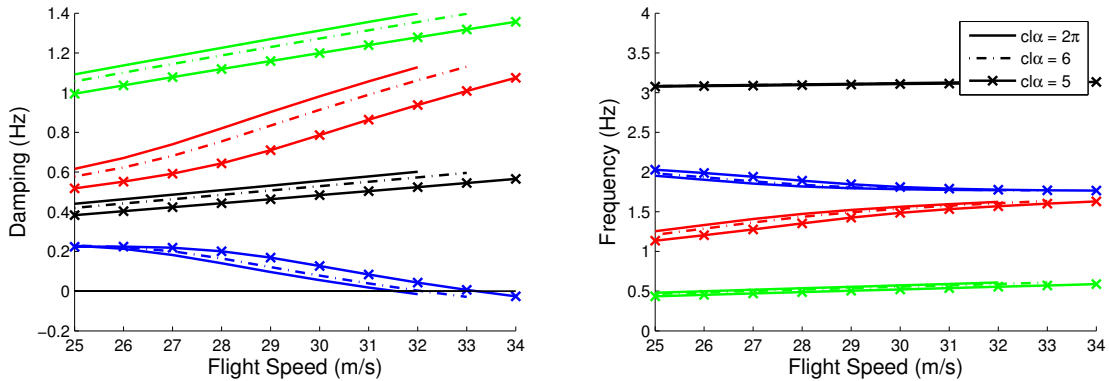


**Figure 16:** Control settings for the “typical” flying wing model for the baseline and after modifying  $c_{l_\alpha}$ .

#### 4.4 Trade Studies on Body Freedom Flutter

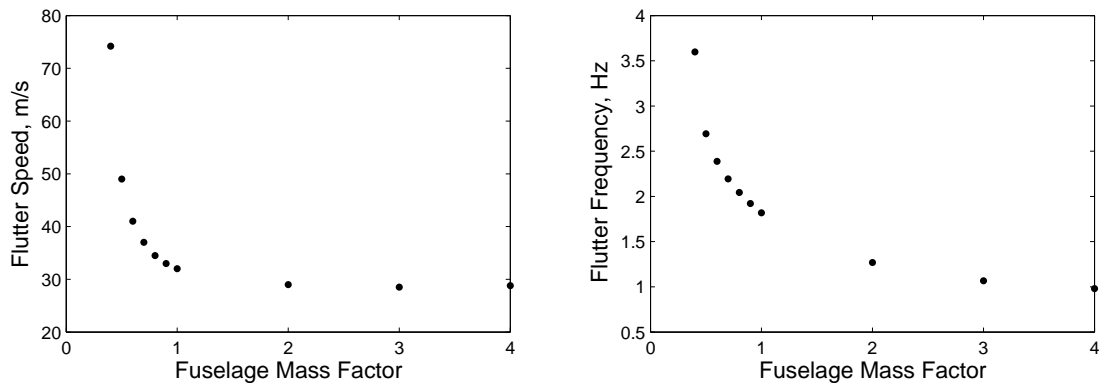
Several trade studies were conducted to examine the effect on the flutter characteristics of changing various physical inputs of the HALE aircraft. These included the fuselage mass, the fuselage CG location and its pitching inertia, and the constitutive and inertial information of the wing. The constitutive and inertial information of the wing was first varied by varying the structural geometry and finding the change of constitutive and inertial properties with VABS, and then specific elements of the mass and stiffness matrix were varied independently to show their effect alone.

##### 4.4.1 Effect of Fuselage Properties on Flutter Speed

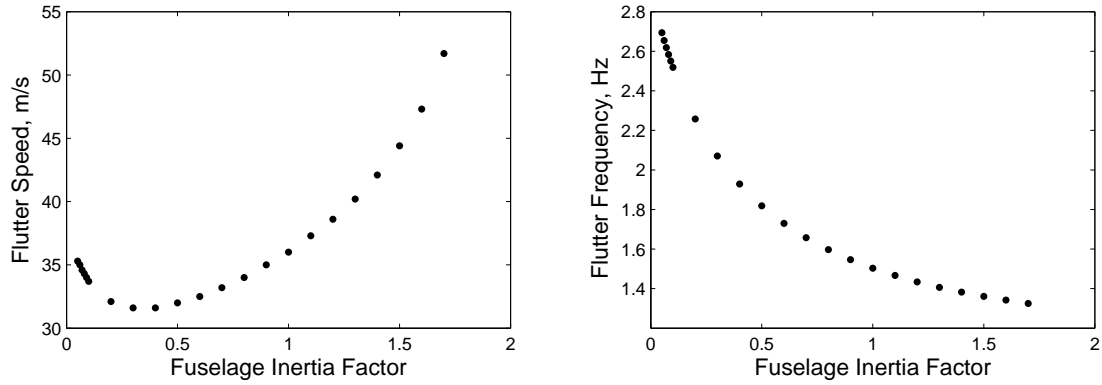
The fuselage properties that were found to impact the body freedom flutter behavior were the total mass, the fuselage inertia, and the fuselage CG location.

Figure 17 shows the results of the fuselage mass factor sweep. The fuselage mass contributed the most effective changes to flutter speed out of the factors listed above. The increased fuselage mass also increased the fuselage inertia, so some of the effects in this figure are due to the increased inertia of the fuselage. To separate the effect of the fuselage mass from the fuselage inertia, the fuselage inertia was itself varied as the total mass was held constant. Figure 18 shows the results of the fuselage inertia factor sweep. The pitch inertia of the fuselage ( $I_y$ ) should have a large impact on the frequency of the SP mode: the approximation for the SP frequency [100] is proportional to  $I_y^{0.5}$  and a similar dependency of  $I_y^{0.5}$  was observed here for the flutter frequency. Here there is a discrepancy between Figs. 17 and 18: for each the fuselage inertia was increased, but only when the fuselage inertia was increased alone the flutter speed increased. Comparison between these two figures reveal that the decreased flutter speed in Fig. 17 is due to the effect of the increased mass.

Figure 19 shows the results of varying the longitudinal CG location. This shows that the flutter speed is highly dependent upon the longitudinal CG location. Figure 20 shows the results of the CG factor sweep along the vertical axis. Like the fuselage inertia, the flutter speed was lowest for the moderate range, reflecting the fact that lowering the fuselage had the affect of increasing the fuselage inertia when calculated at the wing. A different flutter mode occurred whenever the fuselage was placed more than 1.6 m below the wing reference line that was associated with in-plane wing bending and torsion. Allowing the CG position to vary in the longitudinal or vertical direction have the same effect in terms of increasing the apparent inertia of the fuselage, but comparison between Figs. 19 and 20 reveals that longitudinal CG location travel has an additional and significant effect on the BFF behavior.



**Figure 17:** Flutter speed and frequency as a function of a multiplicative fuselage mass factor.



**Figure 18:** Flutter speed and frequency as a function of a multiplicative fuselage pitch inertia factor.

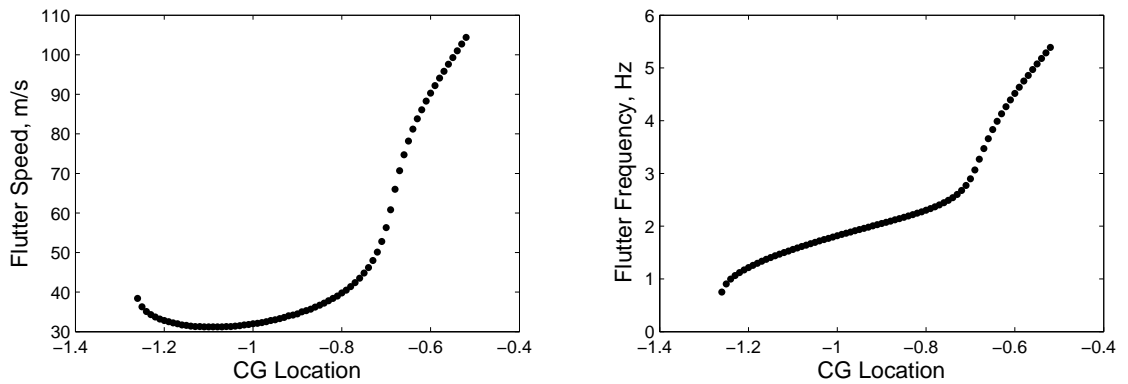


**Figure 19:** Flutter speed and frequency as a function of longitudinal CG location, measured forward of the wing.

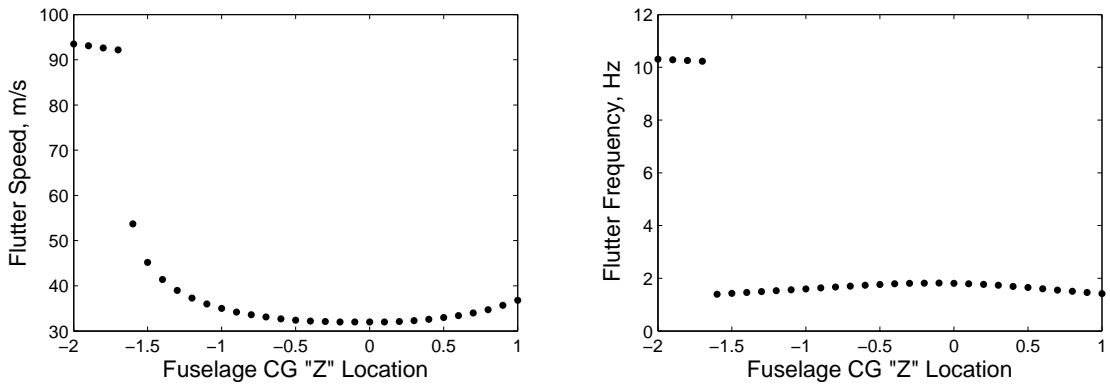


**Figure 20:** Flutter speed and frequency as a function of fuselage  $z$ -location with respect to the wing.

#### 4.4.2 Effect of Changing Structural Geometry

In order to demonstrate more directly the effect of changing structure, trade studies were conducted which varied the skin or flange thickness and used VABS to calculate the corresponding change in stiffness properties. Figure 21 shows the flutter speed and frequency results when varying the skin

thickness in the VABS analysis, and Fig. 22 shows the flutter speed and frequency results when varying the flange thickness. These figures show that increasing the structural geometry indeed had the effect of increasing the flutter speed, as expected. The two structural geometry changes affected the constitutive properties in different ways, as shown in Fig. 23: the skin thickness increase affected many of the constitutive properties, while the flange thickness increase mainly affected bending stiffness and mass per length. The effectiveness of the flutter increase in terms of increased mass and increased bending stiffness is shown in Fig. 23. This figure shows that the flange thickness increase was more effective in increasing the flutter speed in terms of both mass and stiffness. The right side of Fig. 24 shows that the additional constitutive property increases caused by increased skin thickness actually had an adverse effect on the flutter speed.

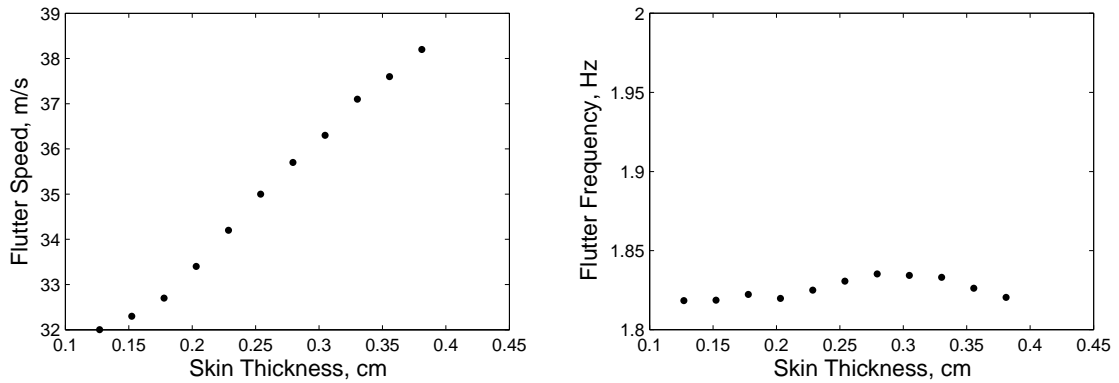


**Figure 21:** Flutter speed as a function of increasing skin thickness.

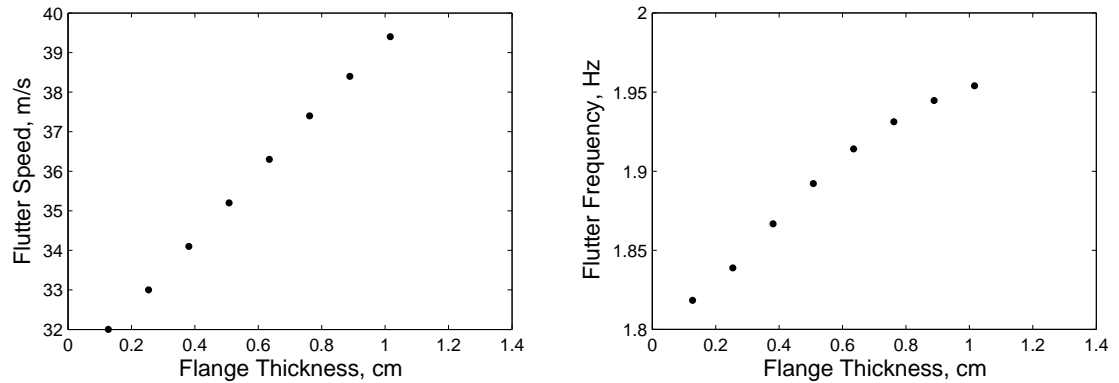


**Figure 22:** Flutter speed as a function of increasing flange thickness.

The increase in skin thickness significantly affected nearly all of the constitutive properties. The increase in flutter speed observed for increasing skin thickness was not as significant as would be expected as if the bending stiffness were increased alone. The effect of each constitutive property was isolated by changing each individually and observing the increase in flutter speed. It was found

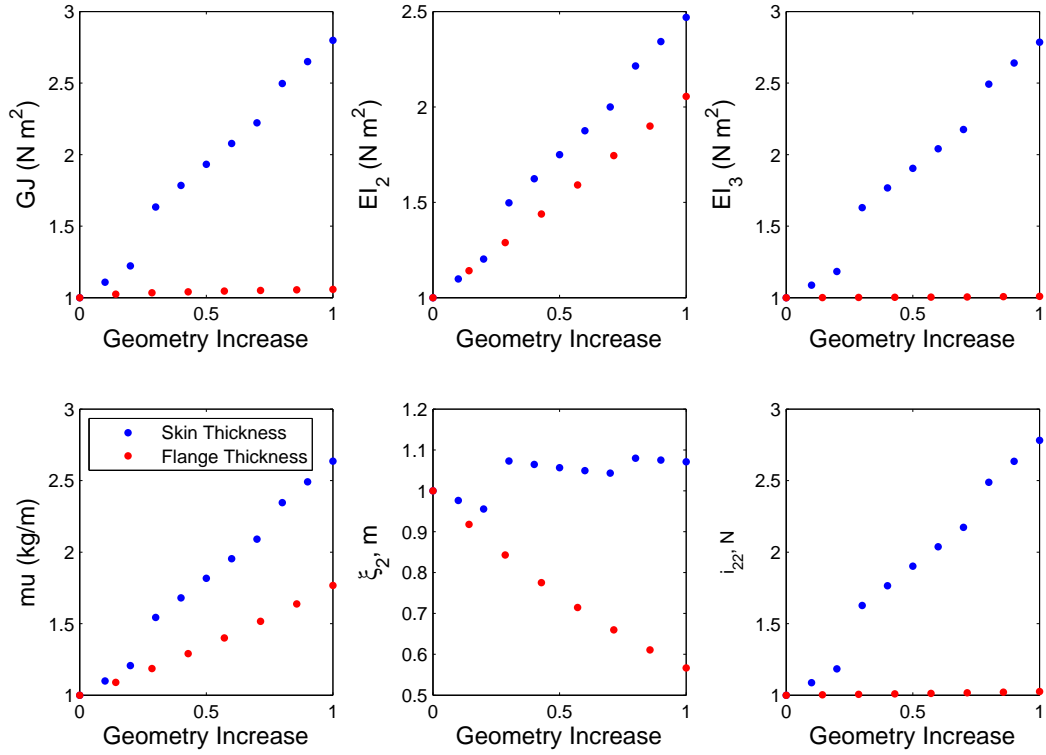


**Figure 23:** Change in constitutive properties as skin thickness and flange thickness were increased from their minimum (Geometry Increase = 0) to their maximum (Geometry Increase = 1). Skin thickness was varied from 0.127 to 0.381 cm, and flange thickness varied from 0.127 to 1.016 cm.

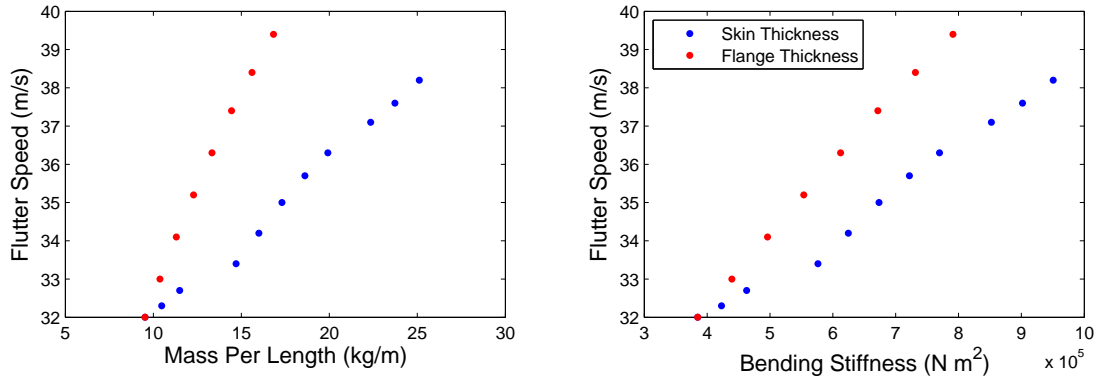


**Figure 24:** Flutter speed as a function of increasing skin and flange thickness as a function of mass per length of the root section (left) or bending stiffness of the root section (right).

through these trade studies that many of the constitutive properties had a small or negligible effect on the flutter speed with the exception of bending stiffness and mass per length. Figure 25 shows the results of the skin thickness sweep in terms of flutter speed compared with the flutter speed results when only the bending stiffness was varied and when only the mass per length ( $\mu$ ) was varied. This Fig. shows that while the increased bending stiffness raised the flutter speed, while the increased

mass per length lowered the flutter speed.

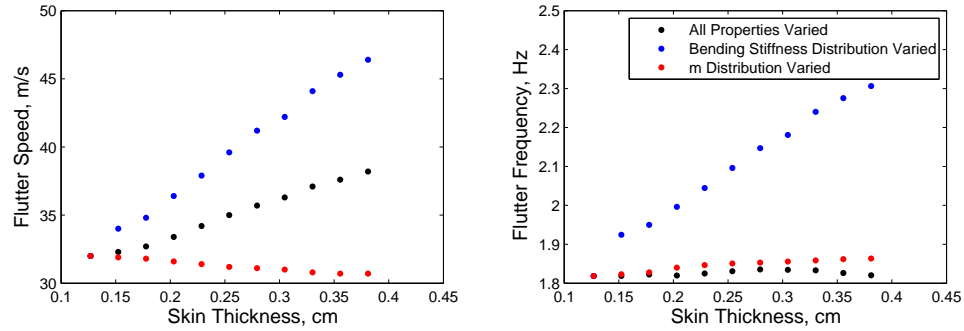


**Figure 25:** Flutter speed as a function of increasing skin thickness, with each constitutive property varied independently.

#### 4.5 Eigenvalue and Eigenvector Analysis for Various Cases

The evolution of eigenvalues and eigenvectors as a function of flight speed for various cases was explored to see if insight into the nature of this type of body freedom flutter could be gained. The cases of maximum skin thickness, maximum flange thickness, low fuselage mass and high fuselage inertia were selected as they all exhibited significant increase in flutter speed.

##### 4.5.1 Maximum Skin Thickness

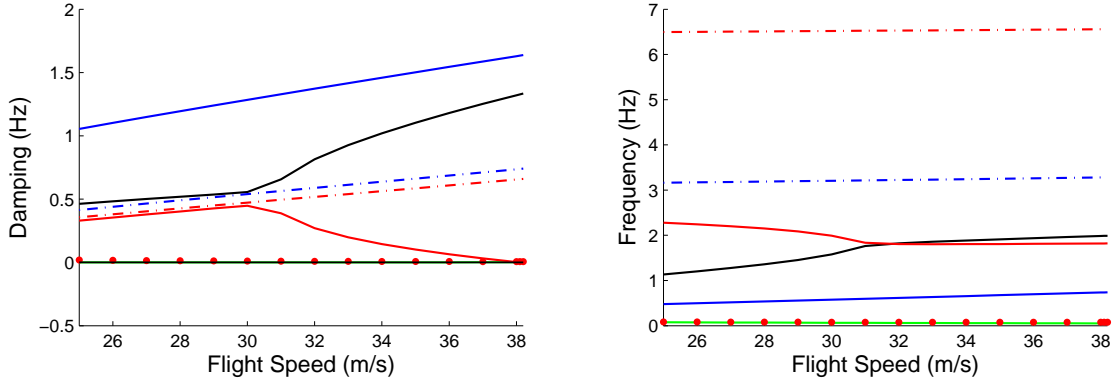
The case of maximum skin thickness has drastically increased stiffness, mass and inertial problems in comparison to the baseline. Figure 26 shows how the eigenvalues change as a function of flight speed for this case. Figure 27 characterizes the SP and SOP modes in terms of magnitude and phase, with the eigenvectors normalized and phase-shifted so that root vertical velocity has a magnitude of 1 m/s and a phase of 0. The qualitative characterization of each eigenvalue has not changed from those given in Table 21.

Figure 26 shows that the frequencies of the SP and SOP modes have indeed “coalesced” in the sense that they come to the same frequency at around 31 m/s, and afterwards the frequencies are very close between the two modes. Before this coalescence, the damping of the SOP mode is increasing with flight speed, but after the coalescence the SOP mode damping decreases rapidly with respect to flight speed.

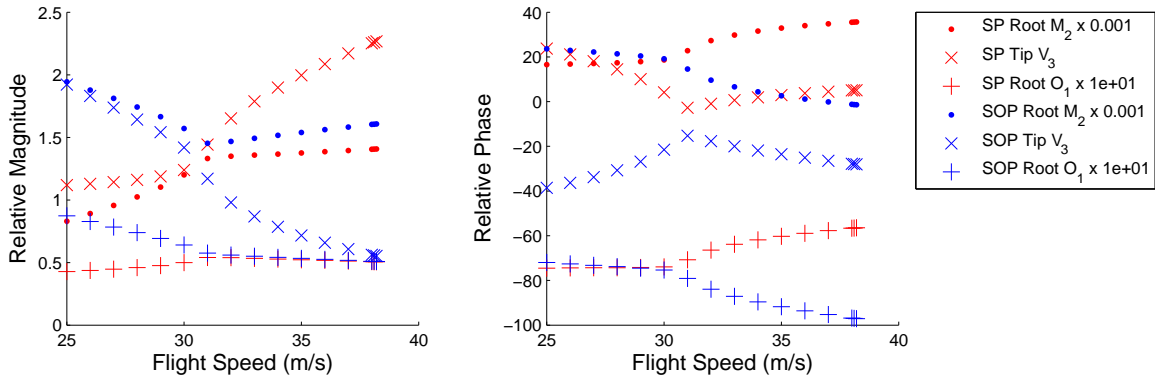
Figure 27 again shows that tip velocity magnitude increases with flight speed for the SP mode but decreases with flight speed for the SOP mode. Interestingly, each component has similar magnitudes in the two modes near the speed where the frequency coalesces. The magnitudes shown in Fig. 27 have trends that closely resemble the trends found in the baseline case (Fig. 14).



Figure 27 again shows many similarities to Fig. 14 in the phase results, with bending moment phase approaching zero at the onset of stability, tip velocity leading the body vertical velocity for the SP mode and lagging the body vertical velocity for the SOP mode. Again the characteristics of the two eigenvectors in terms of magnitude and phase are similar near the “coalescence” flight speed of 31 m/s.



**Figure 26:** Eigenvalue analysis results for the model with maximum skin thickness (0.381 cm). Flutter speed is 38.2 m/s.



**Figure 27:** Short-period (SP) and symmetric out-of-plane bending (SOP) eigenvector characterization in terms of magnitude and phase of root bending moment  $M_2$ , tip vertical velocity  $V_3$ , and root angular velocity  $\Omega_1$ . Eigenvectors were normalized so that root vertical velocity  $V_3$  magnitude was 1 m/s and zero phase. Results are shown for the maximum skin thickness (0.381 cm).

#### 4.5.2 Maximum Flange Thickness

The case of maximum flange thickness has increased bending stiffness and mass per length, but many of the other constitutive properties remain constant. Figure 28 shows how the eigenvalues change as a function of flight speed for this case. Figure 29 characterizes the SP and SOP modes in terms of magnitude and phase, with the eigenvectors normalized and phase-shifted so that root vertical velocity has a magnitude of 1 m/s and a phase of 0.

Examining these three figures in comparison with Figs. 13, 14, 26, and 27, a trend in the behavior of the eigenvalues and eigenvectors can be seen. The “coalescence” flight speed for this case would be approximately 33 – 35 m/s, although the shift in the stability of the SOP mode still occurs around 31 m/s. The cross-over of tip velocity magnitudes in Fig. 29 coincides with the shift of stability of the SOP mode, while the magnitudes of  $M_2$  and  $\Omega_1$  approach each other near the coalescence flight speed. Again, the SOP mode has decreasing tip velocity magnitudes with increasing flight speed while the SP mode has increasing tip velocities with increasing flight speed. Fig. 29 also shows that for the SP the tip velocities lead the centerline velocities while the SOP mode has a phase lag between the two velocities. Finally, the phase of the bending moment  $M_2$  is nearly aligned with the vertical velocity at the onset of instability for the unstable mode.

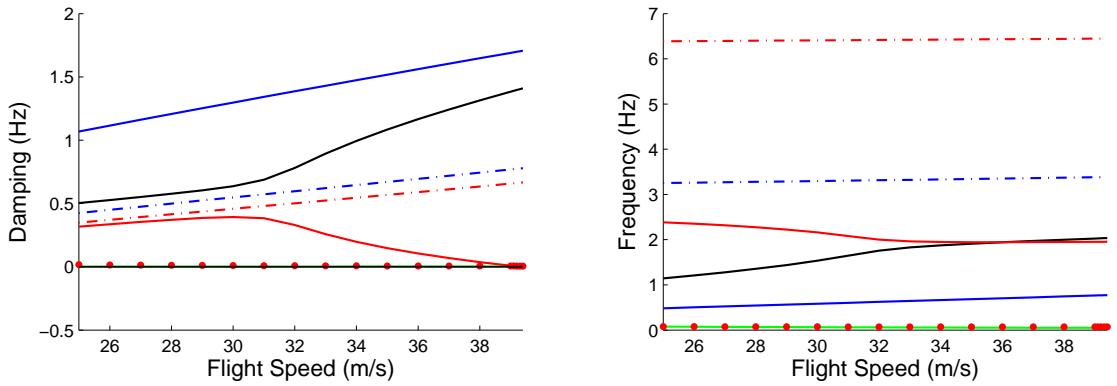


**Figure 28:** Eigenvalue analysis results for the model with maximum flange thickness (1 cm). Flutter speed is 39.4 m/s.

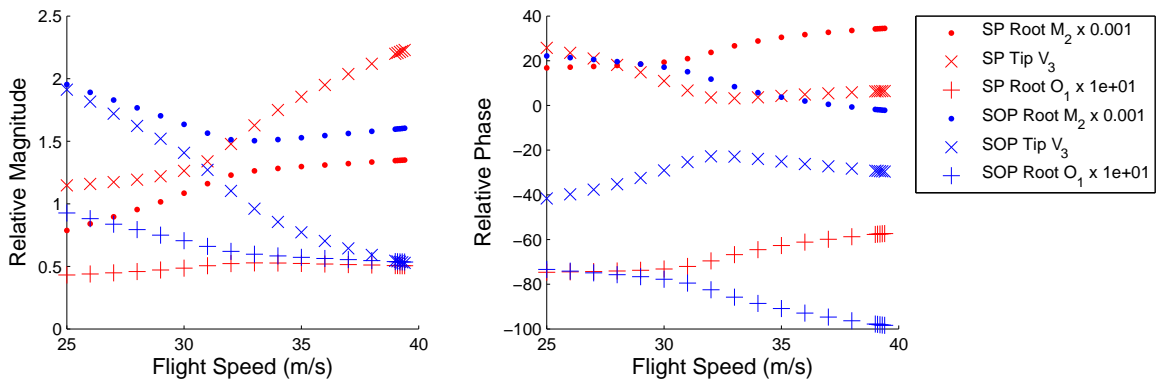


**Figure 29:** Short-period (SP) and symmetric out-of-plane bending (SOP) eigenvector characterization in terms of magnitude of root bending moment  $M_2$ , tip vertical velocity  $V_3$ , and root angular velocity  $\Omega_1$ . Eigenvectors were normalized so that root vertical velocity  $V_3$  magnitude was 1 m/s and phase was zero. Results are shown for the maximum flange thickness (1 cm).

### 4.5.3 Minimum Fuselage Mass

Figures 30 and 31 characterize the eigenvalue and eigenvector behavior over the flight speeds that were analyzed. They show a slightly different picture of what is happening than what happened with the nominal fuselage mass. Figure 30 shows the SP and SOP modes “coalescence” of sorts, but the frequencies never meet each other, instead they begin to increase drastically. The lack of “coalescence” for this case is also partially due to the increased frequency of the *in vacuo* bending mode. Figure 31 again shows the trend of increasing/decreasing velocity magnitudes for the SP/SOP modes with increasing flight speed over the flight speeds from 25-48 m/s. After this flight speed, however, the velocity magnitude trend reverses for the SOP mode and increases from 48-75 m/s. The speed where the velocities magnitudes cross over one another still corresponds to a change in the stability of the SOP mode in terms of increasing flight speed. Figure 31 shows that for the SOP mode the tip velocity phases from negative to positive around 48 m/s, at the same speed where the velocity trend changes as mentioned above. The difference in stability and eigenvector trends between this case and the others is likely due to the much larger frequencies associated with the low fuselage mass.

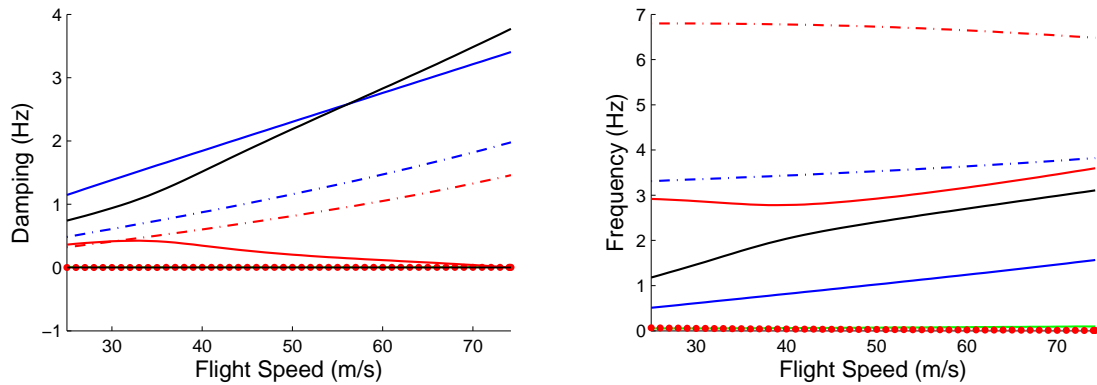


**Figure 30:** Eigenvalue analysis results for the model with small fuselage mass factor of 0.4.

### 4.5.4 Maximum Fuselage Inertia

The eigenvalue and eigenvector characterization was repeated for the case with maximum fuselage inertia, and these characterizations are shown in Figs. 32 and 33. Figure 32 shows that the “coalescence” does not occur as strongly as the previous cases, and also shows an unstable SP mode as opposed to the unstable SOP modes as found before. Figure 33 shows that the character of the eigenvectors has changed significantly, with the SOP mode having much larger components of tip velocity and bending magnitude, and zero pitching velocity magnitudes over the whole flight speed

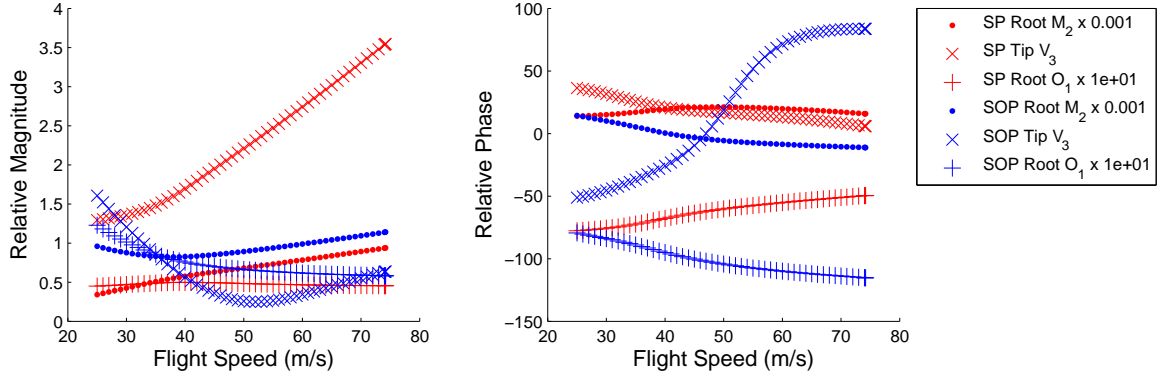


**Figure 31:** Short-period (SP) and out-of-plane bending (SOP) eigenvector characterization in terms of magnitude of root bending moment  $M_2$ , tip vertical velocity  $V_3$ , and root angular velocity  $\Omega_1$ . Eigenvectors were normalized so that root vertical velocity  $V_3$  magnitude was 1 m/s. Results are shown for a small fuselage mass factor (0.4).

regime. The SOP mode frequency changed relatively little with increasing flight speed with this case, which may suggest that the SOP mode frequency changes are due in part to the pitching velocity components. Both modes have increasing tip velocity magnitudes with increasing flight speed. Figure 33 also shows that at the onset of instability the tip velocities are in phase with the vertical velocities.

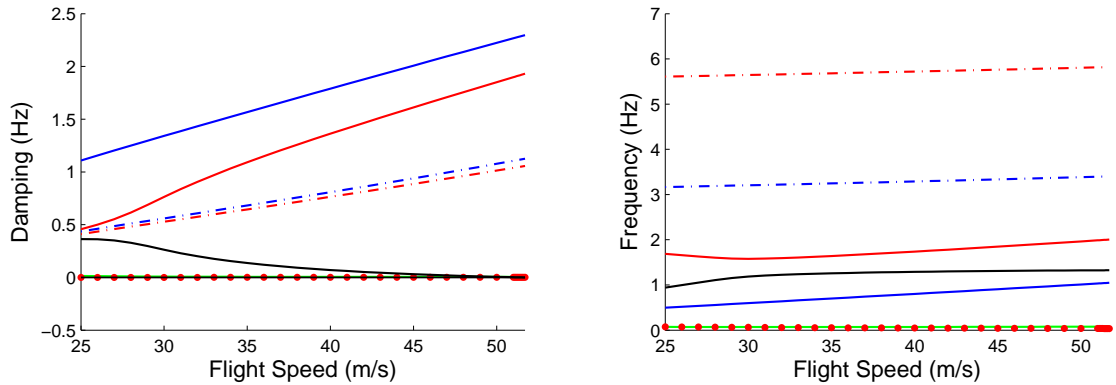


**Figure 32:** Eigenvalue analysis results for the model with a large fuselage inertia factor 1.7.

#### 4.5.5 Comparison Between Linear and Nonlinear Flutter

The linear analysis results presented in the previous sections give a feel for the behavior of the body-freedom flutter mode with respect to changes in inertial or constitutive properties. NATASHA can be also used in a timestepping analysis [110] to assess the nonlinear character of the body-freedom flutter behavior. This capability was used to verify the linear analysis results in terms of some of the trends that were identified. The behavior of the flutter mode was investigated with the nonlinear

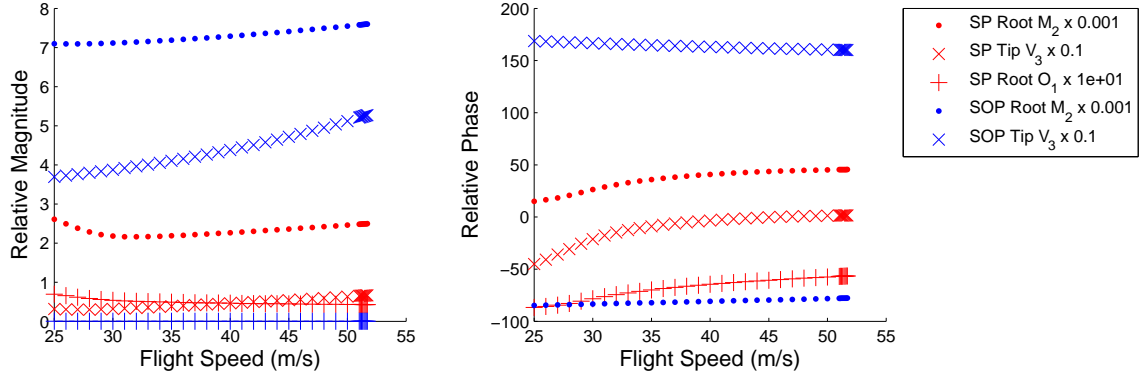


**Figure 33:** Short-period (SP) and out-of-plane bending (SOP) eigenvector characterization in terms of magnitude of root bending moment  $M_2$ , tip vertical velocity  $V_3$ , and root angular velocity  $\Omega_1$ . Eigenvectors were normalized so that root vertical velocity  $V_3$  magnitude was 1 m/s. Results are shown for a large fuselage inertia factor (1.7). Phase of  $O_1$  not shown for SOP mode because for this case the magnitude of  $O_1$  for the SOP mode is zero.

analysis by starting the system at equilibrium and perturbing the flap angle by a very small amount. Below the flutter speed, the flutter mode is very lightly damped, so this mode of vibration persists long after the other modes of vibration have been significantly damped.

An example of raw nonlinear data is shown in the left portion of Fig. 34. The low damping of the phugoid mode made it difficult to identify the SP behavior from the nonlinear results. To eliminate the contribution of the phugoid mode, a Fourier transformation was applied to identify the phugoid mode (green star) and flutter frequency (red star), shown in the middle column of Fig. 34. After that, a high pass filter was applied to the results to remove the phugoid mode and calculate the (negative) damping of the unstable SOP mode, shown in the right column of 34. The frequency of the unstable motion can be determined either by measuring the difference between two neighbouring peaks or looking for the strongest signal (red star) in the Fourier transform result. The damping of the unstable motion was determined by doing a least squares fit on multiple peaks in the filtered signal, shown as the red lines in the right column of Fig. 34.

To verify the damping and frequency results from the linear analysis, the damping and frequency of the nonlinear mode were calculated and compared in Fig. 35. The red line represent the same linear prediction as in Fig. 13. The green line represent the damping and frequency obtained from the above process. To verify the phase/magnitude trends that were identified in the linear analysis results, post-processing was done on the nonlinear results to determine the relative magnitude and phase of tip  $V_3$  with respect to root  $V_3$ . In the linear case, the relative magnitude and phase shift were calculated through an eigenvector analysis. For the nonlinear case, the least squares fitting method described above (red line in Fig. 34) was used on each signal to find the relative magnitudes

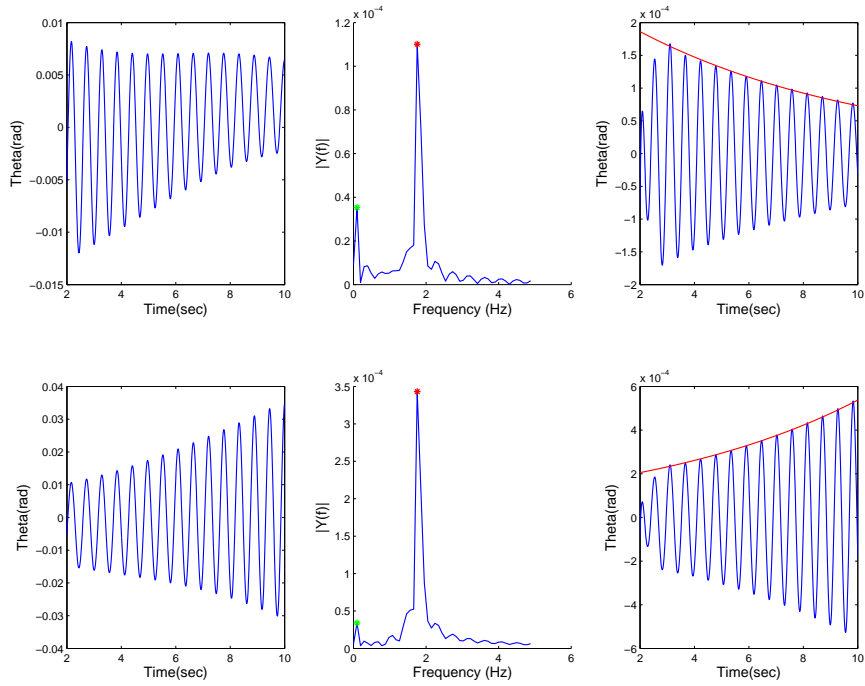


**Figure 34:** Three-plot of transient response (left) with Fourier single-sided amplitude spectrum results (middle) and the filtered signal (right), for below flutter speed (top) and above flutter speed (bottom).

between the two signals. Phase shift was calculated from the average difference between tip peaks and root peaks. Figure 36 shows a comparison between two results.

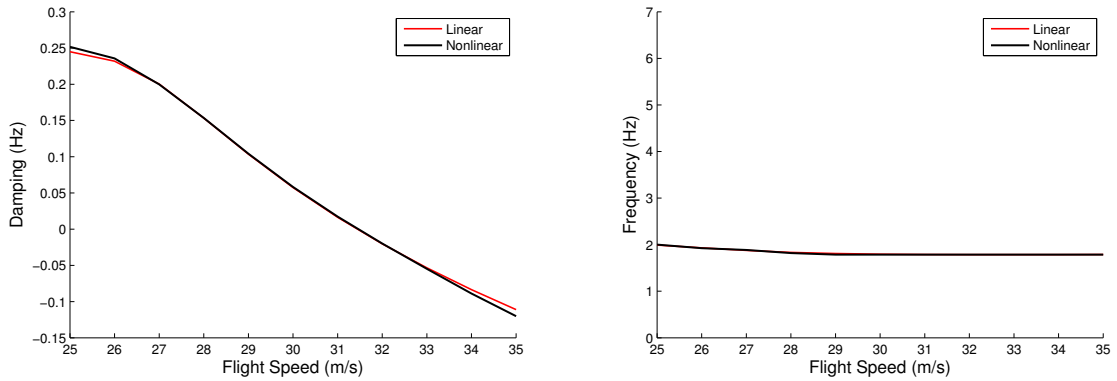


**Figure 35:** Change of damping and frequency of SOP mode with respect to flight speed, comparing linear eigenvalue analysis results with post-process of nonlinear timestep data.

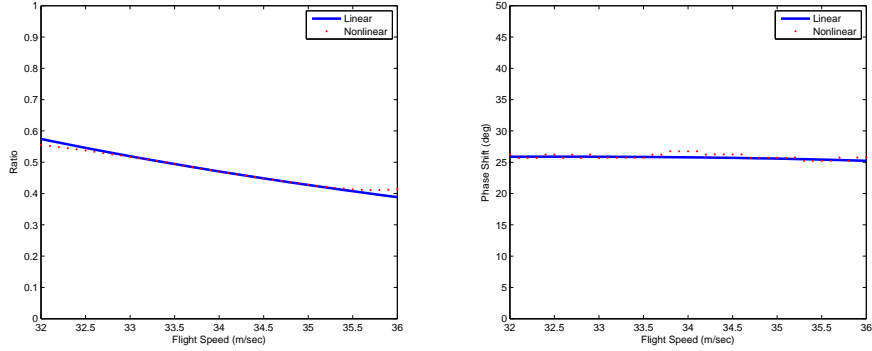


**Figure 36:** Magnitude ratio between tip velocity and root velocity (left). Phase shift between tip velocity and root velocity (right).

## 4.6 Realistic Structural Model for HALE Aircraft

The previous section uses a “typical” flying wing model that was made to be very flexible, in order to ignore the onset of compressibility effects in the case of increased flutter speed. The geometry of the model is representative for current HALE aircraft designs, but the structural design is not. HALE aircraft usually feature advanced composite materials such as fiberglass and carbon fiber. This section will show how the tools described in the previous section can be used for preliminary structural design of a HALE aircraft considering flutter requirements.

### 4.6.1 Design Requirements for HALE Aircraft

The primary design goal for HALE aircraft is to achieve the longest endurance time possible at a given altitude. The basic effects of flying at high altitude is low air density, leading to high  $C_L$  and therefore a high amount of induced drag, and low temperature, leading to a lower speed of sound and therefore higher flight Mach numbers. According to the U.S. Air Force fact sheet, the Global Hawk has a maximum ceiling of 60kft and an endurance time of 28 hours. To accomplish the endurance times, very high aspect ratio wings and high-lift airfoils are often used. Jacob and Smith [61] give a general description of the airfoil profiles used for three HALE aircraft, including the Global Hawk, noting they are often thick (25% or higher) to improve wing structural efficiency. The design condition for the Global Hawk airfoil is given by Jacob and Smith as  $M=0.55$ ,  $C_l = 1.0$  and  $Re = 500,000$ . The density at an altitude of 60 kft is around  $0.115 \text{ kg/m}^3$ , and the speed of sound is 295 m/s, so an approximate design flight speed for the Global Hawk may be around 160 m/s.

#### 4.6.2 Realistic Interior Structure for HALE Aircraft

The structure is divided into three structural components: the skin, the spar caps, and the shear web. General structural requirements such as maximum stress requirements must be met for the structure and each structural component should use advanced composite materials suited to the role of each component. The skin and shear webs are designed to carry shear stresses from torsion and shear forces, with the skin being the optimal component to carry shear flow due to torsion because of the large enclosed area, and the shear web being the optimal component to carry shear flow due to shear forces because of the alignment of the vertical axis. For the skin, a layer of aluminum is retained for the outer layer for erosion protection, and then the rest is replaced with woven fiberglass oriented at  $45^\circ/-45^\circ$ . This is done essentially to approximately align the principal stresses the skin will undergo with the material direction, with the argument that in a state of pure shear, the principal stress direction is either  $\pm 45^\circ$ . Although the skin will also be subject to direct stresses as well, it is assumed that these are dominated by the shear stresses so that the principal stress direction is close to  $\pm 45^\circ$ . A similar argument may be made for the shear web, so it is made entirely of the woven fiberglass material oriented at  $45^\circ/-45^\circ$ . The woven fiberglass material is assumed to have  $E_x$  and  $E_y$  as similar values, with the glass fibers woven in a pattern so that they are oriented in either the  $x$  or  $y$  material directions. However,  $E_z$  is much smaller than the other two values, but fortunately does not play as large of a part in the section analysis. Therefore it is ideal to carry shear stress if the woven fiberglass is oriented at  $45^\circ/-45^\circ$ , because the principal stresses will be aligned with the material  $x$  and  $y$  axes. For the spar cap, it is desired to have a material with very good performance in pure tension or pure compression. Therefore, carbon fibers embedded in epoxy were chosen as they provide a very high stiffness/weight ratio along the fiber direction. The section analysis was set up to assume that the layer thickness was a material property, and therefore three design variables can be used to define the structure. The three variables are  $N_s$ , the number of  $45^\circ/-45^\circ$  fiberglass/epoxy layer pairs in the skin,  $N_c$ , the number of  $0^\circ$  carbon/epoxy layers in the spar, and  $N_w$ , the number of  $45^\circ/-45^\circ$  fiberglass/epoxy layers in the shear web. The material properties of the aluminum outer skin, the woven fiberglass/epoxy, and the carbon/epoxy are given in Table 22.

A baseline realistic structural model was then created by setting  $N_s = 2$ ,  $N_w = 2$ , and  $N_c = 10$ , with a constant layer thickness of 1 mm for all layers. The position of the spar and shear web is identical to the “typical” model presented above as shown in Fig. 12. The eigenvalue analysis was conducted at sea level and the results are shown in Fig. 37, and then the analysis was repeated at



**Table 22:** Material properties for realistic structural design of HALE aircraft wing.

Material	Aluminum	Woven Fiberglass/Epoxy	Carbon/Epoxy
$E_x$ (psi)	$1 \times 10^7$	$1.9 \times 10^7$	$16.6 \times 10^7$
$E_y$ (psi)	$1 \times 10^7$	$1.9 \times 10^7$	$12.1 \times 10^7$
$E_z$ (psi)	$1 \times 10^7$	$1.9 \times 10^6$	$6.1 \times 10^4$
$G_{12}$ (psi)	$3.8 \times 10^6$	$1.7 \times 10^6$	$8.68 \times 10^5$
$G_{13}$ (psi)	$3.8 \times 10^6$	$1.7 \times 10^6$	$8.68 \times 10^5$
$G_{23}$ (psi)	$3.8 \times 10^6$	$8.68 \times 10^5$	$6 \times 10^4$
$\nu$	0.3	0.49	0.3
$\rho$ (lb s <sup>2</sup> /in <sup>4</sup> )	$2.52 \times 10^{-4}$	$1.14 \times 10^{-4}$	$1.67 \times 10^{-4}$

**Table 23:** Trade study of structural design variables for number of skin layers  $N_s$  and number of spar layers  $N_c$ .

$N_s$	$N_c$	Flutter Speed (m/s)	Wing Weight (kg)
2	10	200	306
2	5	171	285
2	4	164	281
2	2	151	273
1	10	174	218
1	5	143	197

60 km altitude, with the results shown in Fig. 38. These figures reveal that the flutter speed has been increased to 70 m/s and 200 m/s at sea level and at 60 km altitudes (respectively) with the updated structure. Trade studies were then conducted on the variables  $N_s$ ,  $N_c$ , and the chordwise location of the spar within the section, and the results of these trade studies are given in Tables 23 and 24. The trade studies reflect the conclusions from Section 4.4.2 in that both  $N_c$  and  $N_s$  can be increased to increase the flutter speed, but increases to  $N_s$  lead to a more severe weight penalty than  $N_c$ . The VABS recovery process was used to obtain the stress results for two configurations:  $[N_s, N_c] = [2, 5]$  and  $[1, 10]$ . The summary of stress results is given in Table 25, and shows generally higher stresses for the case with  $N_s = 2$ . Further investigation revealed this was mainly due to the increase in weight, underscoring the importance of low-weight configurations for HALE aircraft. Both configurations are well within the static stress failure criterion; the stress analysis used the approximate failure stress values in Table 22 to calculate an equivalent Von Mises stress measure, and the results for the comparison study are shown in Table 25.

#### 4.6.3 3D Effects for HALE Aircraft Wings

The 2D model that is implemented in NATASHA can not capture 3D effects that are important for all finite wings. The aspect ratio of the wing in question is approximately 10, which may be high enough for Prandtl-type effects to diminish significantly for a straight wing, but the sweep of the wing leads to increased redistribution effects due to spanwise interaction of lifting elements.

**Table 24:** Trade study of spar chordwise location for realistic HALE aircraft, with number of skin layers  $N_s = 1$  and number of spar layers  $N_c = 10$ .

Spar $x/c$	Flutter Speed (m/s)
0.15	163
0.2	171
0.25	174
0.3	174
0.35	172
0.4	168
0.45	163

**Table 25:** Comparison study of maximum direct ( $\sigma_{11}$ ) and shear ( $\tau_{1s}$ ) stresses at wing root between two configurations at design flight condition of 160 m/s and 60 km altitude. Von-Mises equivalent stress measures ( $\sigma_{eq}$ ) are also given.

$N_s$	$N_c$	Max $\sigma_{11}$ (psi)	Max $\tau_{1s}$ (psi)	Max $\sigma_{eq}$
2	5	4011 psi	500	0.183
1	10	2975 psi	100 psi	0.135

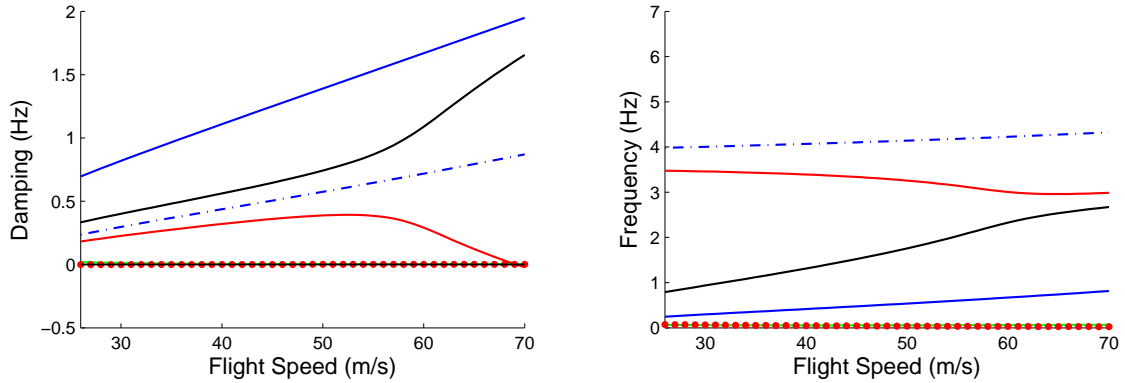


**Figure 37:** Eigenvalue analysis results for the baseline realistic model at sea level altitude.

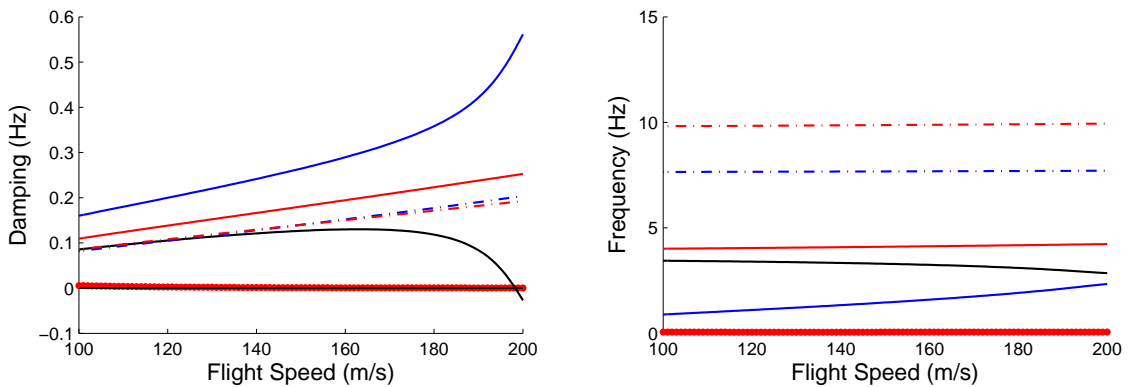


**Figure 38:** Eigenvalue analysis results for the baseline realistic model at an altitude of 60 km.

To model this, the Weissinger method as presented in Bisplinghoff, Ashley, and Halfman [9] was implemented for this model. To add this effect into the NATASHA system, the Newton-Rhapson

(N-R) iteration procedure was modified slightly to account for the additional induced downwash due to 3D effects. To modify the N-R procedure, the nonlinear aerodynamic function evaluations were modified:

$$\begin{aligned} f_{\text{aero}}^n &= f_1(V_1^n, V_2^n, V_3^n) \\ m_{\text{aero}}^n &= f_2(V_1^n, V_2^n, V_3^n) \end{aligned} \quad (39)$$

$$f_{\text{aero}}^{n,*} = f_1(V_1^n, V_2^n, V_3^n + w^n)$$

The nonlinear evaluation of Jacobian entries associated with the aerodynamics were also simply modified by the downwash velocities  $w_i$ , for example:

$$\begin{aligned} \frac{\partial f_{\text{aero}}^n}{\partial V_1} &= f_3(V_1^n, V_2^n, V_3^n) \\ \frac{\partial f_{\text{aero}}^{n,*}}{\partial V_1} &= f_3(V_1^n, V_2^n, V_3^n + w^n) \end{aligned} \quad (40)$$

Then the N-R iteration procedure was modified to update the downwash velocities periodically, and additionally a relaxation factor was added to the downwash velocity magnitudes to help the N-R procedure adjust to large downwash magnitudes. The relaxation factor was necessary because the downwash is essentially introducing a further nonlinearity of the system that is not accounted for within the Jacobian matrix. The Weissinger effect may be expressed as an additional function of the angles of attack at each station,  $\{w\} = W(\alpha^1, \alpha^2, \dots)$ , with  $\alpha^n = \tan^{-1}(-V_3^n/V_2^n)$ . Therefore the Weissinger effect can be expressed generally as  $\{w\} = W(x)$ , where for this section  $x$  are all the NATASHA unknowns. Therefore, the Weissinger effect is here only partially included within the N-R iteration procedure, as the Jacobian matrix is not modified with the derivatives of  $W$ . This was done to simplify the inclusion of the Weissinger effect. The modified procedure is then as follows, using the form of NATASHA equations in Eq. (32):

1. Assume a value of  $x = 0$  and perform standard N-R procedure to find equilibrium solution without Weissinger effect.
2. Begin iteration  $i$ . Calculate the downwash of the model by  $\alpha^n = \tan^{-1}(-V_3^n/V_2^n)$  and calculating  $w_i = c_i W(x)$ , where  $W(x)$  is the Weissinger function and  $c_i$  is a scalar relaxation factor.
3. Perform modified N-R procedure, including the downwash velocities  $w_i$  in aerodynamic function evaluation. A new set of unknowns  $x_i$  are now available that correspond to the relaxed downwash velocities  $w_i$ .
4. If  $c_i=1$ , the procedure is complete. If not, return to step 2 and advance iteration count  $i$ .

For this procedure, the number of iterations  $i$  is fixed, with a N-R iteration performed at each step to update the  $x_i$  to the new relaxed Weissinger velocities  $w_i$ . This has the appeal of solving the equilibrium equations simultaneously with the Weissinger function but also letting the unknowns  $x$  gradually adjust to the imposition of the Weissinger downwash velocities. It also has the appeal of being not explicitly tied to the Weissinger analysis but instead can be applied if there is any correction to the aerodynamic model. The relaxation factor can be made to be a linearly increasing factor and dependent upon the maximum iterations  $I$ , such as  $c_i=i/I$ , and a value of  $I = 10$  was found to give a significant amount of relaxation for all flight speeds.

To simply demonstrate the effect of adding this correction to the model, Fig. 39 shows the trim results for the rigid model with and without the Weissinger correction and Fig. 40 shows how  $C_L$ ,  $C_D$ , and the overall angle of attack AoA of the model are related with and without the Weissinger correction. At high altitude, the significance of 3D effects should be important, so Figs. 39 and 40 were conducted at the new design altitude of 60 km. These Figs. demonstrate the “drag bucket” effect that is to be expected, where parasitic drag is a function of  $V_\infty^2$  but induced drag is highest at the lower flight speeds. Also, the tendency of reduced lift curve slope ( $C_{L_\alpha}$ ) due to 3D lift redistribution has been captured.

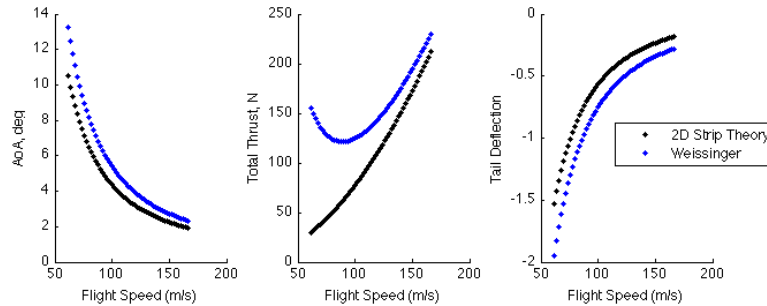


**Figure 39:** Trim results for rigid typical model at altitude of 60 km with and without 3D correction.

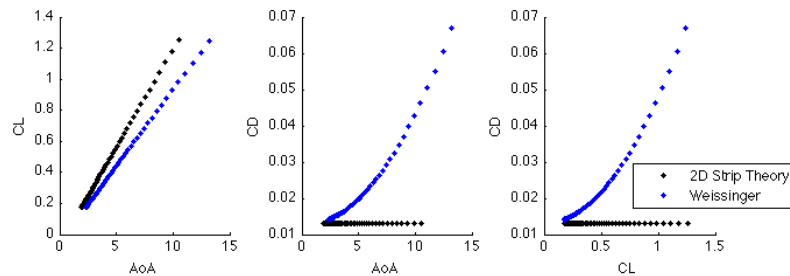


**Figure 40:** Lift and drag polars for rigid typical model at altitude of 60 km, with and without 3D correction.

## 4.7 Aeroelastic Control Design

There are several forms of the aeroelastic equations of motion. Linear gust analysis procedure is clearly outlined by Patil (Ref. [108]) for a linear aeroelastic system of the form below, with  $f_{\text{gust}}$ ,  $f_{\text{cont}}$  representing gust and control inputs:

$$[J_x] \{x\} - [J_{\dot{x}}] \{\dot{x}\} = \{f_{\text{cont}}\} + \{f_{\text{gust}}\} \quad (41)$$

Another form of the aeroelastic equations of motion are used by Patil and Hodges (Ref. [104]) to design a feedback controlled flutter suppression and gust load alleviation system:

$$\begin{aligned} \{\dot{\bar{x}}\} &= [\bar{A}] \{\bar{x}\} + [\bar{B}] \{u\} + [\bar{G}] \{w\} \\ \{y\} &= [\bar{C}] \{\bar{x}\} \end{aligned} \quad (42)$$

This form is more typical, and uses nomenclature more typical of the control design literature with  $[A] - [G]$  as system matrices used for control design. The common standard notation in state-space control design will be utilized for the remainder of this chapter; for example,  $[A]$  represents the state matrix,  $[B]$  the input matrix,  $[C]$  the output matrix,  $x$  or  $\bar{x}$  represents the degrees of freedom and  $y$  represents the measurable outputs of the system. Of course, Eqs. (41) and (42) are related and the inputs  $\{u\}$  are introduced:

$$\{f_{\text{cont}}\} = [F_{\text{cont}}] \{u\} \quad \{f_{\text{gust}}\} = [F_{\text{gust}}] \{w\} \quad (43)$$

$$[\bar{A}] = -[J_{\dot{x}}]^{-1}[J] \quad [\bar{B}] = [J_{\dot{x}}]^{-1}[F_{\text{cont}}] \quad [\bar{G}] = [J_{\dot{x}}]^{-1}[F_{\text{gust}}]$$

However, the matrix  $[J_{\dot{x}}]$  from Eq. (41) is not always invertible: it can contain many rows of all zeros and many columns of all zeros. These correspond to aeroelastic equations that have no time derivatives or NATASHA unknowns for which the time derivative is not included in the equations. This is especially the case whenever elements are rigid so that the time derivatives of strain do not factor in the equations, whenever there is no additional nodal mass or inertia so that the time derivatives of velocity and angular rates do not factor into the nodal equilibrium, or whenever elements are assigned zero mass or inertia and the velocity and angular rate time derivatives do not factor into the elemental equilibrium equation for that element. Therefore, the two systems were related by using MATLAB functionality to create “descriptor” state-space models of the following form:

$$\begin{aligned} [\bar{E}] \{\dot{x}\} &= [\bar{A}] \{x\} + [\bar{B}] \{u\} + [\bar{D}] \{w\} \\ \{y\} &= [\bar{C}] \{x\} \end{aligned} \quad (44)$$

A descriptor state-space model can be translated to a more conventional one, Eq. (42), with further MATLAB functionality. To see how this might be done by hand, consider the case when there is an

equation that does not have time derivatives. The state matrix rows can be arranged so that:

$$[A] \{x\} - [E] \{\dot{x}\} = \{\hat{f}_c\} + \{\hat{f}_g\} = \begin{bmatrix} [A_1] \\ [A_2] \end{bmatrix} \{x\} - \begin{bmatrix} [E_1] \\ 0 \end{bmatrix} \{\dot{x}\} = \begin{Bmatrix} \hat{f}_{c1} \\ \hat{f}_{c2} \end{Bmatrix} + \begin{Bmatrix} \hat{f}_{g1} \\ \hat{f}_{g2} \end{Bmatrix} \quad (45)$$

For the case of no control inputs and no gusting, there is the potential to reduce the degrees of freedom by setting  $\{x\} = \text{null}(A_2) = [XY] \{y\}$ , where  $[XY]$  is the basis of  $\text{null}(A_2)$ . Accounting for control inputs and gusting:

$$\begin{bmatrix} [A_{11}] & [A_{12}] \\ [A_{21}] & [A_{22}] \end{bmatrix} \begin{Bmatrix} x_1 \\ x_2 \end{Bmatrix} - \begin{bmatrix} [E_{11}] & [E_{12}] \\ 0 & 0 \end{bmatrix} \begin{Bmatrix} \dot{x}_1 \\ \dot{x}_2 \end{Bmatrix} = \begin{bmatrix} [F_{c1}] \\ [F_{c2}] \end{bmatrix} \{u\} + \begin{bmatrix} [F_{g1}] \\ [F_{g2}] \end{bmatrix} \{w\} \quad (46)$$

The arrangement of the above equation is performed such that  $[A_{22}]$  is non-singular so that:

$$\{x_2\} = -[A_{22}]^{-1}[A_{21}] \{x_1\} + [A_{22}]^{-1}[F_{c2}] \{u\} + [A_{22}]^{-1}[F_{g2}] \{w\} \quad (47)$$

Substitution of Eq. (47) into (46) allows reduction of the system in terms of  $x_1$  only. These degree-of-freedom reductions are mainly a result of rigid elements and nodes without elemental force or mass. In the latter case, for example, the degrees of freedom are reduced in that  $F_l = [C_{lr}]F_r$  for the node, or in words the internal shear forces are the same to the left and to the right of the node.

Again, the NATASHA variables  $\{x\}$  consist of  $21N_T$  nodal unknowns, 12 boundary condition unknowns, and  $6(N_w + N_t - 2)$  aerodynamic unknowns. This arrangement also corresponds to the column indices of  $[A(x)]$  and  $[B(x)]$ , and the row indices correspond to the aeroelastic equations that are linearized. Next, it is necessary to find a way to calculate  $[F_{\text{cont}}]$  and  $[F_{\text{gust}}]$ . The effect of a control surface deflection, thrust setting, or a gust would be to add either nodal forces or elemental distributed forces and moments to the nodal or elemental equilibrium equations, Eq. (35 or 29).

#### 4.7.1 Control Derivatives

For the wing or stabilizer control surface derivatives, all that needs to be done is find the change in aerodynamic forces due to a flap deflection ( $\beta$ ) for each element, and then relate the control parameter to the proper elements according to which flap it corresponds to (aileron, inner flap, etc.). The aerodynamic force and moment equations (some using the semichord  $b$ ) are

$$L_{\text{aero}} = \rho b V_T^2 (c_{l_0} + c_{l_\alpha} \sin \alpha + c_{l_\beta} \beta) + \rho b V_T V_2 c_{l_\alpha} \alpha_{\text{rot}} \cos \alpha \quad (48)$$

$$D_{\text{aero}} = \rho b V_T^2 (c_{d_0} + c_{d_{\alpha^2}} \alpha^2 + c_{d_{\beta^2}} \beta^2) + \rho b V_T V_2 c_{l_\alpha} \alpha_{\text{rot}} \sin \alpha \quad (49)$$

$$M_{\text{aero}} = 2\rho b^2 V_T^2 (c_{m_0} + c_{m_\alpha} \sin \alpha + c_{m_\beta} \beta) - \rho b^2 V_T V_2 c_{l_\alpha} \alpha_{\text{rot}} / 2 \quad (50)$$

These are translated to the body frame distributed forces and moments ( $\bar{f}_{\text{aero}}$  and  $\bar{m}_{\text{aero}}$ ) by an aerodynamic frame rotation matrix  $[C_a]$  and also according to the angle of attack:

$$\bar{f}_{\text{aero}} = [C_a] \begin{Bmatrix} 0 \\ -L_{\text{aero}} \sin \alpha - D_{\text{aero}} \cos \alpha \\ L_{\text{aero}} \cos \alpha - D_{\text{aero}} \sin \alpha \end{Bmatrix} \quad (51)$$

$$\bar{m}_{\text{aero}} = [C_a] \begin{Bmatrix} M_{\text{aero}} \\ 0 \\ 0 \end{Bmatrix} + \widetilde{y}_{ac} f_{\text{aero}} \quad (52)$$

The value of  $\beta$  for a given element will be the sum of the trim value  $\beta_0$  and a control value  $\Delta\beta$ . The linearized change in aerodynamic lift and moment on an element due to a control surface deflection are given as:

$$\frac{\partial \bar{f}_{\text{aero}}}{\partial \Delta\beta} = \rho b V_T^2 [C_a^n] \begin{Bmatrix} 0 \\ -c_{l_\beta} \sin \alpha - 2c_{d_{\beta^2}} \beta_0 \cos \alpha \\ c_{l_\beta} \cos \alpha - 2c_{d_{\beta^2}} \beta_0 \sin \alpha \end{Bmatrix} \quad (53)$$

$$\frac{\partial \bar{m}_{\text{aero}}}{\partial \Delta\beta} = 2\rho b^2 V_T^2 c_{m_\beta} [C_a] \begin{Bmatrix} 1 \\ 0 \\ 0 \end{Bmatrix} + \widetilde{y}_{ac} \frac{\partial \bar{f}_{\text{aero}}}{\partial \Delta\beta} \quad (54)$$

These distributed aerodynamic forces would be added to the LHS of Eq. (29), so a factor of -1 needs to be applied before they can be added into the control derivatives matrix  $[F_{\text{cont}}]$  to reflect that the terms  $\{f_{\text{cont}}\}$  and  $[\bar{B}]\{u\}$  are on the RHS of Eq. (42).

Similarly, the components of  $[F_{\text{cont}}]$  that correspond to the thrust controls must be determined, but they are much simpler as the nodal force is a direct input to the nodal equilibrium equation, Eq. (35). The offset of the engine CG and also the place where the force acts at is denoted  $\hat{\xi}$ . The thrust settings are scalar values that can be written as the trim thrust  $T_0$ , a change in collective thrust  $\Delta T$ , and a differential thrust  $\delta T$ .  $[C_{bi}]$  is a rotation matrix that accounts for the sweep and initial twist of the wing to orient the thrust forward in the flight dynamic reference frame. The nodal force and moment equilibrium equations can then be written:

$$\hat{F}_r - [C_{lr}]^T \hat{F}_l + T_0 [C_{bi}] \begin{Bmatrix} 0 \\ 0.5 \\ 0 \end{Bmatrix} + \hat{f}_{\text{aero}} + \hat{\mu} g \hat{g}_r - \tilde{\Omega} \hat{P}_r = -\Delta T [C_{bi}] \begin{Bmatrix} 0 \\ 0.5 \\ 0 \end{Bmatrix} - \delta T [C_{bi}] \begin{Bmatrix} 0 \\ 0.5 \\ 0 \end{Bmatrix} \quad (55)$$

$$\hat{M}_r - [C_{lr}]^T \hat{M}_l + T_0 \tilde{\xi}[C_{bi}] \begin{Bmatrix} 0 \\ 0.5 \\ 0 \end{Bmatrix} + \hat{m}_{\text{aero}} + \hat{\mu} g \tilde{\xi} \hat{g}_r - \tilde{\Omega}_r \hat{H}_r - \tilde{V}_r \hat{P}_r = \dots \quad (56)$$

$$\dots = -\Delta T \tilde{\xi}[C_{bi}] \begin{Bmatrix} 0 \\ 0.5 \\ 0 \end{Bmatrix} - \delta T \tilde{\xi}[C_{bi}] \begin{Bmatrix} 0 \\ 0.5 \\ 0 \end{Bmatrix} \quad (57)$$

Using  $\{0, 0.5, 0\}^T$  as the thrust vector means that  $T$  and  $\Delta T$  represent total thrust requirements for the vehicle, evenly divided between the two engines. The value of the thrust vector multiplying the scalar value of  $\delta T$  would be positive for the right engine and negative for the left engine.

The output matrix  $[\tilde{C}]$  is then determined based on what outputs are desired to be tracked and what outputs are desired to be used as feedback for the control system. For implementation of the current stability augmentation system (SAS), the outputs would be the flight dynamic variables: the velocities and rotation rates of the reference node. In this case,  $[\tilde{C}]$  would have six rows and ones in the columns that correspond to  $\hat{V}_r$  and  $\hat{\Omega}_r$  of the reference node.

#### 4.7.2 Symmetric Model

The control design process was demonstrated for a Bihrlle aircraft model for which the details may not be released as they are proprietary. Suffice it to say that the geometry is similar enough to the realistic models described above that the general characteristics of the nature of BFF that are highlighted above were observed for both aircraft models. The layout of the model is similar to the full model as depicted in Figure 12 however a small tail (stabilizer) was added to represent the longitudinal control surface. A symmetric version of the flying wing model was analyzed by replacing the left wing-tip free boundary condition with a symmetric boundary condition placed on the middle node. In the symmetric analysis, only half of the wing and half the stabilizer is modeled. Then, instead of imposing the free boundary condition on the left wing element, symmetric boundary conditions are imposed on the centerline node of the wing. These symmetric boundary conditions, time-differentiated gravity vector constraint and gravity vector size constraints are:

$$\begin{aligned} (\hat{F}_l)_2 &= 0 & (\hat{F}_l)_3 &= 0 & (\hat{V}_l)_1 &= 0 \\ (\hat{M}_l)_1 &= 0 & (\hat{\Omega}_l)_3 &= 0 & (\hat{\Omega}_l)_3 &= 0 \\ (\hat{g}_l)_1 &= 0 & & & & \\ \hat{\Omega}_1 \hat{g}_3 - \Omega_3 \hat{g}_1 &= 0 & \hat{g}_1^2 + \hat{g}_2^2 + \hat{g}_3^2 - 1 &= 0 & & \end{aligned} \quad (58)$$

These nine equations replace the first nine equations for the first beam that usually treat the free end boundary condition, enforce the time-differentiated gravity vector equation and constrain the



gravity vector size. The wing control surfaces were divided into flaps and ailerons, where flaps are control surfaces that have prescribed deflection schedules over different areas of the flight envelope, and ailerons, which are active control devices in the lateral/directional control system. Therefore, neither the wing ailerons, flaps or the differential thrust setting are necessary for inclusion in the longitudinal control system (at least at first). Therefore, the  $\{u\}$  control vector is simply:

$$\{u\}_{\text{long}} = \{\Delta T, \Delta\beta_s\}^T \quad (59)$$

The outputs for the control system are then the velocities and rotations of the reference node, and also to recover the orientation of the aircraft the gravity vector at the reference node. Since  $V_1$ ,  $g_1$ ,  $\Omega_2$ , and  $\Omega_3$  are all zero for this case, it is only necessary to feed out  $V_2$ ,  $V_3$ ,  $\Omega_1$ , and  $g_2$ . The  $[\bar{C}]$  matrix would have four rows, the first having a 1 in the 14<sup>th</sup> column ( $V_2$  of the reference node is the 14<sup>th</sup> unknown), the second having a 1 in the 15<sup>th</sup> column ( $V_3$ ), the third having a 1 in the 16<sup>th</sup> column ( $\Omega_1$ ), and the fourth row having a 1 in the 20<sup>th</sup> ( $g_2$ ) column. See section 4.7.3 for an explanation as to why these outputs were chosen.

### 4.7.3 Linear Output Signal Modification

The states obtained this far as outputs may not exactly correspond to the output states that are used in common SAS design. It is worthwhile to again note at this time that since the states correspond to perturbation values, the outputs that are obtained in the symmetric state-space model are actually  $\Delta V_2$ ,  $\Delta V_3$ ,  $\Delta\Omega_1$ ,  $\Delta g_2$ , and  $\Delta g_3$ . The output signals used in the current SAS model are  $\Delta\alpha$ ,  $\Delta V_T$ ,  $\Delta\theta$ ,  $\Delta\dot{\theta}$ , as these are typical states for use in flight dynamics. In this chapter  $\theta$  represents pitch attitude and  $\alpha$  the angle of attack of the fuselage. The relationship between the total velocity perturbation  $\Delta V_T$  and the two velocities  $\Delta V_2$  and  $\Delta V_3$  can be obtained by linearizing the relationship between  $V_T$ ,  $V_2$  and  $V_3$  and neglecting higher order terms:

$$(V_T)^2 = (V_{T_0} + \Delta V_T)^2 = (V_2)^2 + (V_3)^2 = (V_{2_0} + \Delta V_2)^2 + (V_{3_0} + \Delta V_3)^2 \quad (60)$$

$$V_{T_0}^2 + 2V_{T_0}\Delta V_T + (\Delta V_T)^2 = V_{2_0}^2 + 2V_{2_0}\Delta V_2 + (\Delta V_2)^2 + V_{3_0}^2 + 2V_{3_0}\Delta V_3 + (\Delta V_3)^2 \quad (61)$$

$$V_{T_0}^2 + 2V_{T_0}\Delta V_T \approx V_{2_0}^2 + 2V_{2_0}\Delta V_2 + V_{3_0}^2 + 2V_{3_0}\Delta V_3 \quad (62)$$

$$\implies \Delta V_T \approx \frac{V_{2_0}}{V_{T_0}}\Delta V_2 + \frac{V_{3_0}}{V_{T_0}}\Delta V_3 \quad (63)$$

Fortunately, the relationship between  $\Delta\Omega_1$  and  $\Delta\dot{\theta}$  is direct, so that  $\Delta\Omega_1 = \Delta\dot{\theta}$ . The calculation of  $\alpha$  and  $\theta$  both require use of the inverse tangent function, which can be linearized in the following way:

$$\tan(\alpha) = -\frac{V_3}{V_2} \quad (64)$$

$$\tan(\alpha_0 + \Delta\alpha) \approx \tan(\alpha_0) + \sec^2(\alpha_0)\Delta\alpha \quad (65)$$

$$\frac{V_{3_0} + \Delta V_3}{V_{2_0} + \Delta V_2} \approx \frac{V_{3_0}}{V_{2_0}} + \frac{\Delta V_{3_0}}{V_{2_0}} \quad (66)$$

$$\sec^2(\alpha_0) = \frac{1}{\cos^2 \alpha_0} = \left(\frac{V_{T_0}}{V_{2_0}}\right)^2 \quad (67)$$

$$\implies \Delta\alpha \approx -\frac{V_{2_0}}{V_{T_0}^2} \Delta V_3 \quad (68)$$

Similarly, the pitch attitude is  $\theta = -\arcsin(g_2/|g|) = -\arcsin g_2$ , because  $|g|$  is the magnitude of the gravity vector and is always equal to 1. For a steady cruise analysis, the flight path angle  $\phi$  is zero and the pitch attitude can be approximated as a small angle, so the simplest approximation would be  $\Delta\theta = \Delta g_2$ . For large values of  $\theta$ , for instance in a climb or descent maneuver analysis, the value of  $\theta$  can be determined by numerical integration of  $\dot{\theta}$  by using an integrator or nonlinear inverse. A linearization of the  $\theta$  and  $g$  relationship without assuming a small value of  $\theta$  is given below, by using a global perturbation variable  $\epsilon$  and doing a Taylor series in terms of that variable, and also linearizing the constraint that  $g_2^2 + g_3^2 = 1$ :

$$\tan(\theta) = \frac{g_2}{g_3} \quad (69)$$

$$\tan(\theta_0 + \Delta\theta\epsilon) \approx \tan(\theta_0) + \sec^2(\theta_0)\Delta\theta\epsilon \quad (70)$$

$$\frac{g_{2_0} + \Delta g_2\epsilon}{g_{3_0} + \Delta g_3\epsilon} \approx \frac{g_{2_0}}{g_{3_0}} + \frac{\Delta g_2 g_{3_0} - g_{2_0} \Delta g_3}{g_{3_0}^2} \epsilon \quad (71)$$

$$g_2^2 + g_3^2 \approx 2g_{2_0}\Delta g_2 + 2g_{3_0}\Delta g_3 + 1 = 1 \implies \Delta g_3 = \frac{\Delta g_2 g_{2_0}}{g_{3_0}} \quad (72)$$

$$\sec^2(\theta_0) = \frac{1}{\cos^2 \theta_0} = \left(-\frac{|g|}{g_{3_0}}\right)^2 = \left(\frac{1}{g_{3_0}}\right)^2 \quad (73)$$

$$\implies \tan(\theta_0) + \left(\frac{1}{g_{3_0}}\right)^2 \Delta\theta\epsilon \approx \frac{g_{2_0}}{g_{3_0}} + \Delta g_2 \frac{g_{3_0}^2 + g_{2_0}^2}{g_{3_0}^3} \quad (74)$$

$$\implies \Delta\theta \approx \frac{1}{g_{3_0}} \Delta g_2 \quad (75)$$

The same result can be obtained by using sine and cosine instead of tangent to determine the pitch attitude  $\theta$ :

$$\sin(\theta) = -\frac{g_2}{|g|} = -g_2 ; \quad \cos(\theta) = -\frac{g_3}{|g|} = -g_3 \quad (76)$$

$$\sin(\theta_0 + \Delta\theta) = -(g_{2_0} + \Delta g_2) \approx \sin(\theta_0) + \cos(\theta_0)\Delta\theta \quad (77)$$

$$\implies \Delta\theta \approx \frac{1}{g_{3_0}} \Delta g_2 \quad (78)$$

The linearized version is then shown in Figure 41.

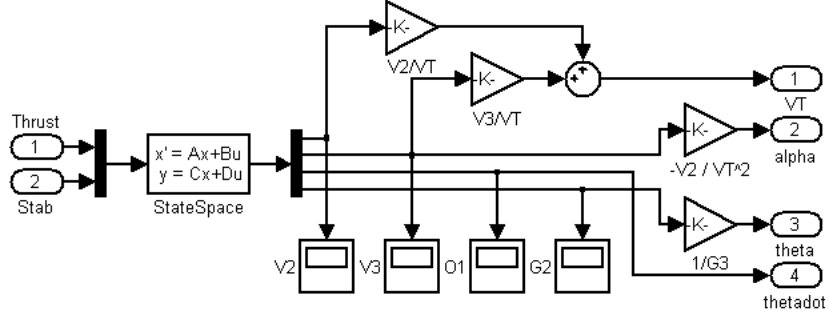


**Figure 41:** Linearized and symmetric state-space model. Note that inputs as well as outputs are perturbations of the trim values. For example, the first output  $V_T$  in the model corresponds to  $\Delta V_T$ .

#### 4.7.4 Linear Gust Analysis

The linear gust analysis reference by Patil [108] describes a procedure for calculating the linear gust response of a geometrically exact, intrinsic model very similar (if not identical) to the one used in NATASHA.

##### *Linear Unsteady Gust Loading*

The gust loading used in Ref. [108] can be obtained from Ref. [9] as

$$L_{\text{gust}}^n = 2\pi\rho V_T b^n \bar{w}_g [C(k_g)(J_0(k_g) - iJ_1(k_g)) + iJ_1(k_g)] e^{i\omega_g t} \quad (79)$$

The method that is currently used in NATASHA seems to line up with one that has been recommended by a student of Patil (Ricciardi, Ref. [118]). This method is to use normalized lift and moment coefficients,  $\bar{L}$  and  $\bar{M}_{1/4}$ , which is provided by Peters (Ref. [111]) as:

$$\bar{L} = \frac{L_{\text{gust}}}{\rho b_n V_T^2 c_{l_\alpha}} = w_0 + \frac{1}{2}w_1 + \frac{1}{2}(\dot{w}_0 - \frac{1}{2}\dot{w}_2) \frac{b}{V_T} \quad (80)$$

$$\bar{M}_{1/4} = \frac{M_{1/4}}{\rho b_n^2 V_T^2 c_{l_\alpha}} = -\frac{1}{4}(w_1 + w_2) - \frac{1}{4}(\dot{w}_0 - \frac{1}{2}\dot{w}_2) \frac{b}{V_T} - \frac{1}{16}(\dot{w}_1 - \dot{w}_3) \frac{b}{V_T}$$

This is then supplemented by a similar form for the dynamic inflow equations:

$$[A]_{\text{inflow}} \left\{ \dot{\lambda} \right\} + \{\lambda\} = \{c\}_{\text{inflow}} \left( \dot{w}_0 + \frac{1}{2}\dot{w}_1 \right) \quad (81)$$

In equation (80),  $w_n$  is the coefficient of the  $n^{\text{th}}$  Chebychev polynomial mode shape when  $w^B$  (the gust velocity in the body frame of the airfoil section) is approximated as

$$w^B = \sum_{i=0}^N w_n T_n \quad T_n = \cos(n\phi) \quad (82)$$

$$\cos(\phi) = x^B/b = x^* \quad w_n = \frac{\int_0^\pi w_B T_n d\phi}{\int_0^\pi T_n^2 d\phi}$$

If the gust velocity in the body frame for a given element with index  $n$  is assumed to be  $w^B = \bar{w}e^{i\omega t}$ , then define the airfoil coordinate for a given section  $x_n = x_{0n} + V_\infty t$ , where  $x_{0n}$  is a value to represent the streamwise offset of each section due to sweep (or if it is the tail section). Then, it can be said that for a given point on the airfoil  $x_n^* = x_n/b_n$ ,  $w(x_n^*) = \bar{w}e^{ikx^*} e^{-ikx_{0n}^*} = w^{n*} e^{ikx^*}$ . The term  $w^{n*}$  is then interpreted as a phase lag from the gust impinging the  $n^{\text{th}}$  element, and can now also be modified to include any span-wise distribution that the gust may have (for instance, the gust may impinge on only the left wing). The terms  $w_0$  through  $w_3$  can be calculated in terms of a Bessel function of the first kind:

$$J_n(k) = \frac{i^{-n}}{\pi} \int_0^\pi e^{ik \cos(\phi)} \cos(n\phi) d\phi \quad (83)$$

$$w_0 = \frac{1}{\pi} \int_0^\pi e^{ikx^*} e^{-ikx_{0n}^*} d\phi = \frac{w^{n*}}{\pi} \int_0^\pi e^{ik \cos \phi} d\phi = J_0(k) w^{n*}$$

$$w_1 = \frac{2}{\pi} \int_0^\pi e^{ikx^*} e^{-ikx_{0n}^*} \cos(\phi) d\phi = \frac{2w^{n*}}{\pi} \int_0^\pi e^{ik \cos \phi} \cos(\phi) d\phi = -2iJ_1(k) w^{n*} \quad (84)$$

$$w_2 = -2J_2(k) w^{n*}$$

$$w_3 = 2iJ_3(k) w^{n*}$$

In this case, the normalized lift and moment coefficients  $\bar{L}$  and  $\bar{M}$  should then be

$$\bar{L} = (J_0(k) - iJ_1(k) + \frac{1}{2}ik[J_0(k) + J_2(k)]) w^{n*} \quad (85)$$

$$\bar{M} = (\frac{1}{2}[iJ_1(k) + J_2(k)] - \frac{1}{4}ik[J_0(k) + J_1(k)] - \frac{1}{8}k[J_1(k) + J_2(k)]) w^{n*}$$

These coefficients are then dimensionalized by the following:

$$\bar{f}_{\text{gust}}^n = [C_a^n] \begin{Bmatrix} 0 \\ -c_{l_\alpha} \rho b V_T V_3 \bar{L} \\ c_{l_\alpha} \rho b V_T V_2 \bar{L} \end{Bmatrix} w^{n*} \quad (86)$$

$$\bar{m}_{\text{gust}}^n = [C_a] \begin{Bmatrix} 2\rho b^2 V_T^2 c_{l_\alpha} \bar{M} \\ 0 \\ 0 \end{Bmatrix} w^{n*} + \widetilde{y}_{ac} f_{\text{gust}}$$

### *Implementation of Linear Gust Analysis*

The gust analysis process involves finding the matrix  $[F]_{\text{gust}}$  such that  $\{\hat{f}_{\text{gust}}\} = [F]_{\text{gust}} \{w^*\}$ , where  $x$  are once again referring to the NATASHA states,  $w^*$  is a vector of the  $w^{n*}$  terms that represent the span-wise distribution of the gust and the phase lag between sections of different streamwise positions. For the open-loop gust response, if the gust distribution is prescribed as  $\{w^*\} = \{\bar{w}\} e^{i\omega_g t}$ , then the response will be of the form  $\{\bar{x}\} = \{\bar{x}\} e^{i\omega_g t}$ . Therefore if there are  $m$  lifting elements and  $n = 21 * N + 12 + 6 * m$  NATASHA states ( $N$  is the total number of nodes), the size of the  $[G]$  matrix is  $n \times m$ .

Some initial studies were undertaken to study the frequency response of the model to various gusts. Two specific types of gusts that were studied were symmetric and anti-symmetric simple harmonic gusting. The frequency response of the model in terms of bending moment are shown in Figures 42 and 43. The frequency response plots show spikes at the free vibration eigenvalues as expected, with symmetric frequencies being excited in Figure 42 and anti-symmetric frequencies being excited in Figure 43. The highest peak occurs as a result of the anti-symmetric gust occurring at the first out-of-plane anti-symmetric wing bending. The peak value is around 1.5, which translates to a bending moment that has increased by 150% as a result of a 1 ft/s magnitude oscillating anti-symmetric gust. This situation is a highly specialized case unlikely to ever exist in nature, and especially would be extremely unlikely in calm weather. If this situation could occur in nature, it seems this type of gusting would be the most dangerous condition. For the symmetric case, oscillating gusting occurring at the first out-of-plane symmetric bending mode would cause a response magnitude of 70% of the steady-state value. For either situation, the increase in bending moment would nearly linearly translate to an increase in stresses; if it did, the maximum safety factor of 15% at low speeds could increase to 30-40%, so static failure is still not expected due to this type of gusting.

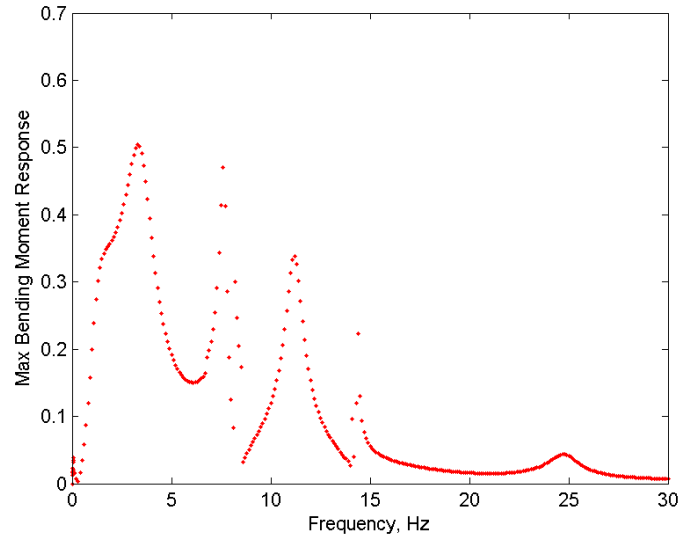


**Figure 42:** Frequency response magnitude of the root wing bending moment response with respect to a uniform oscillating gust. The magnitude is normalized by its steady-state value.

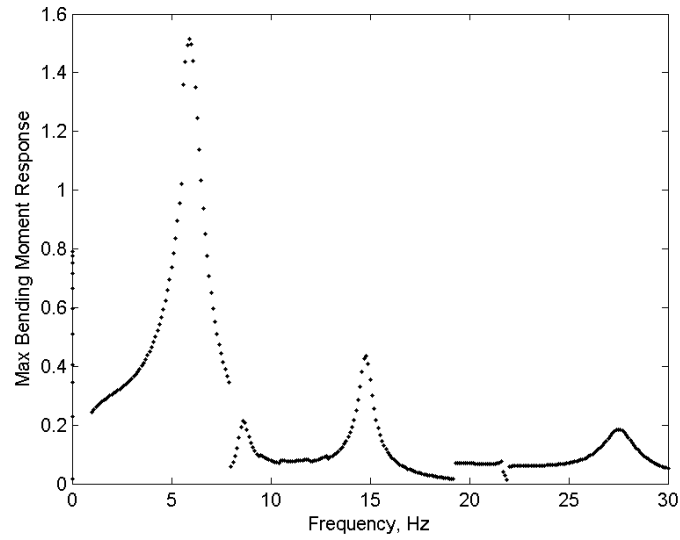


**Figure 43:** Frequency response magnitude of the root wing bending moment response with respect to an anti-symmetric oscillating gust. The magnitude is normalized by its steady-state value.

#### *Interpretation of Linear Gust Results*

The expected power spectral density (PSD) of the gusting velocity is denoted by  $\Phi(\omega)$ . If the response of the system to a gust is denoted as  $[X(\omega)]$  then the PSD of the effective response is:

$$[\Phi_x(\omega)] = [X(\omega)][\Phi_g(\omega)][X(\omega)]^T \quad (87)$$

The response of a given variable is calculated by the following:

$$\sigma_x = \sqrt{\int_0^{\infty} \Phi(\omega) d\omega}$$

$$\bar{A} = \frac{\sigma_x}{\sigma_w} \tag{88}$$

$$N_0 = \sqrt{\frac{\int_0^{\infty} \omega^2 \Phi(\omega) d\omega}{\int_0^{\infty} \Phi(\omega) d\omega}}$$

The  $\sigma_x$  would be interpreted as the RMS value of the response value,  $\bar{A}$  is known as the normalized gust intensity and the characteristic frequency is  $N_0$ . This interpretation was never carried out due to confusion (at the time) about what to use for  $\Phi_g$ , but in future work this could be carried out to interpret the results shown in Figure 42 and 43 in a more realistic way.

#### 4.7.5 Nonlinear Analysis Capability

The linear gust analysis results are useful for determining the turbulence intensities that can be problematic in terms of overly-large responses. The procedure for performing the linear gust analysis including the effect of feedback control is currently unknown (to the author).

MATLAB's control design environment SIMULINK was used for its popularity in control design applications. Within the SIMULINK model, the nonlinear timestepping model for the symmetric case is a block with  $\Delta T$  and  $\Delta\beta_s$ , the thrust and flap control deflections, as inputs and  $\theta$  and  $\dot{\theta}$  as outputs for the SAS controller. Within that block, the model looks as in Figure 45. The core of the nonlinear model is the MATLAB function block, for which the NATASHA timestepping analysis has been modified and performs the actual NATASHA calculations. The MATLAB function block takes as inputs the control inputs, the current gust velocity, and the present state of the NATASHA design variables. The capability for the model to include feedback to the three inboard flaps is also included, but since the flaps are not included in the SAS system all of the flap control laws will be included within the NATASHA model. After the timestep is complete, nonlinear outputs for  $\theta$ ,  $\alpha$ ,  $\dot{\theta}$ , and  $V_T$  are output as well as the altered state of all of the degrees of freedom. The model relies on SIMULINK to keep track of the timestep count, the states, and the history of the gusting velocity by use of the countin/countout, statein/stateout, and gustin/gustout inputs and outputs. The passage of the state variables from the outputs to the inputs of the MATLAB function block also adds the added utility of them being available for feedback to the controls and they are also

saved to the MATLAB workspace for further analysis after the simulation is complete. The history of the gusting velocity is necessary as the gust velocity is propagated downstream of the model with the flight speed. This enforces the fact that if a sharp-edged gust impinges on the nose, a few timesteps later according to the flight speed the gust will later impinge on the tail. A switch was implemented to change from continuous gusting to discrete gusting as necessary, with discrete gusts being set up in the MATLAB work space prior to simulation.

#### 4.7.6 Nonlinear Analysis

A nonlinear SIMULINK model was created by creating a block that runs one timestep of the nonlinear NATASHA analysis. This model was hooked up with the controller provided by Bihrlé. The model consists of two subsystem blocks and two feedback loops. A picture of the general architecture is shown in Figure 44, with the outer loop representing the Bihrlé controller and the inner loop representing the aeroelastic controller. A screen-shot of the inner loop is shown in Figure 45, with all of the steps necessary for the NATASHA nonlinear timestep condensed into the subsystem “NATASHA.” This sub-system is shown in Figure 46 and takes as inputs a gust vertical velocity, which comes from a gust model block shown in Figure 47 that includes a continuous gust model (turbulence) and the capability to analyze user-defined gusting profiles. The model includes a manual cut-on for the control inputs at 0.01 seconds to eliminate start-up noise so anything “interesting” should be set up to begin after this time. The start-up “noise” isn’t really noise in the true sense of the word but comes from the implementation of the model: the state output of the model “stateout” (see Figure 46) at the first timestep is set to all zeros, so that the “Delta States” output is incorrect at the first timestep. The control inputs themselves are constrained to be within a maximum and minimum limit to simulate the inability of flaps to go beyond a certain deflection or the thrust variations to be within a certain limit. Realistic control designs will never reach these limits, so the min/max blocks may not be necessary.

#### 4.7.7 State-Space Model

The process of the controller design begins by generating a state-space model of the linearized dynamics about the trim equilibrium position. The NATASHA trim and eigenvalue analysis process generates the Jacobian and dynamic Jacobian matrices such that:

$$[J_x] \{x\} - [J_{\dot{x}}] \{\dot{x}\} = [f_{\text{cont}}] + [f_{\text{gust}}] \quad (89)$$

Here,  $\{x\}$  is used to represent linear perturbations of the NATASHA unknowns and is size  $N$ , but not all of these unknowns are independent, and there exists an independent set of these unknowns



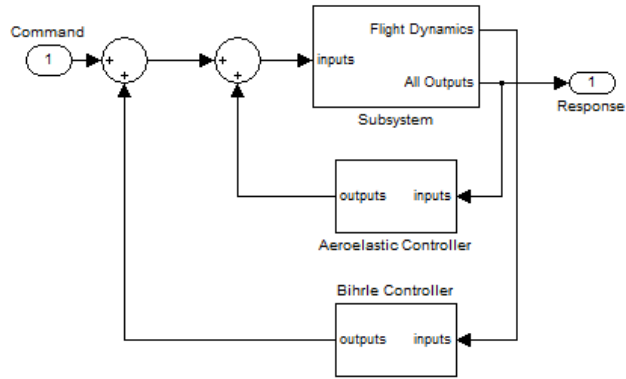


**Figure 44:** The general architecture of the aeroelastic controller within the context of the provided Bihrl controller.

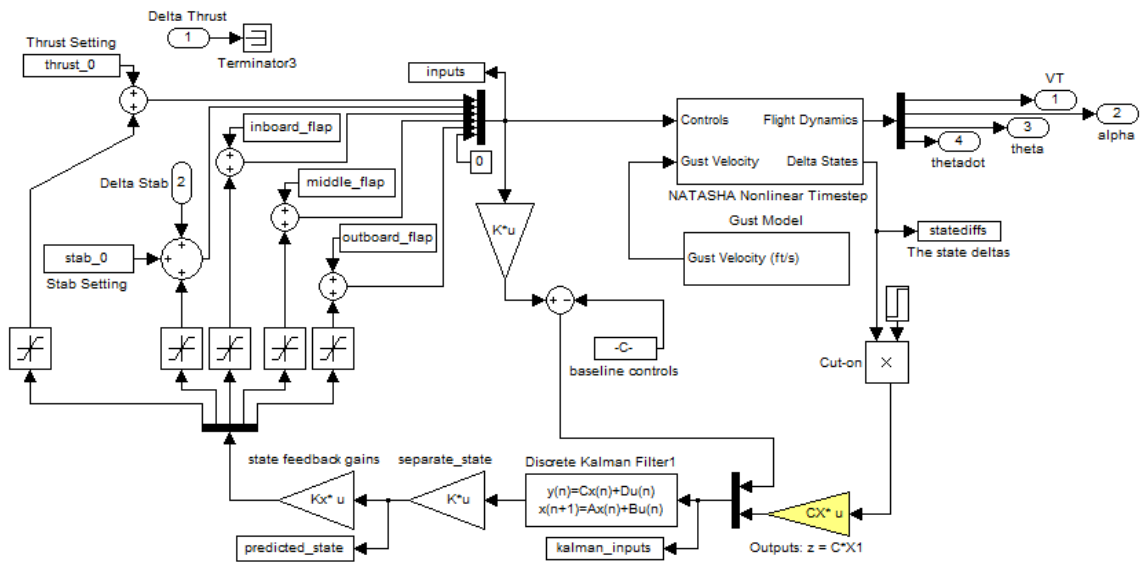


**Figure 45:** The inner feedback loop showing the aeroelastic controller, NATASHA analysis block, and gust model block.

$x$  that can fully describe the system that is size  $n$ . The NATASHA system matrices are input into

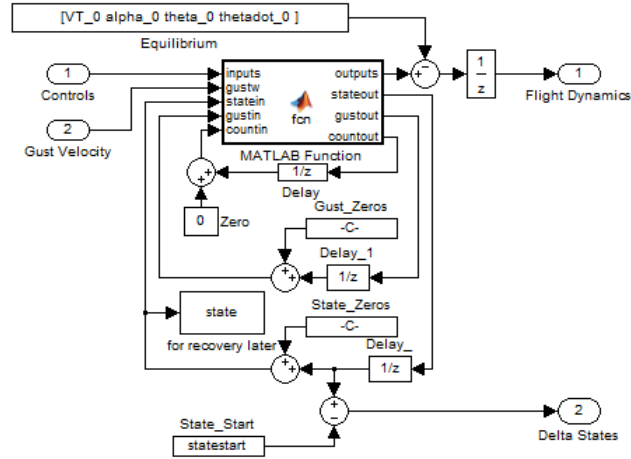


**Figure 46:** The NATASHA analysis process that executes one timestep of the NATASHA nonlinear analysis.

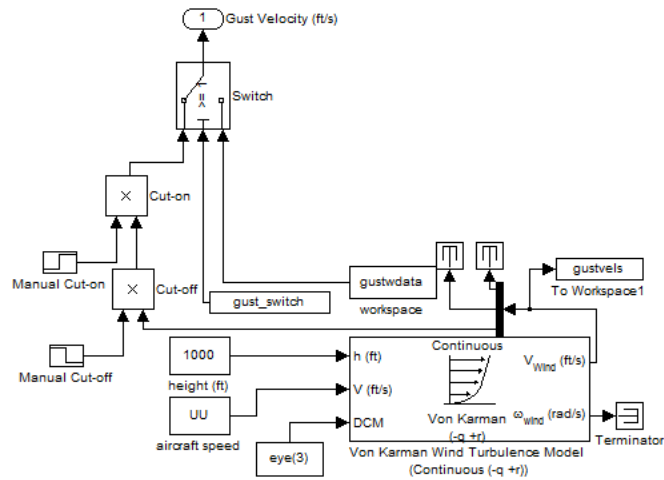


**Figure 47:** The gust model can either be specified by the user in the form of a defined gust profile or if continuous random gusting is desired a continuous gust model is built in.

the MATLAB descriptor state-space model by setting:

$$[E]_{dss} = -[J_{\dot{x}}]$$

$$[A]_{dss} = -[J_x]$$

$$[B]_{dss} = [[F_{cont}][F_{gust}]]$$

$$[D]_{dss} = [0]$$

(90)

MATLAB can then transform the system into a proper state-space model, and it will choose a set of dummy variables  $\bar{x}$ . To work with a set of independent variables  $x$  that are physical and correspond to certain components of  $\{x\}$ , the input  $[C]_{\text{dss}}$  was set up so that the outputs of the descriptor state-space model are the independent variables  $x$ . The set of independent variables that was utilized are the following (for the symmetric case):

1. The four rigid body degrees of freedom at the reference (centerline) node:  $\hat{V}_2, \hat{V}_3, \hat{\Omega}_1, \hat{g}_3$ .
2. Three forces and three moments to the right of the reference node:  $\hat{F}_i, \hat{M}_i, i = (1, 2, 3)$ . These are required to capture the effect of the tail force and moment and the fuselage mass and inertia, which will all act at the reference node.
3. Three forces, three moments, three velocities, and three angular velocities for each node starting at 3 and going to the wingtip:  $\hat{F}_i, \hat{M}_i, \hat{V}_i, \hat{\Omega}_i, i = (1, 2, 3)$ . The information at node 2 is unnecessary because element 1 is a rigid element.

$[F_{\text{cont}}]$  is formed as described in Eq. (53);  $[F_{\text{gust}}]$  is formed using a quasi-steady approximation that  $\Delta\alpha = w/V_T$ , and the same expressions in Eq. (53) were modified by using  $V_T$  instead of  $V_T^2$ , and replacing  $\beta_0$  with  $\alpha_0$ ,  $C_{l_\beta}$  with  $C_{l_\alpha}$ , etc.

The descriptor state-space model is thus set up and the proper state-space model is extracted in terms of physical variables  $x$ , producing  $[\bar{A}]$ ,  $[\bar{B}]$ ,  $[\bar{C}]$  matrices corresponding to the state-space model in the form of Eq. (91). The output matrix  $[\bar{C}] = [x\bar{x}]$  matrix resulting from this process is then the matrix relating the independent dummy variables  $\{\bar{x}\}$  to the the desired set of physical independent variables  $x$ . At this point, it is possible to transform the proper state-space model to utilize the physical independent variables directly, but it was found that the modal reduction was more successful if the dummy variables are retained during this step and the reduction is based on  $[\bar{A}]$  (see section 4.7.8 for the details on the reduction process). The following summarizes the resulting state-space model and the matrices required to translate from the dummy variables  $\bar{x}$  to the set of physical independent variables  $x$  and the NATASHA unknowns  $\{x\}$ .

$$\dot{\bar{x}} = [\bar{A}]\bar{x} + [\bar{B}]u \tag{91}$$

$$\begin{aligned} x &= [\bar{C}]\bar{x} = [C_{\text{dss}}] \{x\} \\ \{x\} &= [C_{\text{dss}}]^T [\bar{C}] \bar{x} = [X\bar{x}] \bar{x} \end{aligned} \tag{92}$$

$$\bar{x} = ([X\bar{x}]^T [X\bar{x}])^{-1} [X\bar{x}]^T \{x\} = [\bar{x}X] \{x\}$$

After reducing the number of unknowns (including independent and dependent variables) to a

set of independent variables, a proper state-space model is available, and for LQR design all that is needed is to call the MATLAB functions “lqr( )”. However control designs based on this full order model were not found to be successful.

#### 4.7.8 Modal Reduction of State Space Model

Section 4.7.7 describes how to obtain independent dummy variables  $\bar{x}$  from reducing the original NATASHA unknowns  $\{x\}$  of size  $N$  to a proper state-space system of size  $n$  that fully describes the original system.

The modal reduction process that was used may not be the only possible modal reduction technique, but it has been numerically verified by the author to give decent approximations of the full system behavior (when it is based on  $[\bar{A}]$  of Section 4.7.7). The modal reduction was inspired by a conference paper of Patil’s, “Decoupled second-order equations and modal analysis of a general non-conservative system” [109].

The modal reduction was based on the eigenvectors  $v_i$  of  $[\bar{A}]$ , which are size  $n$  and consist of real eigenvectors corresponding to real eigenvalues and complex eigenvectors corresponding to complex eigenvalues. The complex eigenvectors occur in complex conjugate pairs, so two complex eigenvectors  $v_i$  and  $v_{i+1}$  can be written:

$$\begin{aligned}
 j &= \sqrt{-1} \\
 v_i &= a_i + b_i j & v_{i+1} &= a_i - b_i j \\
 v_i &= [a_i \ b_i] \begin{Bmatrix} 1 \\ j \end{Bmatrix} & v_{i+1} &= [a_i \ b_i] \begin{Bmatrix} 1 \\ -j \end{Bmatrix}
 \end{aligned} \tag{93}$$

Equation (93) shows how the imaginary eigenvectors are linear combinations of the real vectors  $a_i$  and  $b_i$ , which are real vectors of size  $n$ . Therefore replace each complex  $v_i$  with  $a_i$  and the conjugate  $v_{i+1}$  with  $b_i$  for each eigenvalue that is complex and this forms a purely real basis for  $\bar{x}$ . The response  $\bar{x}$  can be then expressed in a purely real modal basis:

$$\bar{x} = [v_1 \ v_2 \ \dots \ v_N] \begin{Bmatrix} c_1 \\ c_2 \\ \dots \\ c_N \end{Bmatrix} = [a_1 \ b_1 \ \dots \ v_N] \begin{Bmatrix} (c_1 + c_2) \\ (c_1 - c_2)j \\ \dots \\ c_N \end{Bmatrix} = [a_1 \ b_1 \ \dots \ v_N] \begin{Bmatrix} d_1 \\ d_2 \\ \dots \\ d_N \end{Bmatrix} \tag{94}$$

If the purely real basis vectors are arranged into a matrix  $[Q]$  and then orthonormalize it,  $[Q]^T[Q] = \Delta_n$ , then it is a basis for a change of variables  $\bar{x} = [Q]z$ . The arrangement of  $v_i$  in  $[Q]$  is performed

so that the eigenvalues corresponding to each  $v_i$  increase in magnitude, and the left-most  $r$  columns of  $[Q]$  correspond to the lowest  $r$  eigenvalue magnitudes. Then the new set of variables  $z$  can be truncated to size  $r$ , which corresponds with keeping only the eigenvectors that go with the lowest  $r$  eigenvalues. This results in an  $n \times r$  matrix  $[Q]$ , and the reduced system is found as follows:

$$\begin{aligned}\dot{\bar{x}} &= [\bar{A}]\bar{x} + [\bar{B}]u \\ [Q]\dot{z} &= [\bar{A}][Q]z + [\bar{B}]u \\ \dot{z} &= [Q]^T[\bar{A}][Q]z + [Q]^T[\bar{B}]u \\ \{x\} &= [X\bar{x}][Q]z = [Xy]z\end{aligned}\tag{95}$$

$$y = [C][Q]z$$

Preliminary runs of the nonlinear model showed that the IP bending mode was commonly excited and was very lightly damped. Therefore, the model reduction was performed such that this mode was captured and all modes at higher frequencies were neglected, resulting in a new model order of 79. These 79 states then relate to the 5 lowest oscillatory modes along with 69 states relating to the aerodynamics and non-oscillatory rigid body dynamics of the model. Modal reduction techniques which only retain the oscillatory modes are possible but often change the values of the relevant eigenvalues: the modal reduction technique given here succeeded in retaining the exact values of the lowest  $r$  eigenvalues.

#### 4.7.9 Discretized Version of the State-Space Equation

There are situations in which a discrete state-space model is more appropriate than a continuous model. The nonlinear analysis is essentially a discrete model with a fixed timestep. If digital electronics are used in the controller, than the physical version of the controller will behave in a discrete sense. One way the equations can be discretized is by using the forward difference approximation  $\dot{x}\Delta t = x_{n+1} - x_n$ , where  $n$  is the time step, and therefore:

$$x_{n+1} = [I + A\Delta x]x_n + \Delta x[B]u\tag{96}$$

However, a more rigorous approach would be to integrate the continuous version in time so that:

$$x_{n+1} = x_n + \int_t^{t+\Delta t} ([A]x + [B]u)\tag{97}$$

The discretization of the model was performed by MATLAB using the command `c2d()` on the continuous state-space model, which uses a rigorous approach to convert the model with the assumption that all inputs are held from one timestep to the next in a zero-order hold fashion, which is the option ‘zoh’ (as opposed to interpolating inputs between timesteps or something else).

The discrete model has the additional advantage over the continuous model in SIMULINK analysis time. In the continuous model, SIMULINK attempts to take a very small timestep to resolve the high-frequency dynamics of the model (which, by the way, are not all physical). The high-frequency dynamics can be ignored by the use of the variable reduction, allowing for more efficient SIMULINK analysis at the penalty of modeling accuracy. However, the discrete model can be analyzed in SIMULINK efficiently without performing the variable reduction.

#### 4.7.10 Types of Controllers Considered

Three types of controllers were considered: a classical linear quadratic regulator (LQR), an LQR plus a Kalman filter which is known as a Linear Quadratic Gaussian (LQG) controller, and output feedback control. LQR controllers use all of the system states as feedback, which is not feasible. The next type of controller considered was an output feedback controller, but this was never successfully implemented. A successful control design was found by using an LQG controller, which uses a state estimator model to estimate the value of all of the states based on only the few that are available from the output.

The outputs that will be available are from the use of conventional sensors (strain gages or accelerometers) or more advanced sensing equipment (fiber optics, etc.). The use of strain gages combined with the constitutive model allows measurement of internal forces and moments, which are directly used as NATASHA design variables and should be ideal for use in control design. Accelerations obtained from accelerometers could be used directly as feedback or integrated to find linear and angular velocities, again which are directly used as NATASHA design variables. Because NATASHA is based on the intrinsic form of the geometrically exact structural equations, deflections or rotations are not used directly as states. The relationship between the intrinsic variables and the actual linear deflections is nonlinear (involving a matrix inversion), and the relationship between the gravity orientation vector measures  $g_i$  and the angular deflections is also nonlinear. These relationships can be linearized at best but in general the use of deflections or rotations as state variables or feedback is not recommended. It would be far more ideal to use only the NATASHA variables, which are velocities, rotations, forces, and moments, and the gravity vector measures  $g_i$ . Of these, the most easily measured are the internal forces and moments by means of the constitutive

model and curvature measures.

Another commonly used measurement device are accelerometers. To obtain accelerations from the model directly, it may be possible to utilize the state-space model:

$$\{\dot{x}\} = [X\bar{x}]\dot{\bar{x}} = [X\bar{x}][\bar{A}]\bar{x} + [X\bar{x}][\bar{B}]u \quad (98)$$

The relation in Eq. (98) would be implemented by using a feed-forward matrix  $[D]$ . The relation was implemented without using the feed-forward part of Eq. (98) and was not found to be successful.

#### *LQR Controller*

A full-state optimal feedback controller was designed using the both the full linear discrete model and the reduced linear discrete model. These feedback controllers were found to be successful in controlling the response of the linear models, but they rapidly caused instability when they were connected to the nonlinear analysis. However the LQR design was implemented with a Kalman filter with success. The LQR design was conducted using a model order of 79, which was just enough to include the phugoid mode, short-period mode, first out-of-plane bending mode, first twisting mode, and first lead-lag bending mode. The other modes are related to the aerodynamic states and had all real parts. The LQR design requires as input a state weighting matrix and a control weighting matrix. The state weighting matrix was set to all zeros except for the phugoid, unstable SOP, SP and in-plane IP bending modes. The weight of 100 was assigned to the unstable bending-torsion mode and 10,000 to the other weighted modes. The value of the control weighting matrix was set to a diagonal matrix, with each element equal to  $10^{-3}$ . These weighting matrices were chosen from trial and error and based on the controller performance.

#### *Kalman Filtering*

The Kalman filter is a critical part of optimal feedback control when only a limited number of outputs are available but the feedback of many or all of the states is desired for the controller. The Kalman filter is used to predict the values of every state from just the controls and the available outputs. In the state-space models presented so far, the gusting velocity  $w$  was included in  $u$  so that the last column of  $[B]$  corresponds to the transformed version of  $[F_{\text{gust}}]$ . This is now separated again to form the following model in terms of the reduced variables  $z$ :

$$\dot{z} = [A]z + [B]u + [G]w \quad (99)$$

$$y = [C]z$$

The Kalman filter is essentially a state-space model that will take  $u$  and  $y$  as inputs and output the predicted value of the states  $\hat{z}$  and a filtered set of outputs  $\hat{y}$ . In the Kalman filter design process, both the states and outputs are corrupted with noise: “process noise” corrupts the value of each state and “output noise” corrupts the signal values  $z_i$ . In the MATLAB Kalman filter design function “kalman( )”, the following form is given:

$$\dot{z} = [A]z + [B]u + [G^*]w^* \tag{100}$$

$$y = [C]z + [G^{**}]w^* + v$$

A successful Kalman filter design was obtained by observing the similarity between Eqs. (99) and (100) and just setting the process noise matrix to the gust velocity  $w$ . The effect of the gust is then to add a noisy character to the reduced set of variables  $y$ . The Kalman filter has been set up to accept only curvatures from a few elements, first all curvatures were input, then only IP curvatures, and then only bending curvatures. The matrix  $[G^{**}]$  was set to zero. An exhaustive study was not undertaken to find the minimum number of inputs required for the successful control. The remaining inputs are the variance of the noise  $w^*$  and  $v$ , but these two inputs were not found to influence the behavior of the filter significantly. These inputs were set to  $10^{-12}$ .

The gain matrices for LQR and LQG designs were then calculated using the MATLAB function “lqr( ).” The gain matrix is found by solving two coupled Lyapunov equations as described in Ref. [104]:

$$u(t) = [K]y(t)$$

$$K = -R^{-1}B^T SPC^T(CPC^T)^{-1}$$

$$0 = A_c^T S + SA_c + Q - C^T K^T R K C \tag{101}$$

$$0 = A_c P + P A_c^T + V$$

$$A_c = A + B K C$$

$$V = D D^T$$

Note the above equation is a matrix equation with the variables as defined in the original reference.



An adaptive type of kalman filtering was then implemented where all of the vector or matrix inputs are linearly interpolated based on the total velocity  $V = V_T$ . The “Interpolation” block in SIMULINK takes care of the linear interpolation when provided with a matrix and produces a vector. If there are  $N$  values to interpolate from, with the 1<sup>st</sup> value corresponding to the input at  $V_{\min}$  and the  $N^{\text{th}}$  value corresponding to  $V_{\max}$ , then the “Interpolation” block requires an input  $P$  between 1 and  $N$  for which to perform the interpolation. The matrix interpolation required for the Kalman filter was done using the “Prelookup” and “ScheduleMatrix-1D” blocks. The following figures (48, 49, 50) show the modified blocks. The Kalman filter block, although it looks complicated, actually performs exactly the same as the discrete state-space block when the inputs are set up to provide constant system matrices (this was verified with the nonlinear simulation).

As one example of how the interpolation might be performed, if  $V_{\min} = 80$  and  $V_{\max} = 85$ , and  $N = 6$ , and a vector  $A_1$  corresponding to  $V_{\min}$  and a vector  $A_N$  corresponding to  $V_{\max}$ , then an input value of  $P = 1.5$  will interpolate  $A$  based on the values  $A_1$  and  $A_2$ , which would correspond to  $V = 80$  and  $81$ . This is implemented generally by the following:

$$d = \frac{V_{\max} - V_{\min}}{N - 1} \quad P = \frac{V - V_{\min}}{d} + 1 \quad (102)$$

This method is only one example of the implementation of the adaptive controller. Different implementations of adaptive controller would be realized by changing the definition of the interpolation variable  $P$ . Therefore, most of what has been done in terms of trial-and-error methods to improve the success of the adaptive controller is to alter the calculation of this interpolation variable, again which is done at the top of Figure 48.

#### **4.7.11 Nonlinear Simulation with Linear Kalman Filter and Controller**

To demonstrate the instability of the system contrasted with the stability of the system with the flutter controller on, the following figures are presented to show the compared behavior of the system (red) with the uncontrolled system (black). The uncontrolled system has no flutter controller but still has a flight dynamics pitch controller connected. The response to continuous gusting was explored, to demonstrate the behavior of the controller when all of the states were perturbed significantly from there equilibrium point. To demonstrate the ability of the controller to return the system to stability, the gust was cut off after 3s. This section concerns Kalman filters that are designed for a given flight speed and then run at that flight speed. The behavior of the system in response to a continuous gust at 75 kts is demonstrated with (red) and without (black) the flutter controller

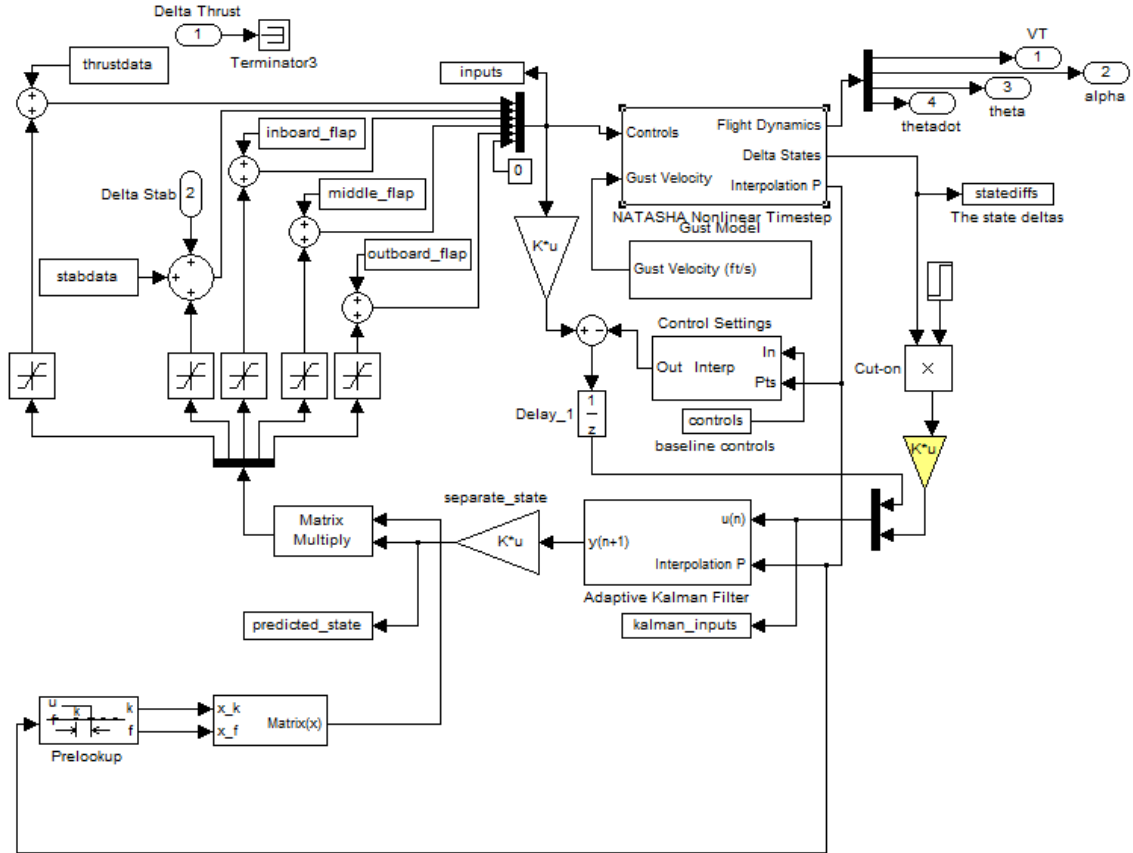


**Figure 48:** The modified SIMULINK model showing the inner loop of the adaptive aeroelastic controller.

in Figure 51, and the continuous gust response is shown at 90 kts in Figure 52. The uncontrolled flutter speed of the model was around 80 kts, so these figures clearly demonstrate the success of the controller. Unfortunately, is an interaction of the flutter controller with the outer loop flight dynamics controller that worsens the transient response due to the gust below the flutter speed, but both flight speeds are stable which was the intended purpose of the controller.

*Perturbed Behavior at 90 kts*

The behavior of the perturbed system at 90 kts is demonstrated with (red) and without (black) the flutter controller in the next few figures.

**4.8 Conclusions**

The body-freedom flutter behavior of a HALE flying wing aircraft has been studied, and the sensitivity of the behavior with respect to various parameters was explored. The BFF was characterized as an interaction between the short-period and bending modes, so the evolution of these modes from

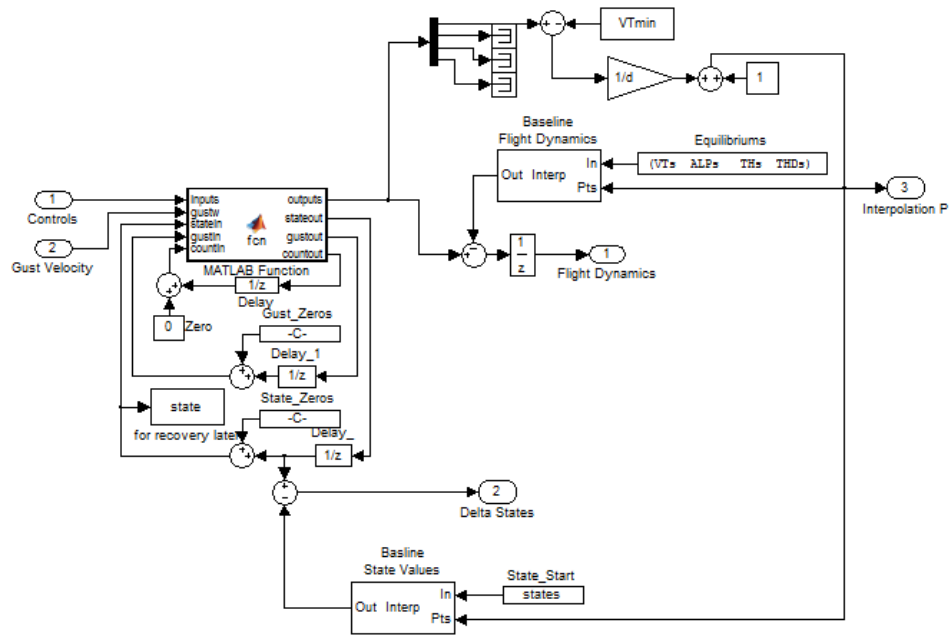


**Figure 49:** The modified NATASHA nonlinear timestep block for the adaptive aeroelastic controller.

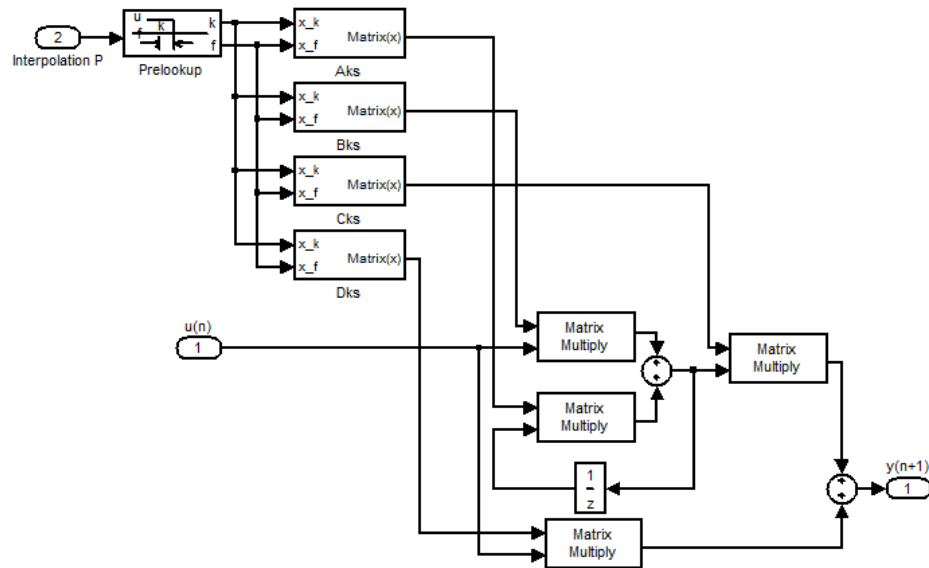


**Figure 50:** The adaptive Kalman filter, which works as a state-space model with linearly interpolated system matrices.

the stall speed to the flutter speed for some selected cases was examined. The structural properties that were found to impact this BFF behavior were the bending stiffness and the mass per length. When the structural parameters are changed, the basic character of the modes was not changed, and flutter occurred in the bending mode and seemed to be associated with decreased tip velocity

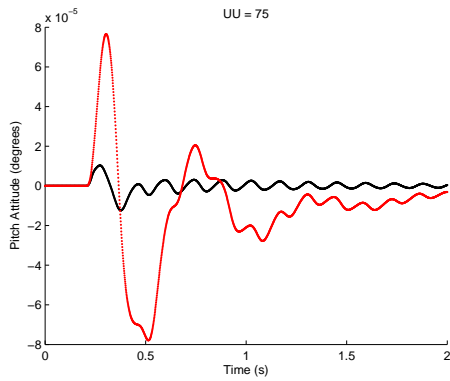


**Figure 51:** The response to a continuous 0.05 s gust at 75 kts: pitch attitude.

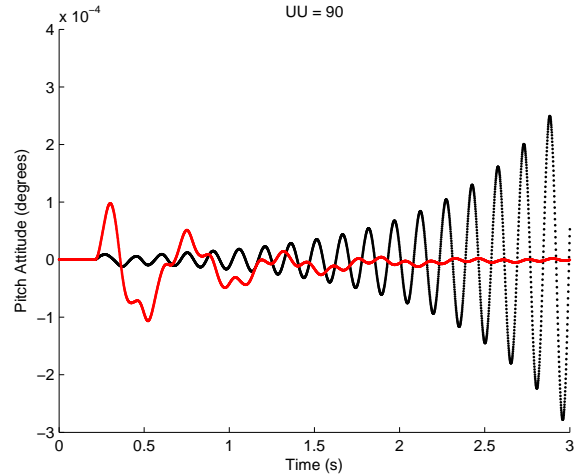


**Figure 52:** The response to a continuous 0.05 s gust at 90 kts: pitch attitude.

magnitudes, root bending moments in phase with fuselage reference point velocity, and a coalescence of the SP and bending mode frequencies. For the baseline and all of the cases with varied structure, the bending mode becomes unstable.

The basic character of the SP and bending modes can be changed by altering the fuselage parameters, in some cases pushing the instability to a higher flight speed and in some cases causing the instability to occur at very low flight speed. The inverse dependency of the flutter speed on the fuselage mass seems to reflect a dependence upon some sort of inertial coupling between the wing and fuselage motion, so that if the fuselage were not present the BFF can not occur. Increasing the pitching inertia of the fuselage had the effect of removing the pitching velocities from the bending mode entirely, and for the maximum fuselage inertia factor the SP mode experienced the instability (instead of the bending mode). It might be said that the lack of angular velocity in the bending mode caused its frequency to change less with increasing flight speed, and therefore stabilized the mode by avoiding “coalescence” between the bending and SP modes. This reflects the fact that angular velocity is a necessary component to the body-freedom flutter behavior of this model.

The linear analysis results were verified by a nonlinear timestepping analysis. This verifies the utility of the linear analysis results to efficiently but accurately characterize the behavior of the flutter mode or other modes of vibration. The NATASHA system is therefore an ideal conceptual design tool for very flexible flight vehicles, especially those which experience body-freedom flutter. The utility of NATASHA for structural and control design was then demonstrated in design of a realistic flying wing. First, structural design considerations for realistic structures were applied to flutter speed maximiation. Then, control design was demonstrated for a realistic HALE aircraft

model to extend flutter and suppress gust vibrations. The flutter margin was successfully increased with the aeroelastic control design, but the flutter controller worsened the transient gust response. This demonstrates the importance of including aeroelastic control design early into the design process for the flight controller, as the inclusion of aeroelastic control after the flight controller had already been designed degraded the performance of the flight controller, even below the flutter speed.

## CHAPTER V

### WT BLADE DAMAGE MODELING AND ANALYSIS

The previous chapters have demonstrated aeroelastic structural and control design from the perspective of rotorcraft and fixed-wing aircraft. However, the main goal of this work is to demonstrate these concepts in the context of mitigating local damage effects for WT blades. Before efforts can be made to mitigate local blade damage effects can be made, this blade damage must be properly analyzed and understood. For this thesis, bond line failure has been selected as a common type of blade damage. Analysis of the local effects of bond line failure can reveal where bond lines are susceptible to failure. The risk of incurring excessive damage growth for a bond line failure can also be estimated by using high fidelity structural analysis techniques. These high fidelity techniques can then be applied to determine the success of aeroelastic structural and control design strategies intended to mitigate local effects of blade damage.

This research will take a multiscale analysis approach to the problem. The “global” analysis tools will be the NREL tools WT\_Perf and FAST/AeroDyn [17, 65], which are both blade element momentum theory solvers for WTs. WT\_Perf does not include blade flexibility, while FAST/AeroDyn includes flexibility of the blades as well as torsional flexibility of the drivetrain and tower bending flexibility. The SNL Numerical Modeling and Design (NuMAD) tool is an open-source tool for analyzing realistic composite WT blades [5]. This tool has the capability of transforming a thin-walled beam model of a WT blade into a high fidelity ANSYS shell model. The beam model of the WT blade is defined by spanwise chord, twist, and airfoil distributions and a detailed cross section structural model. Since this capability is readily available to interested academic and industry parties and it produces a high fidelity model of the blade as a whole, this shell modeling capability was utilized for this study as the “local” analysis. After the VCCT is verified with a simple example and the mesh dependency of the technique is established, the criticality of bond line failures with respect to damage location and size is examined for both the normal operational strategy and the derated strategy. The comparisons will be made at the rated windspeed, where there is a significant difference in loading between the two operational strategies.

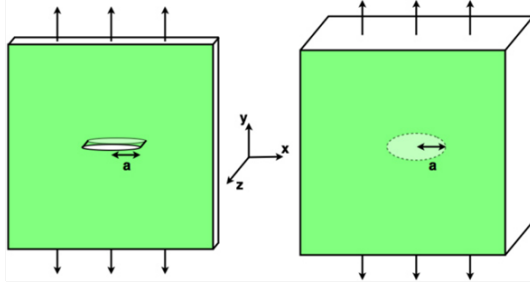


**Figure 53:** VCCT test case: rectangular sample with horizontal mid-plane crack.

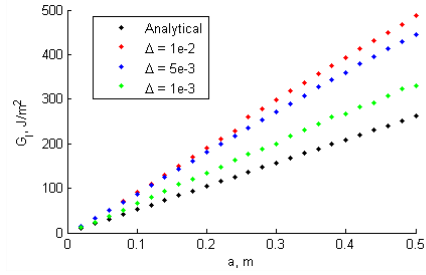


**Figure 54:** VCCT results for rectangular sample with horizontal mid-plane crack.

### 5.1 Validation of VCCT for Isotropic Sections

To validate the VCCT method, a classic example was set up with isotropic materials. The example consists of a horizontal crack in a thin, square plate, with a vertical displacement condition applied to the upper and lower boundaries. The example has a known analytical solution for the SERR, which can be compared to the VCCT results to validate the method. The analytical solution is:

$$G_I = \frac{\pi\sigma^2a}{E} \quad (103)$$

Figure 54 compares the grid convergence of this simple example, which is depicted in Fig. 53. The general trend of the behavior is captured with the smallest mesh density. Another test case was also analyzed with both shell and solid modeling: a double cantilever beam test (DCB). This test case was chosen as it is a common experimental method for calculation of maximum or critical SERRs for a material and a numerical study of the SERR analysis has been undertaken for comparison [28]. The geometry of this test is shown in Fig. 55, the results of the solid model analysis are shown in Fig. 56 (normalized by maximum value) and Table 26 show the numerical results. These results again verify the conclusion that the VCCT method gives good qualitative results even on coarse grids, such as trends and distribution shapes, but for accurate quantitative analysis a fine mesh may be required. For this study the NuMAD shell model was used to examine the qualitative behavior of the SERRs for the WT blade model.

**Table 26:** Strain energy release rate of DCB test with respect to grid size.

Report [28] (fine)	20.2 ( $10^{-4}$ J/m)
1 mm	17.11
0.5 mm	18.86
0.25 mm	19.36

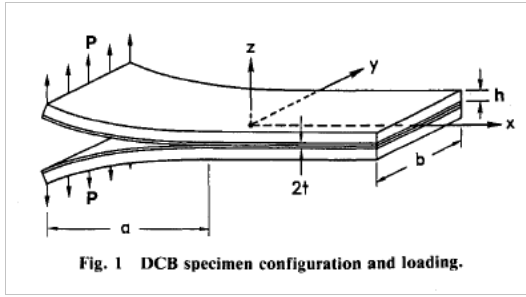


**Figure 55:** VCCT test case: double cantilever beam test.

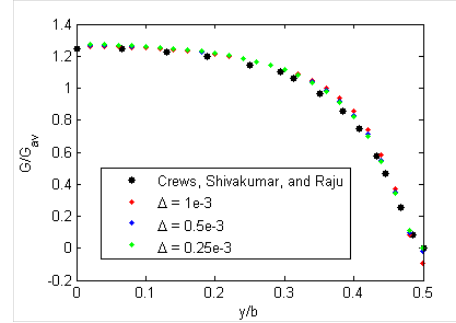


**Figure 56:** VCCT through-thickness normalized distribution results for double cantilever beam test, compared with data from Crews et al. [28].

## 5.2 Damaged Blade Modeling

The NuMAD tool was used to generate an ANSYS model from a description of the NREL 5 MW blade geometry and materials, developed by Resor [117]. The damage location on the WT blade, the coordinate system and the possible directions of damage propagation are depicted in Fig. 57 for a trailing-edge disbond and Fig. 58 for a shear web disbond. In Fig. 58, “upper” refers to the bond line between the shear web and the low pressure side and “lower” refers to the bond line between the shear web and the high pressure side. Three different grid sizes were used for ANSYS analysis; the sizes and basic run-times on a simple PC of the different models are given in Table 27. The ANSYS shell models were modified by removing the connectivity of elements adjacent to the trailing edge, adding coincident nodes along the trailing edge, and reconnecting the upper elements to the new coincident nodes. Then, COMBIN elements, which are essentially nonlinear springs, were used to connect the coincident nodes. The stiffness behavior of the COMBIN elements was modified to have zero stiffness in the “X” (chordwise) and “Z” (spanwise) directions and in the positive “Y” (flapwise) directions, but a very high stiffness in the negative “Y” direction. This approach was verified to model the opening/closing behavior of the disbonds. The loading at rated windspeed during normal or derated operation was calculated using WT\_Perf, which is a blade-element/momentum theory solver for WTs provided by the National Renewable Energy Laboratory (NREL). The distributed loading from the WT\_Perf model was then applied to the ANSYS model via the application of point loads at each external node in the ANSYS model. The value of the point loads was obtained by performing a least-squares regression to determine a value of forces at each node to produce the desired distributed forces and twisting moments. The capability to map distributed loads to the ANSYS model is included in the NuMAD functionality [4].



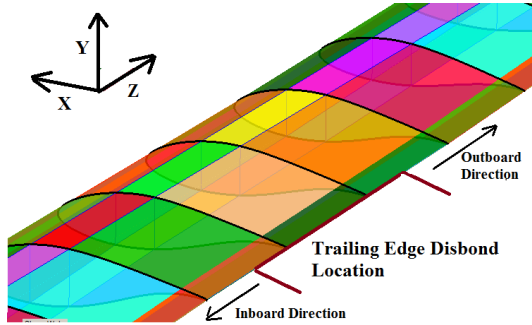


**Figure 57:** Depiction of trailing-edge disbond location on blade, and possible directions of damage propagation.

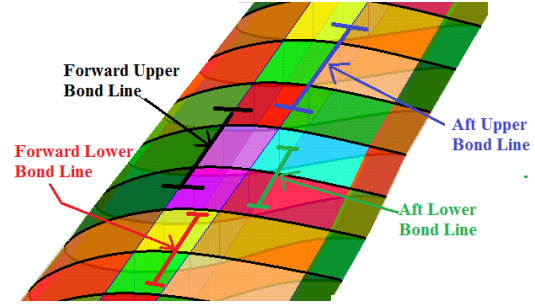


**Figure 58:** Depiction of possible shear web disbond locations on blade, with “upper” referring to the low-pressure side and “lower” referring to the high-pressure side.

**Table 27:** 3D ANSYS blade model grid sizes and approximate run times for one analysis on a simple Windows PC.

Grid Name	# of Nodes	# of Elements	Grid Spacing (m)	Run Time
“Coarse”	18,024	18,671	0.2	30s
“Medium”	67,932	69,147	0.1	5 min
“Fine”	264,900	267,281	0.05	20 min

### 5.3 Healthy Blade Bond Line Stress Results

The healthy baseline stress values  $\sigma_{yy}$ ,  $\sigma_{zz}$ ,  $\sigma_{yz}$ , and  $\sigma_{zx}$  are shown along the trailing-edge bond line in Figs. 59 – 62, respectively, as a function of spanwise position,  $r$ . The stress components  $\sigma_{yy}$  and  $\sigma_{yz}$  are related to opening of the crack due to mode I, and  $\sigma_{zz}$  and  $\sigma_{zx}$  are related to opening of the crack in modes II and III. Note that these healthy stress components show major perturbations in the vicinity of  $r = 10$  m and  $r = 40$  m locations. These locations coincide with the locations where the ANSYS model blends from circular cross sections to blunt trailing edges ( $\approx 10$  m span) and from blunt trailing edges to sharp trailing edges ( $\approx 40$  m span). These transition points are shown in Fig. 63. These regions of high stress in the undamaged blade are therefore of interest when it comes to analysis of damage criticality.

### 5.4 SERR Calculations Under Normal Operation

The SERR was calculated from the ANSYS shell model by using the resulting nodal forces at the crack tip and the opened displacements of the nodes just within the crack tip. A grid convergence study was performed where the basic grid spacing was changed from 0.2 to 0.1 to 0.05. The results from this study indicated a similar trend as with the isotropic cases: a convergence of the results with decreasing grid spacing but a general capture of the trendlines for even the coarsest case. An example of this convergence is given in Figs. 64 and 65.

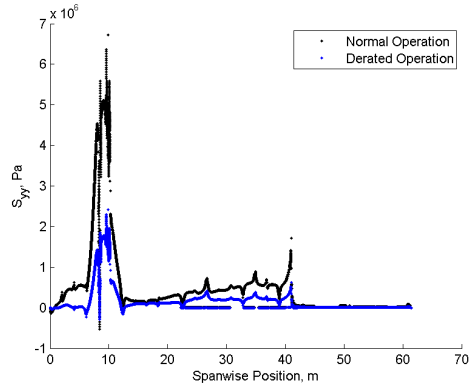


**Figure 59:** Stress results for  $\sigma_{yy}$  along the bond line for the baseline model during normal operation and derated to 50% power level.

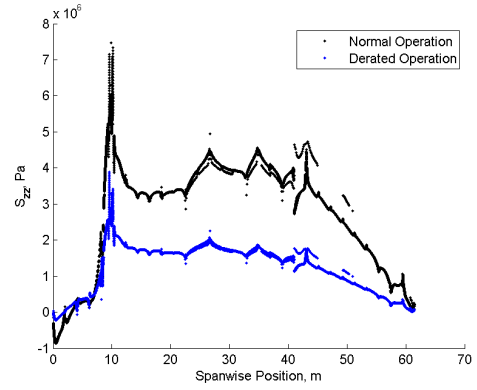


**Figure 60:** Stress results for  $\sigma_{zz}$  along the bond line for the baseline model during normal operation and derated to 50% power level.

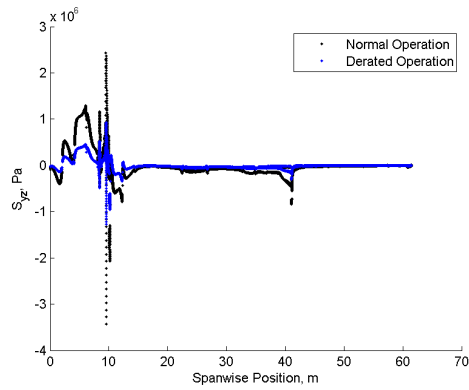


**Figure 61:** Stress results for  $\sigma_{yz}$  along the bond line for the baseline model during normal operation and derated to 50% power level for NREL 5MW blade (61.5 m blade length).

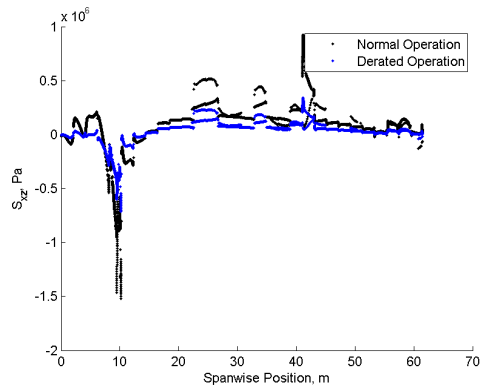


**Figure 62:** Stress results for  $\sigma_{xz}$  along the bond line for the baseline model during normal operation and derated to 50% power level for NREL 5MW blade (61.5 m blade length).

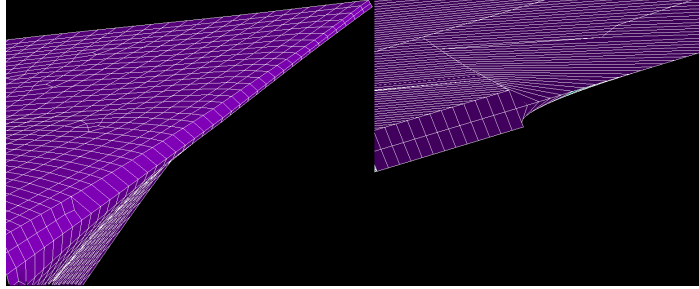


**Figure 63:** Geometry transitions from circular cross sections to airfoil sections with blunt trailing edges (left) and transition from blunt trailing edges to sharp trailing edges (right).

The results for SERRs of the model during normal operation are then shown in Figs. 66 – 71. Note that the results labeled “inboard” would represent the SERR for propagating the crack towards the hub, while results labeled “outboard” represent SERRs for crack propagation towards the tip of the blade. These show that the  $G_I$  values for the inner and outer crack tip are very high when the crack begins around the 10 m span location, and then drop suddenly as the start of the crack moves from 11 m to 12 m. The  $G_{II}$  values are significant only within the most inboard portion of the blade. The results for  $G_{III}$  are lowest in magnitude and also are most significant within the inboard portion of the blade.

The SERR analysis was then conducted for the case of shear web disbonding, and the four possible disbond surfaces were each considered. The results for shear web disbond SERRs of the model during normal operation are then shown in Figs. 72 – 77. These results indicate that shear web bond line failure is the most critical in the inboard portions of the blade, and again a spike in peak  $G_I$  is seen at the 10 m spanwise location. However, between approximately 15 m and 25 m, the SERR results are low for all shear web disbond locations. Outboard of 25 m, there are significant values of  $G_{II}$  so any failure would be dominated by mode II fracture. The SERR results are generally similar in trend for the different possible shear web bond lines, with only differences in magnitude. The bond line failures were generally found to be most severe in the forward upper shear web bond line and least severe in the lower aft shear web bond line.

These damage criticality analyses would be used along with structural health monitoring (SHM) in a derating scenario to determine if the economic advantage of derating is worth the possibility of incurring further blade damage. The SHM system is assumed to be able to identify the type and location of blade damage: see Griffith et al. [46] for TE disbond detection and Myrent et al. [97] for shear web disbond detection. For the skin disbond, the most critical damage location was found to be in the 0-15 m region of the blade, where the SERR values are high. If the TE disbond

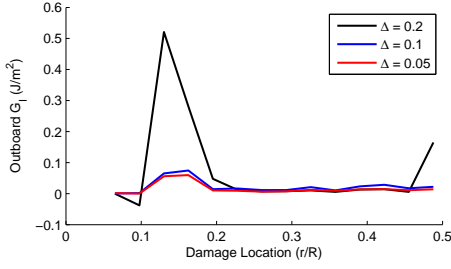


**Figure 64:** SERR for mode I fracture of the inner crack tip of TE disbond starting positions (5 – 40 m), showing convergence of result with respect to grid size.

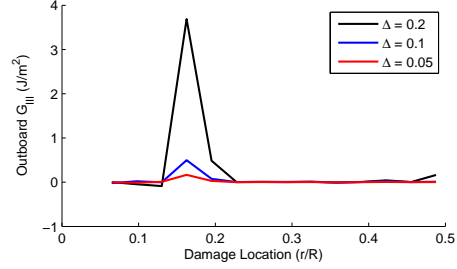


**Figure 65:** SERR for mode I fracture of the outer crack tip of TE disbond starting positions (5 – 40 m), showing convergence of result with respect to grid size.

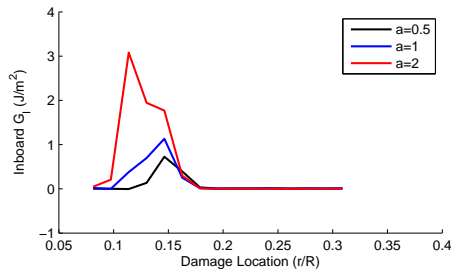


**Figure 66:** SERR for mode I fracture of the inner crack tip of TE disbond starting positions (5 – 40 m) and crack lengths (0.5 – 2 m), normal operation, rated windspeed.

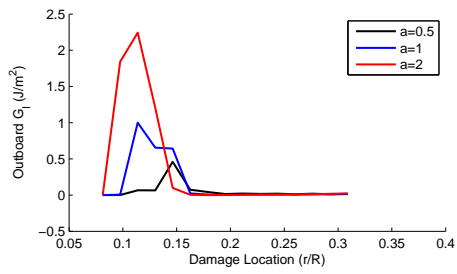


**Figure 67:** SERR for mode I fracture of the outer crack tip of TE disbond starting positions (5 – 40 m) and crack lengths (0.5 – 2 m), normal operation, rated windspeed.

occurs outboard of 15 m the SERR values are low, so it is reasonable to assume that with additional reduction of SERR through derating it would be possible to operate the turbine without further damaging the turbine. Damage to the shear web in the inboard region (0-15 m) was also determined to be critical, so that if SHM detects any type of damage within this region then operating the turbine with a derating strategy may lead to damage growth and increased damage severity. If SHM detects a skin bond line failure occurring outboard of 15 m, then a derating strategy can be used to gain additional revenue from the turbine. Derating would be a viable option if any type of damage is detected within the 15-25 m region, as both the skin and shear web bond line failures have low SERRs in this portion of the blade. Outside of 25 m, a shear web disbond may preclude the use of derating strategies due to the moderate  $G_{II}$  values or may necessitate low derating levels to ensure that damage does not worsen. Because the trends in terms of damage onset location are similar for each shear web, especially outside of 25 m, then the SHM system needs to only identify the location of the shear web disbond, and not which shear web bond line actually failed.

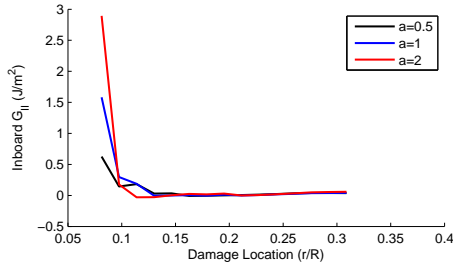


**Figure 68:** SERR for mode II fracture of the inner crack tip of TE disbond starting positions (5 – 40 m) and crack lengths (0.5 – 2 m), normal operation, rated windspeed.

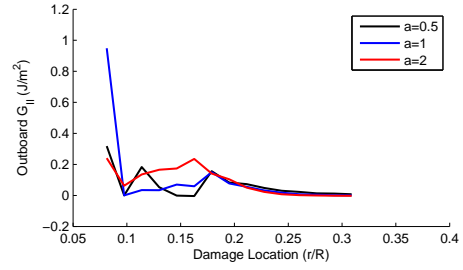


**Figure 69:** SERR for mode II fracture of the outer crack tip of TE disbond starting positions (5 – 40 m) and crack lengths (0.5 – 2 m), normal operation, rated windspeed.

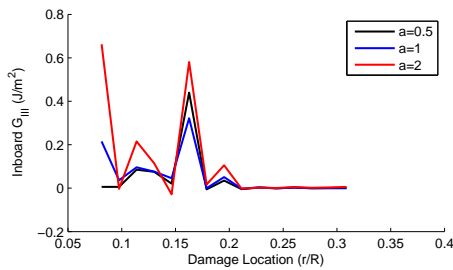


**Figure 70:** SERR for mode III fracture of the inner crack tip of TE disbond starting positions (5 – 40 m) and crack lengths (0.5 – 2 m), normal operation, rated windspeed.

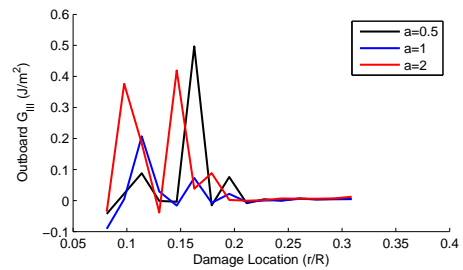


**Figure 71:** SERR for mode III fracture of the outer crack tip of TE disbond starting positions (5 – 40 m) and crack lengths (0.5 – 2 m), normal operation, rated windspeed.

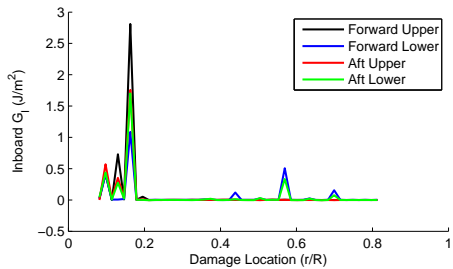


**Figure 72:** SERR for mode I fracture of the inner crack tip of TE disbond starting positions (5 – 40 m) and crack length of 0.25 m, normal operation, rated windspeed.

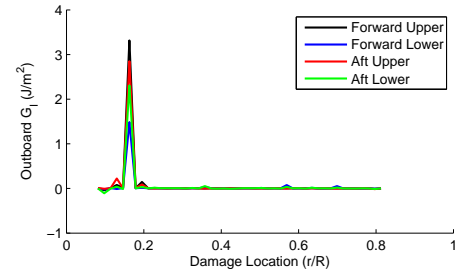


**Figure 73:** SERR for mode I fracture of outer crack tip of TE disbond starting positions (5 – 40 m) and crack length of 0.25 m, normal operation, rated windspeed.

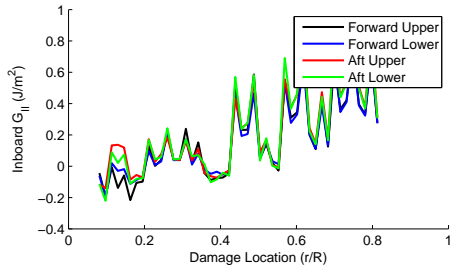


**Figure 74:** SERR for mode II fracture of the inner crack tip of TE disbond starting positions (5 – 40 m) and crack length of 0.25 m, normal operation, rated windspeed.

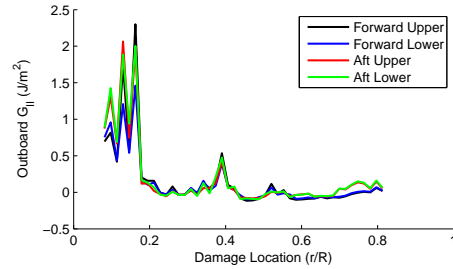


**Figure 75:** SERR for mode II fracture of the outer crack tip of TE disbond starting positions (5 – 40 m) and crack length of 0.25 m, normal operation, rated windspeed.

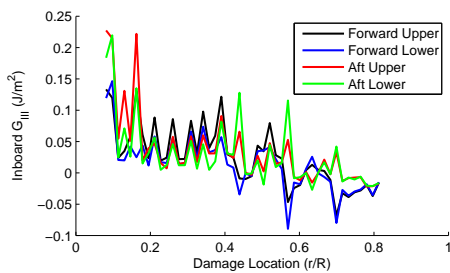


**Figure 76:** SERR for mode III fracture of the inner crack tip of TE disbond starting positions (5 – 40 m) and crack length of 0.25 m, normal operation, rated windspeed.

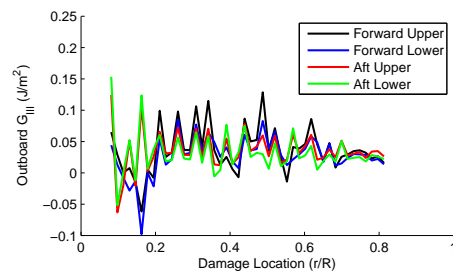


**Figure 77:** SERR for mode III fracture of the outer crack tip of TE disbond starting positions (5 – 40 m) and crack length of 0.25 m, normal operation, rated windspeed.

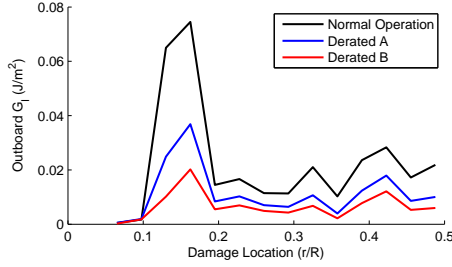


**Figure 78:** SERR for mode I fracture of the inner crack tip of TE disbond starting positions (5 – 40 m) and crack length of 0.5 m, rated windspeed, derated operation.

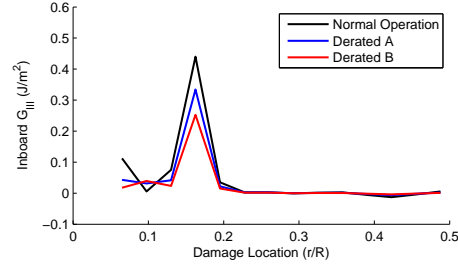


**Figure 79:** SERR for mode III fracture of the inner crack tip of TE disbond starting positions (5 – 40 m) and crack length of 0.5 m, rated windspeed, derated operation.

### 5.5 SERR Calculations Under Derated Operation

The loading at the rated windspeed during derated operation was calculated using WT\_Perf and again mapped to the ANSYS model via nodal point loads. Figures 78 and 79 show selected SERR results for a trailing-edge bond line failure under these derating strategies, at the rated wind speed. These figures demonstrate that the derated values followed trends similar to those under normal operation but with reduced magnitude. This was true for each of the outputs shown in the previous section. For  $G_I$ , the calculated SERRs were reduced by around a factor of 7 by the derating process, and the SERR values for  $G_{II}$  and  $G_{III}$  were reduced by factors of around 5 by the derating process for this wind speed.

The effect of these strategies in reducing the SERRs over the full range of wind speeds was also evaluated. The criticality analysis in Section 5.4 identified the 6 m and 8 m locations as areas of interest. Therefore, these areas were analyzed for  $G_I$  and  $G_{III}$  under the derating strategies “A” and “B.” Figure 80 and 81 show how the SERRs at the areas of interest change with windspeed under normal and derated operation. These figures show a behavior similar to the thrust/moment vs. windspeed behavior (Fig. 84). The SERRs were then summed using a probability-weighted sum (similar to the way AEP is calculated), producing a weighted average SERR for each operating strategy. The Rayleigh windspeed distribution with an average windspeed of 10 m/s was used. This allowed calculation of an effective reduction in SERR due to the derating, which is shown for the 8 m disbond location in Table 28. These effective reductions could be thought of an effective decrease in damage growth rate while operating under the derated strategy. These predictions will then be used to design a more comprehensive operations strategy to maximize power output while also maintaining blade reliability.

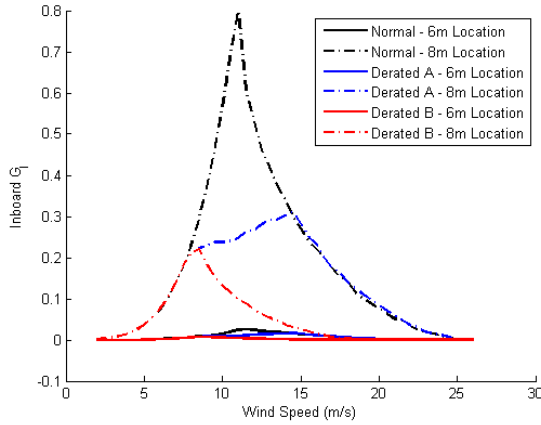


**Figure 80:**  $G_I$  with respect to windspeed for NREL 5 MW turbine in normal/derated operation.

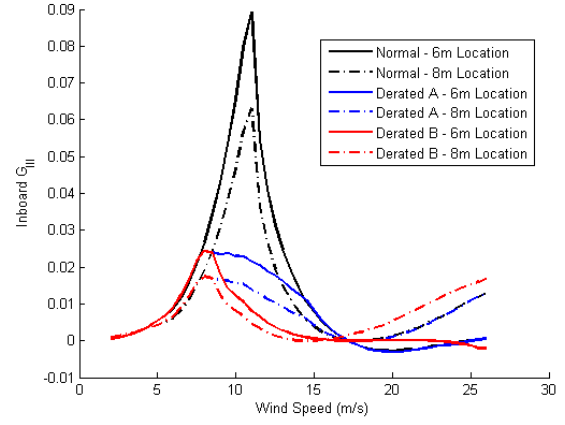


**Figure 81:**  $G_{III}$  with respect to windspeed for NREL 5 MW turbine in normal/derated operation.

**Table 28:** Reduction in averaged SERRs for 8 m disbond location under 50% derated operation, weighted by a Rayleigh wind distribution with average windspeed of 10 m/s.

Mean Wind Speed (m/s)	Derating Strategy	Reduction in $G_I$
7 m/s (Calm)	A	36.8%
	B	58.9%
10 m/s (Mean)	A	35.9%
	B	70.1%
16 m/s (Windy)	A	31.0%
	B	76.9%

## 5.6 Buckling Capacity of Damaged Blades

Buckling capacity is a primary design driver for large WT blades, as buckling of shear web or upper skin would likely lead to drastic blade damage. The most critical design load case for buckling is the parked extreme wind gust case, where a large gust (50-year occurrence level). It is assumed that there will be some meteorological warning for such a gust so that operators can park the turbine, so the design requirements state the 50-year gust analysis must be conducted in the parked (braked) state. Unfortunately this leaves little room for the use of derating or other operation strategies to mitigate the early onset of buckling. Bond line failure tends to reduce the buckling capacity of the WT blade, but not by affecting the primary buckling mode. Instead, a secondary buckling mode is typically introduced that may have a higher buckling factor at low disbond lengths but will have a lower buckling factor at a certain critical disbond length. WT blades are often designed to just satisfy design buckling margins, so the critical disbond length for this study was defined as the length at which the lowest frequency buckling mode changes from the primary (healthy) buckling mode to the secondary buckling mode associated with the bond line failure. There is no opportunity



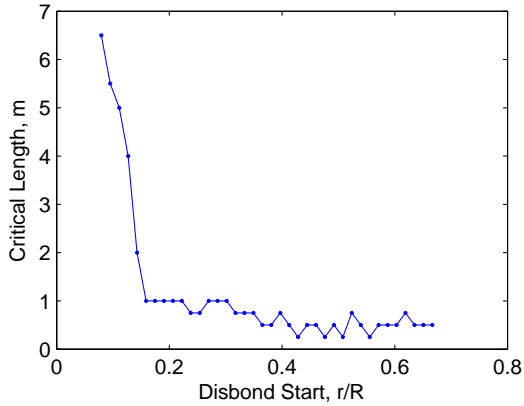


**Figure 82:** Minimum disbond length of trailing-edge disbond to reduce buckling capacity vs. starting position of disbond.

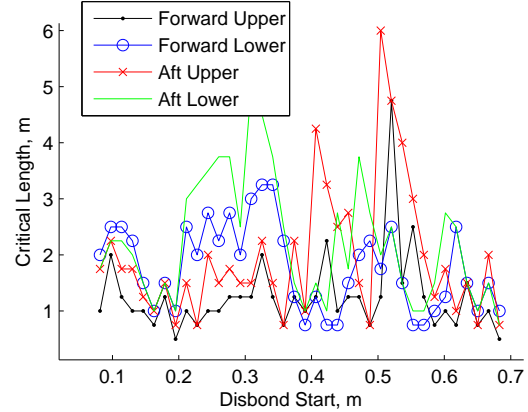


**Figure 83:** Minimum disbond length of shear web disbond to reduce buckling capacity vs. starting position of disbond.

for derating to prevent against buckling failure in the parked state, so this critical bond line length can be seen as an upper allowable limit, after which blade replacement becomes a priority to avoid early onset of buckling.

The primary buckling mode shape for the healthy blade involves a buckling of the skin panel at the location where the shear web has terminated. When a bond line failure becomes long enough, local buckling in the region of the damage will occur at a lower load factor than the primary buckling mode. A comprehensive investigation into the linear and nonlinear buckling performance of the healthy blade as well as blades with bond line failures has been carried out by Griffith et al. [44]. For this study, the performance of the damaged blade ANSYS models in terms of buckling was evaluated to determine the minimum disbond length to influence the primary buckling mode. The results of these analyses in terms of critical disbond length for different disbond locations for the TE disbond is shown in Fig. 82 and the results for the shear web disbond is given in Fig. 83. The TE disbond critical buckling length is very low when the disbond is close to the original region of large displacements in the large buckling mode. Unfortunately, if the TE disbond is near 30 m the critical disbond length is very small, around 0.5 m for disbands between 25-40 m. The shear web critical disbond length analysis indicates that bond line failures are generally the most severe in terms of buckling in the forward upper shear web bond line, but there are many areas where the critical bond length reaches 2 m or more.

## 5.7 Conclusions

Offshore WT accessibility is a major barrier for acceptance of offshore wind, because it leads to long down times for damaged turbines and expensive maintenance excursions. Load-mitigating control

strategies such as derating can be used to safely utilize damaged turbines as an alternative to shut-down. Derating can also be used to delay maintenance for turbines for accessibility reasons or in the context of an advanced maintenance planning strategy, while simultaneously maximizing AEP. In this way, applying the new O&M strategies proposed in this work will reduce the cost of energy of offshore wind both by increasing AEP and by reducing O&M and blade replacement costs.

A framework has been established for high fidelity analysis of damage severity and demonstrated for the common damage type of bond line failure. These efforts demonstrated that the most critical area in terms of damage onset is in the vicinity of the 10 m span location, which happens to be where the cross-sectional shape transitions from circular to airfoil-shaped. Therefore, this transition point is a key area of interest in damage tolerance analysis or designs that account for damage tolerance. If this transition area can be smoothed out or reinforced, it may produce a more damage tolerant blade. For the case of a shear web disbond, if the damage occurs in the 25-45m region may be critical, with large values of  $G_{II}$ . In this research, the area of stress concentration in the baseline (healthy) bond line also had the highest SERR values. This implies that designing the blade considering only healthy bond line stress results may be a valid strategy for producing damage tolerant designs.

The qualitative information gleaned from this chapter has provided a starting point for developing O&M or design strategies for mitigating blade damage. To apply this information quantitatively, that is to calculate the associated growth rates and therefore the remaining fatigue life of damaged blades, material testing would be required to link the SERR values  $G_I$ ,  $G_{II}$ , and  $G_{III}$  with damage growth rates. The form of the damage growth rate model will also answer some of the questions raised so far about what levels of  $G_I$ ,  $G_{II}$ , or  $G_{III}$  are acceptable for safe operation of damaged WT blades. Material testing of adhesive failure was not within the scope of the current work but is recommended for future study.

## CHAPTER VI

### SMART LOADS MANAGEMENT FOR DAMAGED WT BLADES

One of the main goals of this project is to produce smart loads management strategies intended to enable continued operation of WT blades. These strategies will utilize the existing variable-speed, variable-pitch control systems of modern WTs, extend the use of pitch control to individual blades, and investigate novel control strategies such as trailing edge flaps or devices to mitigate loads.

If the modification of the control system involves intentionally limiting the power output of the turbine, then the strategy is referred to as a derating strategy. These strategies are of interest because they can be implemented using only the available WT controls. The simplest derating strategy, simply lowering the power rating of the turbine, has been investigated in static analyses and has been shown to effectively lower strain energy release rates. However, dynamic analysis is still necessary to show how the strategy will perform in turbulent conditions or during dynamic wind events. Several different derating strategies will be compared based on their performance in terms of the overall wind turbine performance as well as the capability to mitigate local damage effects.

Once the control design is complete, the resulting control system designs will then be analyzed with the multiscale analysis technique to quantify their effectiveness to mitigate damage. That is, the loading from steady or dynamic simulations with the new control system active from FAST/AeroDyn will be transferred to the ANSYS shell model generated by NuMAD, and the damaged shell analysis procedure will be used to calculate the reduction in SERRs, and therefore the reduction of growth rates, of the damage.

#### ***6.1 Economic Incentive to Derating***

High wind and sea states can prevent access to offshore turbines in some locations for as long as one to two months, and offshore wind farm operators often find difficulty obtaining offshore cranes appropriate for performing WT maintenance [137]. According to a report on the Nysted wind farm off the coast of Denmark [139], an offshore WT may be inaccessible at wave heights higher than 1.2 m. A report on offshore wind accessibility by Bierbooms et al. [6] gives an upper limit of 2 m wave height and 12 m/s average wind speed using offshore access systems specially designed for offshore turbines, and shows that wave height and wind speed are often statistically correlated, with wave heights of 3 m occurring at wind speeds higher than 12 m/s. A British study of meteorological data

showed correlated wind speeds and wave heights and monthly average wave heights exceeding 2 m during windy seasons; for example Fig. 86 shows the monthly variation of wave heights at one site. A report by Christensen and Giebel [25] notes that adverse weather conditions lead to increased time requirements to perform maintenance tasks, especially if small boats are used for maintenance instead of medium-sized boats equipped with advanced offshore access systems.

These accessibility considerations imply that one or two weeks of down time should be expected for maintenance purposes, and sometimes there may be a short period (around two weeks) between when maintenance is detected and there is an opportunity for access. This delay between damage detection and the opportunity for maintenance access is often increased in the presence of high wind speed conditions. Therefore, derating is proposed to utilize the turbine at a reduced level during this delay. Another way derating can be used to increase the power production of one turbine is when there is a monthly variation in average wind speed. In this case, derating can be used to operate the turbine through the windy season, where profits are highest and maintenance is most difficult, and delay maintenance until the calm season. This would also have a secondary farm-level reduction in O&M costs if the maintenance delay allows multiple turbines to be serviced simultaneously.

The following sections provide scenarios where derating is used to increase the revenue of damaged turbines. They are meant as demonstrative examples to show the potential economic benefits of derating, so a conservative estimate of 10 ¢/kWh was used to convert energy output increase to dollar values. A more realistic price for energy for offshore wind may be as high as 25 ¢/kWh; the higher cost of energy would only increase the possible economic benefits of derating in terms of dollar value.

### **6.1.1 Derating as an Alternative to Shutdown**

The simplest example of a load-reducing control method is to utilize the available pitch-control system to limit the blade RPM and produce power at a lower level [97, 38]. The baseline control system for the NREL 5 MW baseline design is a variable-speed, variable-pitch controller where the rotor RPM is controlled by a torque controller at wind speeds below the rated wind speed, and at wind speeds above the rated speed the generator is at its maximum design torque and the pitch controller is used to control rotor RPM. For this research, the derating was mainly accomplished by using the pitch controller to control the rotor RPM (and therefore the loads and power production). The advantage to using a simple “derating” method is that it would only involve a change in the software of currently operating offshore turbine control systems, and therefore could be easily retrofitted into pre-existing designs.

Two different ways to reduce service bending moments by derating were evaluated: limiting the value of the bending moment or thrust without limiting the power rating (derating strategy “A”), or limiting the power rating (derating strategy “B”). Figure 84 shows an example of the two derating strategies for the case of limiting the bending moment to 50% of its maximum value. The NREL 5 MW baseline design is used for the operations and control strategy evaluations as a representative of “current” offshore blade technology. To demonstrate one potential use of derating, consider the case of an offshore turbine where there is a two-week delay between when the damage is detected on the turbine and the turbine becomes accessible for maintenance. The total annual income of the NREL 5 MW baseline turbine for a possible Alaska location is shown in Table 29, using wind data from Pryor et al. [113]. The location was chosen as a realistic representative site with an average windspeed of  $\approx 10$  m/s. The additional revenue for operating at a derated level for two weeks instead of shutting down is also given in Table 29. There is often a month-to-month variation in the average wind speed, as shown in Figure 85 for a Baltic offshore site, and Table 30 shows how the additional revenue could vary.

### 6.1.2 Derating to Delay Maintenance

There is also the potential of using derating to increase the annual revenue of damaged turbines if there is a large variation in wind speed at a given site annually, such as in Fig. 85. In this case, it could be economically advantageous to derate the turbine and operate through windy seasons while performing maintenance during calm seasons. This also aligns with accessibility concerns with offshore turbines associated with high sea states, which are likely to occur in windy seasons. Using a derating strategy to delay maintenance until calmer time periods would also allow increased use of small boats for access and a lowered increase in maintenance time due to adverse weather. The opportunity for using derating to delay maintenance to damaged turbine was assessed very simply by varying the month in which the damage occurs (damage onset month) and finding the duration in months of derating that optimizes yearly annual AEP. A cost of energy of 10 ¢/kWh was used to convert the annual AEP to annual income for the damaged turbine, and the benefit of using the derating strategy was determined by subtracting the annual income that would result from immediate down-time and repair of the turbine. A visual example of such a calculation is given in Figs. 87-88 showing how the annual profit from a damaged turbine may vary with different damage onset months and derating durations, if derating strategy A is used at a 90% level and considering a downtime duration of 2 weeks. Figure 87 shows a 3D view of the surface plot with the annual energy profits from the turbine shown, while Fig. 88 shows top view of the surface for ease of

visualization. This sample calculation demonstrates the concept of delaying the maintenance until the calm months as the peak of the derating benefits surface aligns with performing the maintenance during months 6 – 8, the calmest months. The optimal number of derating months is dependent upon the level of derating and the downtime duration that is required for the turbine repair, and is plotted as a function of damage onset month in Fig. 89. Figure 89 should be interpreted as the optimal number of months to delay maintenance by using derating, depending on when the damage occurs (damage onset month), what derating strategy is used and how much down time will be required for maintenance. Figure 89 shows that potential for increasing revenue by using derating to delay maintenance becomes viable when the derating level is not too low or if 2 weeks or more of downtime are required for blade maintenance, but that derating strategy A is required. Strategy B can still be used to offset losses (compared with shutdown) if the turbine is not accessible for maintenance.

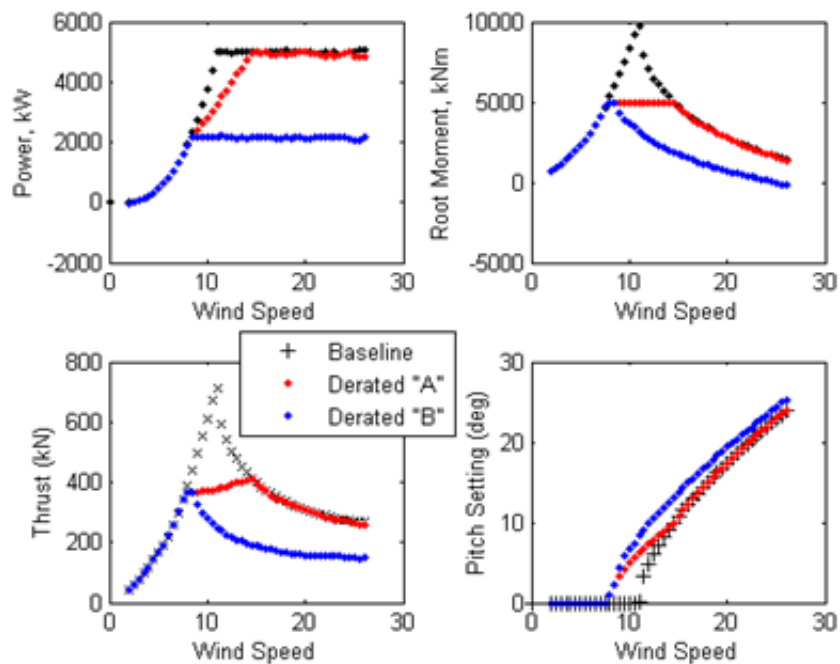


**Figure 84:** Power production, root bending moment, rotor thrust predictions for two derating strategies “A” and “B” and derating level of 50%. The derating strategies are achieved by modifying the pitch control settings as shown in lower-right.

## 6.2 Control Design of WT Blades Using MBC

The control design architecture recommended by Bossanyi [13, 14, 15, 16] decouples the generator speed/torque and collective pitch control from the cyclic or periodic pitch controls. From this

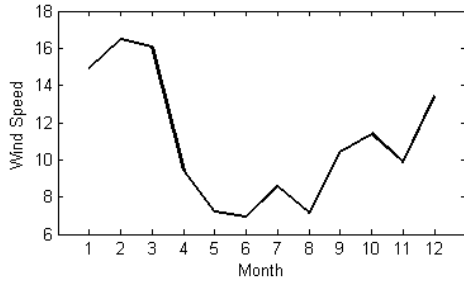


**Figure 85:** Monthly variation in windspeed for a Baltic offshore site with a windspeed average of 11 m/s [103].

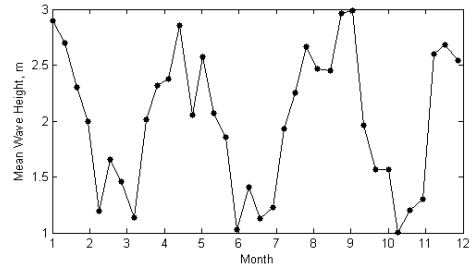


**Figure 86:** Monthly variation in wave height for a British Isles offshore site.

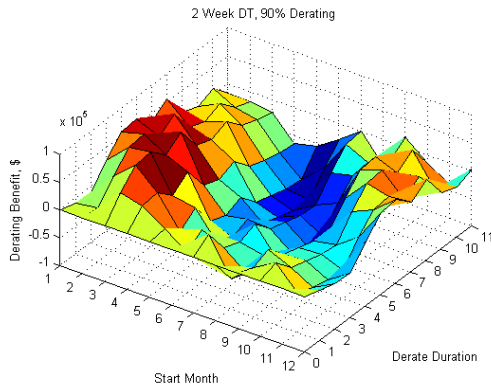


**Figure 87:** 3D surface plot of potential benefits of using a derating strategy to delay maintenance for the NREL 5 MW turbine, compared with immediate repair.

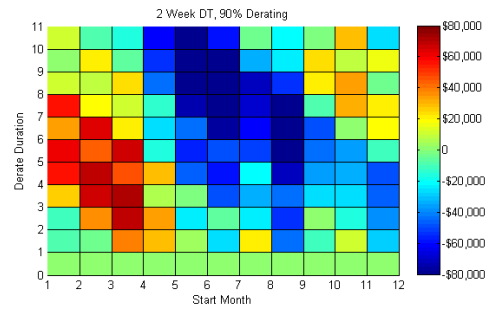


**Figure 88:** 2D contour plot version of Figure 87, showing benefit of using derating strategy (or cost of delaying maintenance using derating strategy if negative).

**Table 29:** Possible revenues (using 10 ¢/kWh) for operating at derated level for two weeks instead of shutdown.

	Alaska Site (9.9 m/s)
Annual Revenue	\$2,420,000
Derating Level	Additional Revenue
75% (A)	+\$108,000
75% (B)	+\$81,600
50% (A)	+\$96,000
50% (B)	+\$64,000
25% (A)	+\$60,400
25% (B)	+\$22,900

**Table 30:** Variations in possible revenue increases (using 10 ¢/kWh) due to monthly windspeed variation, when derating for two weeks instead of shutdown.

Level	Calm (7 m/s)	Windy (16.5 m/s)
75% (A)	+\$63,800	+\$140,000
75% (B)	+\$53,400	+\$99,100
50% (A)	+\$55,800	+\$131,000
50% (B)	+\$44,500	+\$73,800
25% (A)	+\$35,300	+\$96,800
25% (B)	+\$19,200	+\$23,900

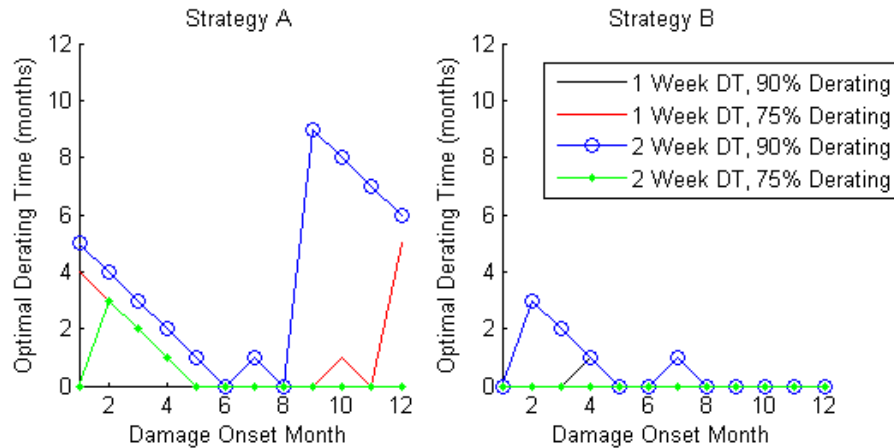


**Figure 89:** Optimal maintenance delay (using derating) in months for derating Strategy A (left) and Strategy B (right), for different derating levels and downtime (DT) durations, for an NREL 5 MW turbine at a Baltic offshore site.

point on in this work  $\beta$  refers to a WT blade pitch angle. Bossanyi recommends using the  $d - q$  transformation, in which signals from the three blades are transformed into a mean value and zero-mean differential values (“direct” and “quadrature” axes). These transformed signals are then used by the controller to provide differential demands for the three blades. The advantage of this method is that the axes can be treated as almost independent, so that a simple conventional controller can be used for the generator speed / torque collective pitch control and another simple conventional controller can be used for the load mitigation differential pitch controls along each axis. The transformation



is identical to the multi-blade coordinate (MBC) transform, and the form of the transformation and its reverse are given below:

$$\begin{Bmatrix} \beta_0 \\ \beta_d \\ \beta_q \end{Bmatrix} = \frac{2}{3} \begin{bmatrix} 1/2 & 1/2 & 1/2 \\ \cos(\theta) & \cos(\theta + 2\pi/3) & \cos(\theta + 4\pi/3) \\ \sin(\theta) & \sin(\theta + 2\pi/3) & \sin(\theta + 4\pi/3) \end{bmatrix} \begin{Bmatrix} \beta_1 \\ \beta_2 \\ \beta_3 \end{Bmatrix} \quad (104)$$

$$\begin{Bmatrix} \beta_1 \\ \beta_2 \\ \beta_3 \end{Bmatrix} = \begin{bmatrix} 1 & \cos(\theta) & \sin(\theta) \\ 1 & \cos(\theta + 2\pi/3) & \sin(\theta + 2\pi/3) \\ 1 & \cos(\theta + 4\pi/3) & \sin(\theta + 4\pi/3) \end{bmatrix} \begin{Bmatrix} \beta_0 \\ \beta_d \\ \beta_q \end{Bmatrix} \quad (105)$$

This transformation allows the separation of the collective ( $\beta_0$ , etc.) and cyclic ( $\beta_{1c}$ ,  $\beta_{1s}$ ) control systems. The variable-speed, variable-pitch control architecture that is common to offshore WTs will be used as a starting point for the collective portion of the control design. This collective pitch controller will then be enhanced with load-mitigating capabilities, and then a cyclic pitch control will be added to further reduce blade loads.

### 6.3 Variable-speed, Variable-pitch Controller

The controller architecture that is commonly used for large offshore WTs is referred to as variable-speed, variable-pitch (VSVP). One VSVP strategy is given in the definition of the NREL 5MW baseline turbine [63] and is based on “Bladed,” a commercial WT analysis tool. In this strategy, the pitch control is used to maintain a constant generator speed, and the torque control is scheduled based on the optimum power production profile and the current generator speed. The pitch control is saturated at  $0^\circ$  pitch so that the pitch controller is only used when the generator speed is higher than the maximum speed, so at generator speeds below this speed the torque control is used to govern the generator speed. The VSVP controller for the NREL 5MW baseline turbine has been implemented in Simulink. Figure 90 shows how the controller is integrated with the FAST Simulink model, and also demonstrates the separation of the controller into collective and cyclic portions. Figure 91 shows the overall architecture of the “Bladed-style” controller. The generator speed is first filtered with a low-pass filter before it is used in the torque or pitch controllers as shown in Figure 94. The generator torque controller is designed to follow a predefined piecewise nonlinear function that determines the applied torque based on the current generator speed. The pitch controller uses PI feedback control to limit the generator speed to its maximum rated speed, and is only active when the generator speed is higher than its maximum rated value (because when it is below that speed, the torque control is active). The pitch controller uses gain scheduling to account for the fact

that pitch changes near  $0^\circ$  not as effective in affecting the total power ( $dP/d\beta$ ) as pitch inputs near the maximum blade pitch angle; the gain scheduling is based on the collective pitch angle and the formula is:

$$GK = \frac{1}{1 + \frac{\beta_0}{\beta_r}} \quad (106)$$

Here,  $\beta_k$  is the pitch angle at which the effectiveness  $dP/d\beta$  is doubled. Both pitch and torque controllers also utilize a sample rate limiter to account for different sampling times of the pitch and torque controllers in case they are larger than the analysis timestep.

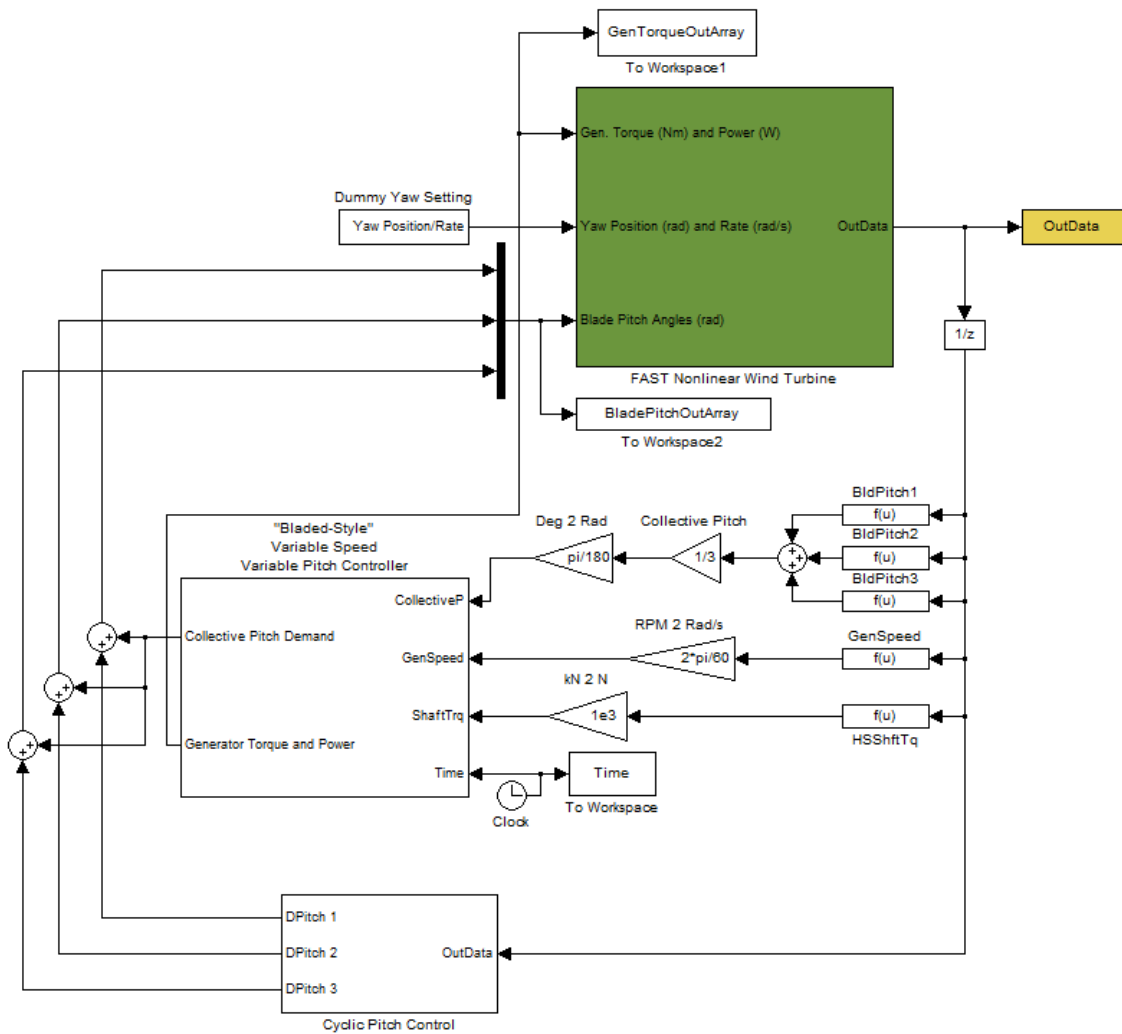


**Figure 90:** “Bladed-style” VSVP controller integrated with FAST in Simulink.

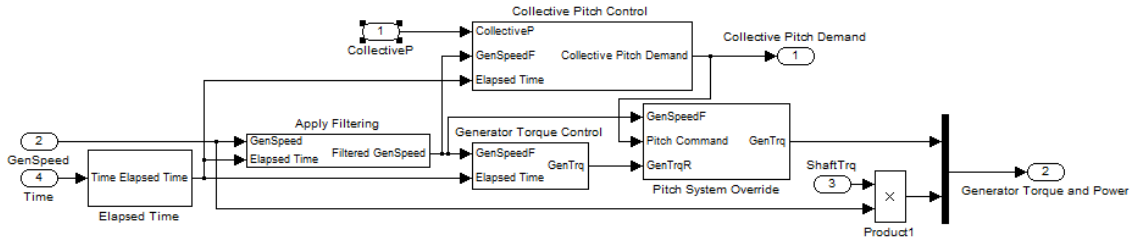


Figure 91: “Bladed-style” VSVP controller showing generator torque controller and pitch controller.

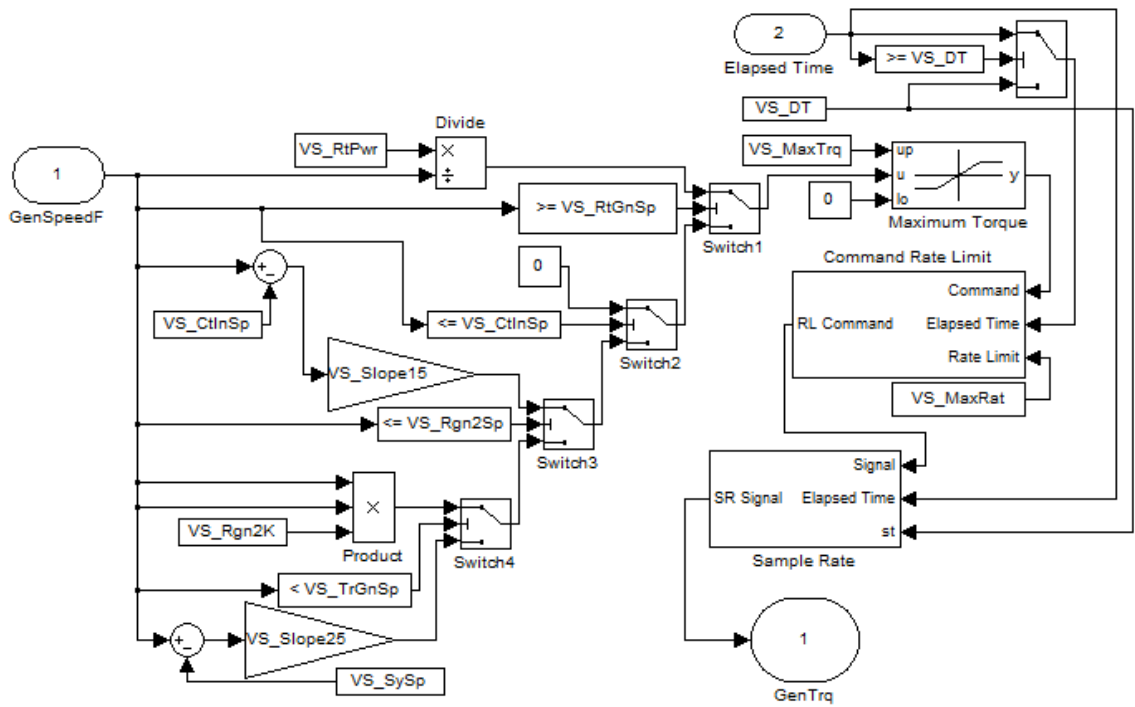


Figure 92: “Bladed-style” VSVP controller showing generator torque controller.

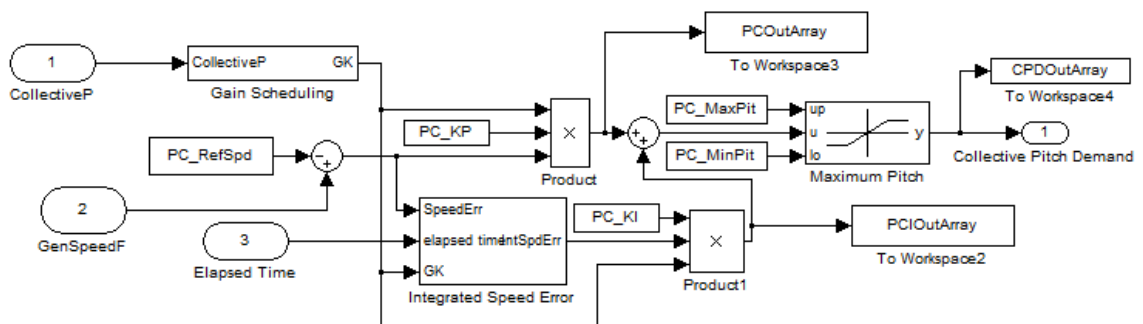
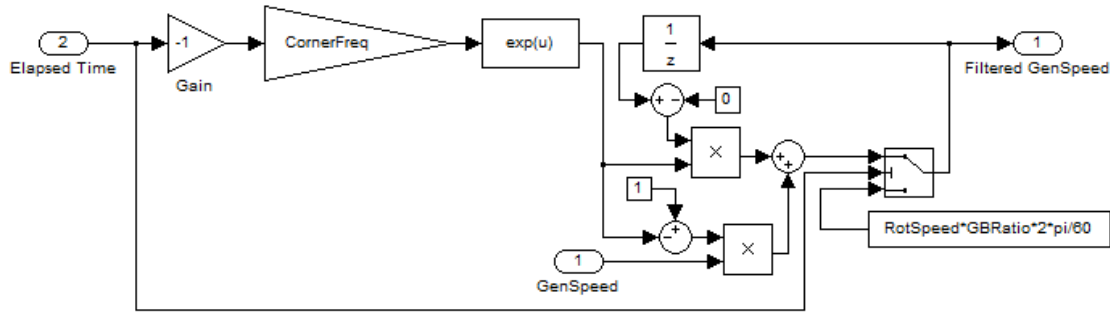


Figure 93: “Bladed-style” VSVP controller showing pitch controller.



**Figure 94:** Low-pass filter applied to high-speed generator shaft speed in “Bladed-style” VSVP controller.

## 6.4 Derating

The simplest form of derating is accomplished by changing the input parameters to the VS-VP controller described in the above section. To achieve the derating strategy “B” which lowers the maximum power production of the turbine, one can adjust the power rating and maximum generator speed for the pitch controller to effectively limit the power production.

The performance of the derating controller at a given power level decrease will depend on the choice of maximum generated speed. If one lowers the power rating but not the maximum generator speed, this will lead to a decrease in shaft torque to meet the new power rating. The pitch control, however, is designed to operate when the shaft torque is at its rated level: in normal operation, above rated wind speed the shaft torque is held at its rated level while the pitch control is used to maintain a constant rotor speed. For example, if the power rating is reduced but the maximum generator speed is not lowered at all, at rated wind speed the generator torque will be below its rated level. The reduced torque then leads to an increase in rotor speed, and the pitch control system will attempt to maintain the rotor speed by commanding a non-zero quasi-steady pitch angle. This scenario often leads to an undesired increase of rotor/generator speed and can violate maximum generator speed constraints. For the NREL 5MW baseline design, the maximum generator speed is  $\approx 1150$  RPM. To demonstrate the performance of the derating controller as well as illustrate the advantages of reducing the maximum generator speed, Figs. 95 – 100 show the quasi-steady performance of several potential derating controllers at the wind speed of 11 m/s and a derating level of 80%. In these Figures, the number of the controller (100, 110, or 120) refers to the RPM of the generator in rad/s, where 120 rad/s is the baseline maximum generator speed. These controllers all produce the same power ( $\approx 4000$  kW) at the wind speed of 11 m/s, but each has a different transient

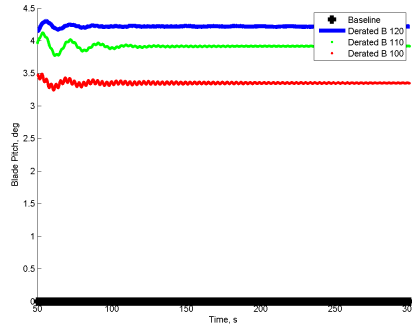


**Figure 95:** Pitch controls for quasi-steady operation at 11 m/s wind speed for each derating strategy.

performance, quasi-steady pitch command, and of course different generator speed and torques quasi-steady command levels. Figure 95 shows that the transient performance of the controllers are comparable, with the lowest generator speed having the worst transient response, but that the lower generator speed produces a lower quasi-steady pitch command as predicted. Figures 98 – 100 show slightly reduced flapwise moment but increases to collective twisting and edgewise moments.

The effect of the derating system on the performance of the WT can also be measured with the SIMULINK model by subjecting it to design load cases from the International Electrotechnical Commission (IEC) [27]. The design load case (DLC) corresponding to the extreme coherent gust with direction change (ECD) has been cited by many authors [120, 90, 66, 117, 45] as the design driver for blade deflection and loads. Therefore, the comparison of the derating controllers was also carried out for this DLC. The results for ECD analysis for 80% derating at 11 m/s wind speed is then shown in Figs. 101 – 106. These show similar performance with each controller, and again Fig. 101 shows a slightly worse transient response in terms of pitch rate demands and settling time with the reduced generator speed controllers. However, Fig. 102 shows that at the reduced speed the dynamic deflections due to the wind gust are reduced.

### ***6.5 Load-mitigating Control Design***

Where derating utilizes the available pitch and speed controls, other load-mitigating control strategies can be devised by adding cyclic pitch or even full nonlinear control. The methods are based on the ANSYS analysis results for the derating controllers and the assumption that reducing cyclic variations of blade loads as well as reducing the collective portion will be effective to mitigate damage growth.

The blade loads can be reduced more directly by feeding back the blade loads to the pitch mechanism. To achieve derating strategy “A,” which uses the pitch mechanism to limit blade root

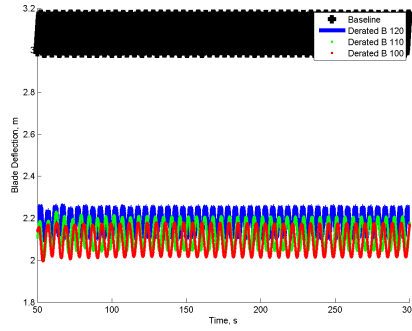


**Figure 96:** Blade out-of-plane deflections for derating controllers for quasi-steady operation at 11 m/s wind speed.

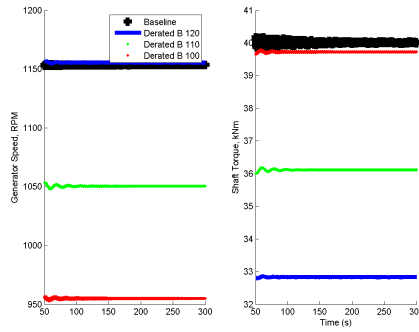


**Figure 97:** Generator speed and torque performance of derating controllers for quasi-steady operation at 11 m/s wind speed.

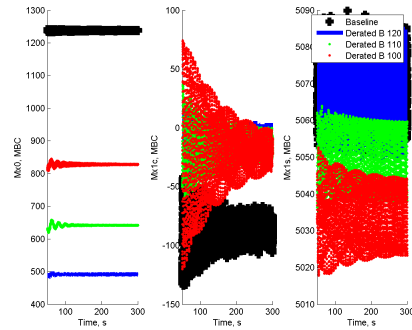


**Figure 98:** Twisting moment ( $M_x$ ) signals from each blade transformed into MBC coordinates for derating controllers for quasi-steady operation at 11 m/s wind speed.

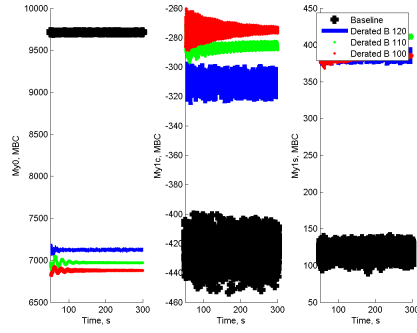


**Figure 99:** Flapwise bending moment ( $M_y$ ) signals from each blade transformed into MBC coordinates for derating controllers for quasi-steady operation at 11 m/s wind speed.

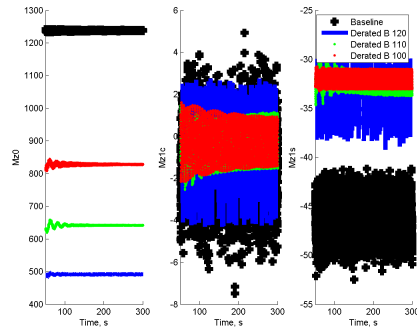


**Figure 100:** Edgewise bending moment ( $M_z$ ) signals from each blade transformed into MBC coordinates for derating controllers for quasi-steady operation at 11 m/s wind speed.

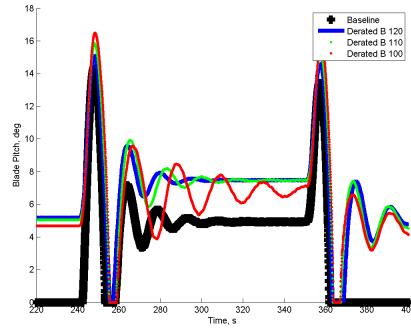


**Figure 101:** Pitch control response for derating controllers during extreme coherent gust with direction change (ECD) load case.

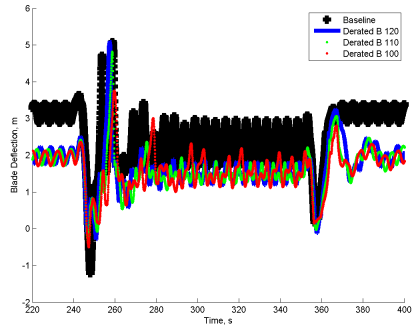


**Figure 102:** Blade deflection signals for derating controllers during extreme coherent gust with direction change (ECD) load case.

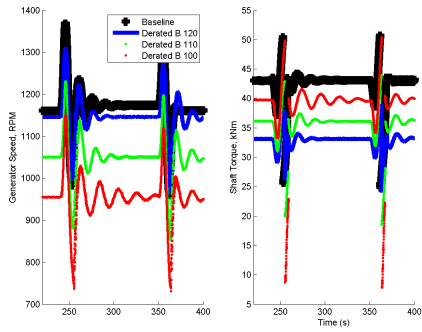


**Figure 103:** Twisting moment ( $M_x$ ) signals from each blade transformed into MBC coordinates for derating controllers during extreme coherent gust with direction change (ECD) load case.

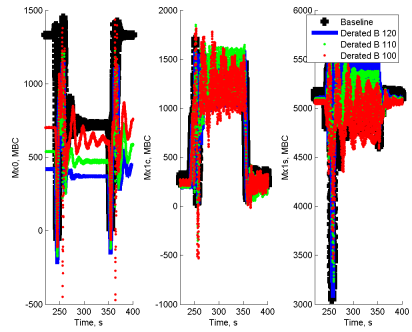


**Figure 104:** Twisting moment ( $M_x$ ) signals from each blade transformed into MBC coordinates for derating controllers during extreme coherent gust with direction change (ECD) load case.



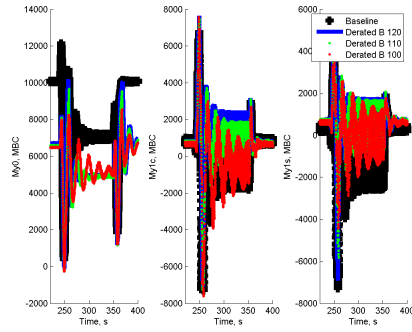


**Figure 105:** Flapwise bending moment ( $M_y$ ) signals from each blade transformed into MBC coordinates for derating controllers during extreme gust with direction change (ECD) load case.

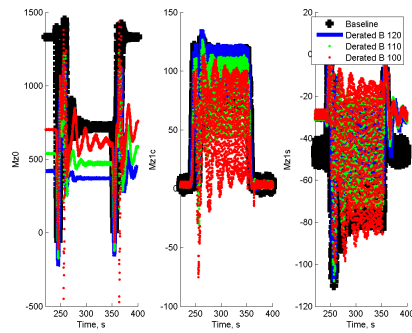


**Figure 106:** Edgewise bending moment ( $M_z$ ) signals from each blade transformed into MBC coordinates for loads management controllers during extreme coherent gust with direction change (ECD) load case.

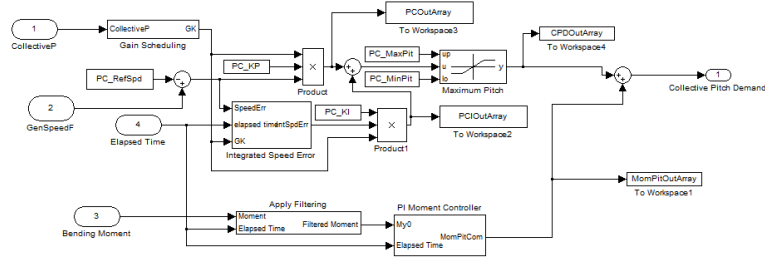


**Figure 107:** Modified collective pitch controller with additional PI controller added to limit collective flap bending moment  $M_{y0}$ .

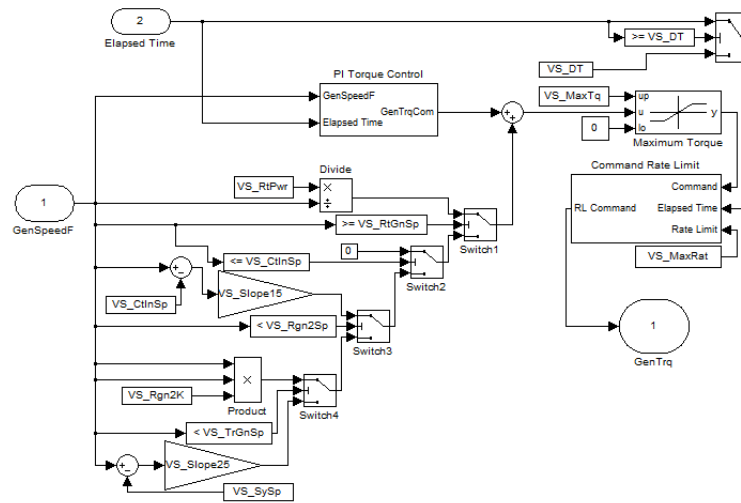


**Figure 108:** Modified generator torque controller with PI controller.

bending moments, the collective portion of the blade flap bending moment  $M_{y0}$  is fed back to the collective pitch mechanism. Then an additional PI controller is added to the pitch control mechanism as is shown in Figure 107.

The strategy of limiting the generator speed to limit the power production can be applied to the torque control, using the torque control to decrease the rotor speed and therefore limit blade loads and power production. One immediately apparent difference between using the torque control to control the generator speed rather than the pitch control is that the torque controller must limit the rotor speed to a lower value to achieve the same reduction in power because of the increase in torque due to the controller itself. Derating with the torque controller was accomplished by adding a torque PI controller to the baseline torque scheduling mechanism as is shown in Figure 108. The form of the PI controller is the same as for the pitch controller shown in Figure 93, but with no gain scheduling applied.

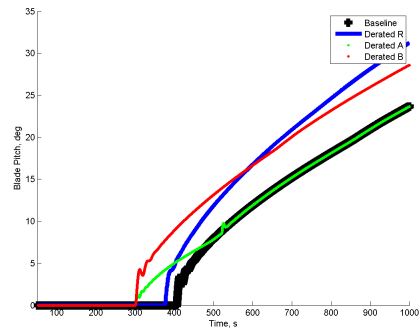


**Figure 109:** Pitch controls for wind sweep load case for each loads management strategy.

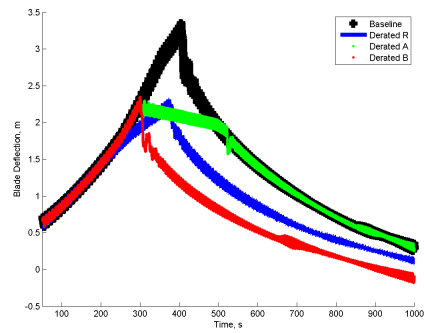


**Figure 110:** Blade out-of-plane deflections for load mitigation controllers during wind sweep load case.

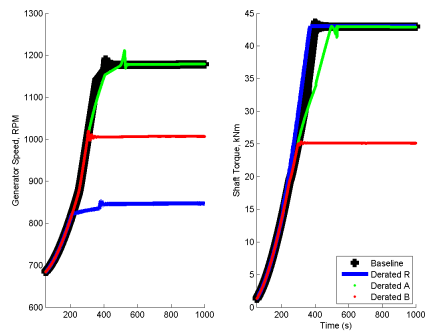


**Figure 111:** Generator speed and torque performance of load management controllers during wind sweep load case.

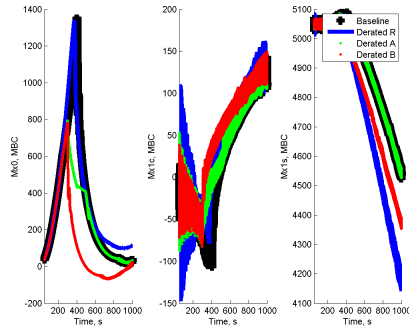


**Figure 112:** Twisting moment ( $M_x$ ) signals from each blade transformed into MBC coordinates for load mitigation controllers during wind speed sweep load case.

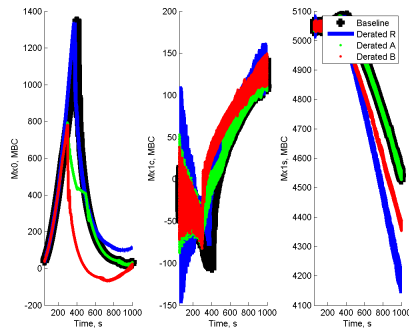


**Figure 113:** Flapwise bending moment ( $M_y$ ) signals from each blade transformed into MBC coordinates for load mitigation controllers during wind speed sweep load case.

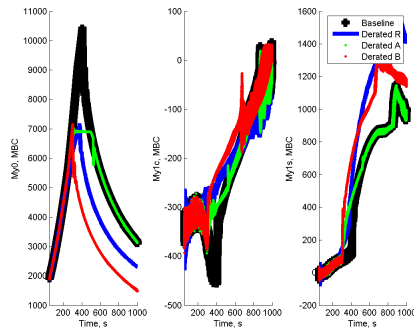


**Figure 114:** Edgewise bending moment ( $M_z$ ) signals from each blade transformed into MBC coordinates for load mitigation controllers during wind speed sweep load case.

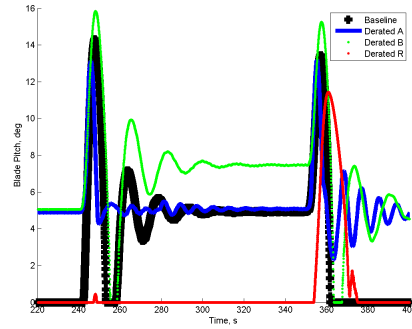


**Figure 115:** Pitch control response for load mitigation controllers during extreme coherent gust with direction change (ECD) load case.

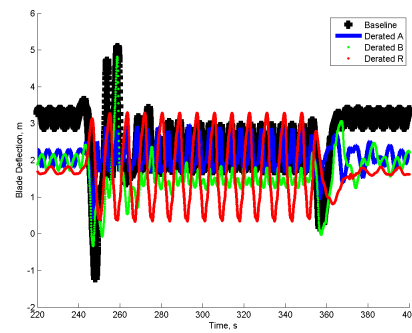


**Figure 116:** Blade deflection signals for load mitigation controllers during extreme coherent gust with direction change (ECD) load case.

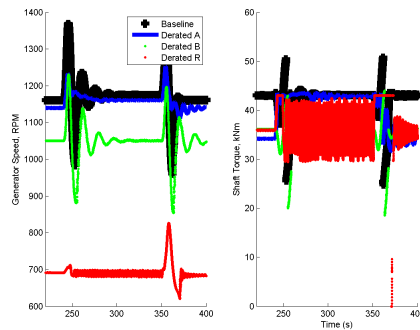


**Figure 117:** Generator speed and torque performance for loads management controllers during extreme coherent gust with direction change (ECD) load case.

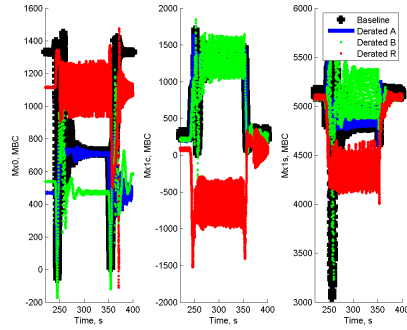


**Figure 118:** Twisting moment ( $M_x$ ) signals from each blade transformed into MBC coordinates for loads management controllers during extreme coherent gust with direction change (ECD) load case.

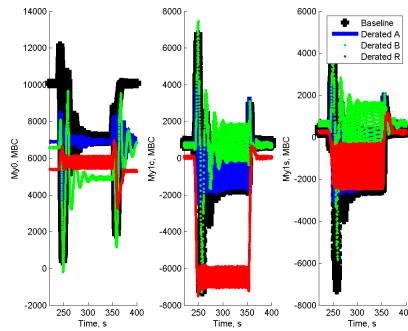


**Figure 119:** Flapwise bending moment ( $M_y$ ) signals from each blade transformed into MBC coordinates for load management controllers during extreme coherent gust with direction change (ECD) load case.

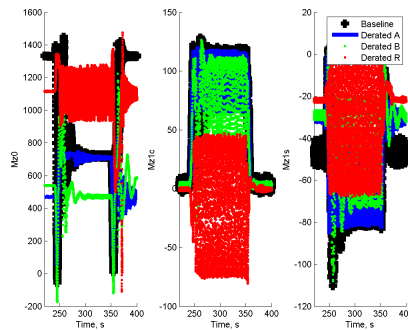


**Figure 120:** Edgewise bending moment ( $M_z$ ) signals from each blade transformed into MBC coordinates for loads management controllers during extreme coherent gust with direction change (ECD) load case.

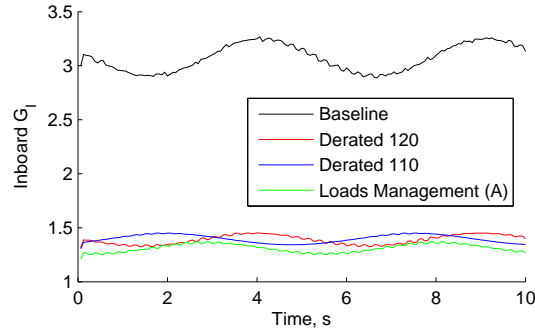


**Figure 121:** SERR results for inboard  $G_T$ , for inboard propagation of trailing-edge disbond from 8 – 8.5 m. Results are from dynamic analysis of 3D finite element model subjected to loads from quasi-steady operation at 11 m/s.

## 6.6 ANSYS Analysis of Damage Mitigation

The success of the load mitigation controllers in terms of steady performance has been demonstrated in Section 5.5. This performance can now be verified in the dynamic case by applying the loads from the FAST/AeroDyn control design evaluation analyses to the 3D damaged blade model for finite element analysis. This was performed for two derated controllers (120 rad/s and 110 rad/s maximum generator speed) as well as for the load mitigation strategy “A” and the baseline design. The trends of the dynamic results followed the trends observed in Section 5.5, however due to a slight difference in loading from FAST/AeroDyn and WT\_Perf, the SERR results reach a different magnitude. Application of the time-averaged or snapshot loads from FAST/AeroDyn, instead of the WT\_Perf loads, resolved this discrepancy. The results of the dynamic analysis can then be interpreted to represent an estimate in the reduction of growth rates due to operation under smart loads management. The maximum SERR values ( $G$ ) as well as the quasi-steady changes in SERR values ( $\Delta G$ ) were observed to decrease with the application of the load management strategies. For example, Fig. 121 shows results for inboard propagation of a trailing-edge disbond from 8 – 8.5 m. These results indicate that for this case a reduction of maximum SERR of a little more than 50% and a reduction of the oscillating portion ( $\Delta G$ ) by more than 60% was achieved by limiting the bending moment by around 30%.

## 6.7 Conclusions

This work has demonstrated a clear economic advantage for derating damaged turbines to avoid shutdown or delay downtime for calm seasons, where WT are more accessible and less profitable to operate. The means to quantify these economic gains has been provided so that WT operators can weight the costs of implementation of SHM and advanced blade sensing against the potential for

increasing profits of the WT farm. The potential to delay maintenance to wind turbines could also allow servicing of multiple turbines, therefore further reducing O&M costs.

Although there were performance differences between the 120, 110, and 100 rad/s maximum speed derating controllers, Figure 121 shows very little difference between the 120 and 110 rad/s maximum speed derating controllers, as well as very little difference between the derating controllers and the load mitigation controller. When comparing the derating controllers for 120 and 110 rad/s maximum generator speed, the lower dynamic deflections associated with the lowest maximum generator speed indicates that reducing the maximum generator speed is advantageous when using derating. For this case, the 100 rad/s maximum generator speed would be the ideal design for the derating controller, as this has reached the limit of maximum shaft torque to produce the desired derated power level.

The load mitigation controller produces more power than the derating controllers, and Fig. 121 verifies that limiting the bending moments is an appropriate strategy to mitigate blade damage growth, because although there were differences in blade deflections, power production, and other features, the blade root bending moment for each controller was approximately the same. Therefore, the load mitigation controller would be the preferred method of operating the damaged turbine if profits are to be maximized, as it has the highest level of power production. The derating controllers remain the more conservative approach, as they will reduce loads more drastically at higher wind speeds than the load mitigation controller. This comparative study serves an example for designing damage tolerant controllers based on their steady performance, their dynamic performance, and high fidelity analysis of the capability of the controllers to effectively mitigate damage.



## CHAPTER VII

### DAMAGE TOLERANT DESIGN FOR OFFSHORE WT BLADES

The previous chapters have presented aeroelastic structural and control design from the perspective of rotor blades and high aspect ratio aircraft wings. A high-fidelity analysis technique for analyzing the local effects of bond line failures has been presented. The first main goal of this work is to demonstrate smart loads management strategies for damaged turbines, and the previous chapter has accomplished this. The second main goal of this work is to propose damage tolerant designs and design strategies for large offshore WT blades. The SNL 100 m blade will be used as a baseline for the damage tolerant designs. The damage tolerant design techniques that will be investigated are combined aerodynamic/structural optimization and airfoil selection. The combined aerodynamic/structural optimization process will be based on HARP-Opt, an open source tool for multi-objective optimization of WT blades provided by NREL [124].

The Sandia 100 m carbon blade design is used as a baseline for the reliable blade design process, as it represents a trend in future blade designs. A significant issue in the 100 m blade design process was panel buckling, and these buckling issues can worsen in the presence of damage. The buckling performance can be improved by reducing the skin panel (chordwise) size, which provides an incentive for low solidity blade designs. The solidity of the blade can be decreased by increasing the operating tip speed ratio and implementing higher lift airfoils. So-called flat-back (FB) airfoils have high-lift properties, and the flat trailing edge provides an ideal location for trailing edge reinforcement. These FB airfoils are compared with a set of Delft University (DU) series airfoils that are used in the NREL 5MW blade definition [63] as well as the SNL 100 m blade [45, 51, 50, 43]. Trailing-edge disbonding is a commonly encountered damage type, and such reinforcement would improve the tolerance of blade designs to this type of damage. So that “apples-to-apples” comparisons can be made between the new airfoils and the baseline airfoils, an optimized design was also produced with the baseline set of airfoils as well. The optimization process resulted in a Pareto front of candidates, which were then analyzed for their performance in terms of damage tolerance. The process indicated that weight reduction and AEP increases can be achieved by increasing the optimum design tip speed ratio and rotor solidity, but that damage tolerance considerations may place a limit on how high the design tip speed ratio should be raised. This is demonstrated by comparing two optimized designs with the

DU series airfoils with two optimized designs with FB airfoils. Blade cost is shown for the optimized results and compared for the two airfoil series as well as for two spar widths.

### ***7.1 Combined Aero/Structural Optimization***

A multi-objective optimization process was conducted using the optimization tool HARP\_Opt, integrated with Sandia National Laboratories NuMAD toolbox and an open source code for composite WT blade structural analysis, CoBlade [124, 1, 123]. CoBlade applies the EB and CLT equations used in PreComp in a form suitable for optimization. HARP-Opt uses the MATLAB GA toolbox and has integrated WT\_Perf to analyze each candidate. The author has modified HARP-Opt to integrate with NuMAD, hereby referred to as "HARP-Opt-S." The HARP-Opt-S tool allows simultaneous optimization of the global and local level problems simultaneously, with NuMAD and WT\_Perf forming the link between local design variables, global design variables, and the aeroelastic performance constraints of the WT. The design variables in HARP-Opt-S are 5 control points (CP) to govern the chord distribution, 5 CP to govern the twist distribution, and a user defined additional number of design variables to govern the distribution of layers in the various structural components. The objective functions of the GA were blade mass and AEP. The output is a Pareto front of candidates comparing the mass and AEP of the candidates. The chord and twist profiles for a given candidate in the modified optimizer are each defined by a Bezier curve with 5 CP, with the spanwise locations of the CP fixed and the values of the CP corresponding to the first 10 design variables. Then, the baseline geometry was defined in the NuMAD convention, except the distribution of layers in the baseline structural components were defined by CP with linear interpolation. After an optimization run, a Pareto front of candidates is produced, comparing the design candidates' AEP with the blade weight in an attempt to weigh the potential for income (AEP) with an equivalent measure of blade cost.

This aero-structural WT blade optimization corresponds to a global level optimization in terms of the multi-level method because it is using a simplified model (the EB/CLT model of CoBlade) to connect a reduced set of design variables to a good approximation of the spanwise distribution of inertial and stiffness properties for the non-uniform blade. The local level optimization portion of the multi-level method was not performed in this case because the level of detail of the NuMAD model lends more fidelity to the beam representation. This demonstrates the advantage of carefully considering the manufacturing process and general structural configuration when constructing the beam model.

The design process is demonstrated in this section for the 100 m blade design using this combined

aero-structural optimizer. The structural configuration for the new blade designs were based on the 100m-02 design definition [43], which represents the latest SNL 100 m blade design, with three variations named “rev0,” “rev1,” and “rev2.” The “rev0” variation uses all of the structural design features of the 100m-02 blade, but allows the twist/chord control points to be varied as well as adding 3 design variables to govern the distribution of spar layers. The “rev1” and “rev2” designs utilize the FB series airfoils, and the same general configuration details as the 100m-02 design. The “rev1” design features a widened spar cap, with a 1200 mm carbon spar cap (as opposed to 750 mm for the baseline, “rev0” and “rev2” designs). The design process was repeated multiple times, with three general configurations analyzed, for example Fig. 122 shows a typical result comparing the candidates for each configuration from a few hundred generations. This Fig. shows a similar performance of the DU and FB series airfoils, with a significant decrease in blade weight corresponding to the increased spar cap width.

The selection of one configuration or one particular candidate along the Pareto front should be based on economic decisions, so the increased costs associated with blade weight, including material and manufacturing costs, should be weighed against the potential for increased power output. However, such a detailed economic model is often based on prior experience and in this case difficult to apply. Therefore, the two candidates on the Pareto front were investigated in terms of blade weight, AEP, and damage tolerance: one candidate with the same AEP as the baseline, and another at an increased level of AEP. Four candidates in total resulted from the optimization process, two with DU airfoils and two with flat-back (FB) airfoils. The FB candidates used the “rev2” configuration, so that each candidate in this comparison has the same spar cap width. The candidates with the same AEP as the baseline will be referred to as DU #1 and FB #1, and the increased AEP candidates are DU #2 and FB#2.

The damage tolerance analyses included a stress-based fatigue analysis based on the S-N law and Miner’s rule. Representative material properties for the carbon fiber, unidirectional glass, and bidirectional skin material were used in the S-N analysis. The number of cycles and loading magnitudes are obtained from FAST/AeroDyn analysis of turbulent operation at each windspeed. Then, Miner’s rule was used to sum the fatigue damage at each windspeed using the design windspeed profile, and the fatigue life was calculated. An ANSYS model of each design was created and used to calculate the buckling capacity at the maximum service loading condition. This ANSYS model was then used to perform a damage criticality analysis (SERRs) of each design.

An overview of each design including the analysis results is given in Tables 31 – 32. The twist, chord, and spar layers distributions of each design are summarized in Figs. 123 – 124. Figures 125

– 127 show some details about the aerodynamic performance of the different designs compared with the baseline. The optimized designs each feature an increased optimal tip speed ratio (TSR), which is demonstrated in Fig. 127 and results in a shift of the power production to lower windspeeds. These results highlight the tradeoff between design TSR, blade solidity, blade weight and AEP. While the “damage tolerance” of the blade design in terms of the fatigue life calculation decreases with increasing TSR (decreasing solidity), the buckling margin increases as the solidity decreases. Therefore, the “damage tolerance” criterion would seem to suggest a moderate increase in the design TSR with respect to the SNL 100-02 design. The fatigue life of the FB airfoils was generally improved with respect to the DU airfoils, especially considering that a lower number of spar layers are used in the FB designs.

The damage criticality analysis was performed for each design for a trailing edge disbond length of 2 m. The resulting SERR values are given in Figs. 132 – 137. The optimized design DU #1, which had the same AEP and airfoil selection as the baseline design, but a greatly increased design TSR and reduced blade solidity, was found to have a higher peak in  $G_I$ , but generally decreased values in  $G_{II}$  and  $G_{III}$ . The DU #2 design, which has a moderately increased TSR, generally has lower SERR values. This suggests that the DU #2 design is the most damage tolerant design with respect to this damage type (TE disbond). The FB designs have lower  $G_{III}$  values, but  $G_I$  and  $G_{II}$  are higher for most of the damage onset locations. The SERR values for the FB designs are lower than the DU designs over the 10 – 20 m span location, which suggests that the FB airfoils could be used over this location to improve the damage tolerance of the baseline design.

The designs were then analyzed in FAST/AeroDyn with a “static” analysis, a simple windspeed sweep, as well as a dynamic load case, the standard “extreme gust with direction change” design load case. The “static” results from the windsweep analysis for the baseline and optimized designs are shown in Figs. 128 – 129. The performance was also evaluated with the ECD design load case, and the performance is shown in Figs. 130 and 131. These show a general reduction in blade loads for the #1 designs, but a possible increase in loads with the #2 designs. However, the SERR calculations effectively replace these measures when evaluating the damage tolerance of each design, and the higher loads shown in Fig. 126 for DU #2 compared with DU #1 actually corresponded with lower SERRs. Therefore, the increased loads in Fig. 130 of the DU #2 design with respect to the baseline or DU #1 designs do not translate to reduced damage tolerance, and similarly the reduced loads of DU #1 do not translate to increased damage tolerance. Dynamic analysis of the SERRs will be required to obtain a more accurate characterization of the damage tolerance of each design.

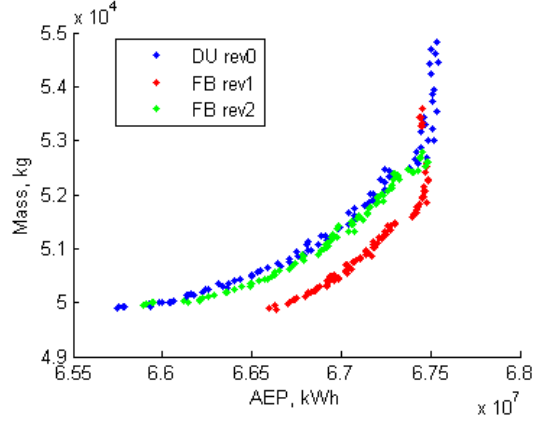


**Figure 122:** Example Pareto front of candidates for 100 m blade designs.

**Table 31:** 100 m blade design candidate details, DU series airfoils.

Design	SNL 100-02	DU #1	DU #2
AEP (GWh)	66.7	66.7	67.3
Weight (kg)	59,043	52,765	55,588
Max Chord (m)	7.59	6.58	7.37
Design TSR	7.35	9.55	8.45
ECD Tip $\Delta$ (m)	10.97	10.62	11.28
Spar Life (yr)	15.3	1.9	14.7
TE Life (yr)	72	16.9	70.9
Buckling	2.19	2.02	1.92

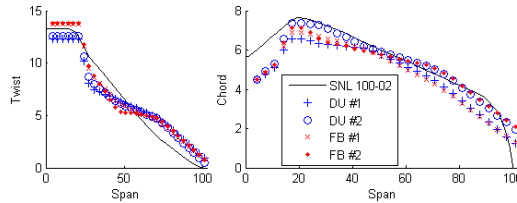


**Figure 123:** Chord and twist distributions for two 100 m designs utilizing either DU series or FB airfoils.

## 7.2 Blade Cost Comparisons

A recent blade cost study by SNL [52] has provided the means to estimate material and manufacturing costs of large WT blades. For comparison of two blades of similar size and configuration, the main difference in costs will arise from material costs, so a material cost model has been integrated into the optimizer system. This materials cost model then provides additional information for WT blade designers in choosing between configurations and Pareto front candidates. The cost model was applied to optimization results from early 100 m blade designs, and Fig. 138 shows the Pareto front of Fig. 122, with blade cost replacing blade weight. This Fig. demonstrates a clear disadvantage of the “rev1” designs: a heavy reliance on the wide carbon spar cap led to a drastic increase in material

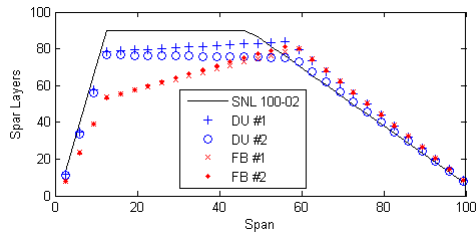


**Figure 124:** Spar layer distributions for two 100 m blade designs.

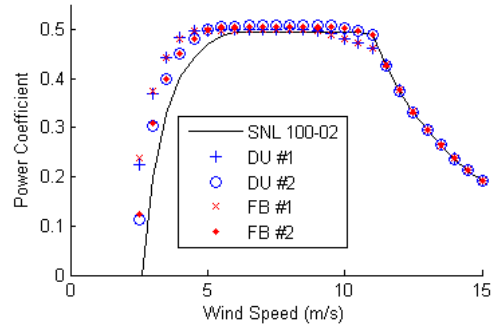


**Figure 125:** Predicted power output in terms of  $C_p$  from the four different designs.

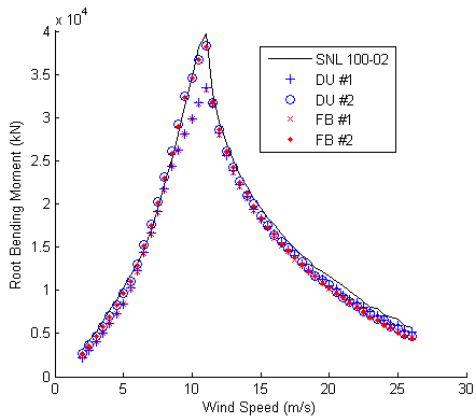


**Figure 126:** Root bending moment predictions in kN for 100 m blade designs.

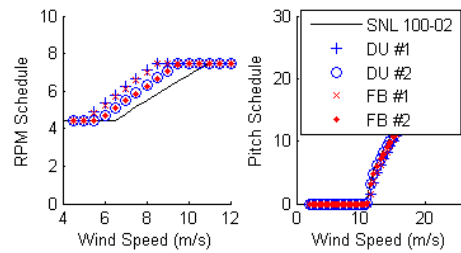


**Figure 127:** Design control scheduling for 100 m blade designs. Pitch schedule is nearly identical for the three designs.

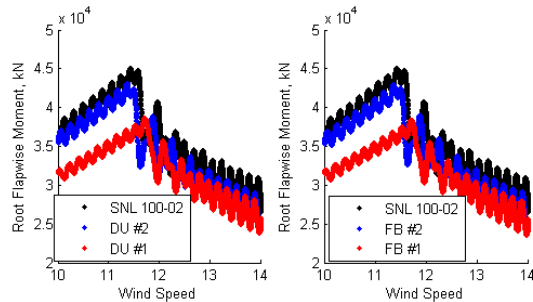


**Figure 128:** Flapping moment predictions for 100 m blade designs from windsweep FAST/AeroDyn analysis.

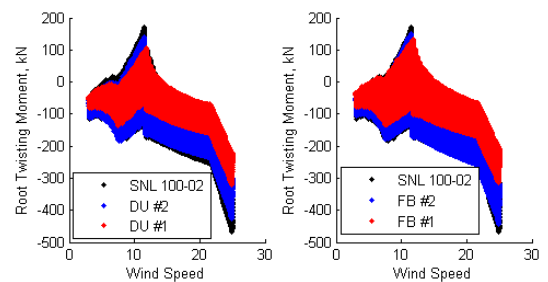


**Figure 129:** Twisting moment predictions for 100 m blade designs from windsweep FAST/AeroDyn analysis.

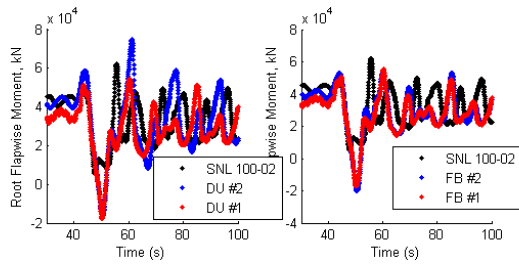


**Figure 130:** Root bending moment (kN) time histories from ECD analysis of competing designs.

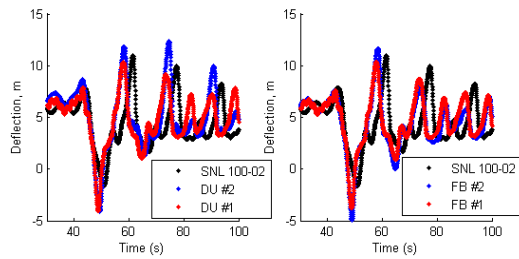


**Figure 131:** Tip deflection time histories from “extreme coherent gust with direction change” analysis of competing designs.

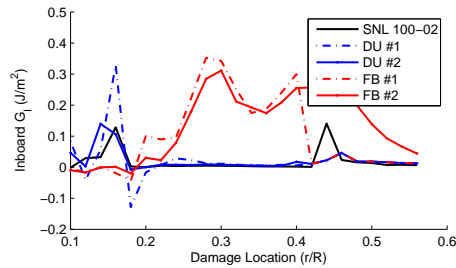


**Figure 132:** Inboard  $G_I$  comparative measures for 100 m blade designs.

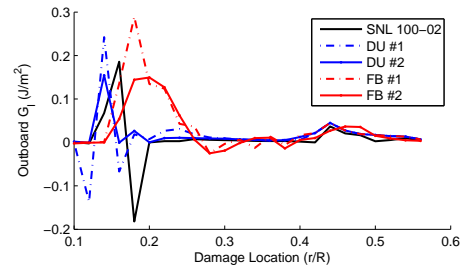


**Figure 133:** Outboard  $G_I$  comparative measures for 100 m blade designs.

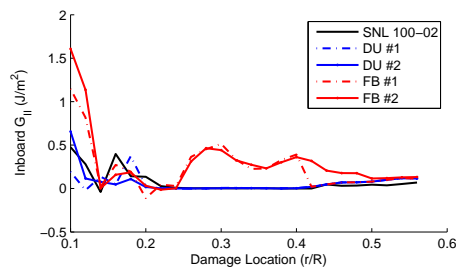


**Figure 134:** Inboard  $G_{II}$  comparative measures for 100 m blade designs.

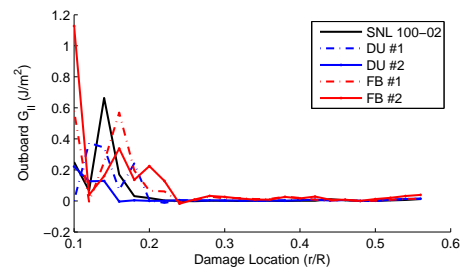


**Figure 135:** Outboard  $G_{II}$  comparative measures for 100 m blade designs.

**Table 32:** 100 m blade design details, FB airfoils.

Design	SNL 100-02	FB #1	FB #2
AEP (GWh)	66.7	66.7	67.3
Weight (kg)	59,043	52,876	55,375
Max Chord (m)	7.59	6.87	7.11
Design TSR	7.35	9.4	8.4
ECD Tip $\Delta$ (m)	10.97	10.47	11.67
Spar Life (yr)	15.3	33.7	8.3
TE Life (yr)	72	130	50
Buckling	2.19	2.63	2.57

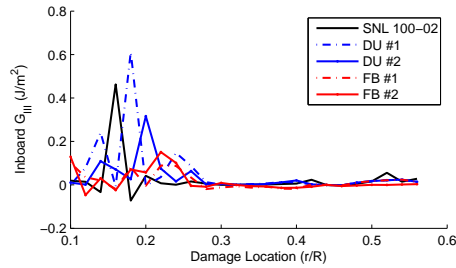


**Figure 136:** Inboard  $G_{III}$  comparative measures for 100 m blade designs.

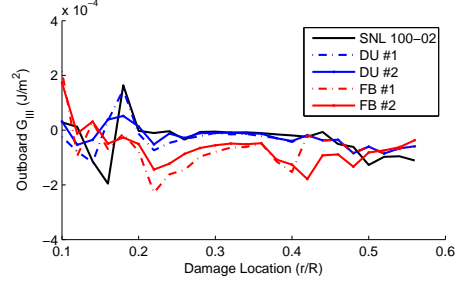


**Figure 137:** Outboard  $G_{III}$  comparative measures for 100 m blade designs.

cost. Blade cost as a function of blade weight is illustrated in Figure 139 for the different designs. For the more slender, lower AEP designs, the “rev1” designs use more carbon fiber layers and are the highest cost per weight, while the “rev2” designs benefit from the structurally efficient nature of FB airfoils and have the lower material use than the DU designs.

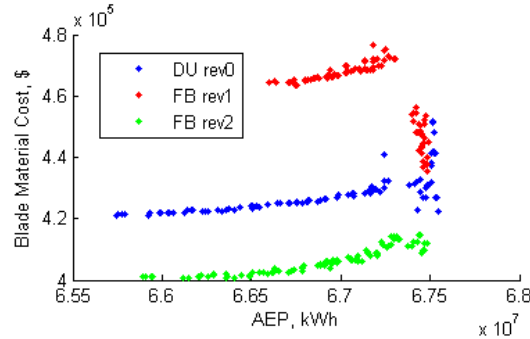


**Figure 138:** Example Pareto front of candidates for 100 m blade designs, with blade weight replaced by material cost model.

### 7.3 Comparison of Potential 100 m Designs

The considerations of Sections 7.1 and 7.2 contributed to a design exploration of 100m-03 blades by Griffith [49]. The 100 m blade designs featured in this work are 100m-02 designs with optimized twist and chord profiles. The wide spar cap structural configuration, or “rev1” configuration, was



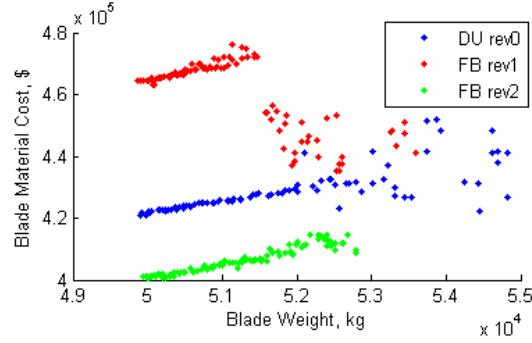


**Figure 139:** Blade material cost as a function of blade weight for 100 m blade design candidates.

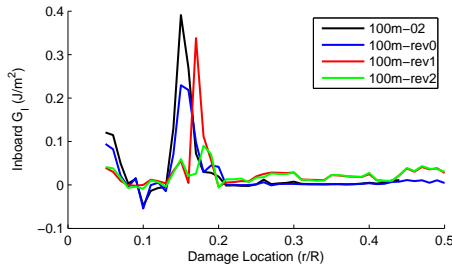


**Figure 140:** SERR for mode I fracture of the inner crack tip of TE disbond starting positions (5 – 40 m) and 100m-03 blade designs, normal operation, rated windspeed.

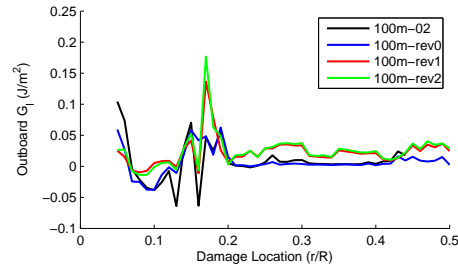


**Figure 141:** SERR for mode I fracture of the outer crack tip of TE disbond starting positions (5 – 40 m) and 100m-03 blade designs, normal operation, rated windspeed.

determined to be infeasible due to the increased cost associated with the additional carbon fiber layers. As noted in previous 100 m carbon designs, spar cap buckling and fatigue considerations provide additional incentive for the 750 mm spar cap width. For the same or similar stiffness capacity, a wider spar cap will lead to a smaller spar cap thickness, and therefore a lower buckling capacity when it is in compression. For the same number of layers, and similar bending stiffness, the wider spar cap configuration will have lower chord length, and therefore more of the bending strain energy is carried by the spar cap. Although this seems ideal, this can lead to early fatigue of the spar cap. Therefore, for the 100m-03 initial design study, the “rev1” design was decreased back to 750 mm and was considered as a more slender version for design comparison purposes. The 100m-03 designs are compared below in Figs. 140 – 145 in terms of damage tolerance of trailing-edge disbond. This comparison shows that the “rev2” design has generally lower SERR values, except for the case of outboard  $G_I$ , where the SERR values are comparable, but the area of damage criticality has shifted outboard approximately 5m. Therefore it may again require a blended airfoil design to mitigate SERR values at all portions of the blade.

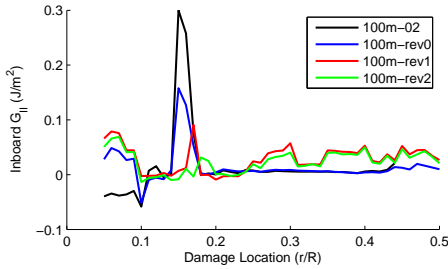


**Figure 142:** SERR for mode II fracture of the inner crack tip of TE disbond starting positions (5 – 40 m) and 100m-03 blade designs, normal operation, rated windspeed.

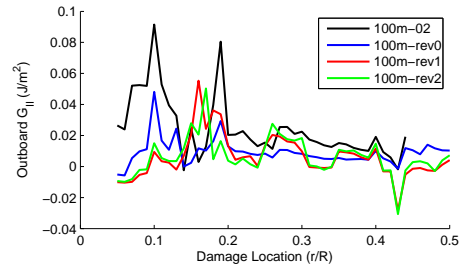


**Figure 143:** SERR for mode II fracture of the outer crack tip of TE disbond starting positions (5 – 40 m) and 100m-03 blade designs, normal operation, rated windspeed.

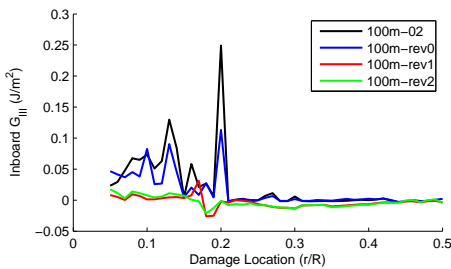


**Figure 144:** SERR for mode III fracture of the inner crack tip of TE disbond starting positions (5 – 40 m) and 100m-03 blade designs, normal operation, rated windspeed.

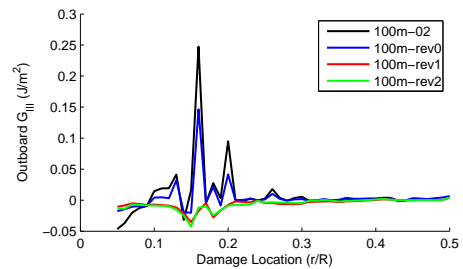


**Figure 145:** SERR for mode III fracture of the outer crack tip of TE disbond starting positions (5 – 40 m) and 100m-03 blade designs, normal operation, rated windspeed.

## 7.4 *Conclusions*

Wind turbine (WT) rotor radius has been rapidly increasing in recent years due to increased balance of station costs for offshore wind and a desire to maximize annual income from an expensive offshore installation. The Sandia National Laboratories 100 m blade design effort seeks to identify design issues that arise from extremely large wind turbine blades. These include common requirements for WT rotors such as aerodynamic performance optimization as well as additional design requirements for dynamic aeroelastic performance, fatigue, buckling. This work adds damage tolerance as an additional optimization goal for the case of trailing-edge bond line failure (TE disbond). These optimization goals can be addressed simultaneously by the use of an aero-structural optimization process that carefully considers manufacturing and material layout requirements to connect “local” design variables for the structural configuration, “global” design variables to govern the spanwise chord and twist, and constraints based on “local” damage tolerance measures and “global” aeroelastic performance requirements. The results from the optimization showed how airfoil selection, blade solidity, design tip-speed ratio (TSR), and structural design are key design variables. The optimization goals of aeroelastic performance, damage tolerance and blade cost were evaluated for a new set of 100 m blade designs. These designs show a reduction in cost and an improvement in performance over the baseline design due to the aeroelastic design process. The design methods that were developed are efficient and user-friendly, and the design process gives the user an intuitive feel for the interplay between key design variables and the aeroelastic constraints. The design methods are also extremely flexible, being able to handle a wide variety of wind turbine structural configurations.

## CHAPTER VIII

### CONCLUSIONS AND FUTURE WORK

#### *8.1 Conclusions*

Offshore wind turbines need to be more reliable for widespread implementation of offshore wind. A main part of this reliability is in the performance of the WT blades in terms of aeroelasticity and damage tolerance, which can be improved from the standpoint of operations and maintenance or by producing better blade designs. From the standpoint of operations and maintenance, it is possible to improve the aeroelastic performance and damage tolerance of a WT blade by adopting aeroelastic control design practices from other aerospace fields to mitigate blade deflections and blade loads. Aeroelastic control design in the field of flying wing aircraft or other aircraft with high aspect ratio wings serves as an example of how aeroelastic design margins can be relaxed by using active controls to suppress aeroelastic effects. From a design standpoint, wind turbine blades are advanced composite non-uniform structures with very detailed structural configurations. Design strategies that can reduce the size of this design space by handling the global and local level problems separately will allow efficient optimization of the structural configuration. This multi-level optimization method has been extended to non-uniform blades and an optimization problem has been demonstrated for a modern composite rotor blade. This design example showed how aeroelastic constraints on the global blade behavior can be reconciled with design variables defining the local structural configuration and included early in the design process. The design example for a flying wing HALE aircraft gave further insight into how design space exploration and optimization of the global blade behavior can give insight into the design goals for the local structural design problem. The nature of body-freedom flutter (BFF) for HALE aircraft was investigated and insight into design recommendations for HALE aircraft to avoid early onset of BFF was gained. This insight included recommendations concerning the fuselage and CG locations as well as how to design the interior wing structure to avoid BFF.

The general lessons from the aeroelastic structural and control design examples from the rotor blade and high aspect ratio wing fields were then applied to the problem of wind turbine blade damage mitigation. First, a high-fidelity analysis technique was developed to compare different structural or control designs in terms of their effectiveness to mitigate local damage effects. This

high-fidelity analysis technique was then applied to a modern wind turbine, and it was discovered that the most critical damage location was the inboard portion of the blade. These high-fidelity analyses, once extended to the next generation 100 m wind turbine blades, also demonstrated a critical area on the inboard portion of the blade. These results alone give wind turbine operators valuable information for how to deal with damaged blades: if the damage lies within this critical inboard area, then it should be addressed quickly, but if the damage lies in a more outboard location there is an opportunity to increase overall profits by using an appropriate derating strategy. Then, actual control design candidates for smart loads management were evaluated within the high-fidelity framework. These demonstrated that reducing blade section loading is a good strategy for mitigating local damage effects, and that when limiting the power rating of a turbine performance benefits can be achieved if the angular speed of the rotor is reduced as well.

Finally, blade design efforts for the 100 m blade project were undertaken as an example of how to perform aeroelastic design for wind turbine blades and within the context of damage tolerant blades. These design efforts found that an increase in blade slenderness (decrease in maximum chord) can result in a lighter, cheaper blade, but that damage tolerance considerations place a limit on how slender the blade should be. The comparison between the baseline set of airfoils for the 100 m blade and a new set of thick trailing edge airfoils (flat-back airfoils) showed that the more structurally efficient flat-back airfoils allowed for more slender blade designs. The 100 m designs utilizing flat-back airfoils had superior blade weight, blade material cost, buckling performance, fatigue performance, and similar damage tolerance. Therefore it is recommended that flat-back airfoils be implemented in the next generation of wind turbine blades.

The present work has produced several important contributions to the state of the art in aeroelastic design of modern rotorblades, flying wing aircraft, and offshore wind turbine blades. These contributions are summarized as follows:

1. The multi-level optimization method, which has been demonstrated only for uniform blades, has been extended to non-uniform blades and is suitable for modern rotorblades, high aspect ratio aircraft wings, or wind turbine blades.
2. The nature of BFF has been explored, with recommendations as to the fuselage, CG placement, and interior structural design of HALE aircraft. Aeroelastic control design to further increase the BFF speed has been demonstrated.
3. A multi-scale framework to evaluate damaged WT blades has been provided. A means to qualitatively compare WT systems in terms of damage tolerance was developed and a method for quantitative estimates of the remaining fatigue life of damaged blades was recommended.

4. Derating strategies and load management strategies for wind turbine blades have been explored and characterized, in terms of their quasi-steady and dynamic performance and a qualitative damage tolerance comparison.
5. Aeroelastic design strategies for the next generation of WT blades has been demonstrated, and new trends concerning the design TSR and blade cost have been discovered. These discoveries may lead to future WT blades that are cheaper, more efficient and more reliable for offshore WT systems.

## ***8.2 Future Work***

The multi-level design procedure for non-uniform blades has been demonstrated in this work for a variety of applications. The examples presented have shown that the aeroelastic design process is successful by integrating key analyses early in design optimization procedures. The control design process could also be worked into this strategy, so that aeroelastic performance improvements from aeroelastic control strategies can translate to weight savings by means of structural redesign. Such a fully integrated design procedure could streamline the design process as well as give insight into how the structural and control design spaces interact.

The multi-scale analysis procedure provided an efficient means of qualitatively evaluating the damage tolerance of control strategies or designs. A quantitative analysis which calculates damage growth rates will require more accurate numerical procedure as well as data from experimental testing of adhesive bond line failures and a corresponding growth model. One way to improve the numerical predictions of the multi-scale method would be to improve the VCCT method with more accurate calculation of the SERRs. For example, moving individual node positions to represent crack growth (instead of successive unequivalencing of nodes) may provide a means to apply the VCCT more accurately. Another option would be to replace the VCCT calculations with cohesive zone elements, which can be used to calculate the SERRs or for damage progression calculations. The analysis procedure can then be used to provide accurate SERR inputs to a growth model obtained from experimental data and the remaining fatigue life of damaged wind turbine blades can be estimated. The quantitative results would allow calculation of the economic risk associated with operating damaged turbines.

Energy-based blade life predictions might be included more directly within the damage process to result in a more successful and comprehensive damage tolerant design process. Throughout the course of evaluating control strategies, baseline designs, etc. it may be possible to identify trends between baseline or undamaged blade stresses with damage growth rates. In the completed work, it

was found that peaks in stresses corresponded with peaks in Strain Energy Release Rates (SERRs). This suggests that designs with reduced healthy stress concentrations will have lower SERRs, and therefore would be damage tolerant in general. The initial work identified two locations of interest for damage tolerant blades: where the circular root airfoils transition to flat/blunt trailing-edge (TE) airfoils and where airfoils with blunt TEs transition to sharp TEs near the tip of the blade.

Airfoil selection is a promising damage tolerant design strategy for WT blades. One category of airfoils that may be appealing for WTs are Flat-back (FB) airfoils [42]. It has also shown that the use of FB airfoils can mitigate peak SERRs as well as provide other advantage in terms of fatigue, buckling, and economic measures. The flat TE is an ideal location for reinforcement to further mitigate SERRs, and the possibility of reinforcement will be investigated to fully explore the potential for damage tolerant FB designs. The cost, ease of implementation, and refined fatigue predictions need to be evaluated for this as well as other reinforcement techniques for damage-critical blade areas.

The initial work on this project has identified the design tip speed ratio (TSR) as a design variable that has significant implications in terms of weight, AEP, and damage tolerance. It is advantageous in terms of buckling capacity and blade weight to increase the design TSR, but there may be an upper limit due to damage tolerance considerations. The effect of changing the design TSR may be demonstrated more clearly if the design TSR is fixed for an optimizer run and a Pareto front could be produced for each design TSR of interest. Then, the cost and damage tolerance considerations may be systematically applied as has been demonstrated here.

## REFERENCES

- [1] “Numerical manufacturing and design tool (NuMAD).” Sandia National Laboratories. [http://energy.sandia.gov/?page\\_id=2238](http://energy.sandia.gov/?page_id=2238). Accessed: July 2013.
- [2] BALDAN, A., “Adhesion phenomena in bonded joints,” *International Journal of Adhesion and Adhesives*, vol. 38, pp. 95–116, 2012.
- [3] BANSAL, P. and PITT, D. M., “Effects of variations in structural properties of a generic wing on flutter prediction,” in *53rd AIAA/ASME/ASCE/AHS/ASC Structures, Structural Dynamics and Materials Conference*, 2012.
- [4] BERG, J., PAQUETTE, J., and RESOR, B., “Mapping of 1D beam loads to the 3D wind blade for buckling analysis,” in *52nd AIAA/ASME/ASCE/AHS/ASC Structures, Structural Dynamics, and Materials Conference. Denver, Colorado*, 2011.
- [5] BERG, J. C. and RESOR, B. R., “Numerical manufacturing and design tool (NuMAD v2.0) for wind turbine blades: Users guide,” Tech. Rep. SAND2012-7028, Sandia National Laboratories, 2012.
- [6] BIERBOOMS, W. and VAN BUSSEL, G., “The impact of different means of transport on the operation and maintenance strategy for offshore wind farms,” in *MAREC 2002, International Conference on Marine Renewable Energy-Conference Proceedings*, 2002.
- [7] BINDOLINO, G., GHIRINGELLI, G., RICCI, S., and TERRANEO, M., “Multilevel structural optimization for preliminary wing-box weight estimation,” *Journal of Aircraft*, vol. 47, pp. 476–489, March-April 2010.
- [8] BIR, G., “PreComp, pre-processor for computing composite blade properties.” National Renewable Energy Laboratory. <https://wind.nrel.gov/designcodes/preprocessors/precomp/>. Accessed: July 2013.
- [9] BISPLINGHOFF, R. L., ASHLEY, H., and HALFMAN, R. L., *Aeroelasticity*. Reading, Massachusetts: Addison-Wesley Publishing Co., 1955.
- [10] BOHLING, G., “Kriging,” October 2005.
- [11] BOLLER, C., CHANG, F.-K., and FUJINO, Y., *Encyclopedia of Structural Health Monitoring*, vol. 2960. Wiley New York, 2009.
- [12] BOSKOVIC, J. D., BERGSTROM, S., and MEHRA, R. K., “Robust integrated flight control design under failures, damage, and state-dependent disturbances,” *Journal of guidance, control, and dynamics*, vol. 28, no. 5, pp. 902–917, 2005.
- [13] BOSSANYI, E., “The design of closed loop controllers for wind turbines,” *Wind Energy*, vol. 3, no. 3, pp. 149–163, 2000.
- [14] BOSSANYI, E., “Individual blade pitch control for load reduction,” *Wind Energy*, vol. 6, no. 2, pp. 119–128, 2003.
- [15] BOSSANYI, E., “Wind turbine control for load reduction,” *Wind Energy*, vol. 6, no. 3, pp. 229–244, 2003.
- [16] BOSSANYI, E., “Further load reductions with individual pitch control,” *Wind Energy*, vol. 8, no. 4, pp. 481–485, 2005.



- [17] BUHL, M. L., “Wt\_perf users guide,” *National Wind Technology Center, National Renewable Energy Laboratory, Golden, CO*, 2004.
- [18] CAO, W., XIE, Y., and TAN, Z., “Wind turbine generator technologies,” *Advances in Wind Power. In-tech Online Book*, 2012.
- [19] CARRAR, P., MENEGHETTI, G., QUARESIMIN, M., and RICONTTA, M., “Crack propagation analysis in composite bonded joints under mixed-mode (I+II) static and fatigue loading: Experimental investigation and phenomenological modeling,” *Journal of Adhesion Science and Technology*, vol. 27, no. 11, pp. 1179–1196, 2013.
- [20] CHANG, C.-S., HODGES, D. H., and PATIL, M. J., “Flight dynamics of highly flexible aircraft,” *Journal of Aircraft*, vol. 45, pp. 538 – 545, Mar.-Apr. 2008.
- [21] CHAVES, F. J., DE MOURA, M., DA SILVA, L., and DILLARD, D., “Numerical validation of a crack equivalent method for mixed-mode I+II fracture characterization of bonded joints,” *Engineering Fracture Mechanics*, 2013.
- [22] CHEN, H., YU, W., and CAPELLARO, M., “A critical assessment of computer tools for calculating composite wind turbine blade properties,” *Wind Energy*, vol. 13, pp. 497 – 516, 2010.
- [23] CHEN, H. and YU, W., “PreVABS: Preprocessor for VABS modeling of sophisticated cross-sections.” AnalySwift. <http://analyswift.com/>. Accessed: July 2013.
- [24] CHITTICK, I. R. and MARTINS, J. R., “Aero-structural optimization using adjoint coupled post-optimality sensitivities,” *Structural and Multidisciplinary Optimization*, vol. 36, no. 1, pp. 59–70, 2008.
- [25] CHRISTENSEN, P. and GIEBEL, G., “Availability of wind turbines in remote places. a statistical and a real-time view,” in *European Wind Energy Conference & Exhibition*, 2001.
- [26] CHRISTIANSEN, S., BAK, T., and KNUDSEN, T., “Damping wind and wave loads on a floating wind turbine,” *IEEE Transactions on Control Systems Technology*, vol. 6, no. 8, pp. 4097–4016, 2013.
- [27] COMMISSION, I. E. and OTHERS, “international standard, wind turbine generator systems-part 1: Safety requirements,” 1994.
- [28] CREWS, J., SHIVAKUMAR, K., and RAJU, I., “Strain energy release rate distributions for double cantilever beam specimens,” *AIAA journal*, vol. 29, no. 10, pp. 1686–1691, 1991.
- [29] DEOBALD, L., MABSON, G., DOPKER, B., HOYT, D., BAYLOR, J., and GRAESSER, D., “Interlaminar fatigue elements for crack growth based on virtual crack closure technique,” in *48th AIAA/ASME/ASCE/AHS/ASC Structures, Structural Dynamics, and Materials Conference*, 2007.
- [30] DOYLE, J. and STEIN, G., “Multivariable feedback design: Concepts for a classical/modern synthesis,” *Automatic Control, IEEE Transactions on*, vol. 26, no. 1, pp. 4–16, 1981.
- [31] DVILA, C., CAMANHO, P., and TURON, A., “Effective simulation of delamination in aeronautical structures using shells and cohesive elements,” *Journal of Aircraft*, vol. 45, no. 2, 2008.
- [32] EDER, M., BITSCHKE, R., NIELSEN, M., and BRANNER, K., “A practical approach to fracture analysis at the trailing edge of wind turbine rotor blades,” *Wind Energy*, vol. 17, no. 3, 2013.
- [33] EDWARDS, K. and DAVENPORT, C., “Materials for rotationally dynamic components: rationale for higher performance rotor-blade design,” *Materials and Design*, vol. 27, pp. 31–35, November 2006.

- [34] FEATHERSTON, C. A., HOLFORD, K. M., PULLIN, R., LEES, J., EATON, M., and PEARSON, M., “An autonomous structural health monitoring solution,” in *SPIE Microtechnologies*, pp. 876302–876302, International Society for Optics and Photonics, 2013.
- [35] FRANGOPOL, D. M., SAYDAM, D., and KIM, S., “Maintenance, management, life-cycle design and performance of structures and infrastructures: a brief review,” *Structure and Infrastructure Engineering*, vol. 8, no. 1, pp. 1–25, 2012.
- [36] FRITZEN, C. P., KRAEMER, P., and BUETHE, I., “Vibration-based damage detection under changing environmental and operational conditions,” *Advances in Science and Technology*, vol. 83, pp. 95–104, 2013.
- [37] FRITZEN, C., KRAEMER, P., and KLINKOV, M., “Structural health monitoring of offshore wind energy plants,” in *4th European workshop on Structural Health Monitoring*, pp. 3–21, 2008.
- [38] FROST, S. A., GOEBEL, K., BALAS, M. J., and HENDERSON, M. T., “Integrating systems health management with adaptive contingency control for wind turbines,” in *51st AIAA Aerospace Sciences Meeting Including the New Horizons Forum and Aerospace Exposition. Grapevine, TX, USA*, 2013.
- [39] GARG, M., ABUMERI, G., and HUANG, D., “Validation of class of applications using progressive failure and discrete cohesive zone model for line and surface cracks,” in *50th AIAA/ASME/ASCE/AHS/ASC Structures, Structural Dynamics, and Materials Conference. Palm Springs, California*, 2009.
- [40] GHOSHAL, A., SUNDARESAN, M. J., SCHULZ, M. J., and PAI, F. P., “Structural health monitoring techniques for wind turbine blades,” *Journal of Wind Engineering and Industrial Aerodynamics*, vol. 85, no. 3, pp. 309–324, 2000.
- [41] GONZALEZ, J. S., PAYAN, M. B., and SANTOS, J. R., “Optimal control of wind turbines for minimizing overall wake effect losses in offshore wind farms,” in *Eurocon, 2013 IEEE*, pp. 1129–1134, IEEE, 2013.
- [42] GRASSO, F., “Hybrid optimization for wind turbine thick airfoils,” in *53rd AIAA/ASME/ASCE/AHS/ASC Structures, Structural Dynamics, and Materials Conference. Honolulu, Hawaii*, 2012.
- [43] GRIFFITH, D. T., “The snl100-02 blade: Advanced core material design studies for the sandia 100-meter blade,” *Sandia National Laboratories Technical Report, SAND2013-10162*, 2013.
- [44] GRIFFITH, D. T., DAVIS, R., and RANDS, C., “Integration of nonlinear finite element analysis of disbonds of wind turbine blades into the numad analysis system,” Tech. Rep. SAND2015-0000, Sandia National Laboratories, 2015.
- [45] GRIFFITH, D. T., RESOR, B. R., and ASHWILL, T. D., “Challenges and opportunities in large offshore rotor development: Sandia 100-meter blade research,” in *AWEA WINDPOWER 2012 Conference and Exhibition. Atlanta, GA, USA*, 2012.
- [46] GRIFFITH, D. T., YODER, N., RESOR, B., WHITE, J., and PAQUETTE, J., “Structural health and prognostics management for offshore wind turbines: An initial roadmap,” Tech. Rep. SAND2012-10109, Sandia National Laboratories, 2012.
- [47] GRIFFITH, D. T., YODER, N., RESOR, B., WHITE, J., PAQUETTE, J., OGILVIE, A., and PETERS, V., “Prognostic control to enhance offshore wind turbine operations and maintenance strategies,” *management*, vol. 5, pp. 8–10, 2012.
- [48] GRIFFITH, D. T., YODER, N. C., RESOR, B., WHITE, J., and PAQUETTE, J., “Structural health and prognostics management for the enhancement of offshore wind turbine operations and maintenance strategies,” *Wind Energy*, 2013.

- [49] GRIFFITH, D. and RICHARDS, P. W., “The snl100-03 blade: Design studies with flatback airfoils for the sandia 100-meter blade.,” tech. rep., Sandia National Laboratories (SNL-NM), Albuquerque, NM (United States), 2014.
- [50] GRIFFITH, D., “The SNL100-01 blade: Carbon design studies for the sandia 100-meter blade.,” Tech. Rep. SAND2013-1178, Sandia National Laboratories, 2013.
- [51] GRIFFITH, D. and ASHWILL, T., “The sandia 100-meter all-glass baseline wind turbine blade: SNL100-00,” Tech. Rep. SAND2011-3779, Sandia National Laboratories, 2011.
- [52] GRIFFITH, D. and JOHANNIS, W., “Large blade manufacturing cost studies using the sandia blade manufacturing cost tool and sandia 100-meter blades,” *Sandia National Laboratories Technical Report, SAND2013-2734*, 2013.
- [53] GUIAMATSIA, I., FALZON, B., DAVIES, G., and ROBINSON, P., “Improving composite damage modelling through automatic placement of cohesive elements,” in *Proceedings of the 49th AIAA/ASME/ASCE/AHS/ASC SDM Conference AIAA*, 2008.
- [54] HAMEED, Z., HONG, Y., CHO, Y., AHN, S., and SONG, C., “Condition monitoring and fault detection of wind turbines and related algorithms: A review,” *Renewable and Sustainable Energy Reviews*, vol. 13, no. 1, pp. 1–39, 2009.
- [55] HANSEN, M. H., HANSEN, A., LARSEN, T. J., and OYE, S., “Control design for a pitch-regulated, variable-speed wind turbine,” Tech. Rep. Riso-R-1500(EN), Riso National Laboratory, 2005.
- [56] HIGGINS, P. and FOLEY, A. M., “Review of offshore wind power development in the united kingdom,” in *Environment and Electrical Engineering (EEEIC), 2013 12th International Conference on*, pp. 589–593, IEEE, 2013.
- [57] HODGES, D. H., BAUCHAU, O., CRAIG, J. I., and VOLOVOI, V. V., “Vabs-ansys toolset for blade cross section stiffness analysis,” 2002.
- [58] HODGES, D. H., “Geometrically-exact, intrinsic theory for dynamics of curved and twisted anisotropic beams,” *AIAA Journal*, vol. 41, pp. 1131 – 1137, June 2003.
- [59] HODGES, D. H., “Corrigendum: geometrically-exact, intrinsic theory for dynamics of curved and twisted anisotropic beams,” *AIAA Journal*, vol. 47, pp. 1308 – 1309, May 2009.
- [60] HU, P., YU, W., HODGES, D. H., and KU, J., “VABS-IDE: VABS-enabled integrated design environment (IDE) for efficient high-fidelity composite rotor blade and wing design,” in *51st AIAA/ASME/ASCE/AHS/ASC Structures, Structural Dynamics, and Materials Conference. Orlando, Florida*, 2010.
- [61] JACOB, J. D. and SMITH, S. W., “Design of hale aircraft using inflatable wings,” in *46th AIAA Aerospace Sciences Meeting and Exhibit. Reno, Nevada*, 2008.
- [62] JAWORSKI, J. W. and DOWELL, E. H., “Comparison of theoretical structural models with experiment for a high-aspect-ratio aeroelastic wing,” *Journal of Aircraft*, vol. 46, no. 2, p. 708, 2009.
- [63] JONKMAN, J., BUTTERFIELD, S., MUSIAL, W., and SCOTT, G., “Definition of a 5-MW reference wind turbine for offshore system development.,” Tech. Rep. NREL/TP-500-38060, 2009.
- [64] JONKMAN, J. M. and BUHL JR., M. L., “FAST user’s guide,” Tech. Rep. NREL/EL-500-38230, National Renewable Energy Laboratory, 2005.
- [65] JONKMAN, J. M. and BUHL JR., M. L., “Fast users guide,” *Golden, CO: National Renewable Energy Laboratory*, 2005.

- [66] JONKMAN, J. M. and BUHL JR, M. L., “Loads analysis of a floating offshore wind turbine using fully coupled simulation,” in *WINDPOWER 2007 Conference and Exhibition, Los Angeles, California, 3–6 June 2007*, Citeseer, 2007.
- [67] JONKMAN, J. M., “Influence of control on the pitch damping of a floating wind turbine,” in *2008 ASME Wind Energy Symposium, Reno, Nevada*, National Renewable Energy Laboratory, 2008.
- [68] KIM, H., KWON, H., and KEUNE, J., “Buckling initiation and disbond growth in adhesively bonded composite flanges,” in *44th AIAA/ASME/ASCE/AHS/ASC Structures, Structural Dynamics, and Materials Conference. Norfolk, Virginia*, 2003.
- [69] KLINKOV, M. and FRITZEN, C.-P., “Wind load observer for a 5MW wind energy plant,” in *Structural Dynamics, Volume 3*, pp. 719–726, Springer, 2011.
- [70] KRAEMER, P. and FRITZEN, C., “Sensor fault detection and signal reconstruction using mutual information and kalman filters,” in *International conference on noise and vibration engineering*, pp. 3267–3282, 2008.
- [71] KRAEMER, P. and FRITZEN, C.-P., “Damage identification of structural components of offshore wind energy plants,” *DEWEK 2008*, 2008.
- [72] KRUEGER, R., “Virtual crack closure technique: History, approach, and applications,” *Applied Mechanics Review*, vol. 57, no. 2, 2004.
- [73] KU, C. and HAJELA, P., “Optimized neural network based controller for a nonlinear aeroelastic system,” *AIAA*, vol. 97, p. 1182, 1997.
- [74] KU, J., *A Hybrid Optimization Scheme for Helicopters with Composite Rotor Blades*. PhD thesis, Georgia Institute of Technology, Atlanta, Georgia, 2007.
- [75] KULLAA, J., “Distinguishing between sensor fault, structural damage, and environmental or operational effects in structural health monitoring,” *Mechanical Systems and Signal Processing*, vol. 25, no. 8, pp. 2976–2989, 2011.
- [76] KUSIAK, A. and SONG, Z., “Design of wind farm layout for maximum wind energy capture,” *Renewable Energy*, vol. 35, no. 3, pp. 685–694, 2010.
- [77] LARSEN, T. J. and HANSON, T. D., “A method to avoid negative damped low frequent tower vibrations for a floating, pitch controlled wind turbine,” *Journal of Physics: Conference Series*, vol. 75, no. 1, 2007.
- [78] LEE, J.-R. and KIM, H.-C., “Feasibility of in-situ blade deflection monitoring of a wind turbine using a laser displacement sensor within the tower,” *Smart Materials and Structures*, vol. 22, no. 2, 2013.
- [79] LEISHMAN, J. G., *Principles of Helicopter Aerodynamics*. Cambridge, U.K.: Cambridge University Press, 2002.
- [80] LI, L., *Structural Design of Composite Rotor Blades with Consideration of Manufacturability, Durability, and Manufacturing Uncertainties*. PhD thesis, Georgia Institute of Technology, Atlanta, Georgia, 2008.
- [81] LIU, B., HAFTKA, R. T., and AKGÜN, M. A., “Two-level composite wing structural optimization using response surfaces,” *Structural and Multidisciplinary Optimization*, vol. 20, no. 2, pp. 87–96, 2000.
- [82] LIU, B., HAFTKA, R. T., and WATSON, L. T., “Global-local structural optimization using response surfaces of local optimization margins,” *Structural and Multidisciplinary Optimization*, vol. 27, no. 5, pp. 352–359, 2004.

- [83] LOVE, M. H., ZINK, P. S., WIESELMANN, P. A., and YOUNGREN, H., “Body freedom flutter of high aspect ratio flying wings,” in *46 th AIAA/ASME/ASCE/AHS/ASC Structures, Structural Dynamics, and Materials Conference*, pp. 1–23, 2005.
- [84] LUENBERGER, D. G., “Dynamic equations in descriptor form,” *Automatic Control, IEEE Transactions on*, vol. 22, no. 3, pp. 312–321, 1977.
- [85] MALCOLM, D. J. and LAIRD, D. L., “Extraction of equivalent beam properties from blade models,” *Wind Energy*, vol. 10, no. 2, pp. 135–157, 2007.
- [86] MANDELL, J., SAMBORSKY, J., WAHL, D., and SUTHERLAND, N., “Effect of mean stress on the damage of wind turbine blades,” in *International Committee on Composite Materials Conference 14, San Diego, CA.*, 2003.
- [87] MARDANPOUR, P., HODGES, D., NEUHART, R., and GRAYBEAL, N., “Effect of engine placement on aeroelastic trim and stability of flying wing aircraft,” in *Proceedings of the 53rd AIAA/ASME/ASCE/AHS/ASC Structures, Structural Dynamics and Materials Conference, Honolulu, Hawaii*, (Reston, Virginia), AIAA, April 23 – 26, 2012. AIAA Paper 2012-1634.
- [88] MARDEN, J. R., RUBEN, S. D., and PAO, L. Y., “Surveying game theoretic approaches for wind farm optimization,” in *Proceedings of the 50th AIAA Aerospace Sciences Meeting, Nashville, TN.*, 2012.
- [89] MARTINS, J. R. and LAMBE, A. B., “Multidisciplinary design optimization: a survey of architectures,” *AIAA journal*, vol. 51, no. 9, pp. 2049–2075, 2013.
- [90] MATHA, D., FISCHER, T., KUHN, M., and JONKMAN, J., *Model development and loads analysis of a wind turbine on a floating offshore tension leg platform*. National Renewable Energy Laboratory, 2010.
- [91] MCGUGAN, M. and SORENSEN, B. F., “Fundamentals for remote condition monitoring of offshore wind turbine blades,” *Structural Health Monitoring*, pp. 1913–1919, 2007.
- [92] MINNETYAN, L., HUANG, D., CHAMIS, C., and F., A., “Cyclic fatigue of composite airfoil structures.” AIAA Archive Set 673., January 1963.
- [93] MOLL, J., KRAEMER, P., and FRITZEN, C., “Compensation of environmental influences for damage detection using classification techniques,” *Proc. 4th EWSHM*, pp. 1080–1087, 2008.
- [94] MORONI, F. and PIRONDI, A., “A procedure for the simulation of fatigue crack growth in adhesively bonded joints based on a cohesive zone model and various mixed-mode propagation criteria,” *Engineering Fracture Mechanics*, vol. 89, pp. 129–138, 2012.
- [95] MULJADI, E. and BUTTERFIELD, C., “Pitch-controlled variable-speed wind turbine generation,” in *Presented at the 1999 IEEE Industry Applications Society Annual Meeting*, 1999.
- [96] MUSIAL, W. and BUTTERFIELD, S., “Future for offshore wind energy in the united states,” in *EnergyOcean 2004 Conference*, pp. 4–6, 2004.
- [97] MYRENT, N., KUSNICK, J., BARRETT, N., ADAMS, D., and GRIFFITH, D., “Structural health and prognostics management for offshore wind turbines: Case studies of rotor fault and blade damage with initial om cost modeling,” Tech. Rep. SAND2013-2735, Sandia National Laboratories, 2013.
- [98] MYRENT, N. J., ADAMS, D. E., and GRIFFITH, D. T., “Aerodynamic sensitivity analysis of rotor imbalance and shear web disbond detection strategies for offshore structural health prognostics management of wind turbine blades,” in *32nd ASME Wind Energy Symposium. National Harbor, Maryland*, 2014.

- [99] NAMIK, H. and STOL, K., “Individual blade pitch control of floating offshore wind turbines,” *Wind Energy*, vol. 13, no. 1, pp. 74–85, 2010.
- [100] NELSON, R. C., “Aircraft stability and automatic control,” 1998.
- [101] NISSIM, E. and LOTTATI, I., “An optimization method for the determination of the important flutter modes,” *Journal of Aircraft*, vol. 18, 1981.
- [102] NORTHINGTON, J. S., “Basis vector quantification of flutter analysis structural modes,” *Journal of Aircraft*, vol. 46, no. 6, p. 2107, 2009.
- [103] PALUTIKOF, J., HALLIDAY, J., WATSON, G., HOLT, T., BARTHELMIE, R., COELINGH, J., FOLKERTS, L., and CLEIJNE, J., “Predicting the wind energy resource in the offshore seas of europe,” in *Symposium on Environmental Applications; American Meteorological Society 82*.
- [104] PATIL, M. J. and HODGES, D. H., “Output feedback control of nonlinear aeroelastic response of a slender wing,” *Journal of Guidance, Control and Dynamics*, vol. 25, pp. 302 – 308, Mar.-Apr. 2002.
- [105] PATIL, M. J. and HODGES, D. H., “Flight dynamics of highly flexible flying wings,” *Journal of Aircraft*, vol. 43, no. 6, pp. 1790–1799, 2006.
- [106] PATIL, M. J., HODGES, D. H., and CESNIK, C. E. S., “Nonlinear aeroelasticity and flight dynamics of high-altitude long-endurance aircraft,” in *Proceedings of the 40th Structures, Structural Dynamics and Materials Conference, Saint Louis, Missouri*, pp. 2224 – 2232, April 12 – 15, 1999. AIAA Paper 99-1470.
- [107] PATIL, M. J., HODGES, D. H., and CESNIK, C. E. S., “Limit cycle oscillations in high-aspect-ratio wings,” *Journal of Fluids and Structures*, vol. 15, pp. 107 – 132, Jan. 2001.
- [108] PATIL, M. J. and TAYLOR, D. J., “Gust response of highly flexible aircraft,” in *Proceedings of the 47th Structures, Structural Dynamics, and Materials Conference, Newport, Rhode Island*, (Reston, Virginia), AIAA, May 2006. AIAA-2006-1638.
- [109] PATIL, M. J., “Decoupled second-order equations and modal analysis of a general non-conservative system,” in *Proceedings of the AIAA Dynamics Specialists Conference, Atlanta, Georgia*, (Reston, Virginia), AIAA, April 3 – 6, 2000. AIAA Paper 2000-????
- [110] PATIL, M. J. and HODGES, D. H., “Flight dynamics of highly flexible flying wings,” in *CEAS/AIAA/DGLR International Forum on Aeroelasticity and Structural Dynamics, Munich, Germany*, June 28 – July 1, 2005.
- [111] PETERS, D. A., KARUNAMOORTHY, S., and CAO, W.-M., “Finite state induced flow models; part I: two-dimensional thin airfoil,” *Journal of Aircraft*, vol. 32, pp. 313 – 322, Mar.-Apr. 1995.
- [112] POLLAYI, H. and YU, W., “Modeling matrix cracking in composite rotor blades within VABS framework,” *Composite Structures*, vol. 110, pp. 62–76, 2014.
- [113] PRYOR, S., NIELSON, M., BARTHELMIE, R., and MANN, J., “Can satellite sampling of offshore wind speeds realistically represent wind speed distributions? part ii: Quantifying uncertainties associated with distribution fitting methods,” *American Meteorological Society*, vol. 43, pp. 739–750, May 2004.
- [114] RANGEL-RAMIREZ, J. G. and SORENSEN, J. D., “Risk-based inspection planning optimisation of offshore wind turbines,” *Structure and Infrastructure Engineering*, vol. 8, no. 5, pp. 473–481, 2012.
- [115] REETZ, J., “Damage detection on structures of offshore wind turbines using multiparameter eigenvalues,” in *Wind Energy*, pp. 301–304, Springer, 2007.

- [116] REMY, N., SHUTUKA, A., LEVY, B., and CAERS, J., “G<sub>s</sub>tl: the geostatistical template library in c++,” June 2001.
- [117] RESOR, B. R., “Definition of a 5mw/61.5 m wind turbine blade reference model,” *Sandia Report SAND2013-2569*, 2013.
- [118] RICCIARDI, A. P., “Utility of quasi-static gust loads certification methods for novel configurations,” Master’s thesis, Virginia Polytechnic Institute and State University, Blacksburg, Virginia, September 2011.
- [119] RICHARDS, P. W., MARDANPOUR, P., HERD, R., and HODGES, D. H., “Effect of constitutive and inertial properties on body-freedom flutter of a flying wing,” in *54th AIAA/ASME/ASCE/AHS/ASC Structures, Structural Dynamics, and Materials Conference. Boston, Massachusetts*, 2013.
- [120] ROBERTSON, A. N., JONKMAN, J. M., and OTHERS, *Loads analysis of several offshore floating wind turbine concepts*. National Renewable Energy Laboratory, US Department of Energy, Office of Energy Efficiency and Renewable Energy, 2011.
- [121] ROE, K. and SIEGMUND, T., “An irreversible cohesive zone model for interface fatigue crack growth simulation,” *Engineering Fracture Mechanics*, vol. 70, no. 2, pp. 209 – 232, 2003.
- [122] ROTEA, M., LACKNER, M., and SAHEBA, R., “Active structural control of offshore wind turbines,” in *48th AIAA Aerospace Sciences Meeting and Exhibit, Orlando, Florida*, 2010.
- [123] SALE, D., “CoBlade, open source software for composite wind turbine blades.” <https://code.google.com/p/co-blade/>. Accessed: July 2013.
- [124] SALE, D., “HARP Opt, horizontal axis rotor performance optimization.” National Renewable Energy Laboratory. [http://wind.nrel.gov/designcodes/simulators/HARP\\_Opt/](http://wind.nrel.gov/designcodes/simulators/HARP_Opt/). Accessed: July 2013.
- [125] SCHAUMANN, P. and WILKE, F., “Enhanced structural design for offshore wind turbines,” in *XICAT 2006, Xian International Conference of Architecture and Technology*, 2006.
- [126] SCHINDLER, H.-J. and LEINENBACH, C., “Mechanics of fatigue crack growth in a bonding interface,” *Engineering Fracture Mechanics*, vol. 89, pp. 52–64, 2012.
- [127] SHET, C. and CHANDRA, N., “Effect of the shape of t– $\delta$  cohesive zone curves on the fracture response,” *Mechanics of Advanced Materials and Structures*, vol. 11, no. 3, pp. 249–275, 2004.
- [128] SNYDER, B. and KAISER, M. J., “Ecological and economic cost-benefit analysis of offshore wind energy,” *Renewable Energy*, vol. 34, no. 6, pp. 1567–1578, 2009.
- [129] SOBIESZCZANSKI-SOBIESKI, J. and HAFTKA, R. T., “Multidisciplinary aerospace design optimization: survey of recent developments,” *Structural optimization*, vol. 14, no. 1, pp. 1–23, 1997.
- [130] SOTOUDEH, Z., HODGES, D. H., and CHANG, C. S., “Validation studies for aeroelastic trim and stability analysis of highly flexible aircraft,” *Journal of Aircraft*, vol. 47, no. 4, pp. 1240 – 1247, 2010.
- [131] SOTOUDEH, Z., HODGES, D. H., and CHANG, C.-S., “Validation studies for nonlinear aeroelastic trim and stability of HALE aircraft,” in *CEAS/AIAA/DGLR International Forum on Aeroelasticity and Structural Dynamics, Seattle, Washington, June 22 – 24*, 2009.
- [132] STRIZ, A. G. and VENKAYYA, V. B., “Influence of structural and aerodynamic modeling on flutter analysis,” *Journal of Aircraft*, vol. 31.

- [133] SUTHERLAND, H., “On the fatigue analysis of wind turbines,” Tech. Rep. SAND99-0089, Sandia National Laboratories, 1999.
- [134] SUTHERLAND, H. and MANDELL, J., “Effect of mean stress on the damage of wind turbine blades,” in *2004 ASME Wind Energy Symposium, AIAA/ASME*, pp. 32–44, 2004.
- [135] TRUMARS, J. M., TARP-JOHANSEN, N. J., and KROGH, T., “Fatigue loads on offshore wind turbines due to weakly non-linear waves,” in *24th International Conference on Offshore Mechanics and Arctic Engineering*, ASME, 2005.
- [136] UTKIN, V., “Variable structure systems with sliding modes,” *Automatic Control, IEEE Transactions on*, vol. 22, no. 2, pp. 212–222, 1977.
- [137] VAN BUSSEL, G. and ZAAIJER, M., “Reliability, availability and maintenance aspects of large-scale offshore wind farms, a concepts study,” in *DOWEC Concepts Project, 2001*.
- [138] VOLOVOI, V. V., LI, L., KU, J., and HODGES, D. H., “Multi-level structural optimization of composite rotor blades,” in *Proceedings of the 46th Structures, Structural Dynamics and Materials Conference, Austin, Texas*, (Reston, Virginia), AIAA, April 18 – 21, 2005. AIAA Paper 2005-2282.
- [139] VOLUND, P., PEDERSEN, P., and TER-BORCH, P., “165 mw nysted offshore wind farm. first year of operation – performance as planned.,” in *ENERGI E2, Denmark*.
- [140] WANG, L., WANG, B., SONG, Y., and ZENG, Q., “Fatigue loads alleviation of floating offshore wind turbine using individual pitch control,” *Advances in Vibration Engineering*, vol. 12, no. 4, pp. 377–390, 2013.
- [141] WENJIN, Z., FOULADIRAD, M., BERENQUER, C., and OTHERS, “A predictive maintenance policy based on the blade of offshore wind turbine,” in *Annual Reliability and Maintainability Symposium-RAMS 2013*, 2013.
- [142] WETZEL, K., “Defect-tolerant structural design of wind turbine blades,” in *50th AIAA/ASME/ASCE/AHS/ASC Structures, Structural Dynamics, and Materials Conference. Palm Beach, Florida*, 2009.
- [143] WOO, K., NELSON, J., CAIRNS, D., and RIDDLE, T., “Effects of defects: Part b – progressive damage modeling of fiberglass/epoxy composite structures with manufacturing induced flaws utilizing cohesive zone elements,” in *54th AIAA/ASME/ASCE/AHS/ASC Structures, Structural Dynamics, and Materials Conference. Boston, Massachusetts*, 2013.
- [144] XIAO, S., YANG, G., and GENG, H., “Individual pitch control design of wind turbines for load reduction using sliding mode method.,” in *ECCE Asia Downunder (ECCE Asia), 2013 IEEE*, pp. 227–232, IEEE, 2013.
- [145] YAMASHITA, A. and SEKITA, K., “Analysis of the fatigue damage on the large scale offshore wind turbines exposed to wind and wave loads,” in *Proceeding of the 14th International Offshore and Polar Engineering Conference*, pp. 166–171, 2004.
- [146] YANG, B., MALL, S., and RAVI-CHANDAR, K., “A cohesive zone model for fatigue crack growth in quasibrittle materials,” *International Journal of Solids and Structures*, vol. 38, 2001.
- [147] YARRINGTON, P. and COLLIER, C., “Failure analysis of adhesively bonded composite joints via the virtual crack closure technique,” in *47th AIAA/ASME/ASCE/AHS/ASC Structures, Structural Dynamics, and Materials Conference*, 2006.
- [148] YARRINGTON, P., ZHANG, J., COLLIER, C., and BEDNARCYK, B., “Failure analysis of adhesively bonded composite joints,” in *46th AIAA/ASME/ASCE/AHS/ASC Structures, Structural Dynamics and Materials Conference. Austin, TX*, 2005.



- [149] YU, W., “VABS: cross sectional analysis tool for composite beams.” AnalySwift Website. <http://analyswift.com/>. Accessed: July 2013.
- [150] YU, W. and BLAIR, M., “Dnad, a simple tool for automatic differentiation of fortran codes using dual numbers,” *Computer Physics Communications*, vol. 184, no. 5, pp. 1446–1452, 2013.
- [151] YU, W., HODGES, D. H., and HO, J. C., “Variational asymptotic beam sectional analysis – an updated version,” *International Journal of Engineering Science*, vol. 59, pp. 40 – 64, October 2012.
- [152] ZHANG, F. and SOFFKER, D., “Active flutter suppression of a nonlinear aeroelastic system using PI-observer,” in *Motion and Vibration Control*, pp. 367–376, Springer, 2009.
- [153] ZHANG, J., CHOWDHURY, S., ZHANG, J., TONG, W., and MESSAC, A., “Optimal preventive maintenance time windows for offshore wind farms subject to wake losses,” in *12th AIAA Aviation Technology, Integration, and Operations (ATIO) Conference and 14th AIAA/ISSM. Indianapolis, Indiana*, 2012.

# VITA

## Place of Birth

Columbia, SC, United States of America

## Education

2009: Bachelors of Science in Aerospace Engineering, Georgia Institute of Technology. GPA: 3.62

2012: Masters of Science in Aerospace Engineering, Georgia Institute of Technology. GPA: 4.0

2015: Doctor of Philosophy in Aerospace Engineering, Georgia Institute of Technology. GPA: 4.0

## Experience / Employment History

Graduate Research Assistant: 1/14/10 - Present

Analyzed aeroelastic performance stability of advanced composite rotor blades and wings. Developed conceptual design strategies considering aeroelastic stability for rotor blades and wings, including optimization methods. Participated in composite wing structural design of a very high aspect-ratio wing airplane for which a prototype was built. Developed active control technologies for gust load alleviation and flutter suppression for advanced composite rotor blades and wings. Investigating offshore wind turbine blade structural and control design for increased reliability.

Undergraduate Research Assistant: 1/14/2009 - 12/31/2009

Used industry standard CFD methods to analyze airfoils experiencing unsteady aeroelastic effects, including dynamic stall. Investigated unsteady helicopter rotor-fuselage interactions as well as unsteady rotor blade aeroelasticity by examining CFD-CSD results. Used CFD to investigate radial jets found on the upper and lower surface of rotor blades in forward flight and their effect on dynamic stall and presented the results at an AHS conference.

Undergraduate Design Challenges 1/14/2007 – 5/1/2009

Participated in extra-curricular undergraduate design challenges for UAV aircraft and detailed aircraft design. The UAV design challenge was the 2008 Design Build Fly competition, an international competition in which the Georgia Tech team designed a 10 lb UAV and placed 7<sup>th</sup>. Participated in 2009 AIAA Student Design Competition to design a 150-seat eco-friendly transport airplane. Team placed 3<sup>rd</sup> with a unique configuration featuring forward-swept wings and engines mounted over the wing; served as lead of aerodynamics, aeroelastic design, and controls.